Systematic study of the rapid optical-NIR variability of blazars and other AGNs

Dissertation
zur Erlangung des Doktorgrades
des Department Physik
der Universität Hamburg

vorgelegt von
José Nicolás González Pérez
aus Teneriffa, Spanien

Hamburg
2018

Gutachterin/Gutachter der Dissertation:	Prof. Dr. Jürgen H.M.M Schmitt Prof. Dr. Jochen Heidt
Gutachterin/Gutachter der Disputation:	Prof. Dr. Jochen Liske Jun. Prof. Dr. Francesco De Gasperin
Datum der Disputation:	11. Dezember 2018
Vorsitzender des Prüfungsausschusses:	Dr. Robert Baade
Vorsitzender des Promotionsausschusses:	Prof. Dr. Michael Potthoff
Dekan des Fachbereichs Physik:	Prof. Dr. Heinrich Graener

Abstract

This thesis studies the variability of active galactic nuclei (AGN), an intriguing class of objects among the brightest and most energetic sources in the sky. The main focus of my work is the rapid variability of blazars, a particularly interesting class of AGNs. Between 1986 and 1999, an extensive optical/NIR observing program was carried out at the Canary Islands observatories. I took data for a sample of 25 objects. The photometric data were collected during to a total of 393 observing nights, using optical and NIR photometry. In addition, polarimetry (linear polarization) was performed for 7 blazars.

To reach high-precision in the photometry, I developed a new algorithm to extract the target brightness from the images that uses a variable number of comparison stars. Applying this improved method of ensemble-photometry, I was able to reach considerably better photometric accuracy: a precision of $\approx$0.5% for stars of magnitude 15—this corresponds to an improvement of up to 40% compared to standard methods.

For nearby AGNs, I corrected the photometry for the host galaxy contribution. To this end, I disentangled these objects into a galaxy and a point source, by fitting the structural parameters of the host. To my knowledge, my method performs this disentangling for the first time in up to seven filters. The magnitude corrections that need to be applied to the photometry of these AGNs are given in this work and can be used by other observers.

Furthermore, I searched for correlations between the redshift, luminosity, spectral index, mean polarization, and the long-term fractional variability parameter. I found a pronounced correlation between the color and the amplitude of variability, particularly significant for BL Lac objects: redder BL Lac objects show stronger variability.

I analyzed the long-term color variability and studied its correlation with the brightness of the sources. By extracting the spectrum of the variable source, I found that in all objects except for flat-spectrum radio quasars (FSRQ) the variable component is bluer than the observed spectrum itself. Although the spectral indices of BL Lac objects and FSRQs are different, the spectrum of the variable component of FSRQs is similar to that of BL Lacs. Most objects in the sample become bluer when brighter; the only exceptions are FSRQs, whose behavior is explained by a two-component model. In 3C 66A and OJ 287, the best-studied objects here, I found that the relationship between the flux and the spectral index becomes notably more significant when outbursts are considered individually. I found that for the AGNs in my sample, different object types have different locations in the spectral variability parameter vs. spectral index diagram, which I explain with simple models of variability.

Finally, I studied the microvariability (i.e., variability on timescales $< 1\,\mathrm{d}$), one of the most intriguing characteristics of blazars. I introduced a new definition of the duty cycle that corrects for the duration of the observations and takes the different detection levels of microvariability into account. I found microvariability in all classes of objects, even in radio-quiet and radio-loud quasars. In blazars, the microvariability is higher in bluer filters and correlates with the average flux, similarly to the rms-flux relation observed in accreting objects. I found no time lags in the microvariability between the optical bands in BL Lac. From a very rapid decay of the flux in BL Lac, I estimated the magnetic field in the jet to be $\sim 4\,\mathrm{G}$.

Zussamenfassung

Diese Arbeit untersucht die Variabilität von aktiven Galaxienkernen (active galactic nuclei, AGN). Diese faszinierende Objektklasse befindet sich unter den hellsten und energiereichsten Quellen am Himmel. Hauptgegenstand meiner Arbeit ist die schnelle Veränderlichkeit von Blazaren, einer besonders interessanten Klasse von AGNs. Zwischen 1986 und 1999 wurde ein ausgedehntes Beobachtungsprogramm im optischen und nahen Infrarotbereich (NIR) an den Kanarischen Observatorien durchgeführt. In diesem Zusammenhang beobachtete ich die Daten von 25 Objekten in Rahmen von 393 Beobachtungsnächte mit optischer und NIR-Photometrie. Zusätzlich habe ich 7 Blazaren polarimetrisch beobachtet.

Um eine hochpräzise Photometrie zu erreichen, entwickelte ich einen neuen Algorithmus zur Ermittlung der Helligkeit der Quelle mit Hilfe einer variablen Anzahl von Vergleichssternen. Durch Anwendung dieser verbesserten Ensemble-Photometrie konnte ich die photometrische Genauigkeit wesentlich erhöhen: auf eine Präzision $\approx$0.5% für Sterne der Magnitude 15 — das bedeutet eine Verbesserung bis zu 40% im Vergleich zu Standardmethoden.

Für nahgelegene AGNs konnte ich die Photometrie um den Anteil der umgebenden Galaxie korrigieren. Hierzu habe ich erstmalig die Objekte in Galaxie und Punktquelle in verschiedenen Filtern zerlegt, wobei die Strukturparameter der Galaxie gefittet wurden. Die Korrekturfaktoren werden hier vorgelegt und können in Zukunft für andere Beobachtungen verwendet werden.

Weiterhin suchte ich nach Korrelationen zwischen Rotverschiebung, Leuchtkraft, spektralem Index, mittlerer Polarisation und “langzeit fraktionalem Variabilitätsparameter”. Es zeigte sich eine bemerkenswerte Korrelation zwischen spektralem Index und Variabilitätsparameter bei BL Lac Objekten: rotere BL Lac Objekte besitzen höhere Variabilität.

Außerdem habe ich die Langzeitvariabilität der Farbe analysiert und die Relation zwischen Farbe und Helligkeit der Quellen untersucht. Durch Extraktion des Spektrums der variablen Quelle zeigte sich, dass in allen Objekten, außer in *flat spectrum radio quasars* (FSRQs), die variable Komponente blauer ist als das beobachtete Spektrum. Obwohl die spektralen Indices von BL Lac Objekten und FSRQs verschieden sind, gleichen sie sich im Spektrum der variablen Komponente. Die meisten Objekte in der Stichprobe werden gleichzeitig blauer wenn sie heller werden. Die einzige Ausnahme stellen FSRQs dar, deren Verhalten mit einem Zweikomponenten-Modell erklärt wird. Bei 3C 66A and OJ 287, den von mir am besten untersuchten Objekten, ist der Zusammenhang von Helligkeit und spektralem Index deutlich signifikanter wenn die Ausbrüche getrennt betrachtet werden. Ich konnte zeigen, dass in einem Diagramm, in dem den spektraler Variabilitäts-Parameter gegen den spektralen Index aufgetragen wird, verschiedene Objekttypen unterschiedliche Positionen einnehmen. Dies konnte ich mit einfachen Variabilitätsmodellen erklären.

Schließlich untersuchte ich die Mikrovariabilität (Schwankungen auf Zeitskalen $< 1\,\mathrm{d}$), eine besonders faszinierende Eigenschaft von Blazaren. Hier führte ich eine neue Definition von Arbeitszyklus (duty cycle) ein, die auf die Länge der Beobachtung korrigiert und die verschiedenen Detektionsempfindlichkeiten der Mikrovariabilität berücksichtigt. Mikrovariabilität fand sich in allen Objekttypen, unerwarteterweise sogar in radioleise und radiolaut quasaren. In Blazaren ist die Mikrovariabilität höher in den blauen Filtern und korreliert mit dem gemittelten Fluss, ähnlich zur rms-flux-Relation, die man in akkretierenden Objekten beobachtet. Ich konnte keine Zeitverzögerungen in der Variabilität zwischen den optischen Bändern bei BL Lac finden. Aus einem sehr schnellen Abfall des Flusses in BL Lac konnte ich das magnetische Feld im Jet als $\sim 4\,\mathrm{G}$ abschätzen.

Contents

List of Acronyms

ACF Auto-Correlation Function

AGN Active Galactic Nucleus

ANOVA Analysis of Variance

ARIES Aryabhatta Research Institute of Observational Sciences

BCES Bivariate Correlated Errors and intrinsic Scatter estimator

BLR Broad Line Region

BLRG Broad-Line Radio Galaxy

BWB Bluer-When-Brighter behavior

BWB Redder-When-Brighter behavior

CAIN Infrared camera on the CST

CGRO Compton Gamma Ray Observatory

CST Carlos Sánchez Telescope

CTIO Cerro Tololo Inter-american Observatory

DC Duty Cycle

DCF Discrete Correlation Function

DSS Digital Sky Survey

EC External Compton

FoV Field of View

FR I Fanaroff-Riley radio galaxy type 1

FR II Fanaroff-Riley radio galaxy type 2

FR/RSS Flux-Randomization/Random-Subset-Selection

FSRQ Flat-Spectrum Radio Quasar

FWHM Full Width Half Maximum

GASP GLAST-AGILE Support Program

HBL High-energy peaked BL Lac object

HPQ High Polarization Quasar

HQM Hamburg Quasar Monitoring program

HST NASA Hubble Space Telescope

IBL Intermediate-energy peaked BL Lac object

IDV Intra-Day Variability

IRAF Image Reduction and Analysis Facility

ITP International Time Project

JKT Jacobus Kapteyn Telescope

LBL Low-energy peaked BL Lac object

LINER Low-ionization Nuclear Emission-line region

LPQ Low Polarization Quasar

NED NASA Extragalactic Database

NIR Near InfRared

NLR Narrow Line Region

NLRG Narrow-Line Radio Galaxy

NOT Nordic Optical Telescope

ORM Roque de los Muchachos Observatory

OT Teide Observatory

OVV Optically Violent Variable quasar

PA Position Angle

PSD Power Spectral Density

PSF Point Spread Function

QE Quantum Efficiency

QSO Quasi-Stellar Object / quasar

RBL Radio-selected BL Lac object

RLQ Radio Loud Quasar

RQQ Radio Quiet Quasar

SBP Surface Brightness Profile

SED Spectral Energy Distribution

SF Structure Function

SMARTS Small & Moderate Aperture Research Telescope System

SMBH Supermassive Black Hole

SSC Synchrotron Self-Compton

SSRQ Steep Spectrum Radio Quasar

SVC Spectrum of the Variable Component

SVP Spectral Variability Parameter

SpbSU Saint Petesburg State University

TURPOL Turku Photopolarimeter

VLBI Very-Long-Baseline Interferometry

WEBT Whole Earth Blazar Telescope

XBL X-ray-selected BL Lac object

ZDCF Z-transformed Discrete Correlation Function

1

Introduction

1.1 Activity in galaxies

ACTIVE galactic nuclei (hereafter “AGNs”) are among the most energetic and luminous sources in the universe. They are strong emitters over the full electromagnetic spectrum, from radio wavelengths to the X-rays and γ-rays range. The extraordinary amount of energy that these objects radiate originates in a very small spatial region.

The adjective “active” refers to the energetic phenomena operating in the central nucleus of these objects, which cannot be ascribed directly to the physics of stars. The spectrum of normal galaxies is the combination of the spectra of individual stars and the emission lines and continuum originated in the gas in star-forming regions. In contrast, most AGNs show strong emission lines broadened up to velocities of 10^4 km/s, which can only be generated by regions subject to a strong gravitational field. Additionally, the line ratios observed in AGNs do not coincide with the line ratios measured in the HII regions (e.g., Veilleux & Osterbrock 1987), but require a harder ionizing spectrum (Kewley et al. 2006). Now it is accepted that AGNs are powered by the accretion of matter onto a central supermassive ($M \geq 10^6$ $M_\odot$) black hole (SMBH, Krolik 1999, Padovani et al. 2017).

The luminosities of AGNs can outshine the host galaxy by a factor as large as $10^3 - 10^4$, reaching values between $10^{42} - 10^{48}$ ergs s^{-1} (e.g., Krolik 1999). These values should, however, be taken with care: if the luminosity of the AGN were lower, it would be challenging to detect it on top of the "normal" nuclear emission of the galaxy, and also many AGNs are obscured by the torus (see below). Besides, Doppler beaming makes some sources appear much brighter than they intrinsically are.

The masses of SMBH present in AGNs range between 10^6 and 10^9 $M_\odot$. SMBHs are not only found in active galaxies, but they are, in fact, common in the nucleus of massive galaxies—it is believed that there exists an SMBH with a mass of $\sim 4 \times 10^6$ $M_\odot$ in the nucleus of the Milky Way (e.g., Schödel et al. 2002, Gillessen et al. 2009). Particularly interesting is the fact that the mass of an SMBH is related to the mass of the bulge of its host galaxy (Kormendy & Richstone 1995 and referenced therein). This relation implies that there is a connection between the growth rates of the SMBH and the galaxy itself. It has been suggested that the SMBH growth is regulated by the feedback from the AGN by jets or hot winds (e.g., Silk & Rees 1998, Di Matteo et al. 2005).

Variability is one of the most striking characteristics of some AGNs. Intensity variations in timescales from years to minutes have been observed in the whole electromagnetic spectrum (e.g., Hughes et al. 1992, Aharonian et al. 2007), which implies extremely compact emitting regions.

1.2 A brief historical background

The observational research on active galaxies started out in the early twentieth century, when Fath (1909), working at the Lick Observatory, performed spectroscopic observations of the central regions of several "spiral nebulae" and noted the presence of six strong emission lines in NGC 1068. Later on, Slipher (1917), taking a higher quality and better resolution spectrum of the galaxy, confirmed these emission lines and noticed, furthermore, that they were also very broadened.

Although several astronomers reported the existence of emission lines at the center of other spiral nebulae, it took almost three decades, until the systematic study of galaxies with nuclear emission lines began. In 1943 Carl Seyfert completed an analysis of six extragalactic nebulae with emission lines in their nuclei. He found that several objects presented narrow forbidden and permitted lines, while some others showed narrow forbidden lines and narrow cores in their permitted lines, but Balmer lines with broad wings. He attributed the broadening of the lines to a Doppler effect (Seyfert 1943). Systems with high-excitation nuclear emission lines were called "Seyfert galaxies". Later on, Woltjer (1959) analyzed several Seyfert objects and concluded that their nuclear regions were very massive and compact (sizes $\leq$ 100 pc). Following that, Seyfert galaxies were classified, according to the type of their emission lines, into two categories: Seyfert 1 and Seyfert 2. Seyfert 1 galaxies present very broad permitted emission lines (FWHM$\sim$1000-10000 km/s) and narrower emission forbidden lines (FWHM$\sim$100-1000 km/s), whereas Seyfert 2 galaxies present permitted and forbidden lines with roughly the same FWHM, similar to the FWHM of the forbidden lines in Seyfert 1.

The fast development of radio astronomy, in particular after the end of the Second World War, had a considerable impact on AGN research. Radio surveys led soon to the discovery of large populations of radio sources in the sky and, consequently, a significant effort was invested in the position determination and optical identification of these objects. Smith (1951), performing interferometry, provided the first precise positions of four radio sources, namely, Taurus A, Cygnus A, Cassiopeia A, and Virgo A. Baade & Minkowski (1954), using the accurate positions supplied by Smith, identified the optical counterparts of Cas A and Cyg A: Cas A was recognized as a galactic emission nebulosity of a new type (a supernova remnant), whereas Cyg A turned out to be an extragalactic object with a redshift of z=0.056. The rich emission line spectrum of Cyg A proved to be very similar to the spectra of Seyfert galaxies. Further advances in interferometry permitted the study of the spatial structure of these radio sources. Jennison & Das Gupta (1953) found that Cyg A was made of two equally bright components, in the form of lobes, separated by 1.5′, and the optical image was located halfway between these lobes. This unexpected morphology turned out to be common among extragalactic radio sources.

In 1959, the first large catalog of radio sources was published, "The Third Cambridge Catalogue of Radio Sources" (3C, Edge et al. 1959), a collection of almost 500 objects at 159 MHz. Soon after, the revised version appeared with a list of 328 sources at 178 MHz (3CR, Bennett 1963). During the following years, great effort was invested in the search for the optical counterparts of these sources.

A breakthrough in the field took place when Hazard et al. (1963), taking advantage of the method of lunar occultation, measured the structure and position of the radio source 3C 273. Its position could be determined to an accuracy of better than 1", and the optical counterpart was associated with an object of star-like appearance. Without delay, Schmidt (1963) obtained the spectrum of the star-like source, and found several bright and broadened emission lines, at first glance difficult to associate with known elements. He soon realized (presumably amazed) that the emission lines corresponded to the Hydrogen Balmer series, but were redshifted to an (at that time) breathtaking z=0.158! With this value, he was also able to identify Mg II λ2798. Such a large redshift had important physical implications: a cosmological redshift of 0.158 (corresponding to an apparent velocity of 47400 km s^{-1}) implied a distance of about 500 Mpc and, at this distance, the apparent flux of the object involved huge amounts of energy. Thus, 3C 273 was an extragalactic object with an extraordinary luminosity, by far the most luminous object ever observed. Right away, other 3C radio sources were also discovered to have large redshifts, as for example, 3C 48 with z=0.367 (Greenstein & Matthews 1963) and 3C 47 and 3C 147, with z=0.425 and 0.545 respectively, (Schmidt & Matthews 1964).

These results changed the field of extragalactic astronomy in a fundamental way: a new class of objects had been discovered. These objects, extragalactic and extremely luminous radio sources with point source appearance in the optical, were named quasi-stellar radio sources, abbreviated as quasars (Greenstein & Schmidt 1964). It was soon revealed that quasars had very blue colors, indeed much bluer than most stars, which permitted to develop search techniques working in the optical domain. Sandage (1965) showed that the majority of quasars had weak radio emission compared with the optical, and consistently, renamed these objects, as quasi-stellar objects (QSO)—regardless of their radio emission. Nowadays both terms, quasars and QSO, are used interchangeably. Further work showed that quasars had indeed even stranger properties. It was shown that many showed variability, on timescales which could be as short as a year.

Just as in the Seyfert galaxies, quasars exhibit two distinct classes of line profiles. Although a connection between QSO and Seyfert galaxies was soon suspected, the investigations on these two classes of objects ran parallel for many years.

BL Lac was discovered by Hoffmeister (1929), formerly classified as a variable star of short period and variability amplitudes higher than two magnitudes. It was detected later as a radio source by Schmitt (1968). This object is the prototype of a new class of AGNs, BL Lac objects, that present high variability and polarization and whose optical spectrum displays a featureless continuum.

In the late 1980s and during the 1990s, much effort was dedicated to the search for a simple model that could explain the different types of AGNs. Antonucci & Miller (1985) discovered that the optical spectrum of the polarized light of NGC 1068 presents not only the narrow emission lines observed before but also broad lines. Urry & Padovani (1995) reviewed the unification models that says that, at least, part of the differences between the types of AGNs are due to inclination effects. For some objects, the broad line regions are occulted by dust, while from another viewpoint this region can be observed. Sect. 1.5 describes the unification models in more detail.

Baade (1956) reported for the first time that the jet of M 87 was strongly polarized in the optical bands. It was suggested that the emission of the jet is due to synchrotron radiation, as in the Crab Nebula. Hoyle & Fowler (1963) proposed that the gravitational energy could play a crucial role in radio sources and the contraction of a supermassive object under its intense gravitational field delivers the energy necessary to explain the AGN phenomenon. Blandford & Rees (1974) described the first model of the formation of the relativistic jet, where the internal energy of the accreting plasma is transformed to the kinetic energy of the collimated jet.

1.3 The physical picture of AGNs

During the last four decades, the understanding of AGNs has been dramatically improved. In the presently accepted black-hole paradigm, the activity is driven by matter, which is being accreted by an SMBH located at the AGN center. Figure 1.1 shows the main physical components of a radio-loud AGN within this model: the central SMBH, the accretion disk, the jets, a torus of dust and gas, the broad and narrow line regions and the hot corona. Their basic characteristics are shortly summarized below.

1.3.1 The central supermassive black hole

It is now accepted that the center of AGNs harbors an SMBH, with masses ranging from 10^6 to 10^9 $M_\odot$. Observational evidence supports the existence of SMBHs: Ford et al. (1994) measured the velocities of the gas near the core of the radio galaxy M 87 and claimed that the only explanation for the results would be that at the center there is a black hole with a mass of 2.4×10^9 $M_\odot$. Miyoshi et al. (1995) observed a water maser rotating in a sub-parsec region at the center of the galaxy NGC 4258: the rotation velocities observed could only be explained by an SMBH with a mass of 4×10^7 $M_\odot$. Also, the short timescales of variability observed in many AGNs constrain the size of the emitting region in such a way, that an SMBH is the only plausible explanation.

The characteristic size scale of a black hole is the Schwarzschild radius $R_S = 2GM_{BH}/c^2$, where G is the gravitational constant, M_{BH} is the mass of the black hole and c the speed of light. The spin of the black hole is another characteristic of the black hole and may have strong influence in the formation of the jet (Blandford & Znajek 1977).

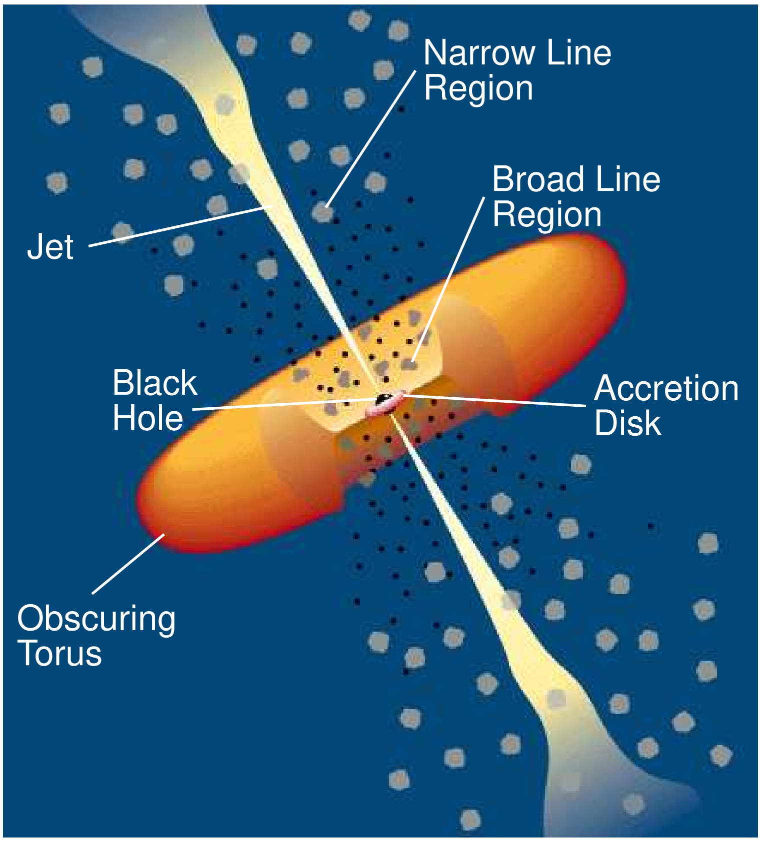

FIGURE 1.1— Schematic structure of a radio-loud AGN. (Credit: Urry & Padovani 1995) from https://heasarc.gsfc.nasa.gov/docs/cgro/images/epo/gallery/agns/index.html)

1.3.2 The accretion disk

While matter is falling onto the SMBH, an accretion disk is formed, due to the conservation of angular momentum. Through viscous and turbulent processes, this accretion disk loses momentum, and consequently, the matter is heated. The disk emits radiation, mostly in the UV and X-ray spectral regions: this is the source of the optical continuum in non-blazar AGNs.

The luminosity produced by the accretion is:

$$L = \eta \dot{M} c^2, \tag{1.1}$$

where $\dot{M}$ is the accretion rate and η is the radiative efficiency, which has been estimated to range between 0.06-0.40, much larger than the efficiency for stellar thermonuclear reactions. However, radiation pressure also hinders the accretion, so that the radiation pressure cannot exceed gravity. In case of spherically symmetric accretion, the upper limit of the luminosity of the accretion is the Eddington luminosity:

$$L_E = \frac{4\pi G M_{BH} m_p c}{\sigma_T}, \tag{1.2}$$

where m_p is the mass of the proton and σ_T is the Thomson cross-section. This luminosity corresponds to an accretion rate of

$$\dot{M}_E = 4\pi \frac{G M_{BH} m_p}{c \sigma_T} \tag{1.3}$$

The accretion disk is responsible for acceleration the particles to highly relativistic energies in narrowly collimated outflows, the jets.

1.3.3 The jets

About 10% of all AGNs exhibit jets emanating from their central region (e.g., de Vries et al. 2006). These jets are made of highly collimated plasma launched perpendicular to the accretion disk. It is believed that the jet plasma is driven by twisted magnetic field lines threading the accretion in a direction parallel to the disk axis and the jet is collimated by the interaction of the twisted magnetic field and ionized material from the disk (Blandford & Königl 1979; Blandford & Payne 1982; Spruit 2010). The exact details of these processes remain, however, poorly understood.

The jet is composed of either plasma (electron-proton) or pair plasma (electron-positron). In the jet, the flow of radiation and energetic particles at relativistic velocities cool off through synchrotron and inverse Compton radiation. Synchrotron radiation is produced by charged particles moving at relativistic velocities in the presence of a magnetic field (see Sect. 1.6.3). Compton scattering is the interaction of a charged particle with a high-energy photon, in which the photon transfers energy to the particle. In the inverse Compton scattering, on the contrary, a relativistic particle interacts with a low-energy photon, and in the end, the photon gains energy (see Sect. 1.6.4).

Jets can form giant radio structures, extending from a few hundreds of kpc to several Mpc. They can interact with the surrounding intergalactic medium and form lobes of turbulent plasma (Blandford & Königl 1979).

1.3.4 The broad line region

The broad line region (BLR) is made of clouds of gas and dust moving rapidly around the black hole. These clouds are located at a distance of ~1 pc from the SMBH and are photoionized by the hot accretion disk. Emission lines with widths of $10^3 - 10^4$ km/s originate in the BLR. The BLR presents high number densities $\sim 10^9$ cm^{-3} or larger, and temperatures of the order of 10^4 K (e.g., Beckmann & Shrader 2012, Gaskell 2009).

The BLR spectrum has been used to determine the mass of the central black hole with reverberation mapping. This method assumes Keplerian motion and the distance at which the BLR is located can be calculated using the delay between variations in the continuum and the emission lines (Netzer & Peterson 1997 and references therein).

1.3.5 The torus

Outside the accretion disk, there is a so-called torus of dust, optically thick to radiation. The exact shape of this structures is not known. It has been speculated that it is (i) a flared disk, where the height of the disk is larger at larger distances from the SMBH (Fritz et al. 2006), (ii) a tapered disk, with a structure similar to the flared disk, but at certain distance it reaches a maximum height, and the height stays constant at larger distances (Efstathiou & Rowan-Robinson 1995), or (iii) a clumpy torus (Nenkova et al. 2008). The torus absorbs the light of the accretion disk and the BLR and re-radiates it in the infrared.

1.3.6 The narrow line region

In this region, located beyond the torus, the narrow emission lines are generated; these lines are narrow in comparison to the broad lines, but still much broader (from 200 to 1000 km/s) than the emission lines in normal galaxies, which are generally originated in regions of star formation. Narrow line regions (NLRs) are located at 10–100 pc from the SMBH and have been spatially resolved in nearby Seyfert galaxies (e.g., Kraemer et al. 2008). They show densities much lower than the BLR ($10^3 - 10^5$ cm^{-3}) and a temperature of $\sim$ 15000 K. Therefore, forbidden and permitted lines are observed. Both the BLR and NLR have low filling factors, which implies that their structure is clumpy, with many individual clouds (e.g., Ferland & Mushotzky 1982).

1.3.7 The hot corona

Around the accretion disk, there is a layer of energetic electrons, known as the corona. The corona is responsible for some X-ray radiation via inverse Compton scattering or bremsstrahlung by these electrons. Its geometrical shape is not known (e.g., Reynolds & Nowak 2003).

1.4 Clasification of AGNs

The early classification of AGNs started out from only the observational characteristics of these objects and the selection method applied. This classification could not take their physical properties into account—they were mostly unknown at that time. As a consequence, a large number of AGN classes emerged (Tadhunter 2008, Padovani et al. 2017), mainly reflecting their different appearances, and giving rise to a rather confuse “AGN zoo”.

A recent review by Padovani et al. (2017) compiles about 50 types of AGNs (see their Table 1), and the authors remark that this list is probably incomplete. It is now clear, however, that many of these classes do not represent distinct physical types of objects. For instance, the optically violent variable quasars (OVV) and the high polarization quasars (HPQ), are now encompassed in the flat-spectrum radio quasar class. Also, the names X-ray-selected BL Lac objects (XBL) and radio-selected BL Lac objects (RBL) are not used anymore, but BL Lac objects are instead divided into low-energy peaked BL Lacs and high-energy peaked BL Lacs depending on the frequency of the peak of their synchrotron component.

In particular, the fact that AGNs are strong emitters over the full electromagnetic spectrum implied that these objects were discovered and classified separately in the different wavelengths regions. The main recognized classifications of AGNs are based on their degree of radio loudness or on their emission line spectra.

A first classification separates the AGNs into radio-loud (RL) and radio-quiet (RQ). Generally, this division is made using the radio loudness parameter $R_L = log(F_{5GHz}/F_B)$—the logarithm of the ratio of the fluxes at 5 GHz and the optical filter B. Those AGNs with $R_L < 1$ are considered radio-quiet and those with $R_L > 1$, radio-loud. Only $\sim 10\%$ of the quasars are radio-loud (e.g., Kellermann et al. 1989, de Vries et al. 2006). However, note that radio-quiet does not mean radio silent (Padovani 2016).

A better designation for this division has recently been proposed since the radio-quiet label may be misleading (e.g., Padovani 2016). One should speak of jetted AGNs for those objects with strong relativistic jets and of non-jetted AGNs, for those without one.

A second categorization is based on the optical spectrum, considering the type and strength of the emission lines. Type 1 objects exhibit broad (FWHM$\sim 1000 - 10000$ km/s) permitted emission lines, such as the Balmer series and MgII. Type 2 AGNs present only narrow (FWHM$\leq$ 1000 km/s) emission lines of both permitted and forbidden transitions. Finally, this historical classification has been extended to the Type 0 objects, which do not show any emission lines or they are very faint.

The most important classes of AGNs are summarized in the following sections:

1.4.1 LINERs

LINERS are the less luminous AGNs, with a luminosity significantly lower than Seyfert galaxies or quasars. The term LINERs stands for low-ionization nuclear emission-line regions and was introduced by Heckman (1980). LINERS display only weak nuclear emission lines, and no other AGN feature. Their spectra are characterized by the relative strength of lines arising from lower ionization states (e.g., [OII]λ3727, [OI]λ6300 or [NII]λ6584) than in other AGNs.

LINER emission is common in the nuclei of galaxies. It has been claimed that they may be present in $\sim 30 - 40\%$ of all spirals (Ho et al. 1997). However, the power source of LINERs is still under debate. It is particularly interesting to discover whether LINERs are indeed AGN, or whether some other mechanism is responsible for their nuclear emission.

1.4.2 Seyfert galaxies

Seyfert galaxies constitute the most common class of AGN in the local Universe. They are typically spiral galaxies that exhibit strong emission lines in their nucleus and show weak radio emission. Regarding their spectral characteristics, Seyfert galaxies have been classified in two groups: Seyfert 1, which have permitted emission lines much broader than the forbidden lines, and Seyfert 2, in which the permitted and forbidden lines have similar velocity widths, both about 1000 km/s. Seyfert 1 galaxies display, apart from broadened lines, a bright star-like nucleus, and a strong continuum from IR to X-rays. Seyfert 2 galaxies, on the other hand, have a weak continuum.

1.4.3 Radio galaxies

Radio galaxies are active galactic nuclei with very strong radio emission (from 10^{45} to 10^{46} erg s^{-1}), typically hosted by giant elliptical galaxies. The dominant source of radio emission is synchrotron radiation from relativistic electrons.

These objects generally display extended radio structures up to Mpc scales. According to their radio morphology, they have been further divided into two groups: the low-luminosity Fanaroff-Riley type 1 (FR I) and the high-luminosity Fanaroff-Riley type 2 (FR II; Fanaroff & Riley 1974). In the FR II objects, characterized by powerful edge-brightened double lobes, sometimes with prominent hot spots, the intensity falls towards the nucleus. In contrast, the radio emission of FR I sources peaks near the nucleus and the jets become fainter when moving away from the center. In FR I radio galaxies only diffuse edge-darkened lobes are present. These differences are probably intrinsic and are caused by more powerful jets in FR II galaxies. As another possibility, this distinction may be caused by the different ambient media surrounding the central engine.

It is often observed that FR I radio galaxies are located in a dense environment, e.g., the center of a cluster, while the FR II radio galaxies are typically observed in a less dense environment, e.g., at the edge of the galactic clusters.

In terms of the properties of the AGN core in radio galaxies, these objects resemble Seyfert galaxies. One finds two optical spectral types, Type 1 and 2. Radio galaxies of Type 1 are called broad-line radio galaxies (BLRG), and those of Type 2 are narrow-line radio galaxies (NLRG).

1.4.4 Quasars

These objects are similar to Seyfert 1 galaxies but with a brightness several orders of magnitude higher, so that the active nucleus outshines the host galaxy. Given the fact, that quasars are the most luminous AGNs and, indeed, the most luminous non-transient objects known, they can be detected out to very large redshifts. More than 115 quasars at redshifts of $z > 6$ had been detected until 2017 (Bosman 2017), two of them with redshifts $z > 7$: ULASJ1120+0641 with a redshift z=7.09 (Mortlock et al. 2011) and ULASJ1342+0928, with a redshift z=7.54, the highest redshift quasar known to date (Bañados et al. 2018). An important characteristic of quasars is their strong variability.

Quasars can be classified as radio-loud quasars (RLQ) and radio-quiet quasars (RQQ), depending on their radio luminosity. RLQs are further divided into steep-spectrum radio quasars (SSRQ) and flat-spectrum radio quasars (FSRQ) according to their spectral index in the radio. The threshold is defined as the spectral index $\alpha = -0.5$, assuming that the radio spectrum can be described as a power law ($F_\nu \propto \nu^\alpha$). Most of the quasars are radio-quiet: the radio-loud represent only $\sim 10\%$ of the quasar population.

1.4.5 Blazars

Blazars are a subclass of RLQs characterized by strong and rapid flux variability in the whole electromagnetic spectrum (e.g. Heidt & Wagner 1996, Wagner & Witzel 1995), strong polarization from radio to optical wavelengths (Fan et al. 1997, Impey et al. 1982, Takalo et al. 1994), and superluminal motion (e.g., Moore & Stockman 1984; Homan et al. 2001; Jorstad et al. 2001). The extreme properties of blazars are explained by assuming that the relativistic jet points close to the line of sight (e.g., Blandford & Rees 1978) and, therefore, relativistic effects boost the observed brightness and increase the variability and polarization. These objects are found to reside typically in elliptical galaxies (Wurtz et al. 1996).

Blazars comprise the BL Lac objects and the FSRQs. BL Lacs do not show prominent emission lines—in some cases they do not show emission lines at all. A criterion based on the equivalent width of emission lines has been adopted to discriminate between FSRQs and BL Lac, with a "cutting limit" of $EW = 5$Å, i.e., BL Lacs have only emission line equivalent widths below 5Å. In particular, OVVs, HPQs, and core dominated quasars are FSRQs that have been selected due to their variability, polarization, and radio morphology, respectively.

The radiation emitted by blazars is predominantly non-thermal, except for the big blue bump observed in FSRQs, a feature produced by the accretion disk. The continuum emission is dominated by the relativistically beamed radiation of the jet. The spectral energy distribution (SED) of the blazars is characterized by a double hump structure (see Fig. 1.2). The first component dominates at lower frequencies, from radio to UV/X-rays, and the second component dominates at higher energies, usually peaking at GeV to TeV energies (e.g., Fossati et al. 1998, Ghisellini et al. 1997, Giommi et al. 1995).

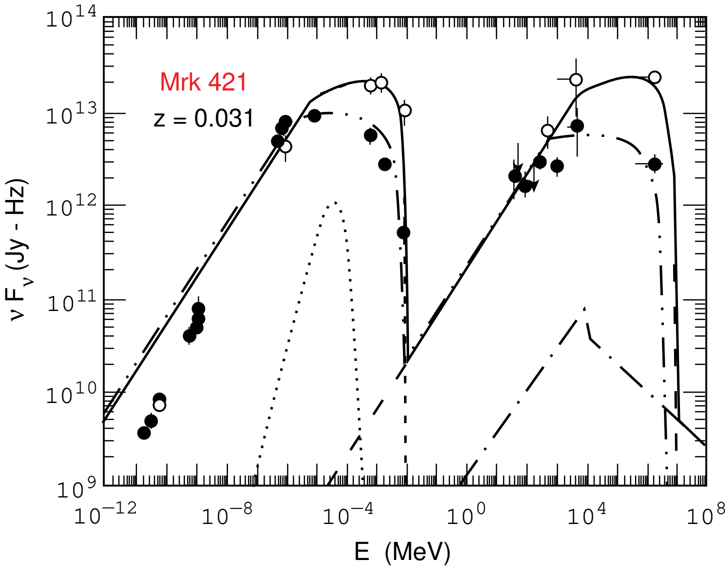

FIGURE 1.2— Spectral energy distribution of the BL Lac object Mrk 421. Credit: M.A. Catanese (Iowa State U.)

The lower energy component is believed to originate from synchrotron emission emitted by non-thermal electrons in the relativistic jet. The origin of the second component is controversial. Some authors believe that it arises from inverse Compton scattering of low-energy radiation by the same electron population that is responsible for the synchrotron radiation. The source of the low-energy photons can be the synchrotron radiation (synchrotron self Compton scenario, SSC), or external photons from the accretion disk, broad line region or the dusty torus, the external Compton scenario (e.g., Kirk et al. 1998, Sikora et al. 1994). Other authors consider, on the contrary, that the second component is originated by hadronic processes initiated by relativistic protons accelerated to relativistic velocities (e.g., Böttcher 2007).

Taking into account the frequency of the peak of the lower energy component (ν_{peak}), blazars have been divided into low-energy peaked (LBL), intermediate-energy peaked (IBL) and high-energy peaked blazars (HBL; e.g., Padovani & Giommi 1995). In LBLs the peak of the first component lies in the near-infrared (NIR)/optical region ($\nu_{peak} < 10^{14}$ Hz) and in HBL in the UV/X-rays regime ($\nu_{peak} > 10^{15}$ Hz; Nieppola et al. 2006). FSRQs usually have an SED similar to LBLs.

The LBL-IBL-HBL classification had led to the definition of the blazar sequence. Using a sample of blazars, Fossati et al. (1998) found that the ν_{peak} is anticorrelated with the source bolometric luminosity, which means that the most luminous blazars have the lowest ν_{peak}. Thus, the frequencies of the lower and higher energy peaks are correlated. They also observed that the most luminous objects have a more prominent high-energy component, i.e., the ratio of the luminosity of the high-frequency and low-frequency components increases with the bolometric luminosity. Today, the blazar sequence has been called into question, and it is seen as the result of the sample selection (e.g., Caccianiga & Marchã 2004; Padovani 2007; Ghisellini & Tavecchio

2008).

There has been some discussion about the difference between BL Lacs and FSRQs. It seems that the absence of emission lines in BL Lac objects is not due to stronger dilution by the jet, but it is intrinsic. Ghisellini et al. (2009) suggested that the differences are governed by different accretion regimes. At low accretion rates, the disk radiates inefficiently, leading to a weak ionizing flux, which results in weak emission lines as observed in BL Lacs. Because of the faintness of the disk and the absence of emission lines, there is not much external radiation that can be upscattered by the inverse Compton effect. If the accretion is more effective, the ionizing radiation is stronger, which implies stronger emission lines as observed in FSRQs and stronger ambient radiation available to cool the electrons of the jet by the inverse Compton scattering (external Compton scenario).

1.5 The unification model of AGNs

The classification of AGNs was built up during the last decades, based mostly on the appearance of the sources in different spectral regions. An important question underlying every classification scheme is whether their classes represent distinct physical systems. In the case of AGNs, it was promptly clear, that the classification was complex and confused, and that the different classes frequently represented different appearances of the same objects.

Unification models appeared with the goal to bring some order to the zoo of AGNs. The idea of the unification scenarios is that the large variety of AGN observed properties can be explained by a relatively small number of physical parameters.

The development of unification models started when it was realized that projection effects could explain the differences between the Type 1 and Type 2 Seyfert galaxies. Rowan-Robinson (1977) suggested the existence of obscuring material, dust, and gas, that could occult the central engine from certain lines of sight. Further, it was proposed that the obscured material be distributed close to the plane of the accretion disk, in a torus or a warped disk (e.g., Pier & Krolik 1992, Sanders et al. 1989). This was supported by observations from Antonucci & Miller (1985), who found broad lines in the polarized light of the Seyfert 2 galaxy NGC 1068.

The basis of the unification models is the inclination of the line of sight relative to the plane of the torus. At high inclinations the accretion disk and the BLR are visible, and thus the continuum is brighter and bluer (due to the influence of the accretion disk), and the spectrum exhibits broad lines. At low inclinations, the torus occults the accretion disk and the BLR, so only the narrow lines are visible. The observations of polarized light in Type 2 galaxies are explained as the scattered light of the BLR by free electrons.

The viewing inclination is also important for the jet. If the axis of the jet is oriented close to the line of sight, relativistic Doppler beaming enormously increases the observed flux of the jet and explains the observational characteristics of blazars (high variability, strong polarization, and superluminal motion).

Unification models have been reviewed by Urry & Padovani (1995), Netzer (2015) and Padovani et al. (2017). A recent unification scheme is depicted in Fig. 1.3. Apart from the

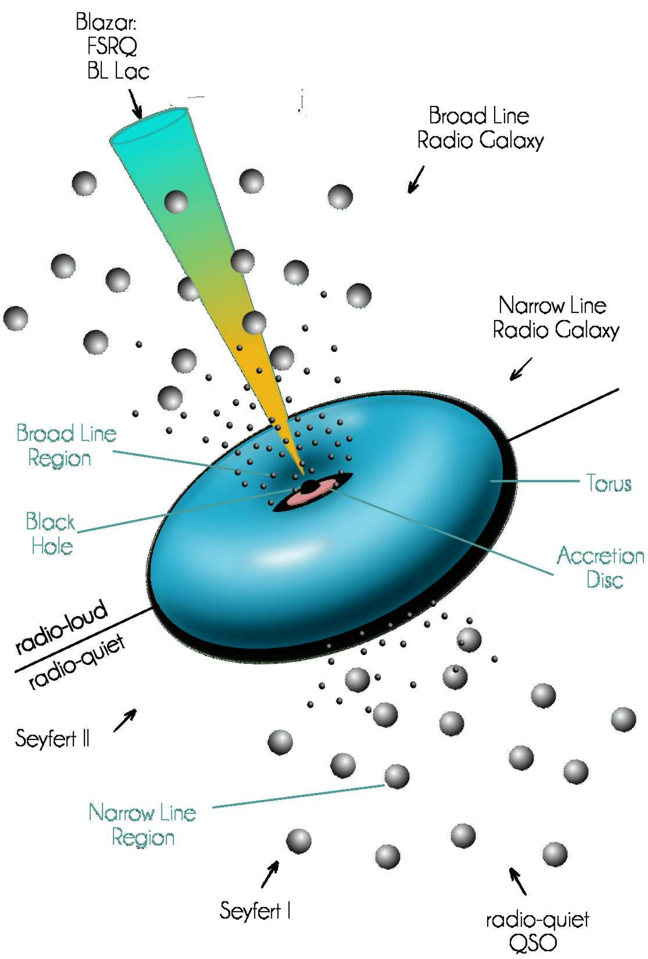

FIGURE 1.3— Diagram of the unified models. Credit: F. Krau after Urry & Padovani 1995

categorization depending on the viewing angle, we have the radio-loud (jetted) and radio-quiet (non-jetted) objects. To the first group belong, sorted by the angle between the jet and the line of sight, blazars, with a small viewing angle and strong Dopper beaming, RLQs, and BLRG, at larger angles, and finally NLRGs, which are observed close to the plane of the molecular torus.

Another parameter to consider is the luminosity or the power. BLRG and NLRG, of type FR I belong to the low power AGNs. BL Lac objects are intrinsically less luminous than FSRQ, and this suggests that the parent population of BL Lac objects are FR I radio galaxies. On the other side, type FR II radio galaxies and quasars belong to the high power objects. FR II radio galaxies would be the parent population of FSRQs. Finally, the radio-quiet group comprises the RQQs, Seyfert 1 and 2 and LINERs.

1.6 Continuum emission mechanisms in AGNs

The emission of AGNs is the sum of the contribution of several emission mechanisms, operating in their different physical components (See Sect. 1.3). Here, we briefly summarize the processes responsible for the continuum emission in AGNs—a more detailed description is provided in, e.g., Rybicki & Lightman (1986) and Ghisellini (2013). The explanation of the mechanisms generating the emission lines is beyond the scope of this thesis and can be found in Osterbrock (1989).

The dominant emission mechanism in blazars is of non-thermal nature. The particles traveling at relativistic speeds in the jets of radio-loud quasars are responsible for the synchrotron radiation and scatter low energy photons to high energies through the inverse Compton process. However, thermal black body emission is dominant in the optical/UV bands in many AGNs. Free-free radiation (bremsstrahlung) may be the responsible process of some X-ray emission radiated by the hot ionized gas located close to the SMBH.

1.6.1 Black body

The emission of a black body, which absorbs all incident radiation and reaches a thermodynamic equilibrium, is dependent solely on the temperature and is described by the Planck's law:

$$u(\nu, T) = \frac{2h\nu^3}{c^2} \frac{1}{exp(h\nu/kT) - 1}, \tag{1.4}$$

where h, c and k are the Planck constant, the speed of light and the Boltzmann constant, respectively. T is the temperature of the black body. The primary source of thermal emission in AGNs is the accretion disk.

The temperature profile of a standard geometrical thick and optically thin disk (Shakura & Sunyaev 1973) decreases with the radial distance as follows:

$$T(r) \propto \left(\dot{M}M\right)^{1/4} r^{-3/4}, \tag{1.5}$$

where $\dot{M}$ is the accretion rate and M is the mass of the central black hole. Therefore, the emission spectrum of an accretion disk is the sum of the emission of the rings at different radii, each one a black body at a certain temperature, and is thus much broader than that of a single-temperature black body. Integrating the Planck's law over all rings, it is obtained that the emitted luminosity of the accretion disk is

$$L_{disk}(\nu) \propto \nu^{1/3}, \qquad \text{if } h\nu \ll kT_{max} \tag{1.6}$$

up to a frequency corresponding to the maximum temperature (T_{max}). Beyond this frequency, there is an exponential drop. At very small frequencies, we see only the black body produced by the outer radius of the accretion disk, and it can be approximated by the Raleigh-Jeans emission of the black body at that radius.

The typical temperatures of accretion disks range between 4000 and 40000 K. This implies that the accretion disk emission is dominant in the optical/UV and is observed in many AGNs as the big blue bump (e.g., Malkan & Sargent 1982).

1.6.2 Bremsstrahlung

Bremsstrahlung or free-free radiation is emitted when a charged particle is accelerated in the presence of a Coulomb field. Typically, an electron interacts with an another charged particle, for example, a proton. This type of scattering takes place, for instance, in hot, but not relativistic plasma, as in the intracluster gas or maybe in the hot corona of an accretion disk.

Bremsstrahlung is an optically thin thermal process. If the opacity increases, the radiation becomes more and more similar to a black body. The bremsstrahlung radiation depends on the total volume of particles involved. The free-free radiation emitted by a thermal particle distribution has a flat spectrum with an exponential cutoff at about $h\nu \sim kT$.

1.6.3 Synchrotron

Synchrotron emission is caused by the acceleration of relativistic particles in the presence of a magnetic field. This is the emission produced by the relativistic plasma of jets in AGNs at frequencies lower than UV/X-rays. The charged particles in the plasma follow helical paths around the magnetic field lines and are continually accelerated by the Lorentz force. The synchrotron emission is linearly polarized.

For a charged particle of mass m, charge e and velocity v, leading to a Lorentz factor of $\gamma = 1/\sqrt{1-(v/c)^2}$, most of the synchrotron luminosity occurs at the critical frequency,

$$\nu_c = \frac{eB\gamma^2}{2\pi mc} \tag{1.7}$$

where B is the magnetic field. Due to the beaming, the radiation is concentrated in the forward direction within a narrow emission cone with a half-angle $1/\gamma$.

If the emitting region is composed of a distribution of particles, with energies following a power law of the form

$$dN(E)/dE \propto E^{-p}, \tag{1.8}$$

where E is the energy of the particles, then the observed synchrotron emission is also a power law $S(\nu) \propto \nu^{-\alpha}$, and the relation between the indices is $\alpha = (p-1)/2$.

This power law only applies if there is no absorption by the emitting regions. For compact regions, the emitted photons can be absorbed by the emitting electrons themselves, the so-called synchrotron self-absorption and produces a spectrum with shape $S(\nu) \propto \nu^{5/2}$.

Therefore, the synchrotron spectrum has two components that both can be represented as power laws, one at lower frequencies with a spectral index of 5/2, modified by the self-absorption, and beyond the turnover frequency, the spectral index of the other section is $-(p-1)/2$.

The cooling time of the electrons due to synchrotron radiation is (e.g., Ghisellini 2013)

$$\tau_{sync} = \frac{24.57}{B^2\gamma} \quad \text{years} \tag{1.9}$$

where B is the magnetic field in Gauss.

1.6.4 Inverse Compton

Compton scattering is the interaction of a charged particle (an electron) with a high energy photon. The photon loses some of its energy and momentum, which are transferred to the electron. For Compton scattering, the energy of the photon is comparable to m_ec^2. Otherwise, when $h\nu \ll m_ec^2$, one speaks of Thomson scattering.

For inverse Compton scattering, we have the reverse situation. A relativistic particle transfers energy to a low-frequency photon, producing a higher frequency photon. In the rest frame of the electron, the process will behave as Thomson scattering.

Inverse Compton is the dominant process that generates the high energy photons in blazars. The relativistic electrons of the jet, the same that cause the synchrotron emission, transform IR/optical photons to X-ray/γ-ray photons.

The inverse Compton requires a dense photon field. There are several possibilities for the source of the low energy photons. First, we have the synchrotron photons emitted by the relativistic electrons of the jet (SSC), which are upscattered to high energies by the same electron population. Second, there can be enough photons coming from an external source: the accretion disk, the broad line regions, or the dust torus. In these cases, we have the external Compton scenario.

The mean energy of the photons after scattering with an electron is larger than before scattering by a factor of γ^2 and the luminosity of the inverse Compton radiation is proportional to the energy density of the seed photon field (U_{ph}),

$$L_{IC} \propto U_{ph}\gamma^2 \tag{1.10}$$

In the case of a relativistic jet, where we have a power-law distribution of particle energies, the luminosity of the inverse Compton radiation is

$$L_{IC} \propto U_{ph}\frac{\gamma_{max}^{3-p} - \gamma_{min}^{3-p}}{3-p}, \tag{1.11}$$

where γ_{max} and γ_{min} are the maximum and minimum Lorentz factors of the electron distribution, and p is the power-law index of the electron distribution (Eq. 1.8).

In relativistic jets, the inverse Compton scattering repeatedly occurs, with the photons gaining energy in the successive scatterings, until the condition $h\nu << m_ec^2$ is no longer satisfied.

The shape of the resulting spectrum depends on the original spectral shape of the seed photons, the electron temperature and the Compton depth of the source.

1.7 Variability in the continuum of blazars and other AGNs

Variability is one of the key characteristics of active galaxies. AGNs show strong flux variations over the entire electromagnetic spectrum, from γ-rays to radio wavelength (Beckmann & Shrader 2012). These variations in luminosity, detected in continuum and broad-band emission, provide a powerful tool to investigate the nature of AGNs (Ulrich et al. 1997). The observed characteristics of the variability can be used to probe the power of the central engine and the physical process in AGNs (e.g., Kawaguchi et al. 1998; Trevese et al. 2001).

The properties of the AGNs variability, i.e., timescale and amplitude, vary over a wide range. Observed timescales range from a few hours to months and years and, while some AGNs show amplitude variations $\leq$0.5 mag in a month, others can change their luminosities by more than 1 mag in hours. According to the characteristics of their variability, AGNs can roughly be separated into two groups. To one group belong objects that can present large amplitudes of variations on short timescales, and to the other, sources with small amplitude variations on timescales of weeks or years—this second group comprises most of the AGNs.

The study of strong and rapid flux variations (also referred as microvariability or intra-night variability) is particularly interesting, because it provides a great amount of information: it allows us to probe the smallest regions that can be observed in AGNs, and it may be used to estimate the mass of the black hole.

In this work, we focussed on the study of the variability of an AGN class, included in the first group above, the blazars. Blazars, the most powerful sources among AGNs, show variability at all wavelengths and timescales explored, from minutes to years. In the optical, they can vary faster than 0.1 magnitudes in an hour and up to $\sim$ 5 magnitudes over long timescales (e.g., Raiteri et al. 2017); in X-rays and γ-rays, their variability amplitudes can be as high as several orders of magnitudes over several days (Feigelson et al. 1986; Mattox et al. 1997). Usually, the variability of blazars has larger amplitudes at frequencies around and above the synchrotron peak (e.g., Ulrich et al. 1997).

Blazars are characterized by relativistic jets, whose angles are presumably closely aligned with the line of sight. Variability in blazars, as the emission, is believed to be dominated by the relativistic jet (Begelman et al. 2008). But some variability may be generated in the accretion disk, by pulsations or hot spots, if the source is in a low state.

The properties of variability depend strongly on the frequency. Therefore, simultaneous multi-band observations are necessary to maximize the constraints of the physics working in the AGNs. Correlations and delays between the flux observed at different wavelengths are key diagnostics of the emission processes. For this reason, many multi-telescope campaigns have been coordinated to monitor several blazars, involving dozens of observatories worldwide to minimize the observing gaps produced by the day-night cycle. An example of one such effort is the Whole Earth Blazar Telescope (WEBT, e.g., Villata et al. 2002b, Bhatta et al. 2013).

Sometimes, multi-wavelength studies have produced contradictory results. The BL Lac object AO 0235+164 has shown clear evidence of a correlation between the radio and the optical data, with the optical preceding the radio by ~ 60 days (Raiteri et al. 2001). This is in disagreement with results obtained by Takalo et al. (1998), who did not find any correlation at smaller timescales and lower states. Osterman et al. (2007) reported a similar behavior: the degree of correlation between the optical and X-ray light curves of the blazar PKS 2155-304 was found to be stronger when the brightness of the source was higher.

The commonly accepted origin for the optical continuum variability in blazars is the propagation of shocks down the jet, which provides an acceleration mechanism for the electrons to reach relativistic velocities. As these shocks propagate, the resulting emission is frequency dependent, and higher frequencies tend to have larger amplitudes of variability (e.g., Marscher & Gear 1985).

Valtaoja et al. (1992) developed a generalized shock model for the variability. Within this model, the evolution of the jet has three stages: growth, plateau, and decay. In the first stage, the peak of the shock moves to lower frequencies, while its flux increases; the cooling of the electrons in this stage is mainly due to Compton losses. In the plateau stage, the emitting region is cooled by synchrotron radiation; the frequency of the peak keeps decreasing, and its flux remains constant. Finally, in the last stage, both frequency and flux of the peak decrease with time and the emitting region expands and cools adiabatically.

An alternative for the origin of the variability is the helical jet model (e.g., Villata & Raiteri 1999, Raiteri et al. 2017). In this scenario, the variability is produced by a change of the viewing angle of the different emitting regions of the jet, which leads to a variation of the Doppler beaming and hence of the observed flux.

1.8 Goals and structure of the Thesis

Much work has been done in the area, yet most of the properties of the blazars variability are still under debate, e.g., the mechanism that originates the rapid variability. The best approach to tackle this question is through multi-band dense monitoring of these sources.

The main purpose of this thesis is the characterization of the variability of blazars, with special emphasis on their short-term (rapid) variability. To achieve this goal, I carried out an extensive optical and NIR monitoring of a small sample of AGNs: the Canary Island Blazars Monitoring Program. For more than a decade (between 1986 and 1999) observations were carried out at the Canary Island observatories. We took photometric data during more than 300 nights: for all objects we took optical broad-band data and for 11 out of the 14 blazars, we also took JHK NIR observations. Besides, we took also polarimetric observations for 7 blazars. The sample is made of 25 objects, 15 blazars and 10 quasars, what enable to compare the variability characteristics of different types of AGNs.

I investigate the properties of the rapid variations of the sample sources, and compare them to their long-term variability, with timescales up to several years, as well as study their spectral changes. The main advantage of this work is the use of an extensive collection of photometric data, taken simultaneously in up to seven broad-band filters. Only with such a large dataset, it is possible to derive the large number of observables required to strongly constraint the predictions of the models.

The size of the sample is large enough to allow to search for general trends and make comparisons among the objects—in particular, between blazars and other types of quasars. On the other hand, the number of objects was kept sufficiently small to permit a thorough study of each of the sources.

The work of this Thesis is structured as follows:

Chapter 2 presents the Canary Island Blazars Monitoring Program, an extensive optical and NIR monitoring program of blazars and other AGNs conducted for more than a decade at the Canary Islands Observatories. Here I introduce the AGN sample, describe the observations and summarize the main steps in the data process. In Chapter 3, I explain the photometric calibration of the data. To reach the required photometric precision, I developed a new algorithm that uses a variable number of stars in the field of view of the target as comparison. Some of the AGNs in our sample are sufficiently close to make the host galaxy visible, which may, therefore, influence the photometry. I outline in Chapter 4 the method applied to correct the photometry of these objects. The host galaxy was modeled with a 2D Sersic profile in all available filters, and this model was used for the photometric correction. In Chapter 5 I present the first results on long-term variability of the sample, with magnitude, color and polarimetric time series. From the light curves, I derived average magnitudes and colors. I also reconstructed the SED of the sources and list the mean polarization and polarization angle. The analysis of the spectral variations and its amplitude are given in Chapter 6. I also present a detailed study of the relationship between the spectral and flux variations. Chapter 7 describes the results of the analysis of the microvariability (variability on timescales less than a day), its amplitudes, color and flux dependence and time lags between the different bands. Finally, the conclusions are presented in Chapter 8.

In Appendix A, I describe some of the most important current and past photometric monitoring of blazars. Appendix B describes some technical topics on the photometry, focusing on those aspects that may have a strong influence on the photometric results. Appendix C lists the photometric correction that needs to be applied to the nearby objects to decontaminate the photometry of these AGNs from the host galaxy. Finally, Appendix D describes the structure function and gives the fit parameters of the structure function.

2

The Canary Islands Blazar Monitoring Program

An extensive optical and NIR monitoring program of blazars and other active galactic nuclei was conducted for more than a decade at the Canary Islands observatories: the Canary Islands Blazar Monitoring Program. The main purpose of this project was to investigate the variability of blazars, with special emphasis on their short-term variability. In this chapter, I introduce the monitoring program, describe the observations and summarize the main steps of the data process. We observed a total of 25 objects—15 blazars and 10 quasars. Photometric data were taken during 393 observing nights: for all objects, we collected optical broad-band photometry, and for 11 (out of the 14) blazars, we also took JHK NIR data. Additionally, polarimetry was done for 7 blazars. Optical data were processed using standard routines available in IRAF, while NIR and polarimetric data required the use of devoted packages.

2.1 The Canary Islands Blazar Monitoring Program

We have performed an extensive observing program of blazars and other AGNs, working for fourteen years at the Canary Islands observatories. The purpose of this program was to study the characteristics and properties of the variability in the continuum of these intriguing objects, mostly by means of optical and infrared photometry. Other types of observations, such as polarimetry, spectroscopy, and spectropolarimetry, were also carried out to complement the photometric information. Specifically, our goal was the study of the photometric variability on timescales ranging from hours to a few days—a common phenomenon of blazars. Additionally, using the same data, we also analyzed other aspects of variability, such as the long-term evolution and the spectral variations.

The sample was deliberately kept small, to ensure that each object receives an acceptable level of light curve coverage. Occasionally, we added sources that were targets of multifrequency campaigns, particularly in coordination with the Compton Gamma Ray Observatory (CGRO).

The optical program started in 1986 at the Jacobus Kapteyn Telescope (JKT), located at the Roque de los Muchachos Observatory (ORM; La Palma). Infrared observations began in 1988, with the Carlos Sánchez Telescope (CST), located at the Teide Observatory (OT, Tenerife). A few IR observations were carried out in Service Observing mode, but most were done in Visitor Mode. At the CST, typically, 3-7 nights of observations were obtained every two months, as it was also the case for the optical observations. It is worth noting that CST was, at that time, the only telescope in the world that maintained a long-term infrared monitoring program of blazars during the duration of this program.

A programme, called OJ-94, jointly coordinated from Tenerife and Tuorla (Finland), was awarded time in 1993/94 as an International Time Project (ITP). This project received 5% of the observing time on the telescopes of the Canary Islands Observatories during the ITP period—half a year in the Autumn of 1993. The main goals of the OJ-94 project were to confirm the predicted optical outburst of OJ 287, and to collect extensive monitoring observations. Apart from OJ 287, a secondary set of blazars (3C 66A, AO 0235+164, S5 0716+71 and 3C 345) were also observed as control objects. After OJ 287, the most extensively observed source during this period was 3C 66A.

After the completion of the ITP programme, we continued with the monitoring of these sources, at the IAC-80 telescope and CST, but with a greater emphasis on the short-term variability with timescales of hours as well as an in the color changes. The objects 3C 273 and 3C 279 were also observed.

In 1996 we started simultaneous optical-NIR monitoring of a small sample of blazars with the CST and IAC-80. These two telescopes are just ∼50 m apart and thus, subject to identical observing conditions. These data allowed us to analyze how the continuum spectrum changes in epochs of microvariability and violent variability. Also, they offer the possibility to distinguish between models and to disentangle the different components of variability.

A description of other important optical and NIR monitoring programs of variability of blazars is presented in Appendix A.

2.2 Observations, data reduction and calibration

2.2.1 The Sample

The selected sample consists of 25 AGNs, which can be grouped in three different sets. Firstly, several blazars were selected as part of the OJ-94 project to study the long-term variability in the visible, NIR or both. These targets were additionally subject to microvariability studies. Secondly, another group of blazars and quasars was added to our program on request for specific observations, especially for multifrequency follow-up simultaneous with high-energy satellite observations. Subsequently, these objects were observed continuously, but with lower frequency. And finally, a group of normal quasars (not blazars), mainly low polarization quasars, were chosen for microvariability studies. There is no difference in the mode of observation or the analysis of the data for these objects.

The final sample of objects is shown in Table 2.1. In column 4 we give the type of AGN; RQQ: radio-quiet quasars; RLQ: radio-loud quasars; FSRQ: flat spectrum radio quasar; and BL: BL Lac object. The redshift is z, V is the mean magnitude in the V-band and finally, S_{6cm} is

TABLE 2.1— Our sample of AGNs.

Object	RA (h m s)	Dec (° ′ ″)	Type	z	V	S_{6cm} (Jy)
III Zw 2	00 10 31.0	+10 58 13	RLQ	0.089	15.4	0.28
I Zw 1	00 53 34.9	+12 41 36	RQQ	0.061	14.4	0.003
NAB 0205+02	02 07 49.8	+02 42 56	RQQ	0.155	15.4	0.002
3C 66A	02 22 39.6	+43 02 08	BL	0.444	15.5	0.81
AO 0235+16	02 38 38.9	+16 36 59	BL	0.940	19.0	1.95
PKS 0405-12	04 07 48.4	−12 11 37	RLQ	0.573	14.8	1.30
PKS 0528+134	05 30 56.4	+13 31 55	FSRQ	2.060	20.0	2.99
S5 0716+71	07 21 53.4	+71 20 36	BL	>0.3	15.5	0.79
87GB 073840.5+545138	07 42 39.8	+54 44 25	FSRQ?	0.723	18.5	0.27
B2 0742+31	07 45 41.7	+31 42 57	RLQ	0.461	15.3	0.96
OJ 287	08 54 48.9	+20 06 31	BL	0.306	15.0	2.65
PG 1008+133	10 11 10.8	+13 04 12	RQQ	1.287	16.2	0.00001
Mkn 205	12 21 44.1	+75 18 38	RQQ	0.071	14.5	0.001
3C 273	12 29 06.7	+02 03 09	RLQ/FSRQ	0.158	12.9	44.63
3C 279	12 56 11.1	−05 47 22	FSRQ	0.536	17.5	13.00
PG 1351+640	13 53 15.8	+63 45 45	RQQ	0.088	14.8	0.032
PKS 1510-08	15 12 50.5	−09 06 00	FSRQ	0.360	16.5	3.25
AP Lib	15 17 41.8	−24 22 19	BL	0.042	15.1	2.01
PKS 1622-29	16 26 06.0	−29 51 27	FSRQ	0.815	20.5	1.86
3C 345	16 42 58.8	+39 48 37	FSRQ	0.593	16.0	7.20
Mkn 501	16 53 52.2	+39 45 37	BL	0.034	14.1	1.37
3C 351	17 04 41.3	+60 44 30	RLQ	0.372	15.3	1.26
II Zw 136	21 32 27.8	+10 08 19	RQQ	0.063	14.6	0.002
BL Lac	22 02 43.3	+42 16 40	BL	0.069	14.5	3.59
3C 454.3	22 53 57.7	+16 08 54	FSRQ	0.859	16.1	15.93

TABLE 2.2— Number of nights observed in each year with each telescope and instrument. Note that the CST was used with two different NIR instruments. The only polarization instrument is TURPOL on the Nordic Optical Telescope (NOT).

	JKT CCD	IAC80 CCD	CST CVF	CST CAIN	NOT TURPOL	Total
1986	15	-	-	-	-	15
1987	9	-	-	-	-	9
1988	3	-	6	-	-	9
1989	8	-	14	-	-	22
1990	-	-	7	-	-	7
1991	-	-	28	-	-	28
1992	-	-	23	-	-	23
1993	3	4	17	-	-	24
1994	4	27	8	-	-	39
1995	7	26	10	-	-	43
1996	-	29	7	1	4	41
1997	-	27	6	13	8	54
1998	24	23	5	24	-	76
1999	-	6	-	9	-	15
Total	73	142	131	47	12	405

the flux density at 6 cm. Redshifts, V-band magnitudes, and flux densities were obtained from the NASA/IPAC Extragalactic Database[1] (NED).

2.2.2 Photometric data

Photometric observations in the optical and near-infrared were obtained during different observing runs from 1986 to 1999. In total, we accumulated data from ∼390 nights. In those cases where the IAC-80 and CST were used simultaneously, the nights are counted separately. On several nights only a few images were taken. Table 2.2 shows the number of nights observed each year with each telescope/instrument combination. The sampling of the observations increased towards the end of the program, especially in 1998, when we obtained measurements for a total of 76 nights. The bulk of the optical observations were carried out with the IAC-80 telescope, while the most extensively used telescope was the CST, with more than 170 nights. Below, we briefly describe the telescopes and equipment used, the techniques employed to perform the observations and the steps followed in the data reduction process.

[1]The NASA/IPAC Extragalactic Database (NED) is operated by the Jet Propulsion Laboratory, California Institute of Technology, under contract with the National Aeronautics and Space Administration; https://ned.ipac.caltech.edu

Photometric observations in the optical

Optical observations were obtained with the 82 cm IAC-80 telescope located at the Teide Observatory and the 1m F/13.8 Jacobus Kapteyn Telescope (JKT) at the Roque de los Muchachos Observatory. The optical photometry of the AGNs was carried out using CCD imaging. At the IAC-80 we worked with a broadband BVRI filter set, whereas in the JKT we used UBVRI.

We collected more than 10,000 images with a total exposure time of more than 700 hours. Total exposure times for each object are displayed in Table 2.3. OJ 287 and 3C 66A were the most extensively observed targets: we took nearly 2,000 images for each one, which translates to more than 150 hours of total exposure time each. Additionally, we collected more than 100 frames for 17 AGNs and the total exposure time is higher than 10 hours for 14 objects. During the period 1990-1992 no optical photometric measurements were obtained.

We have taken CCD images in all broadband optical filters (UBVRI) to obtain color information, but the sampling is better in V and R. This is because we usually observed with a VBVRVIVBV or a VRBVRIVRBV cycle, which provides color information as well as more frequent measurements in V or VR, respectively, for rapid variability.

The image reduction was performed, using the standard procedures available in the IRAF package[2]. The frames were reduced in the usual manner using the routine CCDPROC. The first step was the subtraction of the *bias* level. To do that, we obtained several *bias* images every night. In addition, a section of the chip, the "overscan" region, which typically covers a few tens of columns at the edge of the frames, was used to correct for possible variations in the bias level through the night.

The next step was the flat-field correction, needed to remove the multiplicative gain and illumination variations across the chip. In order to do that, a series of flat fields were obtained of the dawn and dusk sky in each filter (sky flats). When twilight flats were unavailable, dome images with dome lights on were used (dome flats). The set of flat frames taken in each filter was averaged with a rejection algorithm to remove the effects of cosmic ray hits. On some occasions, when we had observations from consecutive nights, a master flat field was built averaging the flat frames taken in all nights, after carefully checking that the flat frames were similar in all nights. Finally, all the science frames were divided by the corresponding normalized flat-field.

In order to calibrate the quasar fields, stars from Landolt (1992) were observed on many photometric nights. These observations allowed us to calibrate the brightness of numerous stars located close to the AGNs that were finally used to calibrate each frame. The calibration of stars in the AGN fields has been presented in González-Pérez et al. (2001).

Photometric observations in the infrared

Infrared observations were taken using the CST, a 1.52 m f/13.3 Cassegrain reflector operating at the Teide Observatory at 2340m. The high altitude ensures that the precipitable water vapor

[2]IRAF: Image Reduction and Analysis Facility distributed by National Optical Astronomy Observatories, operated by the Association of Universities for Research in Astronomy, Inc., under a cooperative agreement with the National Science Foundation (USA). http://www.iraf.noao.edu; http://www.iraf.net

Table 2.3— Total exposure time and number of measurements of the objects in our sample, sorted by RA. While in the optical it is displayed the total exposure time, in the NIR the observations are divided by the instrument used. With the imaging instrument CAIN, it is shown the total exposure time, and with the photometer CVF, it is shown the number of measurements.

Object	Optical (h)	CAIN (h)	CVF meas.
III Zw 2	6.99	–	–
I Zw 1	9.00	–	–
NAB 0205+02	8.39	–	–
3C 66A	151.66	22.54	1513
AO 0235+164	28.91	13.03	103
PKS 0405-12	2.83	–	–
PKS 0528+13	3.17	–	–
S5 0716+71	7.03	–	–
87GB 073840.5+545138	19.90	3.42	–
B2 0742+31	6.79	–	–
OJ 287	159.91	29.54	363
PG 1008+133	5.98	–	–
Mkn 205	22.84	–	–
3C 273	21.19	20.09	212
3C 279	20.32	2.27	152
PG 1351+640	17.96	–	–
PKS 1510-089	2.03	1.55	–
AP Lib	1.87	–	–
PKS 1622-29	3.99	–	–
3C 345	61.63	14.52	226
Mkn 501	21.34	11.88	–
3C 351	23.02	–	–
II Zw 136	20.90	–	–
BL Lac	53.22	11.57	530
3C 454.3	34.56	11.89	–
Total	715.43	142.30	3099

content in the atmosphere above the telescope is very low, as is the ambient temperature at night during most of the year. This gives a high sensitivity and excellent photometric stability. The CST had two instruments available at its Cassegrain focus: a single channel photometer (CVF) and an infrared camera (CAIN). During a period in 1989-90, when the CVF was unavailable due to technical work, a similar backup photometer – the Oxford cryostat – was used.

Due to the high and variable background in the infrared, especially in the band H (because of OH airglow) and K and K_{short} (due to thermal emission of the sky, telescope and dome) a different procedure than in the visible is needed for observing and reducing near-infrared (NIR) data. A typical measurement has contributions from the source, the sky, the background from the warm telescope and dome, and scattered light. Some of these contributions vary not only temporally (even on timescales of minutes), but also spatially. Thus, it is necessary to obtain sky measurements to remove the contribution of the variable background.

CVF photometry: The CVF used an InSb detector, cooled to 50 K with pumped Nitrogen, and a focal plane chopper. A standard ABBA cycle, with an aperture of $15''$, a typical chopper throw of $25''$ in East-West direction and a chopper frequency of 8 Hz were used. With this configuration another infrared source was located in the sky beam of BL Lac; hence we used for this object a chopper throw of $31''$. During the night the chopper distance remained unchanged as it causes the zero-point of the photometry to change (de Diego 1994a).

Quasi-simultaneous photometry was obtained by sequentially integrating in J, H and K band in Beam 1 (A), then passing to Beam 2 (B) and integrating once again in JHK, before completing the cycle by repeating the measurement in Beam 1. This cycle was repeated until a good signal to noise ratio was reached. The total integration time ranged between ten and thirty minutes. To compensate for beam shifting relative to the guide image due to flexure of the instrument the aperture was recentered at regular intervals using a nearby bright star.

To calibrate the extinction and zero-point of the photometry we observed more than 15 calibration stars during each night. Whenever possible, a standard star close to the quasar was observed directly before and after the quasar. This star was also usually used to recenter the aperture. CVF data was reduced using a routine developed by Hammersley (1996; Private Communication), which fits the extinction to correct the zero point drift of the system.

Table 2.3 shows the number of infrared magnitude data points collected with CVF during this project. More than 3000 measurements were obtained in total and half of them of 3C 66A. BL Lac and OJ 287 were also extensively observed.

CAIN photometry: CAIN is an infrared camera with a 256×256 NICMOS 3 detector. Before May 1998 the scale was $0\farcs4/pix$, with a field of view of $1\farcm7$, and after this date, a new optic was installed, providing an alternative scale of $\sim 1''/pix$ in a $4\farcm2$ field of view. The filters used for the observations were J, H, and K_{short} filters—the last one, very similar to the K filter, was preferred because it considerably reduces the thermal background for ground-based telescopes.

Since the background level is high in the NIR, the exposure time of the individual frames must be short enough to avoid the count level to reach the non-linear regime (typically 10-20 s in J and 4-8 in H and K_{short}). In order to obtain a good signal to noise ratio, we need to add a number of frames—typically between 5 and 50 depending on the filter and the object brightness. Therefore, images are composed of multiple layers, i.e., they are three-dimensional image cubes.

For every observation, between two and five images were taken with the object in different positions on the dithering. For every image, the rest of the set is median-averaged to compute its sky level. In observations with just two images per set, great care was taken in not positioning objects at the same array site in the different images, to avoid having an object in the sky image contaminating the source in the main image during sky subtraction. When exposing, the autoguiding was switched off to dither the frames further. When re-centering the layers of the image cube before combining them, the dithering helps to remove the effects of bad pixels. Given our short exposure time, the guiding was good enough for the stars not be elongated in a single frame.

To create a proper flat-field that includes only information on the overall response of the telescope/camera combination, it is necessary to have two types of flat images, one with a high level of counts (bright) and another one with a low level (dark). The subtraction of the dark from the bright flat provides the final flat-field. Bright and dark flat-fields were taken during twilight when possible. When not possible, dome flats were obtained taking exposures of the dome with the lamps on and off. When there was no significant difference between the flats acquired during different nights of a run, grand averaged flats were computed to maximize the signal to noise ratio.

The first step in the data reduction was to create a bad pixel mask by dividing two flat fields with different count levels. This mask was then applied to every raw image to replace bad pixels by an interpolated value using the neighboring good pixels. Afterward, every individual layer was sky subtracted with the sky image described previously. During some epochs, CAIN suffered from a high electronic noise, which manifests itself as fringes, caused by grounding problems at the telescope. This noise was correlated in the four segments of the NICMOS detector. A task, kindly provided by Dr. P. Hammersley and Dr. F. Garzón and modified by us, identifies and removes this correlated noise. Subsequently, the flat field correction was applied. The layers were aligned using a bright object on the image and, finally, several layers were averaged with a σ clipping algorithm to obtain a better signal to noise ratio.

The routines dedicated to the reduction of these images (except the one used to remove the correlated noise) were created as IRAF tasks. On photometric nights, standards from the list of faint UKIRT standard stars and Hunt et al. (1998) were observed in the same filters as the science targets. This allows to calibrate the stars close to our objects (González-Pérez et al. 2001).

The total CAIN exposure times for each object are presented in Table 2.3. We collected more than 4,000 images with a total exposure time of almost 150 hours. OJ 287, 3C 66A, 3C 273 and BL Lac are the most frequently observed objects with more than 400 images and 10 hours of total exposure time each.

2.2.3 Optical polarimetry

We obtained polarization data working with the Turku Photopolarimeter (TURPOL) at the Nordic Optical Telescope. TURPOL is a chopping double-beam photopolarimeter with five channels, which obtains exactly simultaneous UBVRI observations through the use of four dichroics and five detectors. Each dichroic has a reflection bandwidth very similar to the Johnson/Kron-Cousin UBVRI filters. In photopolarimetric mode, a calcite plate is placed before the focal plane, and the two apertures are occupied by the ordinary and extraordinary beams from the half-wave retarder, therefore, sky chopping is impossible in this mode.

We used a diaphragm of $7\farcs5$ for all the observations. Data were taken for dark or gray sky; when observing in gray conditions, the Moon was always less than 50% illuminated. With the Moon below the horizon, the main variation in the sky background is the faint auroral glow, which is mainly present in R and I, and which only shows slow variations with a typical timescale greater than one hour. However, with the Moon above the horizon, the strongly polarized scattered moonlight, which peaks at 90° from the Moon, is a severe problem for faint sources.

We centered our source carefully on acquisition. A bright guide star was used to autoguide, ensuring reliable tracking on the source throughout the integration. The flux from the source was measured in eight position angles of the retarder, with an integration time of 20 seconds in each position, 10 seconds in each beam. Including overhead time, each measurement takes approximately 3.5 minutes. The measurements were made in sets of four, each preceded by a sky integration. With the Moon above the horizon, more frequent sky measurements were usually taken.

High and low polarization standard stars were observed each night to check the instrumental polarization, the zero points and the detection efficiency of polarization. In order to photometrically calibrate the data, in AGN with a published photometric sequence, a star from their field was also observed before and/or after the quasar. When no sequence was available, standard stars were observed between the quasar observations.

The reduction software for the TURPOL photopolarimetric data was developed by Piirola (TURPOL data reduction manual[3]). The routines interpolate the sky integrations on either side of each measurement, taken 30″to the north, to give a more accurate sky subtraction, particularly in cases of significant background variations. A total of four to six "sets of four" were taken during each night for each object, depending on the brightness and polarization of the objects and the conditions and circumstances of the observation. Faint objects ($V > 17$ mag) may need 12–16 "sets of four" to obtain acceptable errors ($< 0.5\%$).

The reduction routine fits the background-subtracted data to a sine curve of the retarder position angle to obtain the total polarization and its position angle. Each measurement is examined individually by the routine, and highly discrepant values are discarded before calculating the fit.

The error on the polarization is estimated by comparing the error expected from photon

[3]http://www.not.iac.es/instruments/turpol/prog/programs.html

statistics and the error obtained from the sine fit and taking the larger of the two values. The individual integrations provide a check on the reliability of these results; these typically show a dispersion lower than their mean error, thus suggesting that the reduction software provides a rather conservative error estimate.

The zero points and the efficiency of detection of polarization, from the observation of high and low polarization stars, confirm that the values calculated by Piirola (1996, private communication) in October 1996 are both reliable and, within the errors, constant for all the observations except the August 1997 observing run. For this observing run, made after instrumental maintenance and readjustments, an additional correction of the position angle of the instrumental polarization was required.

3

Ensemble-based differential photometry

In this chapter I introduce ensemble differential photometry, the approach applied throughout this work to derive accurate photometry of AGNs. Ensemble-based differential photometry is a generalization of differential photometry, which uses a variable number of stars in the field of view of the target to extract the magnitudes of the object of interest. Ensemble photometry maximizes the data accuracy and, at the same time, enables an independent estimation of the error of the data. My approach also works when not all stars in the field of view are present in all images.

3.1 Photometric context

ALTHOUGH some blazars show dramatic variations on long timescales (up to 5 mag), the amplitude of variability of most radio-quiet quasars and the short-term variations of blazars are much weaker (a few tenths of magnitude or less). Therefore, to fully characterize the variability of these sources, precise photometric measurements are essential.

Differential photometry can provide a much better accuracy than absolute photometry: with CCDs as imaging devices, the light of all stars and sources in the field are subject the same extinction and to the same seeing, as long as the field of view is relatively small. As demonstrated by Robinson et al. (1995), in a controlled laboratory environment, CCDs can perform differential photometry measurements with precisions of the order of one part in 10^5.

In addition, differential photometry allows obtaining useful photometric data even in non-photometric conditions. The difference in the instrumental magnitude of two sources close to each other and observed at the same time (i.e., same atmospheric conditions and same airmass) is equal to the difference in the true magnitudes of these objects with a color term correction, which only depends on the instrument and the source intrinsic color. Also working in photometric conditions, differential photometry is more accurate, since absolute photometry does not permit to remove high-frequency variations in the atmospheric transparency.

The first step when doing differential photometry (as in any other photometric measurements) is the extraction of the instrumental magnitude. There are two main methods to derive the instrumental magnitude of an object: aperture photometry and Point Spread Function (PSF) photometry. With aperture photometry, the counts of the pixels located inside an aperture (usually circular) are added, and the sky contribution within this aperture is removed. On the other hand, when working with PSF fitting, a model of the instrumental PSF is fitted to the image of a target. The integrated signal of the resulting scaled PSF models yields the instrumental magnitude—this method is particularly suited to analyze data from crowded fields.

We used aperture photometry throughout this work. As our fields are not crowded, and the objects have a reasonable S/N, aperture photometry is preferred to PSF fitting because it is simpler and less CPU time-consuming. Furthermore, some of our objects are extended, i.e., they are not point sources, which significantly complicates PSF fitting.

In the Appendices some other topics regarding our photometrical measurements are discussed: Appendix B.1 describes in detail how to calculate the photometric error from CCD images and Appendix B.2 outlines how the photometry is affected by the flat field, centering, computation of the sky background, pixelization, variations in response inside the pixels, FWHM variations, stray and scattered light, and dust spots in the CCD images.

Although this Chapter and the discussion in Appendix B focus on CCDs, most aspects of these sections also apply to other digital imaging devices, such as the NIR imaging array that we used in the CST.

3.2 Why ensemble differential photometry?

As explained above, differential photometry is more accurate than absolute photometry. Yet, naturally, it has some limitations. In this work, we aim to reach the fundamental precision limit in our photometrical measurements, defined by the photon statistics and the sky background. However, when normal differential photometry is performed, it is usually found that the actual precision obtained is lower (by as much as a factor 2) than the theoretically predicted value (see, e.g., Gopal-Krishna et al. 1995, Garcia et al. 1999, Stalin et al. 2004, and references therein). We suspect that two factors are responsible for that, both related to the determination of the calibration frames, namely, the flat field and the non-linearity of the CCD response. The limit to the precision due to these two factors may be up to 1% or even larger (see Sects. B.2.1 and B.2.10).

The use of ensemble photometry allows us to improve the accuracy of the results as well as to estimate the errors better. Ensemble photometry simply means that we use numerous comparison stars, instead of a single one. The large field of view (FoV) of modern CCDs usually allows us to observe many stars simultaneously. This set of stars (the "ensemble") is an ideal standard to use for calibration, with the obvious exception of variable stars. However, even if a few stars in the ensemble are low amplitude variables, the average intensity of the ensemble is expected to dilute these variations and be almost constant over time.

Ensemble photometry is applicable as long as the fluctuations induced by changes in the atmospheric properties are coherent over the full frame. This is true for sufficiently long exposures and a relatively small FoV, even if the night is highly non-photometric. Furthermore, the use of numerous comparison stars not only increases the precision of differential photometry but also tends to average out residual systematic flat field errors or non-linear behavior of the detector.

With a large number of stars in the ensemble, it is also possible to allow for color and position dependence in performing the ensemble normalization. This can be useful for correcting the color and spatial dependencies of the extinction. However, this must be done with care: removing the dependence on color or position can interfere with the measurement of true, intrinsic variations in the object— in particular, if there are few stars in the ensemble, if there are few bright stars with a large weight in the fit that dominates the ensemble, or if there are one or two stars with strongly different colors.

Ensemble photometry is not a new procedure (Gilliland & Brown 1988). This approach has been used to search for solar-type oscillations (Asteroseismology) in stars of several galactic clusters, such as M 67 (Gilliland & Brown 1988, Gilliland et al. 1991, Gilliland et al. 1993) and NGC 752 (Gilliland & Brown 1992) and to detect planetary transits across sun-like stars (Charbonneau et al. 2000). These papers claim that with CCD ensemble photometry it is possible to attain a measurement precision limited only by the fundamental and irreducible terms of the photon-counting statistics and atmospheric scintillation.

The same idea, but with a slightly different approach, has been applied by Honeycutt (1992), who describes the monitoring performed by the Indiana Automated CCD Photometric Observatory (Honeycutt et al. 1989). Pointing errors of the telescope lead to different sets of comparison stars being registered in different observations of the same object. In order to minimize the photometric errors, they developed an algorithm in which it is not necessary that all stars in the ensemble appear in all images.

3.3 Description of our procedure

With the aim of obtaining the most accurate photometrical measurements that our observations allow, we decided to use for ensemble differential photometry. We have developed a number of routines to apply this technique—all of them working within the IRAF environment. Our approach to the problem is a combination of the two methods described above (Gilliland & Brown 1988 and Honeycutt 1992).

We distinguish between program sources, the targets for which we want to compute the light curve, and ensemble stars, the stars used as comparison. Note that the light curve of all ensemble stars are extracted and analyzed with the aim of assessing that they are constant.

The first step in our procedure is (1) to search for all stars in each frame and extract their aperture photometry. After this step, we do not use the images anymore, but only the files containing the photometry. Next, (2) we match each frame field to a master field using the coordinates of the stars. After selecting the objects that belong to the ensemble and program sets, (3) the necessary information is extracted from the photometric files. From the best images, i.e., those with the highest S/N and the largest number of stars, (4) the average flux of the ensemble stars is computed. Subsequently, (5) the zero-point magnitude offset between each frame and the ensemble mean is derived and, finally, this zero-point offset is applied to all objects in the frame.

The following sections explain the individual steps (1) to (6) in detail.

3.3.1 Photometry of all stars detected in each image

After applying the necessary corrections (bias, flat field, bad pixel interpolation), each frame is interactively characterized by the standard deviation of the sky and the FWHM of the seeing, both required to search for the sources. Although the estimation of these parameters for each individual image can be a tedious task (particularly when dealing with a large number of frames), it is important to find accurate values, because the search program is sensitive to them, especially to the FWHM. This is the only indispensable interactive step in our ensemble analysis.

The search for the stars in each frame was carried out with the IRAF task DAOFIND, which requires the above mentioned input parameters. This program gives a list of all stars located in the image, whose peak exceeds the local background by a certain value—in this case, five times the standard deviation of the sky. All images were then manually checked to verify that the search was satisfactory. Finally, aperture photometry is performed on all stars detected by DAOFIND. We use the PHOT task with the centering and sky fitting parameters described in Appendix B. From now on, the reduction process only uses the photometric files.

3.3.2 Matching with a master field

In order to identify the AGNs and comparison stars among the sources found in the previous step, we proceeded as follows:

For each AGN we created a master field with the Online Digitized Sky Survey (DSS[1]) using a field size of 10×10 arcminutes, large enough to contain all the stars in the frames (our largest FoV was provided by the IAC-80 with $7\farcm5 \times 7\farcm5$). The source detection and the extraction of the photometry of the stars were also carried out on the master field, following the steps described in Sect. 3.3.1. We used the master field as a reference and matched all the frames with it.

The master field could, in principle, also be created using our science images. Nevertheless, since the telescope does not repeatedly point at exactly the same position, we need a master field with a size larger than the science images and the DSS is ideal for this purpose.

The IRAF task XYXYMATCH was used to match the science image fields and the master fields. XYXYMATCH provides two algorithms to match two lists of positions. The first one is the *triangles* algorithm (Groth 1986), which matches two lists of positions based on the triangles that are formed by triplets of stars in each list. This algorithm is particularly useful when the coordinate transformation between the two lists is unknown. The second algorithm is called *tolerance*; this algorithm assumes that both lists are in the same coordinate system, and it matches an object from the two lists if their positions are closer than a predefined tolerance.

We generated a script that extracts the positions and magnitudes of the objects from the master field and the science image. It performs a first match between the lists with the 30 brightest objects from each of the two lists using the *triangles* algorithm of XYXYMATCH. If

[1] http://archive.eso.org/dss/dss/

there are less than 30 sources in a list, all of them are employed in this step. A coordinate transformation between the lists is defined using this match and applied to the science fields. Finally, the program matches the entire two lists with the *tolerance* algorithm. As output, we obtain a list containing the correspondences between the sources in the science image and the master field.

Next, we select those objects that appear in the majority of the images, are not extended and are not close to another object, and extract their magnitude, FWHM, sky value, and position.

3.3.3 Definition of the ensemble mean

An ensemble mean is required in order to normalize each frame, and there are several possibilities for constructing it. Gilliland et al. (1993) used the average intensity for each star over 10 frames near the meridian passage. However, here we chose a different approach because not all stars are necessarily present in all frames, as is the case in Gilliland et al. (1993).

First, we selected the 10-30 best images, with the highest S/N for each filter. We chose fairly bright and isolated stars to form the ensemble, which also should be non-variable. A priori we do not know if a star is variable or not, but at the end of the process, we obtain a light curve for all of them. And, if any star is found to be variable, we remove it from the ensemble and start again from this point, creating the ensemble mean by an iterative process.

To compute the ensemble mean we fit the following function (Honeycutt 1992) to all stars in the ensemble:

$$m(e, s) = m_0(s) + z(e), \tag{3.1}$$

where $m(e, s)$ is the instrumental magnitude of the star s in the frame e, $m_0(s)$ is the mean instrumental magnitude of the star s, and $z(e)$ is the zero-point difference of the frame e. We also demand that $z(1) = 0$. After solving this set of equations, we obtained the ensemble mean, $m_0(e)$, for each star e in the ensemble.

This set of equations was solved using GaussFit (Jefferys et al. 1987[2]), a routine written in the C programming language, originally designed for astrometric data reduction of NASA Hubble Space Telescope (HST) data. GaussFit facilitates the solution of least squares and robust estimation problems. It is easy to use and, in particular, the implementation of the model to be fitted results simple.

Using the calibrated stars in the field of our AGNs (González-Pérez et al. 2001), we also calibrated the ensemble mean to the standard system. This requires at least one star present in the ensemble to which the calibration can be applied. We solve, for each filter, the set of equations:

$$M = m_0 + aC + z_0 \tag{3.2}$$

[2] http://clyde.as.utexas.edu/Software.html

where M and m_0 are the calibrated magnitude and the instrumental ensemble magnitude respectively, a is the color coefficient of the CCD corresponding to the current filter, obtained from the standard stars calibration (González-Pérez et al. 2001). The variable z_0 is the zero-point offset between the instrumental ensemble magnitudes and the standard magnitudes. The color of the star, C, depends on the filter in Eq. 3.2, being e.g., $B - V$ if the filter is B or V, $V - R$ if the filter is R and $R - I$ if the filter is I.

Finally, using the obtained z_0 of each filter, Eq. 3.2 is inverted and applied to all filters simultaneously to obtain the ensemble magnitudes in the standard system.

3.3.4 Ensemble photometry

After estimating of the ensemble mean magnitudes in the standard system, the proper ensemble photometry can be started. This final step comprises calculating the zero-point offset between the instrumental magnitude of each frame and the standard ensemble mean, and applying this zero-point to the instrumental magnitude of the program sources.

To this end, we used the same approach as Gilliland et al. (1993), without fitting any color or positional dependency. However, we computed the zero-point offset once for each program star. If the star belongs to the ensemble, it is not used to compute the offset, avoiding the problems encountered by Gilliland et al. (1993).

This task needs the color of all ensemble and program sources and the color coefficient of the instrument as input. For the ensemble stars, the color is known since the ensemble mean has been calibrated. However, for those program sources which are not in the ensemble, the color is not known in advance. So, initially the color of the program objects is assumed to be zero, and it is then computed iteratively while creating the light curves.

For each frame, the zero-point is calculated as the weighted mean of

$$z(s) = m(s) - m_o(s) - aC(s), \tag{3.3}$$

where $m(s)$ and $m_0(s)$ are the instrumental magnitude of the star s and the calibrated ensemble mean, respectively; a is the color coefficient of the CCD, and $C(s)$ is the standard color of the star s. The weight, $w(s)$ for each value $z(s)$ is computed as:

$$w(s) = \left(\sigma^2_{m(e,s)} + \sigma^2_{m_0(s)}\right)^{-1}, \tag{3.4}$$

where $\sigma_{m(e,s)}$ is the photometric error of the instrumental magnitude $m(e,s)$, and $\sigma_{m_0(s)}$ is the error of the calibrated magnitude $m_0(s)$. A rejection algorithm is applied, and all $z(s)$ that deviate from the estimated zero-point by more than $3\sigma_{m(e,s)}$ are removed from the weighted average. Thus, if one of the ensemble stars has an erroneous magnitude in this frame, e.g., due to a cosmic ray hit or a dust spot in the frame, this erroneous magnitude does not influence the ensemble magnitude.

For each science image, an extra number is also calculated, that, quadrately added to the

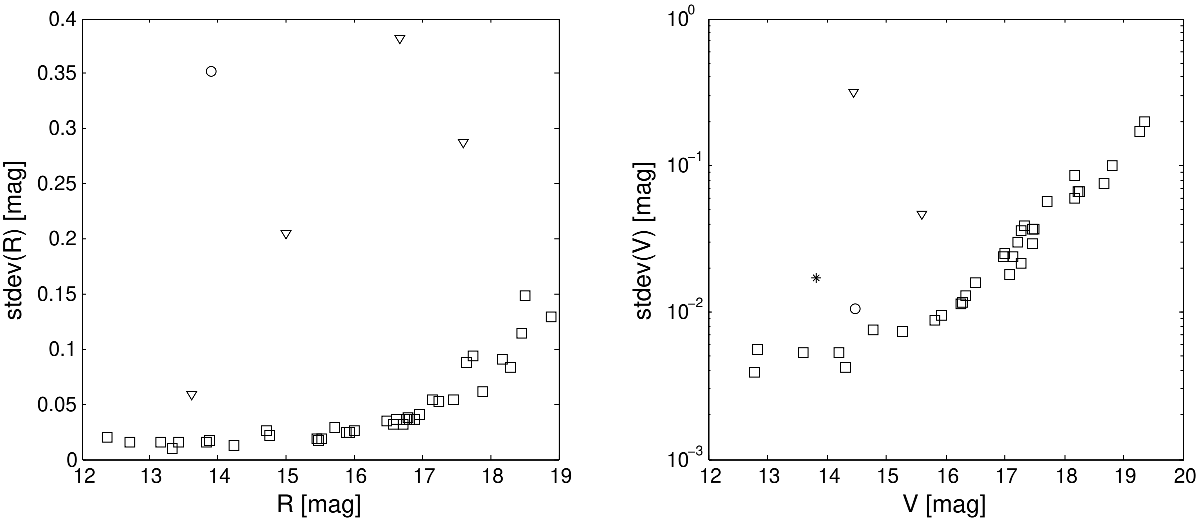

FIGURE 3.1— Sample plots of the standard deviation of magnitude as a function of the average magnitude for the objects in the field of 3C 66A. The left panel shows the plot for the whole set of observations in the R band, and the right panel shows the plot for the observation on the night of October 4/5, 1998 in V. Objects marked with squares are stars, objects marked with triangles are double or extended objects (double or extended objects seem variable because seeing variations affect to point and extended objects in a different way). A circle represents 3C 66A which is clearly detected to be variable in the full data set but only marginally on the night of October 4/5, 1998. The object marked as an asterisk is a suspected variable star.

nominal error of the photometric magnitudes, $\sigma_{m(e,s)}$, is in agreement with the standard deviation of $z(s)$ (Eq. 3.3). This extra factor accounts for those sources of error that have not been considered by Eq. B.4, as for example, errors in the determination of the flat field. This factor is added quadratically to all $\sigma_{m(e,s)}$ to obtain the final photometric error of the measurements.

By applying the zero-point for all stars in the frame, we obtain their magnitudes. As a final step, a plot of magnitude vs. its standard deviation is inspected to check if any of the ensemble stars are variable (two examples of these are shown in Fig. 3.1). In this plot, a variable star would have a standard deviation higher than the standard deviation of other stars with similar magnitude. As can be seen in the right panel of Fig. 3.1, in a good night, a photometric precision of around 0.5% is reached in the V-band, and even sources with an rms variability of 1% are detected as variables. In Fig. 3.1 one can distinguish two opposite regimes: a linear one for faint stars, for which the photometric errors are photon-dominated, and the regime for bright stars, with an exponential limit dominated by other error sources like the flat fielding.

We also check the light curves of the ensemble stars, to ensure that they are constant. If any of them shows variability, it is removed from the ensemble list and the ensemble mean is again computed (Sect. 3.3.3).

3.4 Discussion and application of the method

We built an IRAF package to perform ensemble photometry with our CCD or NIR array images. Our approach to ensemble photometry ensures that we use as many 'well-behaved' comparison stars as possible in each science frame. In this sense, we minimize the statistical errors of the magnitudes of the target sources.

We achieve the most precise photometry with detectable variability magnitudes of rms $< 1\%$ in good atmospheric conditions by using many stars for comparison, carefully checking these stars to remove problematic sources, such as variables and stars with a close companion. If only a few of the comparison stars are low amplitude variables, they do not significantly affect the photometry. As a secondary output of this method, we also extract the light curves of the stars present in the field; this can be useful to find and study variable objects (stars, or other AGNs).

Ensemble-based approaches to differential photometry have already been presented by Gilliland & Brown (1988) and Honeycutt (1992). For our application, we favor our approach, because (i) it does not require all the ensemble stars to be present in all frames (strict ensemble photometry) as is assumed by the method of Gilliland & Brown (1988). Furthermore, (ii) the method described by Honeycutt (1992) does not assume a strict ensemble, but it fits the ensemble mean and the zero-point offset for all science frames simultaneously. In this case, if the number of frames is very high, as for some of our objects, fitting such a large number of equations can be computationally expensive. Since we separate the calculation of the ensemble mean from the computation of the zero-point offset of each frame, the requirement of computational resources is moderate. In fact, the ensemble mean does not need to be computed from a very large number of images; using the 10-20 best images to build the ensemble is sufficient.

Finally, (iii) with our method, new observations are easily added to previous data as we do not need to recompute the ensemble mean. With the method of Honeycutt (1992), new observations require to refit the whole set of observations. As an additional weakness, the inclusion of low-quality science frames in the calculation of the ensemble mean, as is done in Honeycutt (1992), only increases the noise in the determination of its values.

Two examples of the application of this method are presented in Figs. 3.2 and 3.3. The left panels show the instrumental magnitudes, differential magnitudes and magnitudes computed using our method of a star in the field of 3C 66A (Fig. 3.2) and a star in the field of OJ 287 (Fig. 3.3) for a photometric night. The right panels show the magnitudes of the same stars in a non-photometric night. The small variations seen in the raw magnitude for the photometric nights are due to seeing and airmass changes and not to thin clouds. The use of the ensemble-based differential magnitude instead of the normal differential magnitude results in a precision improvement in the precision of the photometry in the range of 10-40%. With our data and our reduction process, photometry with a precision of $\sim 0.5\%$ and $\sim 1\%$ can be attained for stars of magnitudes 15 and 16.5 respectively with exposure times of $\sim$5 minutes at the IAC-80 telescope.

Notably, for non-photometric conditions, the photometry of the stars only shows a moderate increase in the uncertainty. Therefore, good photometry can also be obtained in non-photometric conditions, provided that the number of photons detected remains large enough.

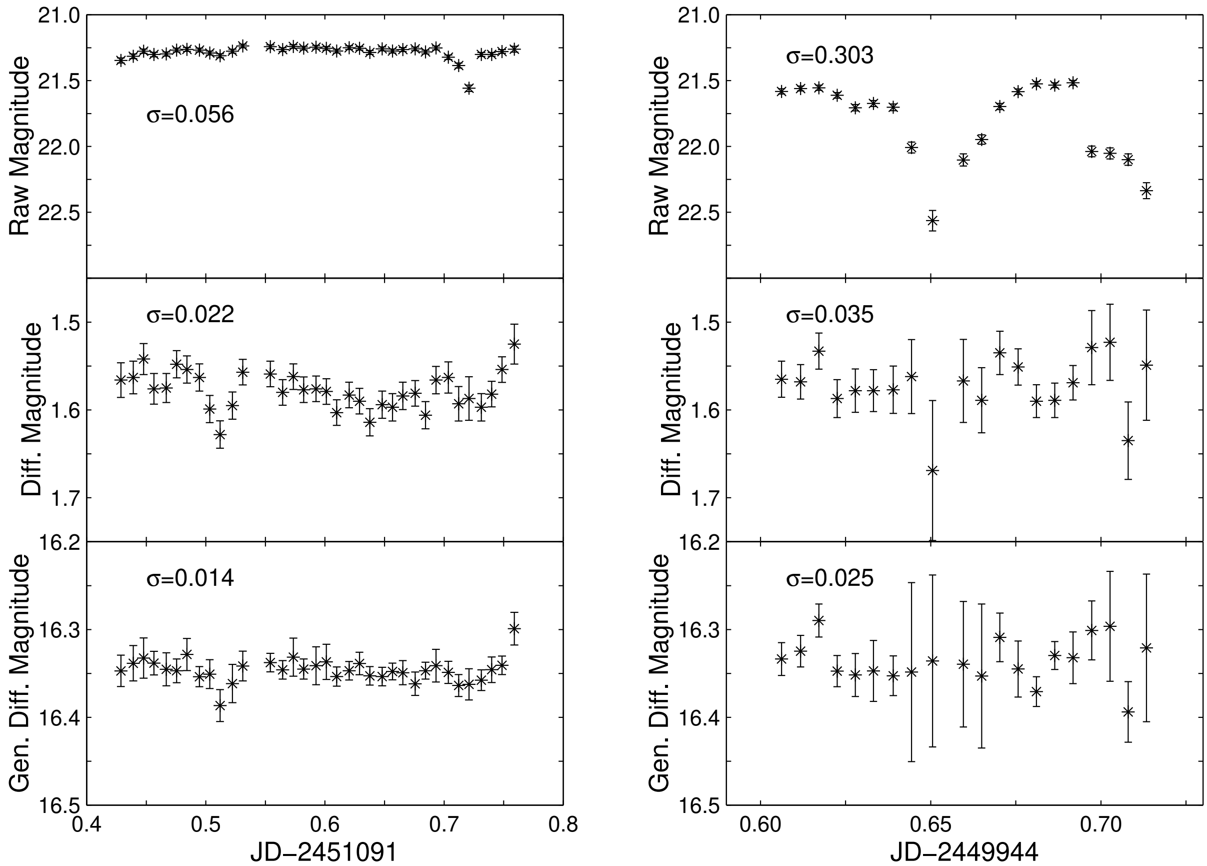

FIGURE 3.2— Uncalibrated instrumental magnitudes (top panel), defined as $m_{inst} = const - 2.5 \log(counts)$, where counts is the integrated counts of the star within our photometric aperture, usual differential magnitudes (middle panels) and ensemble-based differential magnitude as explained here (bottom panel) for a star of $V = 16.35$ within the field of 3C 66A. On the left, the light curves are from a photometric night (October 4/5, 1998) and on the right, the light curves from a non-photometric night (August 14/15, 1995).

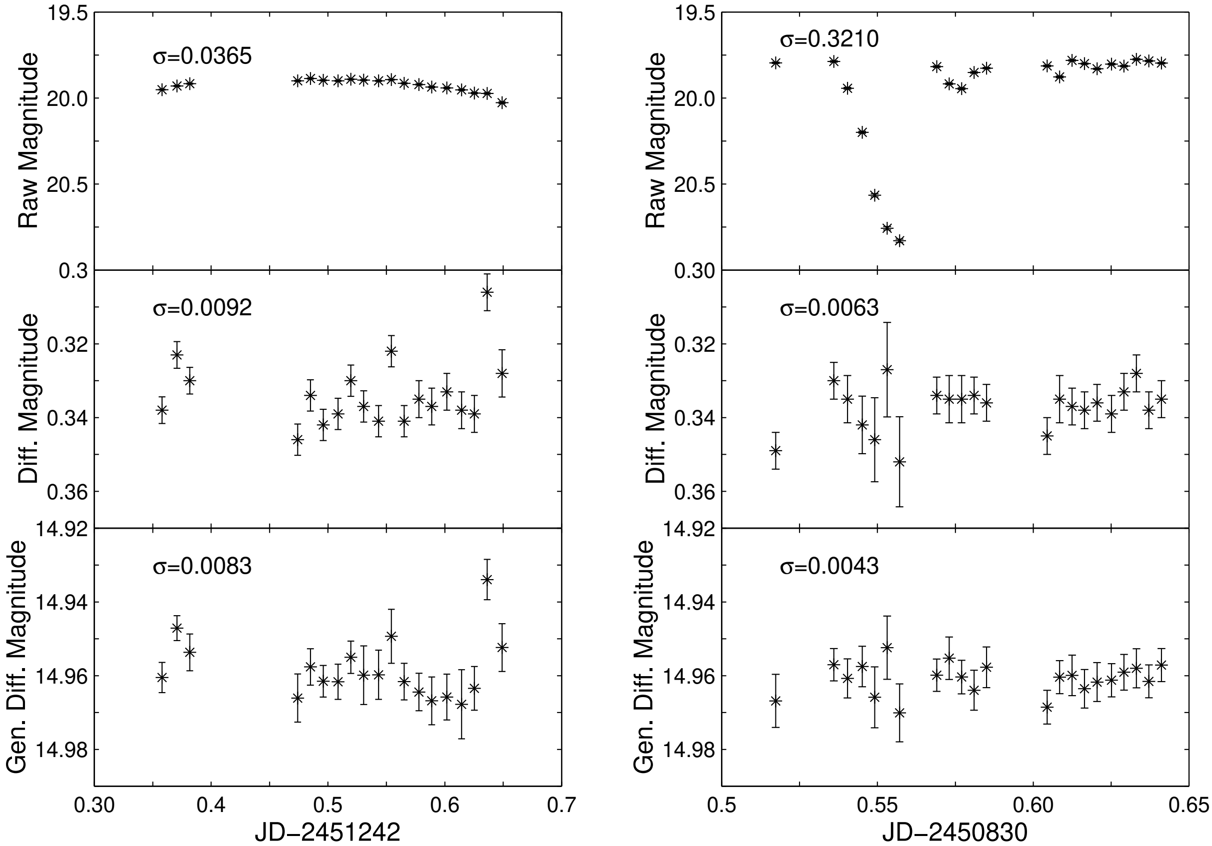

FIGURE 3.3— Same as Fig. 3.2, but for a star with $V = 14.96$ of the field of OJ 287. Left panel shows the light curves of the night March 4/5, 1999 (a photometric night) and right panel shows the light curves of the night January 16/17, 1998 (non-photometric night).

4

Photometry of AGNs with a prominent host galaxy

This chapter outlines the method that I applied to obtain accurate photometry of nearby sources with a significant contribution from the galaxy host. The simulations that I ran show the strong influence that the host galaxy can have in the photometry. After a discussion of the different procedures in the literature, I opted for a decomposition of the object in at least two components: a point source AGN and an extended host galaxy. The surface brightness profile of the host galaxy was fitted by a Sersic function using the 2D fitting algorithm GALFIT. This galaxy decomposition was carried out in the BVRI optical filters and JHK in the NIR for the first time to my knowledge. I discuss the results of this decomposition and present the tables with the photometric correction of this objects that can be used for other observers.

4.1 Introduction

Some of the AGNs in our sample are relatively nearby sources (with redshifts, $z \leq 0.1$; see Chapter 2). The Surface Brightness Profile (SBP) of these objects does not resemble that of a point source, but the host galaxy, which is large enough to be resolved by relatively small ground-based telescopes, can significantly contribute to the total flux. To obtain accurate photometry of these sources we cannot simply apply the technique of differential aperture photometry, as introduced in the previous Chapters, but some additional work is required.

We have calculated the fluxes of the objects by means of differential photometry— a highly efficient technique, as it can be applied even in non-photometric conditions (see Chapt. 3). In order to obtain accurate results, this technique requires the use of relatively small apertures. However, caution is necessary when working with small apertures and extended objects, because turbulence in the terrestrial atmosphere can affect the distribution of the light across the image. In particular, an extended source may show spurious changes in brightness as the result of a variable fraction of the total flux inside the photometric aperture, produced by fluctuations in the seeing (Carini et al. 1991, Cellone et al. 2000). Hence, some additional effort must be made in order to obtain accurate photometry of AGNs with a prominent host galaxy.

Two different approaches have commonly been adopted to address this question. Cellone et al. (2000) analyzed the influence of the host galaxy on aperture photometry of AGNs when the seeing varies. They found that apertures with a radius similar to the FWHM of the seeing, recommended by other authors (e.g., Howell 1989), should be avoided, because relatively small seeing variations can cause the AGN to appear variable to a level of a few hundredths of a magnitude. They propose to perform the photometry with a very large aperture, which enables to measure the intrinsic brightness variations of the source (Cellone et al. 2000). However, a large aperture implies that the ratio between the flux from the galaxy and the flux from the quasar is higher and therefore, any intrinsic variations of the quasar are diluted.

Alternatively, an appropriate correction factor can be applied (Nilsson et al. 1999, Nilsson et al. 2007). This second procedure is more intricate because the SBP of the galaxies must be calculated, but it is also more accurate, as it does not dilute the variations in the quasar brightness, and allows to extract a non-contaminated AGN magnitude. Therefore, we opted for this second throughout this thesis.

In this Chapter, we describe in detail how we carried out the photometry of AGNs with a prominent host galaxy. As a byproduct, we obtain the structural parameters of the host galaxies. Finally, we derive the photometric correction that must be applied to extract uncontaminated photometric measurements of the AGNs.

4.2 How the host galaxy affects the photometry

To quantify the effects of the host galaxies on the photometry of the AGNs, we carried out several simulations. We computed the photometry of artificial AGNs, superimposed on host galaxies with different structural parameters; these calculations were made for different values of the seeing.

It has been found that the SBP of many galaxies can be well described by a Sérsic law (Sersic 1968, Ciotti 1991). This formula gives the observed intensity of the galaxy, I, as a function of the radius r such that

$$I(r) = I_e \exp\left\{-\kappa\left[\left(\frac{r}{r_e}\right)^{1/n} - 1\right]\right\}, \tag{4.1}$$

where n is the Sérsic index; κ is defined so that half of the total flux of the galaxy is within the effective radius, r_e, and I_e is the intensity at the radius r_e.

The Sérsic profile can be considered as a generalization of the exponential and de Vaucouleurs fitting functions. In the de Vaucouleurs law (de Vaucouleurs 1948 and de Vaucouleurs 1953) the n index is fixed to 4:

$$I(r) = I_{1/2} \exp\left\{-7.67\left[\left(\frac{r}{r_{1/2}}\right)^{1/4} - 1\right]\right\}. \tag{4.2}$$

A de Vaucouleurs profile describes well the typical structure of elliptical galaxies as well as the bulge of spirals.

Setting the Sérsic index to $n = 1$ we get the exponential profile

$$I(r) = I_0 \exp\left(-\frac{r}{r_0}\right) \tag{4.3}$$

where I_0 is the central intensity and r_0 is the scale length. In this case $r_0 = r_e/1.678$. Also, a Gaussian profile is a special case of the Sérsic profile ($n = 0.5$).

We simulated the host galaxy using both, a de Vaucouleurs and an exponential profile, with different scale lengths. We generated artificial AGNs combining a host galaxy and a point source, with different relative contributions of both components. The parameters of the simulations are: i) the total magnitude of the host, ii) the size of the host, and iii) the magnitude of the point source. Although the output of the simulations does not depend on the absolute values of the individual input parameters (but on the ratio between them), realistic values, covering the range observed in the sample AGNs, were chosen. Also, for every simulated AGN, we changed the seeing, in order to compute how these variations affect the observations.

In this way, we created artificial observations of galaxies with a total magnitude of 15, with scale lengths in the range $5 \leq r_{1/2}, r_0 \leq 30$ pixels. The ellipticity of the host galaxy ranged from $\epsilon = 0$ to $\epsilon = 0.5$. At the center of each galaxy, we added a point source with a magnitude between 13 and 19.

We added a point source separated from the galaxy to the artificial frames. This point source was used as a comparison star when we calculated the differential photometry of the AGN.

The frames were finally convolved with a Moffat profile:

$$I(r) = \left[1 + \left(2^{1/\beta} - 1\right)\left(\frac{2r}{\mathrm{FWHM}}\right)^2\right]^{-\beta} \tag{4.4}$$

where β is an index that controls the shape and has typically a value of 2.5 for the profile of observed stars. The width of the profile was selected to simulate seeing conditions from FWHM = 2 to FWHM = 14 pixels. All artificial images were produced with the IRAF package ARTDATA.

Aperture photometry of the galaxy and the comparison star was performed using a set of apertures ranging from 1 to 55 pixels. The photometry of the galaxy was then compared with the photometry of the stars as in standard differential photometry.

Figure 4.1 displays the differential magnitude of the simulated AGNs as a function of the FWHM of the seeing for distinct apertures. The left panel shows galaxies with a de Vaucouleurs profile, and a scale length, $r_{1/2} = 20$ pixels, whereas galaxies with an exponential profile, and a scale length, $r_0 = 20$ pixels, are shown on the right panel. In both cases, the magnitude of the central point source is $m_n = 19$. It is apparent from the figure that seeing changes can yield large variations in the differential magnitude if small apertures are used: e.g., for an 8 pixels

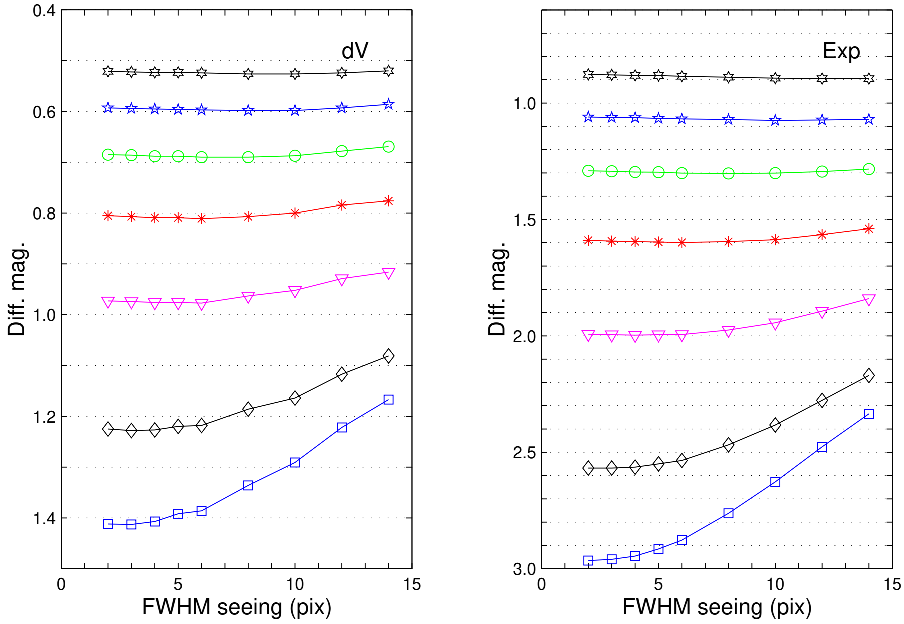

FIGURE 4.1— Differential magnitude of the AGN model (host galaxy + point source) compared to a point source for different apertures as a function of the seeing. The host galaxy model has a de Vaucouleurs (left panel) and an exponential (right panel) profile. The scale length of the host galaxy is $r_{1/2} = r_0 = 20$ pixels, the total magnitude of the host galaxy is 15, and the magnitude of the central point source is $m_n = 19$. The apertures used are 8 pixels (blue squares), 10 pixels (black diamonds), 14 pixels (magenta triangles), 18 pixels (red asterisks), 22 pixels (green circles), 26 pixels (blue five-pointed stars) and 30 pixels (black six-pointed stars).

aperture, differences up to 0.25 mag appear using a de Vaucouleurs model, and up to 0.65 mag using an exponential one. However, for larger apertures, this effect is much less pronounced: for apertures larger than 15-20 pixels only a few hundredths of magnitudes are expected.

While for small apertures the object is apparently brighter when the seeing is worse, the effect is the opposite for large apertures. This has also been noticed by Cellone et al. (2000). For small apertures (with a radius similar to the FWHM) a point source is relatively more affected by the seeing than the flatter profile of the host galaxy plus the active nuclear point source. Therefore, less light from the nucleus plus galaxy falls outside the aperture than from the comparison star if the seeing increases, making the AGN apparently brighter. However, for large apertures, a point source is barely influenced by the seeing, while for an extended object a significant part of its light falls outside the aperture as the seeing increases.

In Fig. 4.2 we show how the differential magnitude varies with the seeing for host galaxies with different scale lengths. Usually, for smaller seeing values the AGN model seems to be fainter as the seeing increases, while for larger seeing values the model appears brighter as the seeing increases. This behavior is found in almost all cases. This has been used by Licandro et al. (2000) to fit the relationship between the differential magnitude of comets and the seeing by a second-degree polynomial. In contrast to AGNs with an exponential host galaxy, for the AGNs with a de Vaucouleurs host galaxy profile, the variations in the differential magnitude are

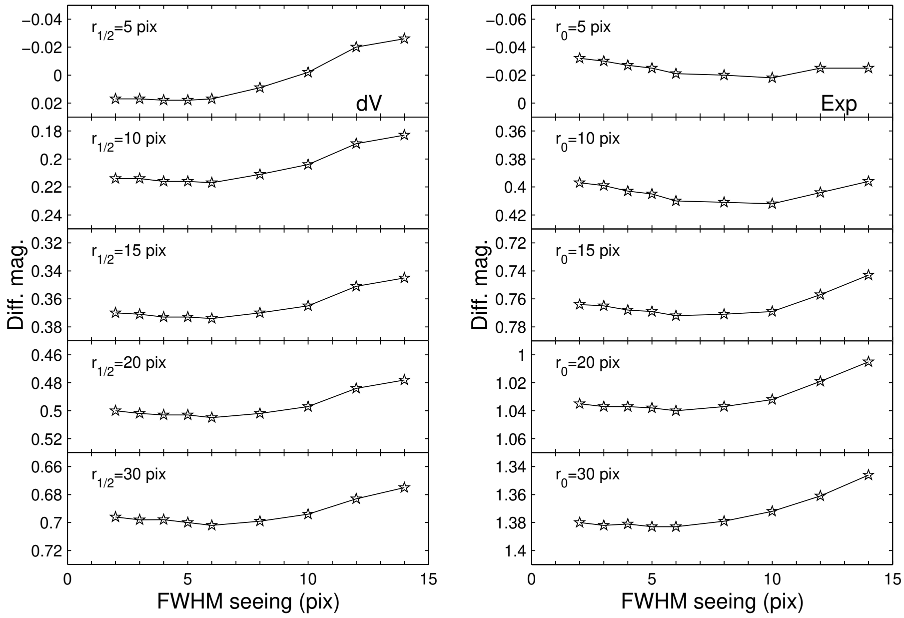

FIGURE 4.2— Same as Fig. 4.1 for host galaxies of different scale lengths, $r_{1/2}$ for a de Vaucouler profile (left panel) and r_0 for an exponential profile (right panel). The photometry was performed with an aperture of 18 pixels, the total magnitude of the model host galaxy and the central point source is $m_h = m_n = 15$.

larger as the $r_{1/2}$ becomes smaller.

We also studied the variations in the differential magnitude with the seeing for host galaxies with different ellipticities. Figure 4.3 shows that, apart from an absolute shift in magnitude, the relation between the differential magnitude of the AGN model and the FWHM of the seeing has the same shape, irrespective of the value of the ellipticity of the host galaxy.

Finally, we show in Fig. 4.4 how the differential magnitude varies with the seeing for AGNs models with various magnitudes of the central point source. The magnitude of this point source, which represents the active component of the model, ranges from $m_n = 13$ (the central component dominates the emission) to $m_n = 19$ (the active component is almost totally diluted by the emission of the galaxy). As expected, the dimmer the nuclear component is, the larger are the variations related to the seeing changes. Even in the case of a bright central source ($m_n = 13$), there are apparent variations caused by seeing changes which, however, remain small ($\sim 1\%$).

4.3 How to correct for host galaxy effects

The problem of the effect of a host galaxy on aperture photometry has been addressed by several authors, not only in the context of AGN photometry but also in the framework of comets. Using simulations, Cellone et al. (2000) estimated the effect of the host galaxy and seeing in the differential photometry of AGNs and recommended to choose an aperture size so that the expected variations due to the seeing are at most 0.01 mag.

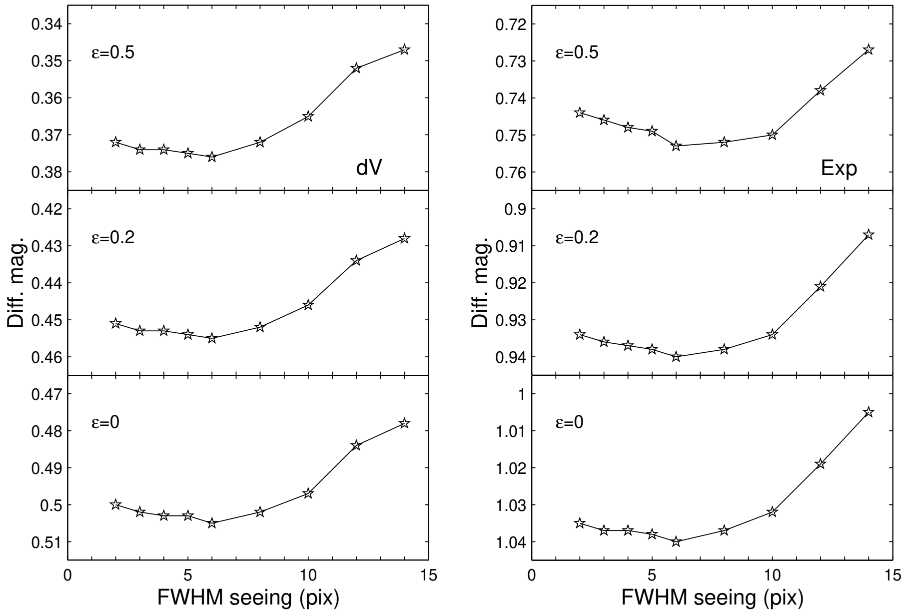

FIGURE 4.3— Same as Fig. 4.1 for host galaxies with different ellipticities (ε). The total magnitude of the host galaxy and the magnitude of the nuclear point source that comprise the AGN model is $m_h = m_n = 15$; the effective radius, $r_{1/2}$ of the de Vaucouleurs profile (left panel) and the scale length, r_0 of the exponential profile (right panel) are both 20 pixels. As in Fig 4.2, the radius of the aperture is 18 pixels.

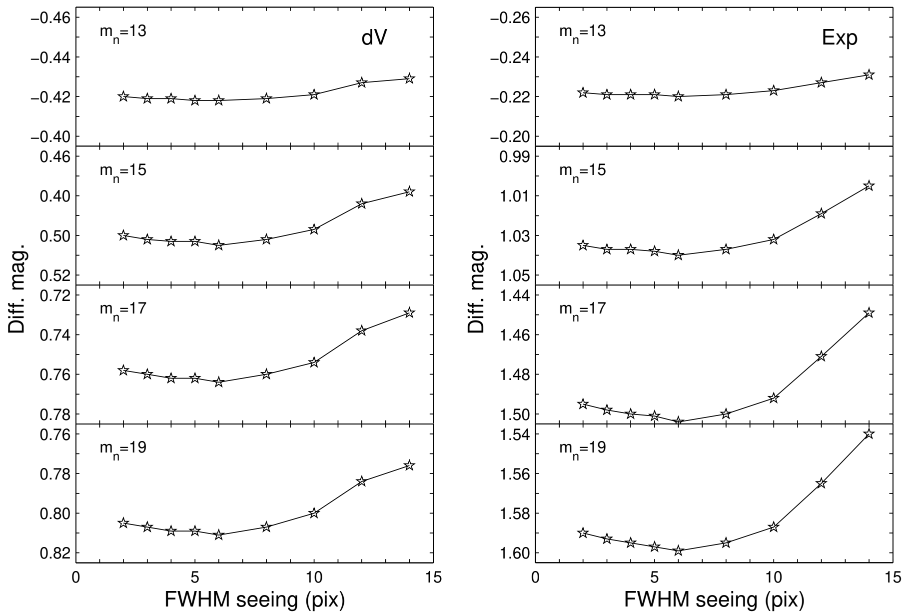

FIGURE 4.4— Same as Fig. 4.1 for different magnitudes of the nuclear component, m_n. The total magnitude of the host galaxy is $m_h = 15$, and its scale length is 20 pixel. The aperture used is 18 pixels.

Licandro et al. (2000) analyzed the influence of seeing on the photometry of active comets. The authors demonstrated, using simulated and real images, the strong effect (up to ~ 0.5 mag) that seeing variations have on aperture photometry of comets when very small apertures are used. Convolving the image with the best seeing with Gaussians of different width, they found a strong correlation between the measured magnitudes and the seeing. Their relation is then used to correct the instrumental photometry. This method requires that the comet profile does not vary during the night, so it can only be applied when the intrinsic variations in the profile of the object are small.

A different approach to this problem is to fit the profile of the host galaxy with a suitable function and then use this model to decontaminate the nuclear component:

In Sánchez Portal (1999) no assumption about the shape of the active nuclear component is made. The author derived the parameters of the bulge (the profile of the bulge is assumed to be that of Eq. 4.2) and the disk (Eq. 4.3) in the external parts of the galaxy, where the seeing and the central component have a negligible influence. With these parameters, a two-dimensional seeing-free model of the galaxy is created. A PSF model is fitted by a sum of two Gaussians using some bright stars in the frame. Finally, the galaxy model is convolved with this PSF, and both are compared with the actual data. By subtracting the seeing-convolved galaxy model from the actual data, the contribution of the nuclear component is obtained. The main drawback of this method is that it requires that the size of the galaxy (and the bulge) are much larger than the seeing FWHM in order to find enough pixels unaffected by the seeing to be used in the fitting. Therefore, this method works best with bright, nearby galaxies.

Kotilainen et al. (1992b) and Kotilainen et al. (1992a) extracted azimuthally averaged radial SBPs from NIR images of a sample of X-ray selected AGNs. They created a galaxy model (the sum of a bulge, defined by a de Vaucouleurs profile, and an exponential disk), which is convolved with a two-Gaussian seeing PSF. To this galaxy model, a central point source with a certain intensity is added. Finally, the extracted profile is fitted to this model. However, the authors use a one-dimensional convolution that is not satisfactory to recover the central point source (Sánchez Portal 1999). This problem is solved by Zitelli et al. (1993) by making a proper two-dimensional convolution before extracting the SBP of the seeing-convolved model.

Most of the works that decompose the observed object into a central point source and a galaxy aim at studying the properties of the host galaxy. However, Nilsson et al. (1999) pursue the same goal as us: to use the galaxy parameters extracted from the fit to correct the aperture photometry of the central source. In particular, the contribution of the host galaxy in a fixed aperture is estimated in order to remove it when aperture photometry is performed. Nilsson et al. (1999) modeled the host galaxy by a two-dimensional Sérsic profile using a proper two-dimensional fitting routine. With the adopted model, the SBPs of the objects are reasonably well described over a range of $\sim$10 mag. The nuclear component of the model is subtracted from the images, and aperture photometry is then performed on the residuals—i.e., the host galaxy. In this way, Nilsson et al. (1999) computed the photometric correction needed to be applied to the aperture photometry, in order to obtain the magnitude of the central source.

4.4 Decomposition of the host galaxy and the nuclear source

In this section, we explain the procedure applied to decompose our images into the host galaxy and the point source component, i.e., the AGN, whose magnitude we are interested in. The method we apply is similar to the one introduced by Nilsson et al. (1999). Because the individual images obtained for the photometry of the AGNs are not deep enough to reliably detect the outer parts of the galaxies, and the seeing is not always sufficient to easily separate the nuclear and the galaxy components, we adopted the following procedure:

4.4.1 Preparation of the data

We selected, for each object and filter, the images with better S/N and seeing. These frames were centered, using several bright and isolated stars, and the sky background was removed, after measuring it in source-free sections of the frame. Finally, the images were scaled to the same flux level, by multiplying with a factor so that the mean flux of a sample of reference stars remains constant. A weighted mean of these corrected images was used to create the final frames to be analyzed. The weight of each image is computed as the inverse of the variance of the sky after scaling to improve the estimate of the flux levels in the outer parts of the galaxies, which have a flux level similar to the sky background.

Table 4.1 shows, for each object (Col. 1) and each filter (Col. 3), the characteristics of the final images used to carry out the decomposition. Column 4 shows with which telescope the images were obtained; the seeing FWHM and the total exposures time in seconds are given in Cols. 5 and 6, while the redshift of the object is displayed in Col. 2.

4.4.2 Fitting the host galaxy profile: 1-D vs. 2D analysis

The final averaged images of the AGN were fitted to a model consisting of at least two components: a point source and a galaxy. We perform the fit using version 3 of the 2-D fitting algorithm GALFIT (Peng et al. 2010). The point source is the AGN itself, whereas the galaxy component is modeled with a Sérsic profile. This method allows disentangling the active nucleus emission from the host galaxy.

There are usually two ways to fit a galaxy profile with a parametric function: a one dimensional fit of the azimuthally averaged profile and the two-dimensional fit. If the galaxy and the PSF have an axisymmetric light distribution, both methods are equivalent. The one dimensional fit is computationally simple (although this is not a significant issue anymore), but it presents some drawbacks: the 1-D profile of non axisymmetric components such as bars may resemble those from galaxies with axisymmetric bulges; nearby sources must be masked out, which in some cases, e.g., a crowded field or an object too close to the galaxy, is not an option, while in the 2-D approach nearby objects can also be modeled.

Yet, the most important reason why we decided to use a 2-D analysis is that for compact objects, such as our galaxies, which are a few tens of an arcsecond large, the effect of seeing must be taken into account. In this case, 1-D profile convolution is no longer mathematically equivalent to 2-D convolution— for a more detailed comparison between 1-D and 2-D profile

TABLE 4.1— Properties of the images used for the decomposition host galaxy-nuclear source.

Object	z	Filt	Telescope	FWHM ″	T_{exp} s
III Zw 2	0.089	B	IAC-80	1.9	1400
		V	IAC-80	1.9	1900
		R	IAC-80	1.9	1500
		I	IAC-80	1.9	1200
I Zw 1	0.061	B	JKT	1.6	540
		V	JKT	1.4	840
		R	JKT	1.3	840
		I	JKT	1.5	480
Mkn 205	0.071	B	JKT	2.0	5200
		V	JKT	1.2	4800
		R	JKT	1.2	4200
		I	JKT	1.7	1550
PG 1351+640	0.088	B	JKT	1.7	1560
		V	JKT	1.8	1260
		R	JKT	1.7	1100
		I	JKT	1.5	960
AP Lib	0.042	B	IAC-80	2.0	400
		V	IAC-80	2.6	400
		R	IAC-80	2.3	450
		I	IAC-80	2.3	150
Mkn 501	0.034	B	IAC-80	2.3	5650
		V	IAC-80	2.1	5100
		R	IAC-80	2.0	3050
		I	IAC-80	2.0	2150
		J	CST	2.3	1095
		H	CST	2.3	760
		K	CST	2.4	1060
II Zw 136	0.063	B	JKT	2.0	3200
		V	JKT	1.3	4030
		R	JKT	1.4	2350
		I	JKT	1.4	1250
BL Lac	0.069	B	IAC-80	1.7	6650
		V	IAC-80	1.6	10150
		R	IAC-80	1.7	4740
		I	IAC-80	1.7	4340
		J	CST	2.6	1040
		H	CST	2.4	640
		K	CST	2.5	750

fitting see Peng et al. (2010) and Erwin (2015).

Galfit is a stand-alone two dimensional fitting algorithm, that allow us to decompose an image of the galaxy into an arbitrary number of parametric functions (Sérsic, de Vaucouleurs, exponential, Moffat, etc.) and enables, therefore, to simultaneously fit any number of galaxies or point sources present in an image. The new version 3 of galfit also permits the fit of non-symmetric shapes as spiral arms, bars, rings, and truncated shapes. The program uses a Levenberg-Marquardt technique to carry out a nonlinear least-squares fit. To account for the effects of seeing, galfit convolves the model with a PSF given by the user before the actual image is compared with the model in each step of the least-squares fitting routine. A detailed description of galfit can be found in Peng et al. (2010)[1].

Galfit reads the FITS images that are going to be analyzed and can produce FITS images of the individual model components or the residuals; it also generates a file with the fitted parameters. The regions of the image irrelevant to our analysis and most nearby objects were masked out from the fit. However, in a few cases, objects are so close to the galaxy, that they also had to be fitted, as a point source or a Sérsirc profile, depending on their characteristics. Whether this step is actually necessary depends on the observed filter, because an object that is "embedded" in the galaxy in one filter may be clearly separated in another, due to the different S/N. The sky background was fixed to a value calculated using several regions of the images close to the galaxy and free of stars. In this way, we can avoid the coupling between the Sérsic index n and the sky value if this is also fitted (Peng et al. 2010).

In our images, with typical galaxy sizes of about 10 to 15 arcseconds, a good estimate of the PSF is crucial to account for the smearing of the model by the PSF. The PSF was constructed using several isolated bright stars located in the image. In the optical, we used between 5 and 14 stars, whereas in the NIR, due to the smaller FoV, mostly 3-4 stars were used.

The subimages containing the stars were aligned, and the sky was subtracted; the images were then scaled so that the different stars had the same exposure level and finally the weighted average of those images were calculated. In order to obtain the photometry of the host galaxies with different apertures, which is our final goal, we also fit one star in the FoV that was photometrically calibrated (González-Pérez et al. 2001).

The parameters of the fit are the following: from the galaxy, we need the x and y position of the center, the integrated magnitude, the effective radius, the Sérsic index n (see Eq.4.1), the axis ratio between the minor and the major axis and the position angle (PA). From the active nucleus, we have its position (x, y), which is fixed at the center of the galaxy, and the magnitude. Finally, for the comparison star, we fit its position and its magnitude. The fit of the galaxy + AGN is independent of the fit of the comparison star because they are located at a different positions in the image.

This adds up to a total of 11 parameters. Because most of our galaxies are small, we have fixed the Sérsirc index of the host galaxy. To calculate this value, we first let galfit fit the Sérsirc index and then use the average of the values in the V, R, and I filters as the fixed one.

Once the fit is done, we derived the magnitude of the galaxy in the following way. We created

[1]see also http://users.obs.carnegiescience.edu/peng/work/galfit/galfit.html

a set of PSF images with different seeing values from 1 to 8 arcseconds, using a Moffat profile with a Moffat index of 3, which is a value close to the typical one in our images if we fit the profiles of the stars to a Moffat function. Then, the models of the galaxy obtained from the fit without the nuclear component and the comparison star were convolved with the different artificial PSFs.

The aperture photometry of these two objects in the model image was calculated using different apertures. Knowing the magnitude and color of the comparison star (González-Pérez et al. 2001), we calculated the final magnitudes of the host galaxies for different apertures after applying the instrumental color correction using the values presented in González-Pérez et al. (2001).

4.4.3 Error analysis

The formal errors of the fitting parameters given by this and other algorithms are known to underestimate the real errors (Peng et al. 2010) because systematic errors dominate the residuals of the fit (e.g., galaxies or stars that are not fitted). Such systematic effects are flat field errors and imperfect matches to the data of the profile function. Many elliptical galaxies show a deviation from the Sérsirc profile with disk components present in their central part, central "cusps" and dust lanes (Nilsson et al. 2007 and references therein).

Therefore, to estimate the errors of the parameters and the photometry of the galaxy, a different procedure is required. We proceeded as follows:

We created a series of 100 simulated images by adding Poisson noise, with the same characteristics as in the real data, to the original frame. These simulated images were fitted and analyzed in the same way as the original ones. The random error of the parameters, σ_{ran}, is determined as the standard deviation of the values calculated in the fit of the simulated images. For the simulations, we used the original image and not the fitted model, knowing that this means that in the simulations the Poisson error is doubled in each pixel, because the model does not consider the real structure of the galaxy and this may affect the fit.

As explained, σ_{ran} is only one part of the error budget. For the photometric measurements of the host galaxy, we also need to add the error in the photometric calibration, σ_{cal}, derived in González-Pérez et al. (2001). Besides these two sources of errors, systematic effects also contribute to the error budget. A systematic effect occurs, e.g., when the galaxy does not follow the smooth functional form we assumed; or if the PSF was not correctly estimated, because we neglected its possible variations along the chip.

To take into account possible systematic effects, we calculated the photometry with different apertures of three estimates of the host galaxies: First, the subtraction of the nuclear component from the original image. Second, the photometry of the modeled galaxy (Sérsirc profile with the fitted parameters) convolved with the original PSF. And third, the photometry of the modeled galaxy, but now convolved with an artificial PSF created using a Moffat profile, which has the same FWHM as the PSF of our image. We calculated the standard deviation of these three estimates of the magnitude for each aperture and assumed that this standard deviation is the contribution of the systematic effects to the error budget, σ_{sys}. In this step, the outliers of the relation σ_{sys} vs. aperture were corrected using the values of similar apertures (due to the small number of estimates used in the calculation of the standard deviation).

Finally, the error of the aperture photometry of the host galaxy (given in Appendix C) was computed as

$$\sigma_{mag} = \sqrt{\sigma_{ran}^2 + \sigma_{sys}^2 + \sigma_{cal}^2} \tag{4.5}$$

4.5 Results and discussion

In Table 4.2, we present the results of the best fitting parameters of the galaxies. Columns 1 and 2 display the object name and the filter, respectively. Columns 3 and 4 give the total observed magnitude of the galaxy and the absolute magnitude, also corrected for galactic extinction[2]. The effective radius in arcseconds and kpc is shown in column 5 and 6, respectively. The last three columns display the axis ratio of the galaxy in column 7, the position angle in degrees in column 8 and the Sérsic index in column 9.

The azimuthally averaged radial profiles in the R filter of our sample and the different components obtained from the best fitting parameters are shown in Fig. 4.5. The plots of the profiles for all filters and all galaxies can be found in Appendix C. Each plot shows the profile data, as well as the profile of the PSF, the modeled galaxy and all other modeled objects close to the AGN.

The aim of our analysis is to decontaminate the contribution of the host galaxy to the photometry. The tables with the magnitudes of the host galaxies with different apertures for distinct seeing values in all filters are also presented in Appendix C. Although the photometry of almost all AGNs in our sample was performed with an aperture radius of 1.8-2.0 arcsec FWHM, for the nearby objects, for which the host galaxy is detected, with $z \lesssim 0.15$, the radius of the aperture was fixed to $5''$ to ensure consistent photometry from night to night. Finally, the contribution to the photometry of the host galaxy inside the aperture is removed for all of our observations using the tables of the photometry of the host galaxy. For this step, the crucial point is the estimation of the seeing of all observations. This was performed with the IRAF task FITPSF for several non-saturated bright stars in the images.

The estimated error in the photometry of the host galaxy inside the aperture is usually less than 0.2 mag and in many cases less than 0.05 mag. This is accurate enough in most cases because the contribution of the host galaxy to the total luminosity is not very high in most of our objects. However, for one of our best-observed sources, Mkn 501, the host galaxy has a strong influence on the photometry: $\sim 70\%$ of the light inside an aperture of $5''$ originates from the host galaxy in R and $\sim 75\%$ in H, so the accuracy of the decontamination presented here is not good, particularly in the NIR bands.

There are several reasons in favor of the reliability of our decomposition analysis. Except in

[2]We adopt a cosmology with $H_0 = 73\ km\ s^{-1}\ Mpc^{-1}$, $\Omega_m = 0.27$ and $\Omega_\lambda = 0.73$. The K-correction was done using the "K-correction calculator" available at http://kcor.sai.msu.ru/. The Galactic extinction was calculated from Schlegel et al. (1998), using the NASA/IPAC extragalactic database (http://ned.ipac.caltech.edu)

TABLE 4.2— Parameters of the best fits for the host galaxies of the AGNs in our sample.

Object	F	mag		M	r_e ($''$)		r_e (kpc)		b/a		PA (deg)		n	
III Zw 2	B	17.53	±0.23	-20.84	7.2	±1.2	11.4	±1.8	0.78	±0.13	-23.0	±2.0	2.2	
	V	16.34	0.10	-21.92	6.6	0.5	10.4	0.8	0.73	0.02	-24.3	1.1	2.2	
	R	15.48	0.06	-22.73	7.9	0.2	12.6	0.2	0.83	0.02	-10.6	1.4	2.2	
	I	14.97	0.07	-23.17	6.5	0.3	10.4	0.5	0.81	0.02	-13.5	0.9	2.2	
I Zw 1	B	15.68	0.14	-21.57	7.5	2.0	8.1	2.2	0.83	0.02	37.3	1.6	5.5	
	V	14.90	0.07	-22.28	6.1	1.4	6.6	1.5	0.90	0.01	30.5	2.3	5.5	
	R	14.47	0.04	-22.67	5.3	0.7	5.7	0.7	0.88	0.01	32.5	0.9	5.5	
	I	13.75	0.05	-23.35	3.6	0.7	3.9	0.8	0.85	0.01	27.9	0.8	5.5	
Mkn 205	B	17.03	0.13	-20.59	2.6	0.7	3.4	0.9	0.80	0.05	2.3	2.2	3.1	
	V	15.87	0.03	-21.71	3.7	0.1	4.8	0.2	0.82	0.01	23.1	0.3	3.1	
	R	15.35	0.02	-22.20	3.1	0.2	4.0	0.2	0.80	0.01	19.7	0.3	3.1	
	I	14.57	0.02	-22.95	2.5	0.1	3.2	0.1	0.76	0.01	24.5	0.7	3.1	
PG 1351+640	B	17.16	0.22	-20.87	1.2	1.9	1.9	3.0	0.90	-	-40.0	-	4.7	
	V	16.41	0.14	-21.61	1.2	2.3	1.9	3.6	0.90	-	-40.0	-	4.7	
	R	15.93	0.05	-22.07	2.5	0.5	3.9	0.8	0.92	0.01	-40.1	2.6	4.7	
	I	15.24	0.09	-22.76	2.7	0.7	4.3	1.1	0.88	0.02	05.9	2.1	4.7	
AP Lib	B	14.67	1.09	-22.56	26.4	12.2	24.6	11.4	0.84	0.22	15.6	6.1	6.5	
	V	14.92	0.10	-22.17	3.3	1.1	3.0	1.1	0.89	0.04	9.2	5.2	6.5	
	R	14.19	0.11	-22.81	4.8	0.5	4.5	0.4	0.99	0.01	-3.7	6.5	6.5	
	I	13.32	0.35	-23.58	6.6	4.4	6.2	4.1	0.88	0.06	31.9	3.6	6.5	
Mkn 501	B	14.11	0.12	-21.73	19.2	6.9	12.3	4.4	0.73	0.01	-12.8	0.4	6.8	±2.5
	V	12.79	0.05	-23.04	30.2	3.6	19.4	2.3	0.74	0.01	-12.3	0.1	8.2	0.2
	R	12.06	0.02	-23.76	33.9	0.9	21.8	0.6	0.75	0.01	-12.3	0.1	8.8	0.2
	I	11.30	0.08	-24.50	43.6	5.3	28.1	3.4	0.75	0.01	-12.6	0.1	10.6	1.4
	J	10.94	0.05	-24.84	6.9	1.3	4.4	0.8	0.76	0.01	-8.3	0.1	5.6	0.2
	H	10.23	0.05	-25.54	5.6	1.4	3.6	0.9	0.75	0.01	-10.3	0.2	4.5	0.3
	K	9.93	0.04	-25.84	5.1	1.2	3.3	0.8	0.72	0.01	-6.6	0.2	6.5	0.2
II Zw 136	B	16.52	0.24	-20.80	13.6	2.6	15.6	2.9	0.47	0.03	59.6	0.3	2.7	
	V	15.78	0.10	-21.49	10.0	0.7	11.5	0.8	0.48	0.02	56.9	0.3	2.7	
	R	15.23	0.08	-22.02	9.2	0.6	10.5	0.6	0.47	0.02	53.8	0.2	2.7	
	I	14.53	0.03	-22.68	8.8	0.2	10.1	0.2	0.47	0.01	52.2	0.1	2.7	
BL Lac	B	17.29	0.16	-21.46	14.9	1.7	18.6	2.1	0.48	0.03	40.5	0.9	5.1	
	V	15.83	0.10	-22.59	16.5	2.5	20.5	3.1	0.50	0.01	41.2	0.3	5.1	
	R	14.99	0.05	-23.22	15.1	0.7	18.8	0.9	0.51	0.01	43.7	0.3	5.1	
	I	14.32	0.05	-23.65	13.9	0.6	17.3	0.8	0.50	0.02	45.3	1.1	5.1	
	J	12.90	0.09	-24.73	5.1	1.0	6.3	1.2	0.59	0.02	46.9	0.6	5.1	
	H	12.15	0.12	-25.38	6.7	1.1	8.3	1.4	0.51	0.03	41.1	1.1	5.1	
	K	11.62	0.08	-25.83	7.1	0.5	8.8	0.6	0.56	0.03	44.3	0.6	5.1	

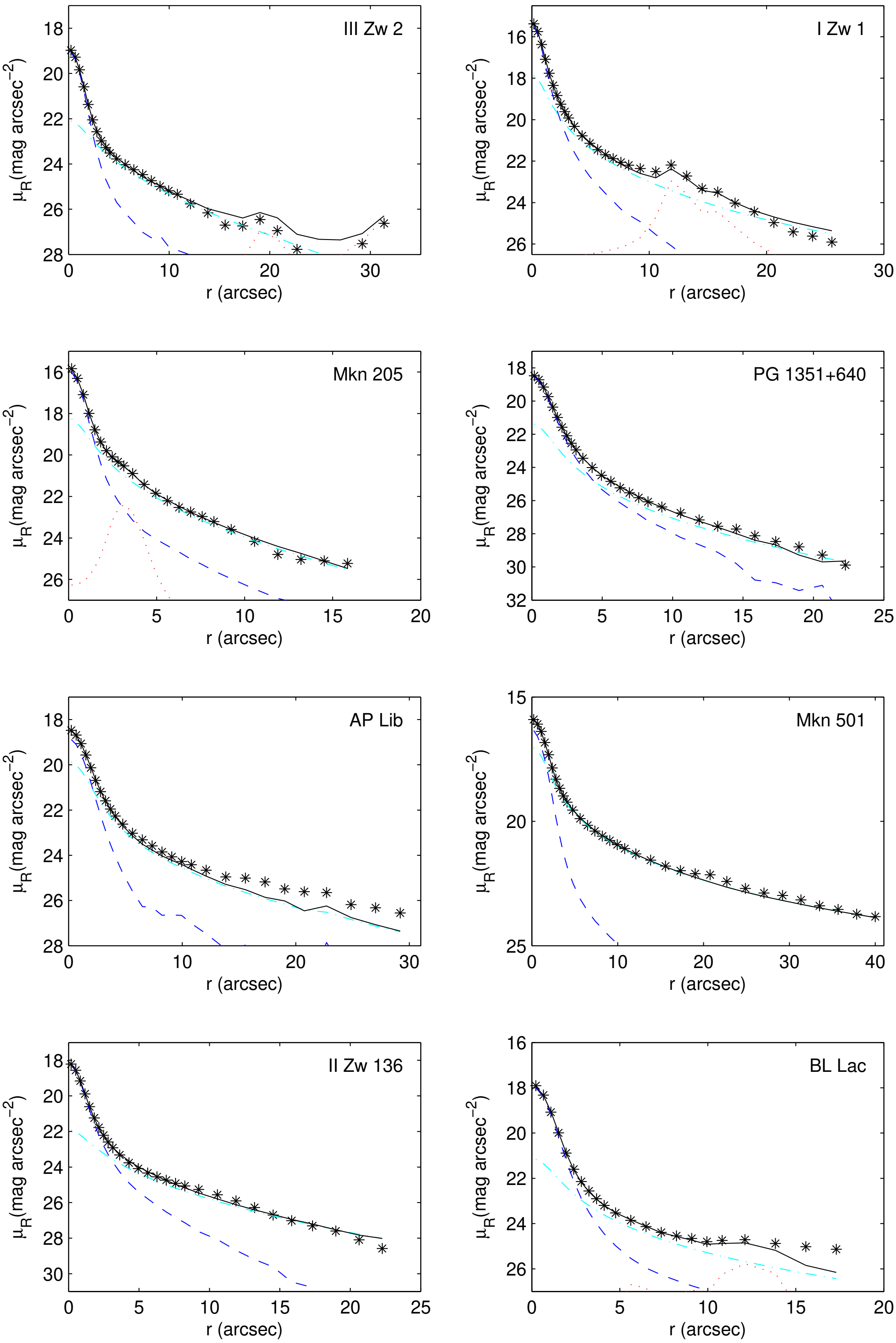

FIGURE 4.5— Surface brightness profiles in the R filter. Asterisks represent the observed azimuthally averaged profile. The blue dashed line is the nuclear point source model component, the cyan dot-dashed line represents the profile of the model host galaxy, the red dotted line the additional components corresponding to close object that was also fitted. Finally, the solid black line shows the sum of the profiles of the galaxy and nuclear source.

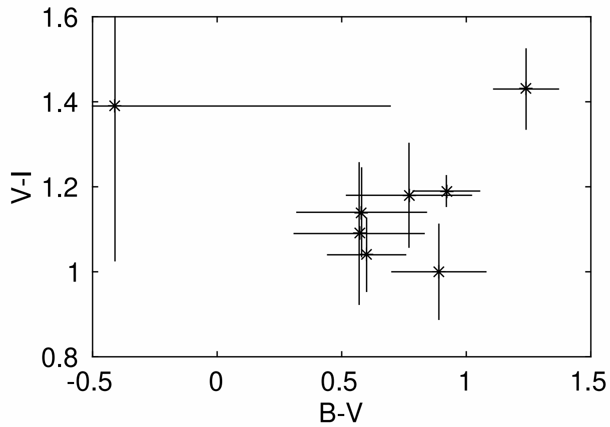

FIGURE 4.6— Absolute colors B-V vs V-I for the host galaxies studied in this thesis.

a few cases, commented below, the SBPs are well described as a combination of a point source and a simple host galaxy model (see Fig. 4.5). Furthermore, all blazars analyzed in this chapter (AP Lib, Mkn 501, and BL Lac) live in an elliptical galaxy with $n \geq 4$. Many authors (e.g. Scarpa et al. 2000, Urry et al. 2000 and references therein) also find this result. Another point that supports our confidence in the analysis is that the effective radii of the fitted host galaxies are consistent across the different filters. The exceptions are due to the low S/N of these data.

The average absolute colors of the host galaxy of our sample are $B - V = 0.80$ (the color of AP Lib is not considered in the average due to its large measurement error), $V - R = 0.55$, $V - I = 1.18$ and $J - K = 0.955$. Figure 4.6 shows the color-color plot of the host galaxies. These colors are similar to those found by other authors for typical field galaxies (e.g., the isolated sample of Johansson & Bergvall 1990, Fukugita et al. 1995).

Several correlations between the Sérsic parameters and the galaxy properties have been found by earlier studies. In a sample of elliptical and S0 galaxies, Caon et al. (1993) found a good correlation of the Sérsic index with global parameters of the galaxies, such as the total luminosity and the effective radius. Galaxies with a larger value of n are generally more luminous and bigger. The same correlations were later confirmed by Graham et al. (1996) in a sample of the brightest cluster galaxies. In Fig. 4.7 we plot the absolute magnitude in R against the Sérsic index and the effective radius: the host galaxies presented here show a correlation between the Sérsic index and the brightness. One would expect that larger galaxies are brighter and also this correlation, which has been observed in other studies (e.g., Häußler et al. 2013), is clearly evident in our data (Fig. 4.7).

As mentioned above, we fixed the Sérsic index in our sample, except for Mkn 501. The reason for this was the limited resolution and S/N ratio of our data. The analysis of the GAMA sample of galaxies (Vulcani et al. 2014, Kennedy et al. 2015) has shown that for larger Sérsic indices (n$\geq$2.5), n only presents slight variations with wavelength. In our case, most galaxies have a Sérsic index larger than this value, hence this result supports our simplification.

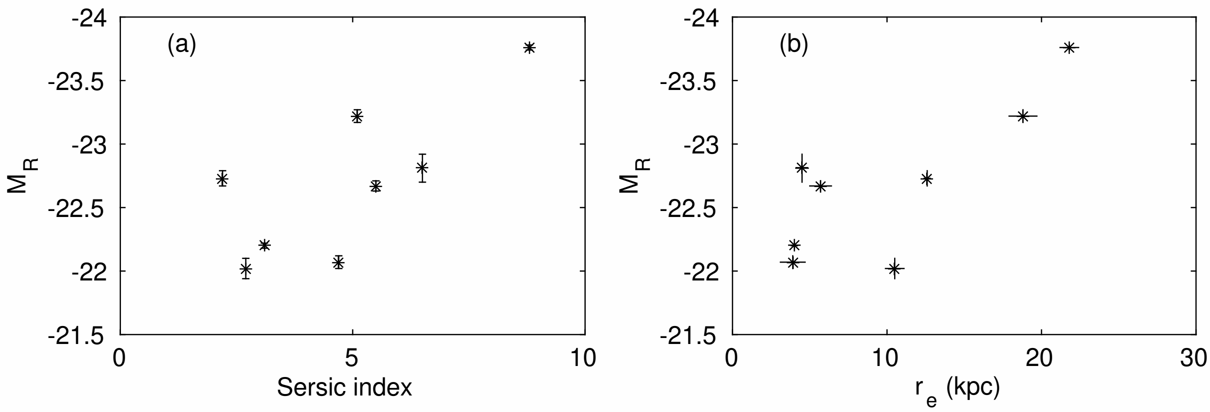

FIGURE 4.7— (a) R-band absolute magnitude of the host galaxies against the Sérsic index. (b) R-band absolute magnitude of the host galaxies vs effective radius in kpc.

As reported by Nilsson et al. (2003), one can recover the host galaxy parameters without bias if the PSF is calculated with sufficient high S/N and the host galaxy is relatively large (several times larger than the PSF). This is the case for most of our objects. But with the NIR data, in which the pixel scale is large ($1''$), the FWHM of the PSF is only 2.3-2.6 pixels, so that the convolution may be not precise enough. For that reason, the decomposition of the NIR data should be taken with care.

In Table 4.3 we present the results of the host galaxy decomposition for some of our objects made by other authors. Column 1 shows the name of the object, and Col. 2, the reference; the filter used is found in Col. 3, while the total magnitude of the host galaxy is displayed in Col. 4. The effective radius of the galaxies in arcseconds and kpc is presented in Cols. 5 and 6, respectively. Columns 7 and 8 show the axis ratio, and the Sérsic index found. Finally, some remarks are given in the last column. It is clear from the table that different authors obtained quite different values for the host galaxy. This is partly due to the fact that they are not using the same model or method (1D vs. 2D). However, after correcting from these effects, the differences are much higher than the quoted errors. This suggests that there are systematical errors coming from the S/N, host galaxy/nucleus ratio or the method of analysis (Nilsson et al. 2007).

Except for a few outliers, our values of the total magnitude agree well (to a precision of 0.2 mag) with those provided in the recent literature. Also, the axis ratio agrees very well with the values found by other authors. This, however, is not always the case for the effective radius. First, there is some coupling between the effective radius and the Sérsic index, so that if one fixes the Sérsic index to a value lower than the optimum, as in the case of fitting a de Vaucouleurs profile, the r_e value will be smaller than the optimal value. This partly explains the dispersion of the values of the effective radius found in the literature. Furthermore, the difference in the SBP for different Sérsic indices is more pronounced when the inner and outer regions of the galaxy are compared (Graham et al. 1996). However, in the analysis of the AGN host galaxies, the inner regions are contaminated by the point source of the active nucleus, while the profile

TABLE 4.3— Results of the host galaxy decomposition by other authors.

Object	Ref.[a]	Filter	m_{host} mag	r_e $''$	r_e kpc	b/a	n	remarks[b]
III Zw 2	1	R	15.9		13.9			1D, exp
I Zw 1	2	I			3.7	0.90		2D, dV
AP Lib	3	B	16.5	2.9				1D, dV
AP Lib	4	R	14.6	5.7				1D, dV
AP Lib	5	R	14.4	8.7		0.95	4.5	2D, Sérs
AP Lib	6	R	14.4	3.7				1D, dV
AP Lib	7	R	14.3	6.7				1D, dV
Mkn 501	5	B	14.4	22.1		0.75	5.3	2D, Sérs
Mkn 501	3	B	14.2	9.4				1D, dV
Mkn 501	3	V	13.0	9.4				1D, dV
Mkn 501	4	R	12.7	9.3				1D, dV
Mkn 501	5	R	12.8	20.0		0.75	5.5	2D, Sérs
Mkn 501	8	R	11.9	45		0.76	10.0	2D, Sérs
Mkn 501	7	R	12.4	17.2				1D, dV
Mkn 501	9	R	11.9	48.2		0.76	11.1	2D, Sérs
Mkn 501	10	H	10.4	5.3				1D, dV
II Zw 136	11	V	15.6		4.5			1D, exp
BL Lac	5	B	17.5	8.5		0.68	1.7	2D, Sérs
BL Lac	3	B	17.3	3.2				1D, dV
BL Lac	5	R	15.3	5.8		0.65	1.5	2D, Sérs
BL Lac	6	R	15.4	4.8				1D, dV
BL Lac	7	R	15.0	6.6				1D, dV
BL Lac	9	R	15.0	10.4		0.57	5.3	2D, Sérs
BL Lac	10	H	12.2	1.0				1D, dV

(a) References: 1: Granato et al. (1993); 2: Zheng et al. (1999); 3: Hyvönen et al. (2007); 4: Abraham et al. (1991); 5: Stickel et al. (1993); 6: Scarpa et al. (2000); 7: Pursimo et al. (2002); 8: Nilsson et al. (1999); 9: Nilsson et al. (2007); 10: Kotilainen & Falomo (2004); 11: Smith et al. (1986a);
(b) 1D: 1-D fit; 2D: 2-D fit; exp: exponential galaxy profile; dV: de Vaucouleurs galaxy profile; Sérs: Sérsic galaxy profile.

in the outer region depends on the estimate of the sky background.

For Mkn 501 there is a big difference in the r_e values between the optical and the NIR bands. This difference is much larger than expected (Vulcani et al. 2014 and Kennedy et al. 2015). The fact that there is also a relatively large difference in the Sérsic index could imply that there is an unidentified systematic error in the fit, maybe the sky background, which is much larger in the NIR bands and also more difficult to estimate correctly. However, we did not analyze this issue any further.

Although the profile preferred by the fit in I Zw 1 has a large Sérsic index ($n = 5.5$), corresponding to an elliptical galaxy, the images of this quasar clearly exhibited two arms. These could be tidal tails produced by merging (Zheng et al. 1999, Scharwächter et al. 2003). At the end of one of the arms, there is a point source, possibly a foreground star, that is responsible for the bump which the profile displays at $r = 12''$. The surface brightness profiles of Mkn 205 also show a bump at intermediate levels. This is due to a foreground star that is only at a distance of $3''$ from the nucleus of this AGN. In both cases, these close objects were also fitted (as can be inferred from Fig. 4.5 and the figures in the Appendix C and were included in the magnitude correction tables presented in Appendix C.

5

Long-term Variability

This chapter presents results on the long-term variability properties of our sample of AGNs. I built light curves, color curves and produced plots of the temporal evolution of the polarization. From the light curves, I derived average magnitudes and colors and discussed these results in the framework of current theoretical models. I also reconstructed the SED of the sources and list the mean polarization and polarization angle. I quantified the AGNs variability through the fractional variability parameter and found that blazars show stronger variations than other types of quasars. I searched for correlations between the redshift, luminosity, spectral index, mean polarization, and the fractional variability parameter. I found a remarkable correlation between spectral index and the fractional variability parameter, particularly significant for BL Lac objects: redder BL Lac objects display stronger variability.

A great number of publications has been devoted to the study of the long-term variability of AGNs during the last decades. Although several of these works deal with large (assumed to be complete or representative) samples of objects (e.g. Hook et al. 1994, Giveon et al. 1999, Garcia et al. 1999, de Vries et al. 2003), most of them focus on the study of a few, or even a single, source (e.g. Pursimo et al. 2000, Takalo et al. 1996, Villata et al. 2000a, Qian & Tao 2004, Villata et al. 2004). Also, theoretical models reveal the color as a variable as important as the flux to discriminate among the different possible mechanisms of variability; yet, only recently, systematic observations have been carried out in more than one spectral band (de Vries et al. 2003).

Our monitoring program of AGN variability carried out at the Canary Islands Observatories, observe a sample of 25 AGNs, in broad-band filters. In this chapter, we discuss the first results from our monitoring program. Here, we focus mainly on the long-term variability, but several overall properties of the objects (colors, luminosities, etc.) are also investigated. We show the light curves and the plots of the color and optical polarization time series. Further, we present a statistical analysis centered on the mean color and the spectral distributions of the AGNs and quantify their long-term flux variability. We also investigate the correlations among the luminosity, colors, optical polarization and variability.

A detailed study of the color of the objects, in particular, its variability and its relation with the flux, is postponed to the next chapter.

5.1 Temporal sampling and extinction correction

Because an important goal of our project is to study the rapid variability of AGNs, one or two objects were followed on many single nights for several hours, while in some others the same sources were observed only once or twice. Here we consider only nightly averaged magnitudes (or polarimetric measurements), to avoid problems derived from some nights having different statistical weights from others, as a result of inhomogeneous temporal sampling.

The photometry presented here is corrected for Galactic extinction (with the exception of Table 5.1, in which observed magnitudes are shown). This facilitates the comparison of results from different objects, in particular, their colors. However, this must be taken into account when comparing with other works.

The observed magnitudes were corrected for Galactic extinction by using the absorption coefficient from Schlegel et al. (1998), obtained from NED[1], and the standard extinction law (Cardelli et al. 1989). Most of the objects in our sample have a V extinction coefficient $A_V < 0.3$; some sources, near the plane of the Galaxy, have much larger extinction values—for example, $A_V(BL\ Lac) = 1.09$; $A_V(PKS\ 1622-29) = 1.43$; and for our most extinguished object, $A_V(PKS\ 0528+134) = 2.78$.

5.2 Light Curves

In this Section we present the light curves for all the observed objects; when available, also the color curves and the temporal evolution of the polarization are shown. In order to allow for easy comparison among light curves of the different sources, all light curves and color plots are displayed in the same magnitude scale—unlike the polarization plots. Only errorbars larger than 0.1 mag are shown in the light curves (to avoid overcrowding the plots).

Below, we briefly comment on some results for a few of the most interesting AGNs of the sample.

5.2.1 Notes on selected objects

3C 66A

This BL Lac object is one of our most intensively studied sources; the first NIR observations date back to 1991, while the first optical data are from 1993. The light curves (Fig. 5.4) are dominated by an outburst (Kidger et al. 1994a), more evident in the NIR bands (where we have observations before and after the outburst) than in the visible. By contrast to other objects, such as AO 0235+164, OJ 287, and BL Lac (see below), the outburst in 3C 66A last longer (roughly five years, from 1993 to 1998) and is smoother, with fast variations (lasting few months) superimposed, but not as conspicuous as in the other blazars. The amplitude of variation in the optical is $\Delta V \sim 1.7$ mag. We see apparent color variations, with an amplitude > 0.2 mag

[1]The NASA/IPAC Extragalactic Database (NED) is operated by the Jet Propulsion Laboratory, California Institute of Technology, under contract with the National Aeronautics and Space Administration.

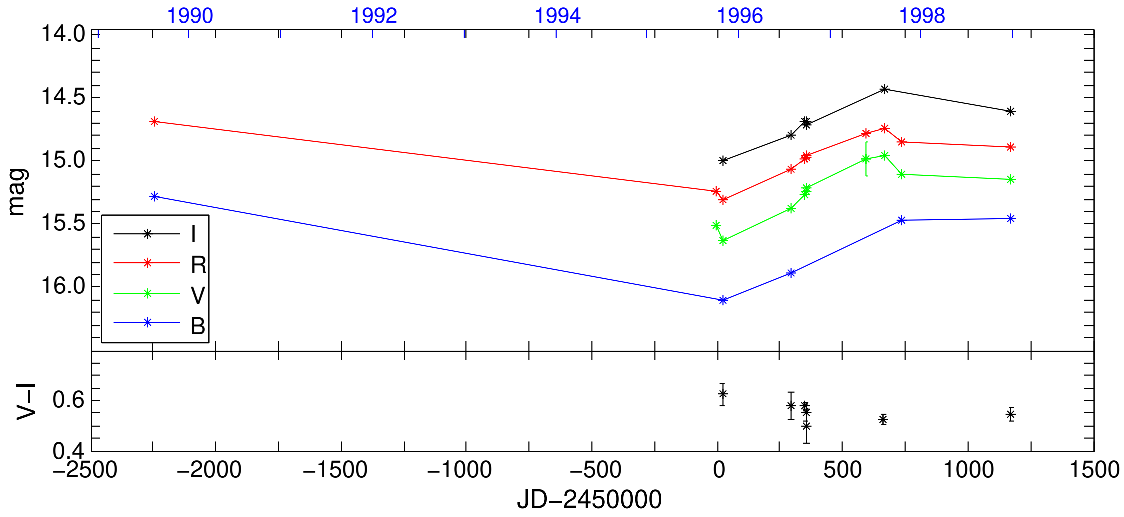

FIGURE 5.1— Light curves in the BVRI bands (top panel) and temporal evolution of the V-I color (bottom panel) of III Zw 2.

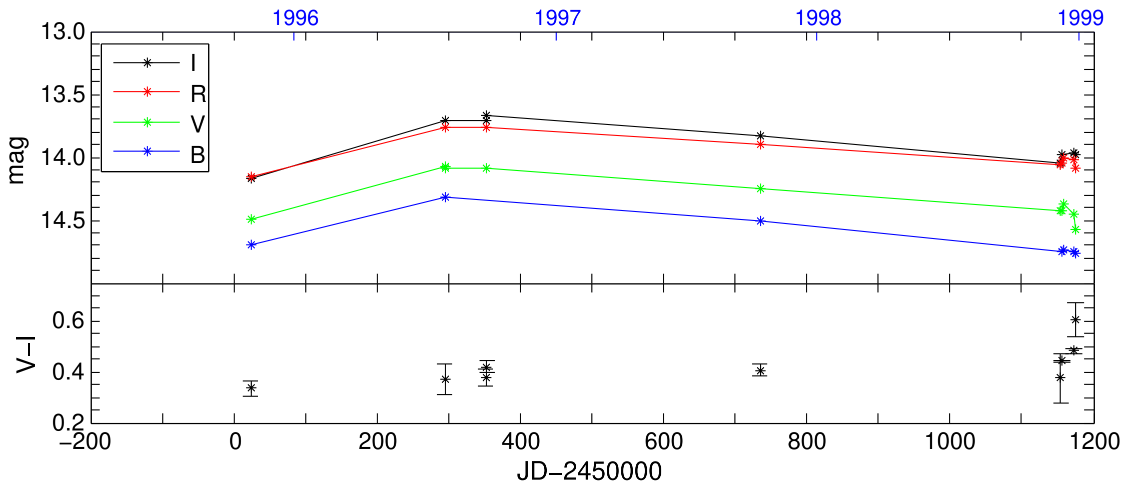

FIGURE 5.2— Light curves in the BVRI bands (top panel) and temporal evolution of the V-I color (bottom panel) of I Zw 1.

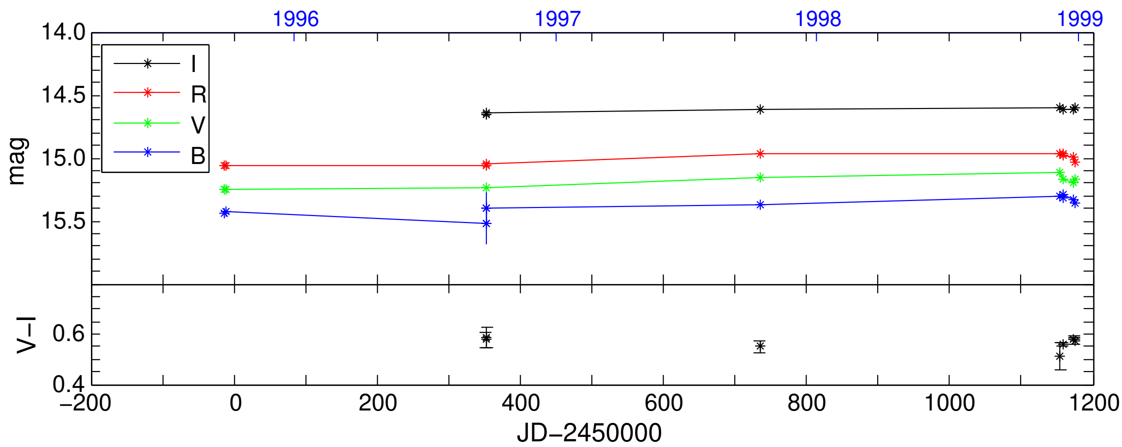

FIGURE 5.3— Light curves in the BVRI bands (top panel) and temporal evolution of the V-I color (bottom panel) of NAB 0205+02.

(Fig. 5.4) which, at least in the period after the maximum in the outburst (i.e., from mid 1995 until 1999), show a clear correlation with the flux: 3C 66A becomes bluer when it is brighter.

Photopolarimetric results are shown in Fig. 5.5. The degree of polarization fluctuates in the range of 15-20% in all bands (short term variations), but there are no significant long-term variations. The polarization angle varied in the range from 10-50°.

AO 0235+16

The BL Lac object AO 0235+16 underwent the largest amplitude of variation ($\Delta V > 4$ mag) in the sample. In its light curve (Fig. 5.6), a very large outburst occurred in 1998, stands out. Because of the faintness of this blazar in quiescence, only a few optical observations were taken before the outburst, but NIR data show that the object exhibited at least two big outbursts between 1989 and 1993.

Most of the color measurements are concentrated in the outburst of 1998 (see Fig. 5.6). The total amplitude of the color variations is $\Delta(B - V) \gtrsim 0.45$ mag, but note that this value is determined by a single point with large uncertainties.

S5 0716+71

The light curve of this blazar (Fig. 5.9) resembles that of 3C 66A: large-scale slow variations dominates, with short-term flares in scales of few months. We did not observe this object as intensively as 3C 66A, but the light curves are still fairly well sampled. The observed amplitude of variability in the V band was 1.5 mag. This BL Lac object could not be observed in the NIR, because its high declination prevented observations with the CST.

Short-term variations dominate the color variations of S5 0716+71 (see Figure 5.9), and

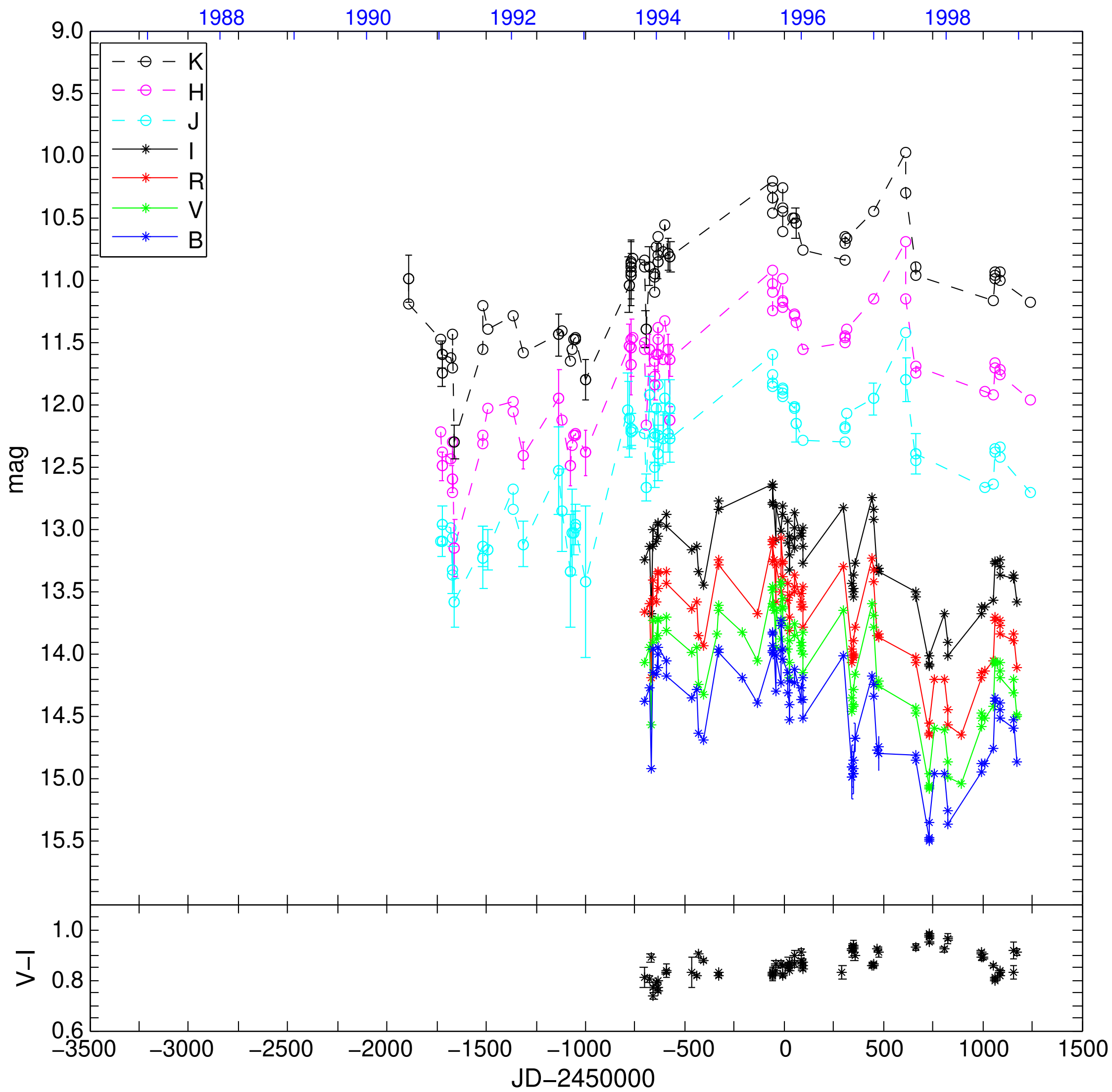

FIGURE 5.4— Light curves in the BVRIJHK bands (top panel) and temporal evolution of the V-I color (bottom panel) of 3C 66A.

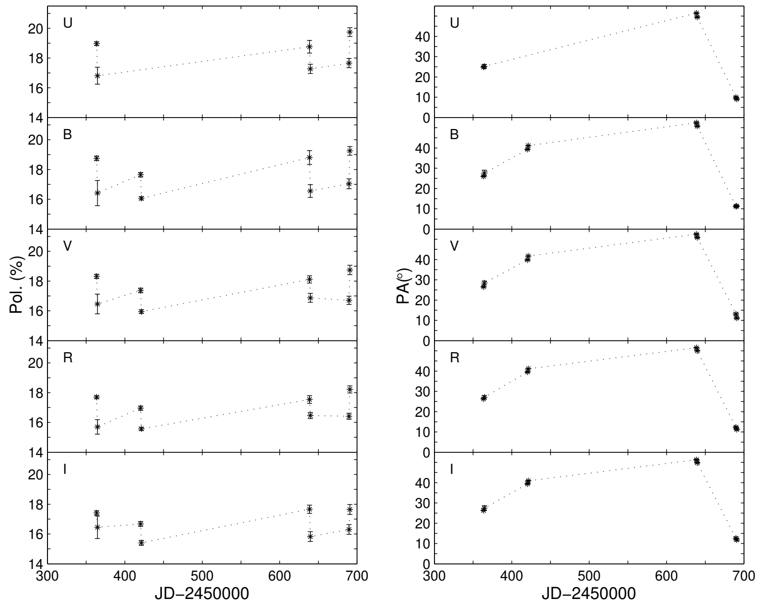

FIGURE 5.5— Polarization value and position angle vs time of 3C 66A in the UBVRI bands.

there is evidence for a correlation between the color and the magnitude of the object: the object is bluer when brighter. The observed polarization was around 5-10% (Fig. 5.10). Nevertheless, S5 0716+71 displayed large variations in position angle (between $30° - 120°$).

87 GB 073840.5+545138

Our observations confirm the blazar nature of this source. The photometric data (Fig. 5.11) show that this object is very active, with an amplitude of variability ($\Delta V \sim 1.4$ mag) similar to other blazars, such as 3C 345 or 3C 66A. At the beginning and the end of our observations, 87 GB 073840.5+545138 showed flares with amplitudes $\Delta V > 1$ mag. Our color data (Fig. 5.11) have large uncertainties, so color variations could not be observed, except at the end of 1999, when the object was brighter.

We have detected polarization (although with large uncertainties) at a level of around 5%, and evidence of variability in the polarization (Fig. 5.12).

OJ 287

This BL Lac object is our most intensively monitored AGN (Kidger et al. 1995; Sillanpaa et al. 1996a; González-Pérez et al. 1996; Hagen-Thorn et al. 1998). In its light curves (Fig. 5.14), we clearly distinguish the two-peaked outburst, exhibited by this blazar between 1994 and 1996. The two peaks took place at exactly the predicted time according to the supermassive binary black hole model of Sillanpaa et al. (1988). A number of smaller amplitude flares are superimposed to this outburst. At the end of our optical campaign, OJ 287 shows a steep decline in brightness,

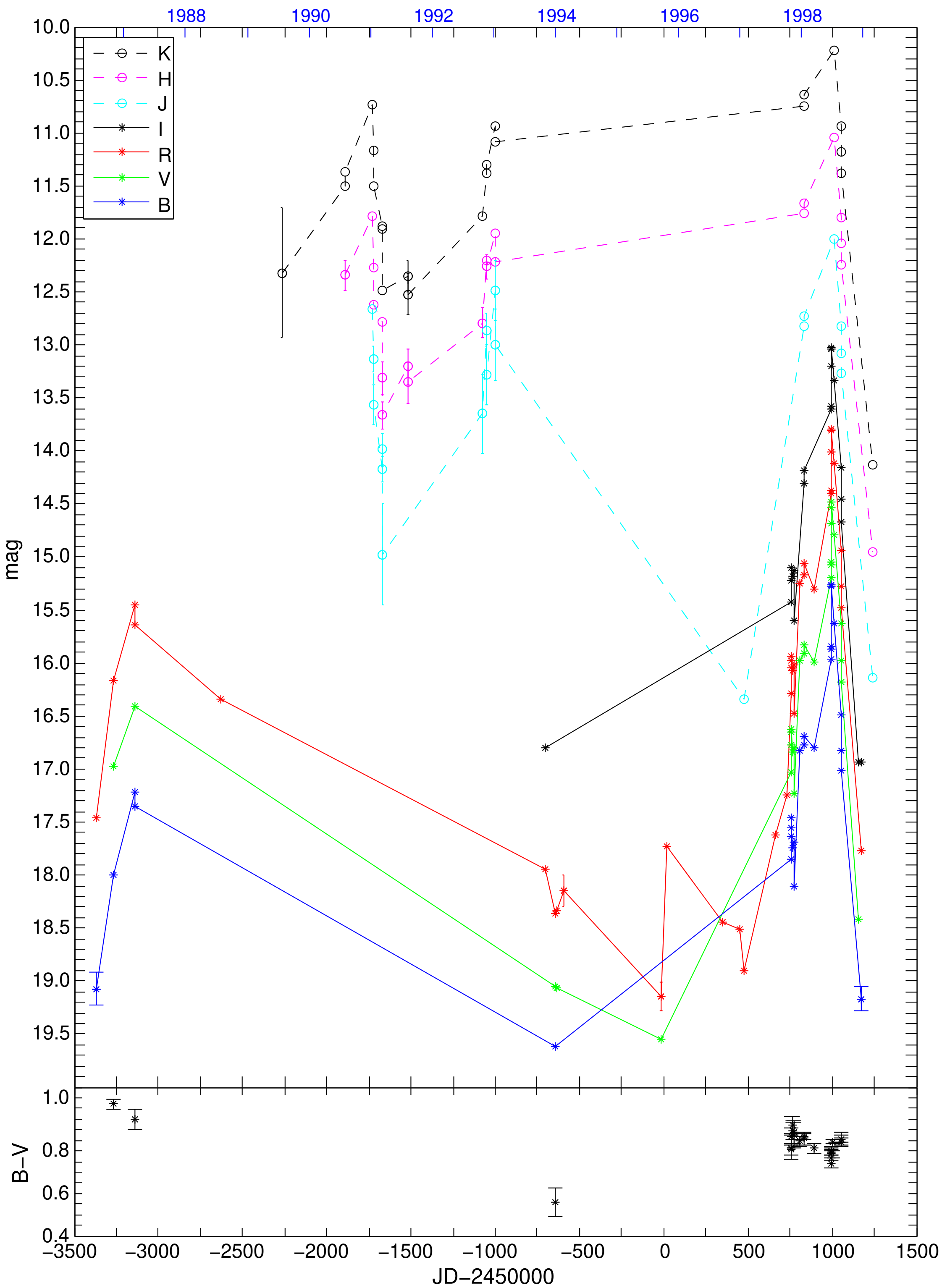

FIGURE 5.6— Light curves in the BVRIJHK bands (top panel) and temporal evolution of the B-V color (bottom panel) of AO 0235+16.

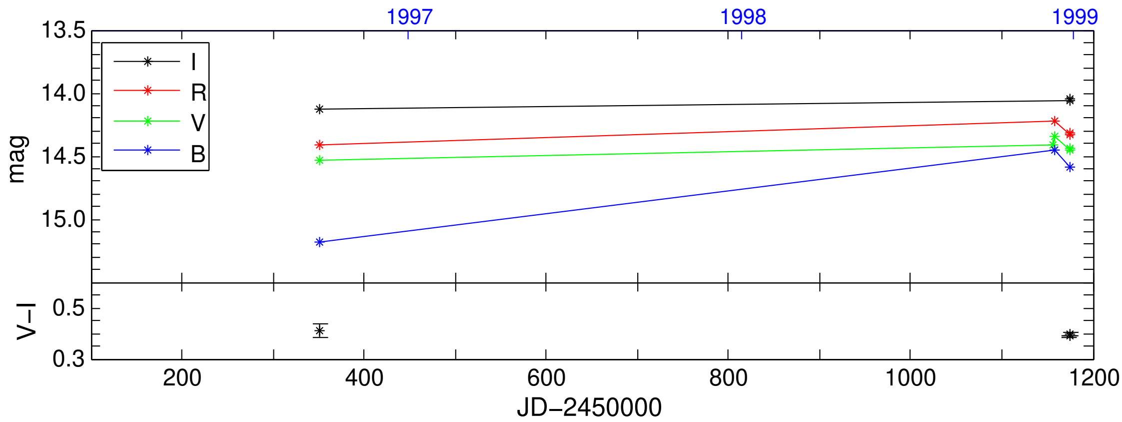

FIGURE 5.7— Light curves in the BVRI bands (top panel) and temporal evolution of the V-I color (bottom panel) of PKS 0405-12.

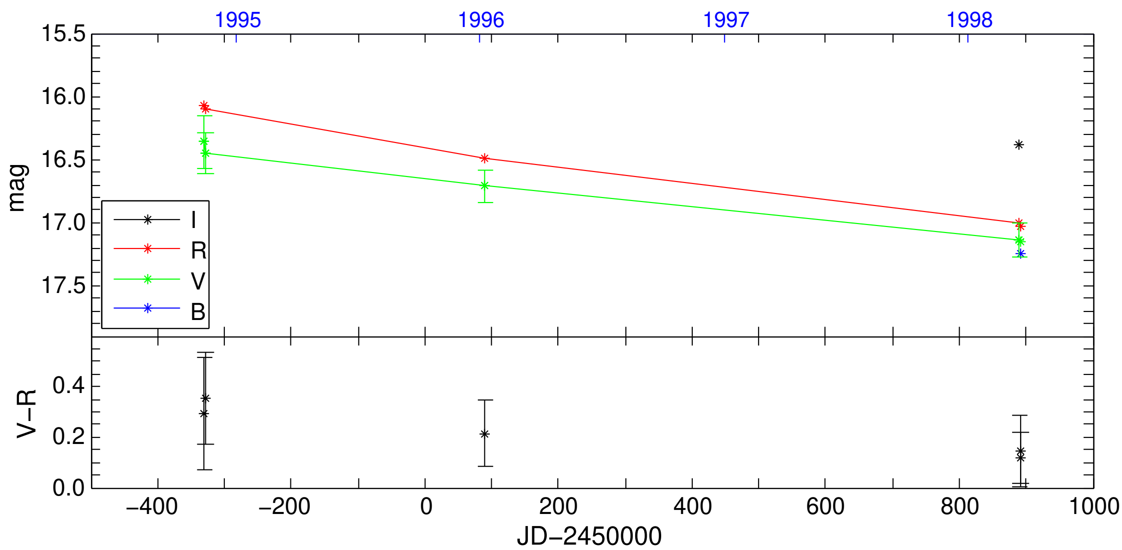

FIGURE 5.8— Light curves in the BVRI bands (top panel) and temporal evolution of the V-R color (bottom panel) of PKS 0528+134.

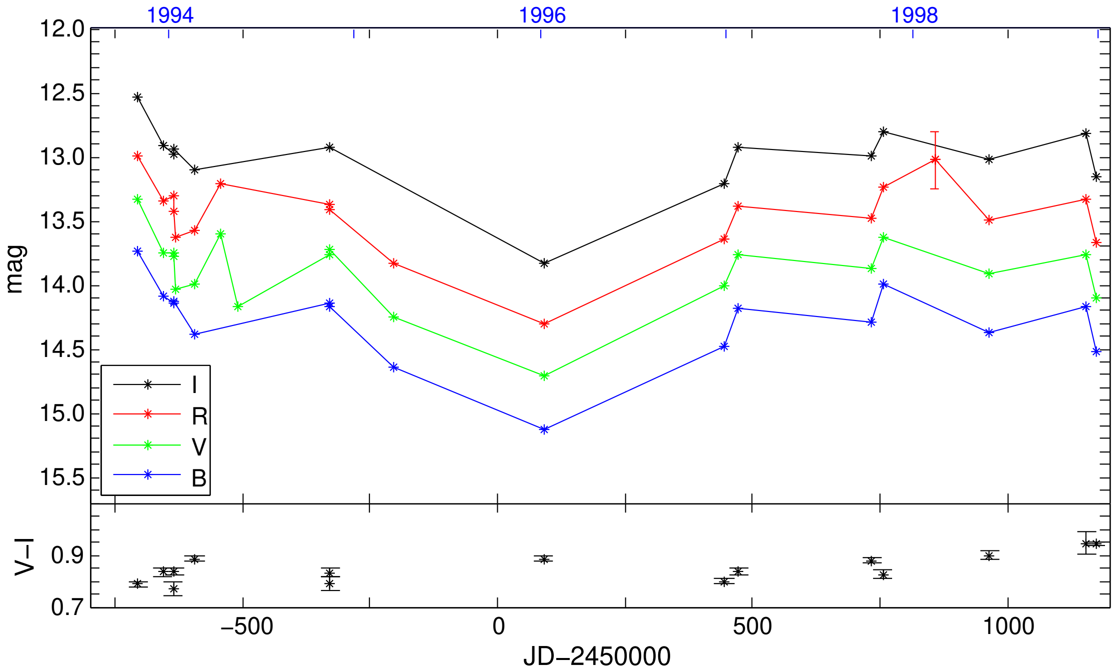

FIGURE 5.9— Light curves in the BVRI bands (top panel) and temporal evolution of the V-I color (bottom panel) of S5 0716+71.

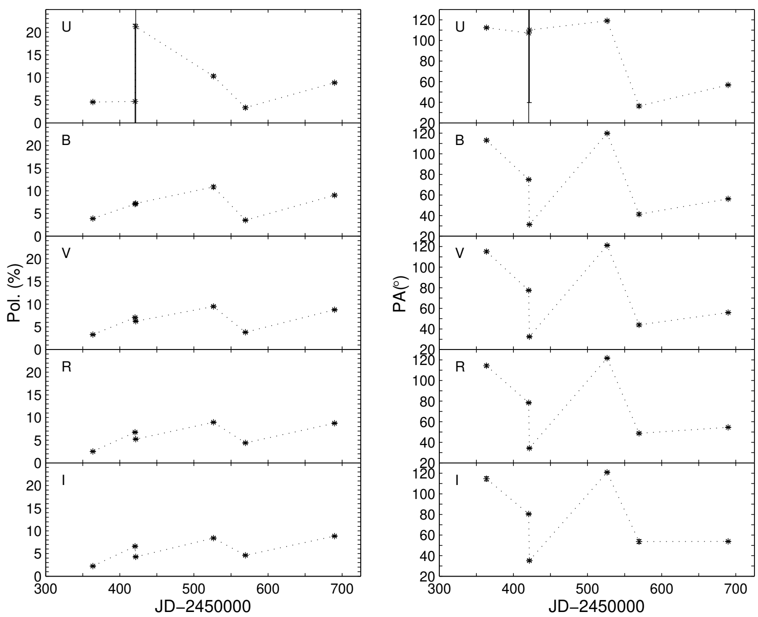

FIGURE 5.10— Polarization value and position angle vs time of S5 0716+71 in the UBVRI bands.

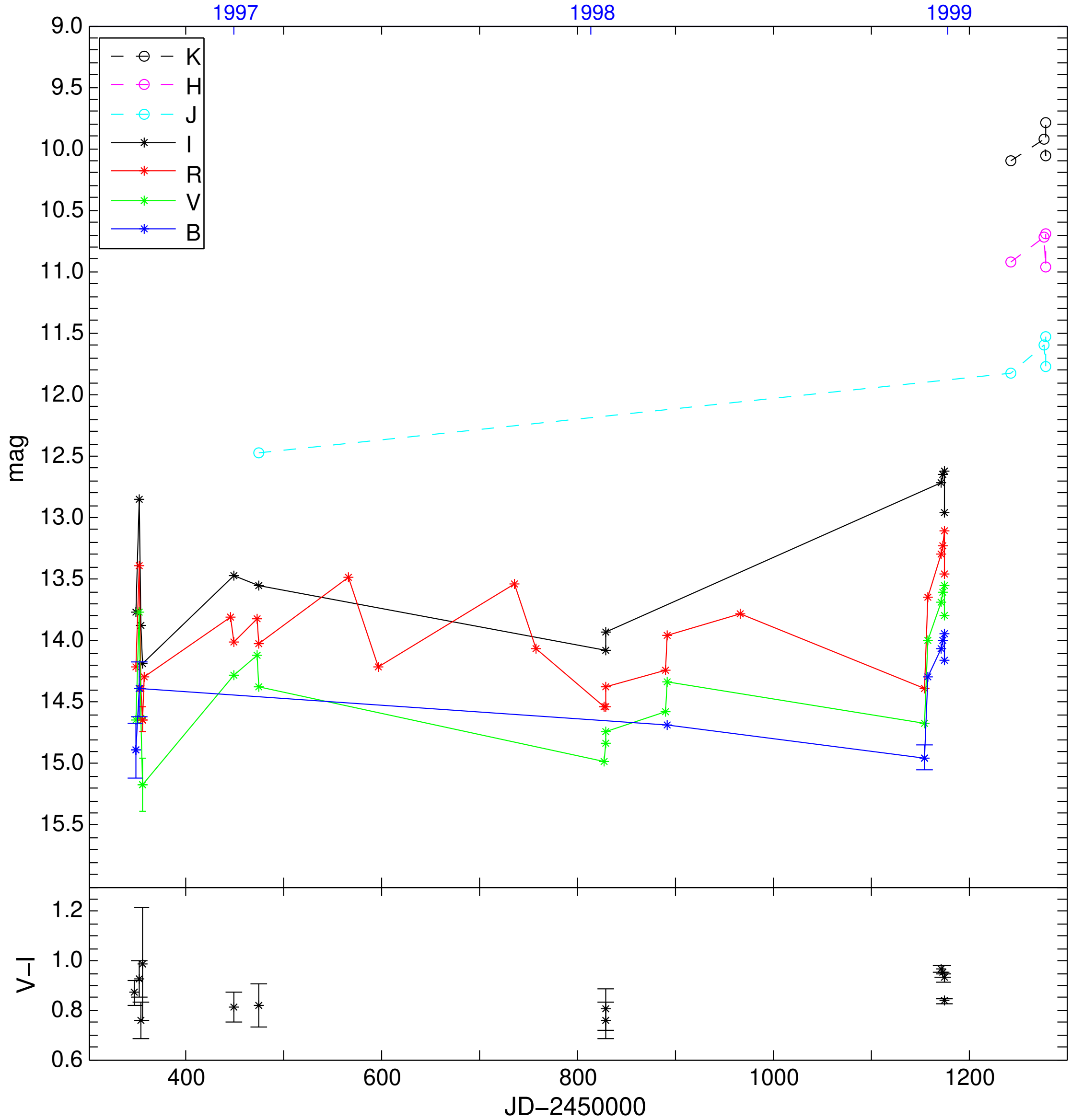

FIGURE 5.11— Light curves in the BVRIJHK bands (top panel) and temporal evolution of the V-I color (bottom panel) of 7GB 073840.5+545138.

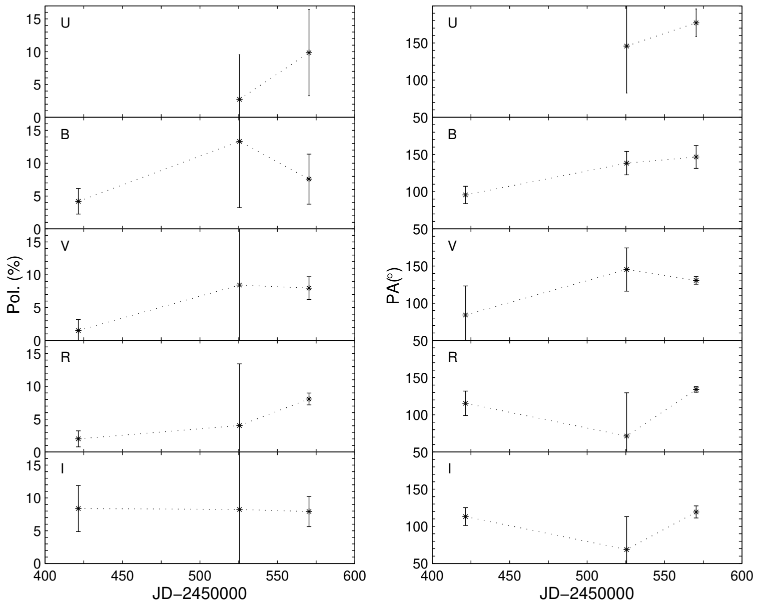

FIGURE 5.12— Polarization value and position angle vs time of 87GB 073840.5+545138 in the UBVRI bands.

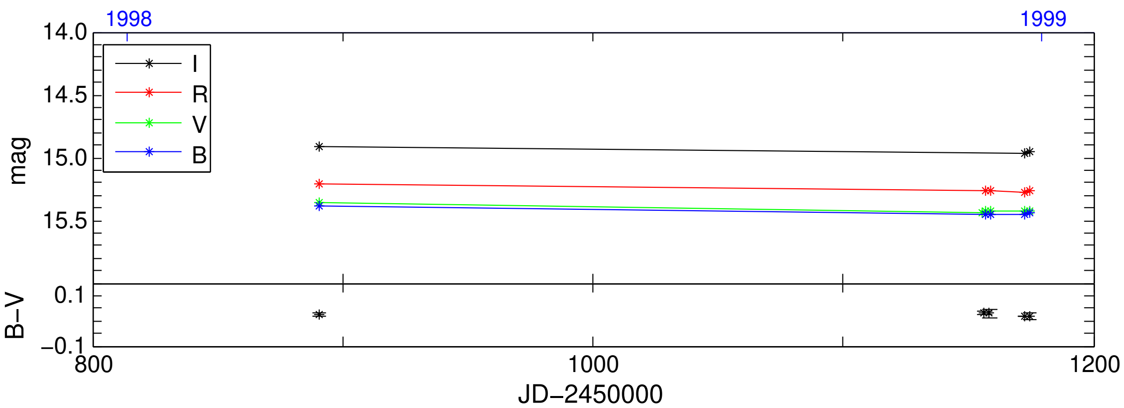

FIGURE 5.13— Light curves in the BVRI bands (top panel) and temporal evolution of the B-V color (bottom panel) of B2 0742+31.

reaching a minimum V$\sim$16.8 and H$\sim$13.5. A month later (April 1999) the object was even fainter in the NIR (H$\sim$13.8).

The colors (Fig. 5.14) show unexpected behavior. While in the magnitudes we clearly see the rise and decay of the outburst, the color plot shows a redward trend, with positive and negative excursions that coincide with the outbursts in the flux plot. This behavior, which has also been observed in other blazars, such as 3C 279 (see below), is suggestive of large injections of relativistic electrons (Kidger et al. 1995).

OJ 287 exhibited strong polarization (Fig. 5.15), with peaks around 30%. There is a trend in the polarization data (Fig. 5.15), which continuously decreases after the outburst, with small fluctuations superimposed.

Mkn 421

We do not discuss photometric results for Mkn 421—two very bright stars in the field and the lack of suitable comparison stars nearby (González-Pérez et al. 2001) makes the optical photometry of this object very difficult. Thus, we present only the polarization plots (Fig. 5.17). The polarization ranges between 3-10%, despite the high degree of dilution of the blazar flux by the host galaxy, and the position angle fluctuates around 60°.

Mkn 205

The light curves of this object (Fig. 5.18) show fluctuations of small amplitude typical of quasars. We did not detect any significant color variations (Fig. 5.18). Despite the presence of a bright foreground galaxy, we did not detect polarization.

3C 273

The RLQ 3C 273 shows slow fluctuations in the optical (Fig 5.19); the variations are more violent in the NIR, with some indications of rapid flares. However, larger and faster variations in the bluer bands are usually found in AGNs. Our observations of 3C 273 can be understood if the optical emission is dominated by the accretion disk and the NIR emission by the jet (see below). Valtaoja et al. (1990) suggest that 3C 273 is a miniblazar in which $\sim$10% of the flux comes from a blazar component. In fact, this object is sometimes classified as an FSRQ. All models show that the jet-induced variability is faster and of higher amplitude than the variations induced by the accretion disk and Courvoisier et al. (1988) found that synchrotron flaring emission contributes in the optical-NIR emission of 3C 273. We detected color variations (Fig. 5.19), with amplitudes $\Delta(V-I) \sim 0.15$ mag; as expected, the source shows bluer colors when it is brighter.

PG 1351+640

As for other RQQs in our sample, the light curves of PG 1351+640 (Fig. 5.21) show only variations of small amplitude ($\Delta V \sim 0.5$ mag). Despite the small amplitude of the flux variations, we detected color variations that correlate with the brightness (as usual, the source is bluer when

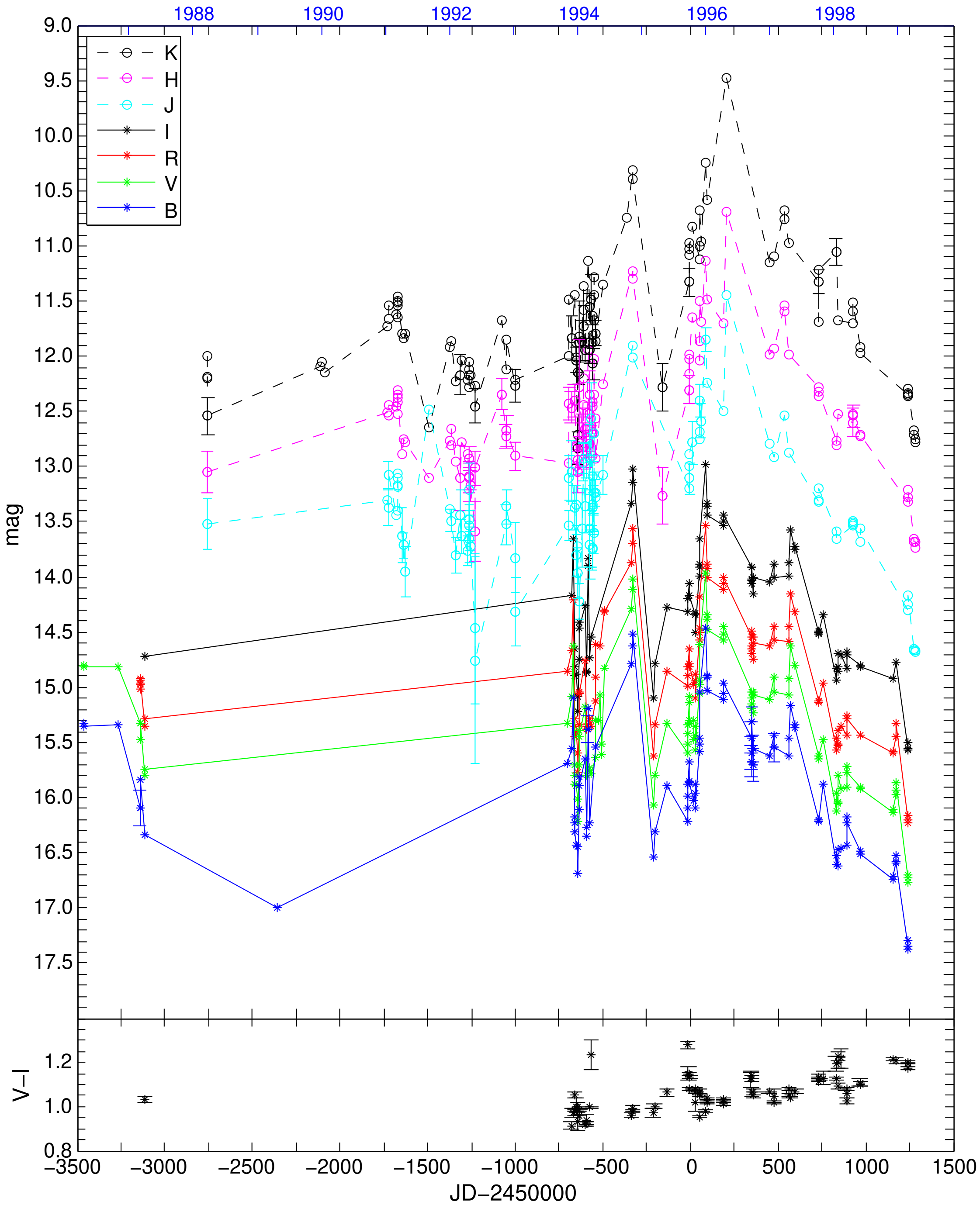

FIGURE 5.14— Light curves in the BVRIJHK bands (top panel) and temporal evolution of the V-I color (bottom panel) of OJ 287.

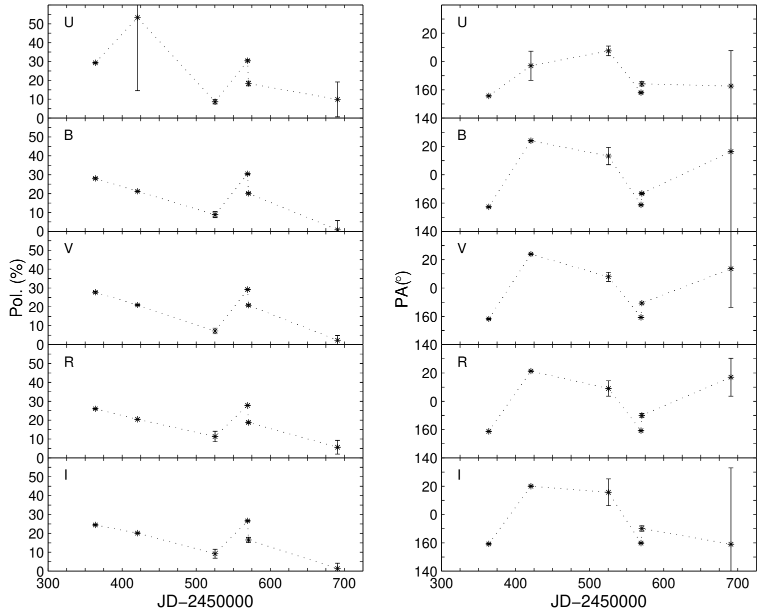

FIGURE 5.15— Polarization value and position angle vs time of OJ 287 in the UBVRI bands.

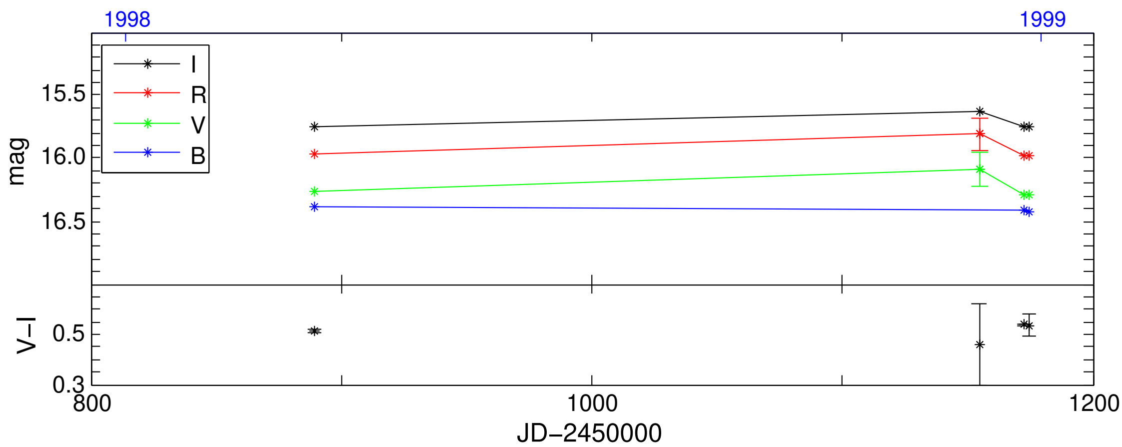

FIGURE 5.16— Light curves in the BVRI bands (top panel) and temporal evolution of the V-I color (bottom panel) of PG 1008+133.

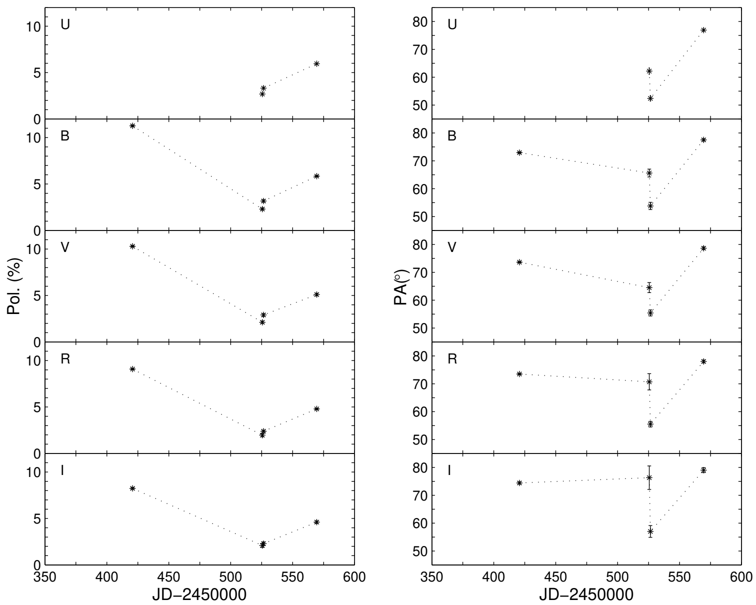

FIGURE 5.17— Polarization value and position angle vs time of Mkn 421 in the UBVRI bands.

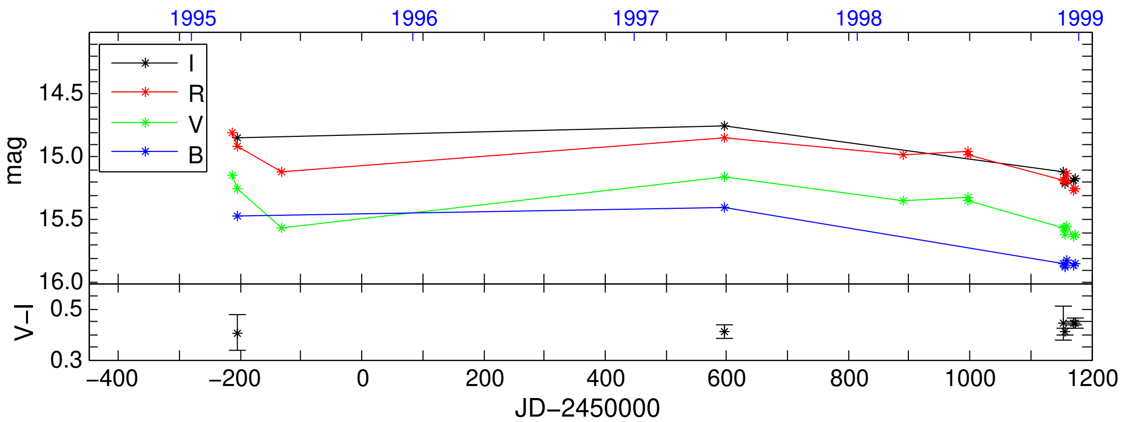

FIGURE 5.18— Light curves in the BVRI bands (top panel) and temporal evolution of the V-I color (bottom panel) of Mkn 205.

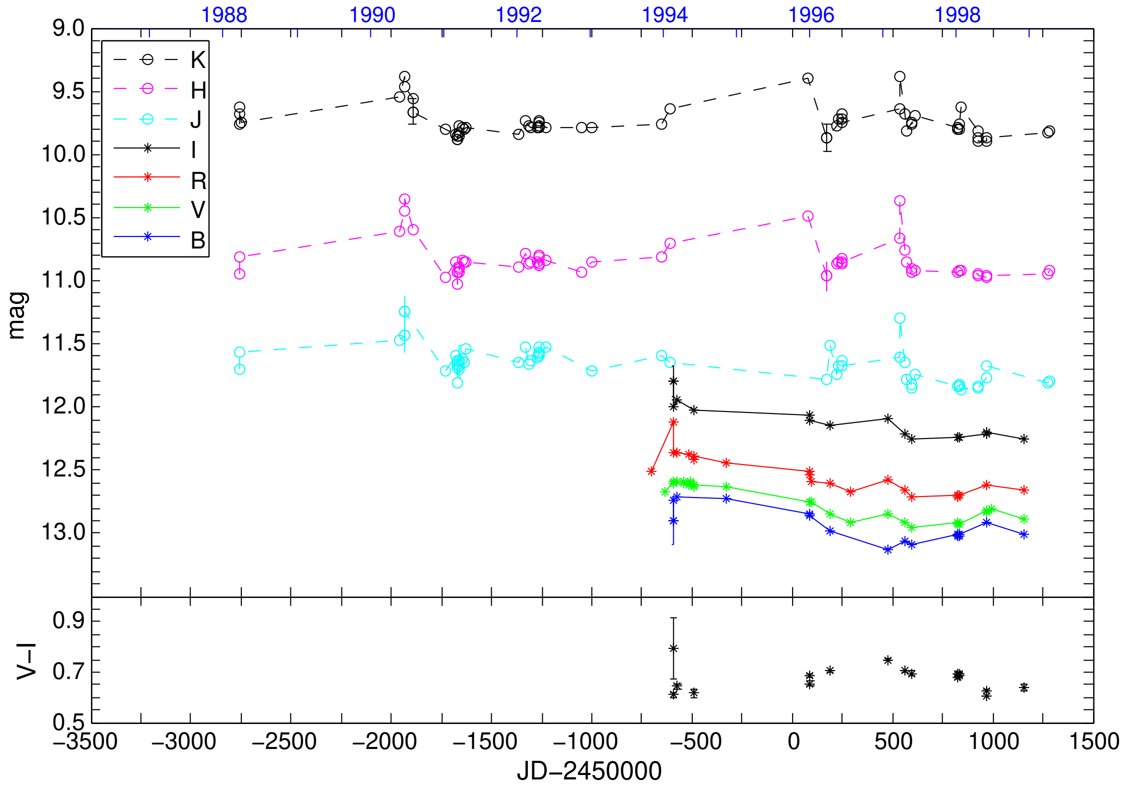

FIGURE 5.19— Light curves in the BVRIJHK bands (top panel) and temporal evolution of the V-I color (bottom panel) of 3C 273.

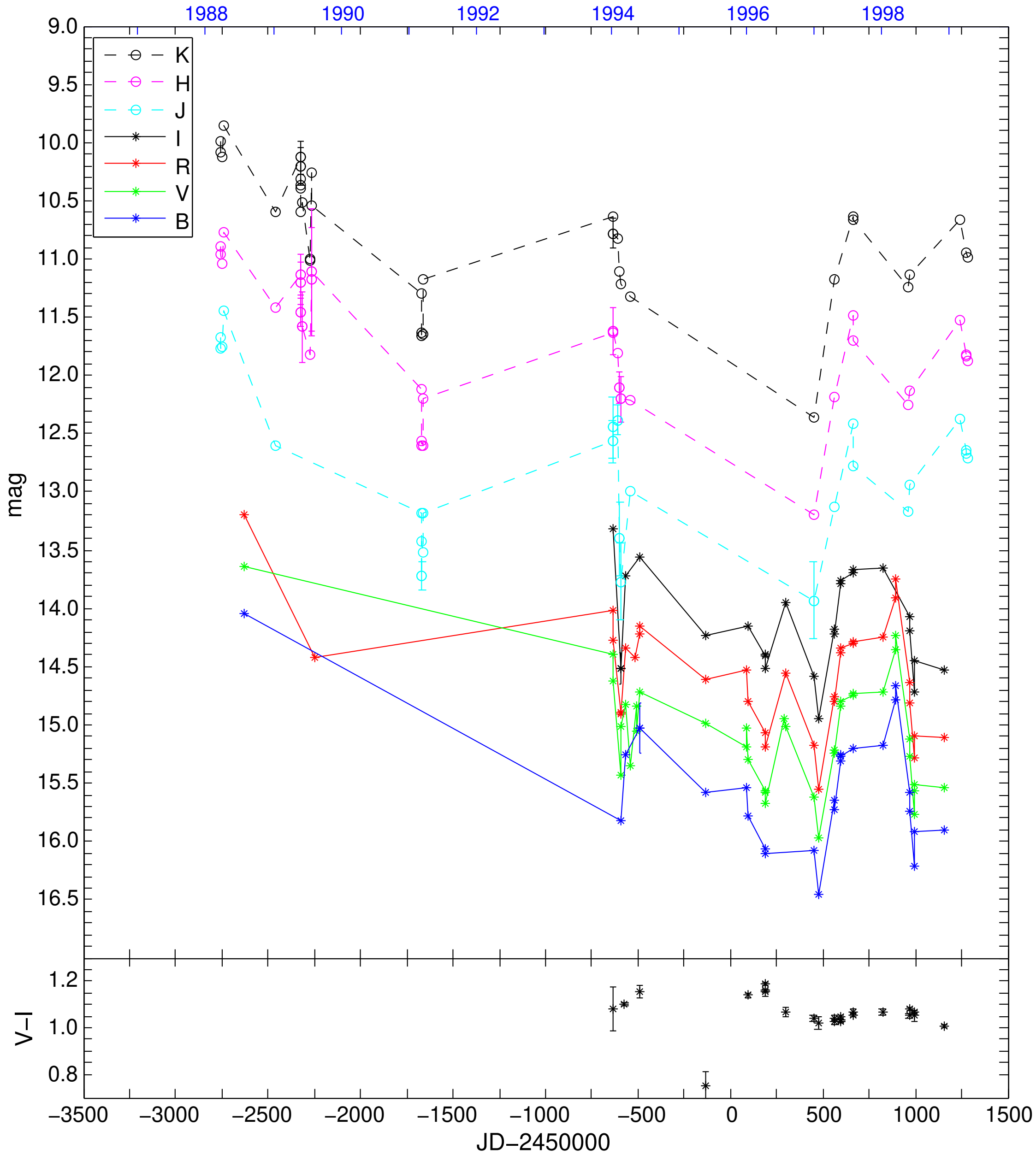

FIGURE 5.20— Light curves in the BVRIJHK bands (top panel) and temporal evolution of the V-I color (bottom panel) of 3C 279.

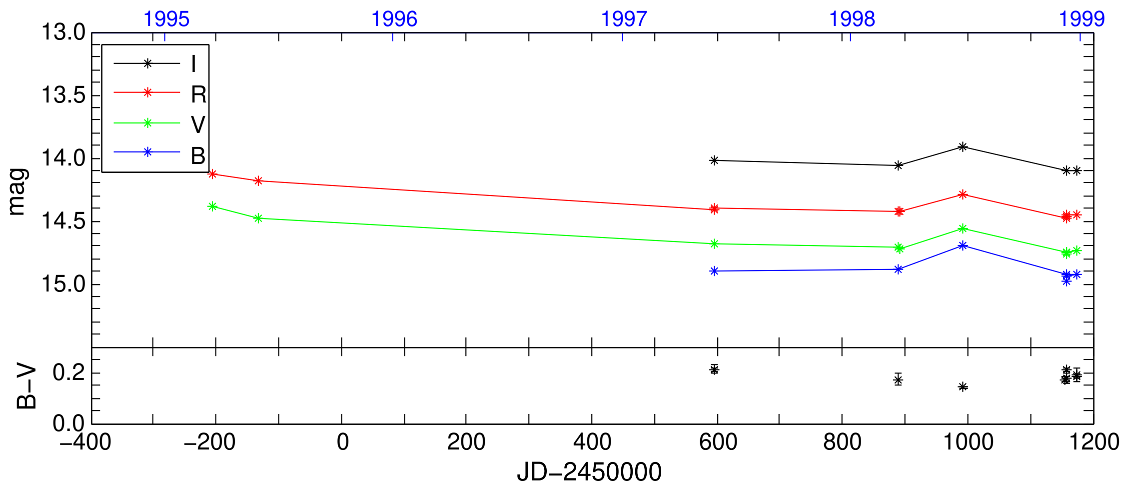

FIGURE 5.21— Light curves in the BVRI bands (top panel) and temporal evolution of the V-I color (bottom panel) of PG 1351+640.

brighter). We monitored the polarization of this low polarization quasar (LPQ) and found that the polarization and the position angle are stable around 1-2% and 0°, respectively (Fig. 5.22). This is the highest polarization level that our group has found in a low polarization quasar (de Diego 1994a).

AP Lib

This BL Lac object was observed, as was PKS 1510-08, at the beginning and the end of our observation period (1987 and 1997-1998), as is shown in Fig. 5.24. From these data, we can just say that this object exhibited variability. In contrast, we intensively studied the polarization (Fig. 5.25). It remained at a quite stable level around 4% (note that the polarization is diluted by the large emission of the host galaxy), while the position angle changed steadily from 40° to 160° in ~6 months. Note that the changes in the position angle are intrinsic and cannot be due to a variable contribution of the host galaxy originated from fluctuations in the seeing.

PKS 1622-29

This source has been identified as a large amplitude variable object ($\Delta R \sim 3.5$ mag)—it is, along with AO 0235+16, the object of largest amplitude in our sample. Due to its faintness, PKS 1622-29 could not be observed on many nights (only 7 nights in the R-band and less in the other filters). The light curves presented in Fig. 5.26 also show a strong outburst, peaking in 1996.

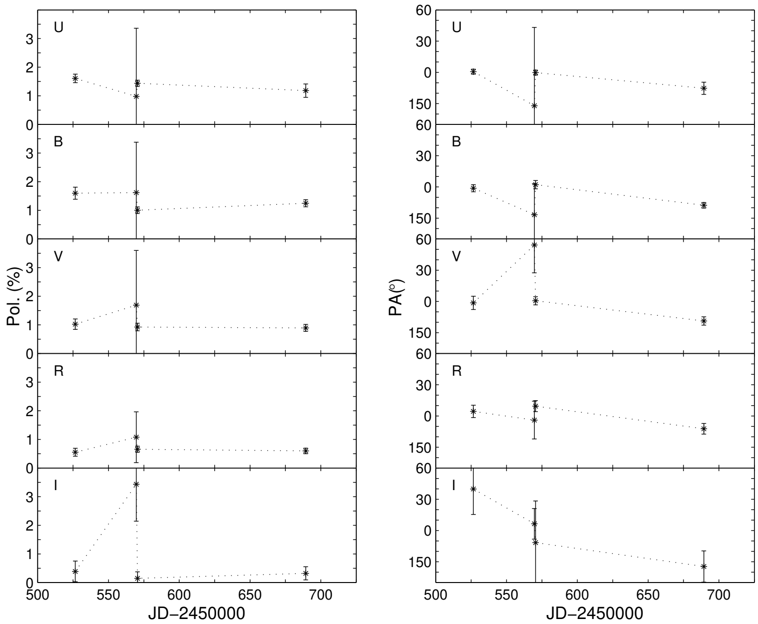

FIGURE 5.22— Polarization value and position angle vs time of PG 1351+640 in the UBVRI bands.

3C 345

The variations of this blazar (see Fig. 5.27) are well sampled in the optical, but not in the NIR, due to the object faintness. The optical light curves reveal that the source has a slowly varying base level and, superimposed on it, there are flares of short duration with an amplitude of 0.5-1.0 mag. The color curve (Fig. 5.27) exhibits a different behavior, with slower variations and an amplitude of 0.4 mag. There is not an evident relation between color and flux.

We observed this object in polarization mode during 6 nights (Fig. 5.28). The polarization did not show large variations, and its level was around 4%, although polarization as high as 35% was detected in the object during its decline from the 1983 outburst (Smith et al. 1986b).

BL Lac

BL Lac showed the fastest brightness variations in our sample; while the total amplitude of variability is lower than that observed in AO 0235+16, PKS 1622-29, and OJ 287, this source showed variations larger that 1 mag on a night-to-night basis. The light curve (Fig. 5.32) is characterized by a series of strong and rapid flares in 1998-1999. During this period, the object displayed strong activity, which was also observed by other groups (e.g., Villata et al. 2000a, Villata et al. 2004, Papadakis et al. 2003). The color variations (Fig. 5.32) are not large ($\Delta B - V \sim 0.3$ mag) and are dominated by the short-term variations.

BL Lac also exhibited strong activity in polarization (Fig. 5.33), with observed variations between 5-25% although the position angle remained quite stable between 120 and 140°.

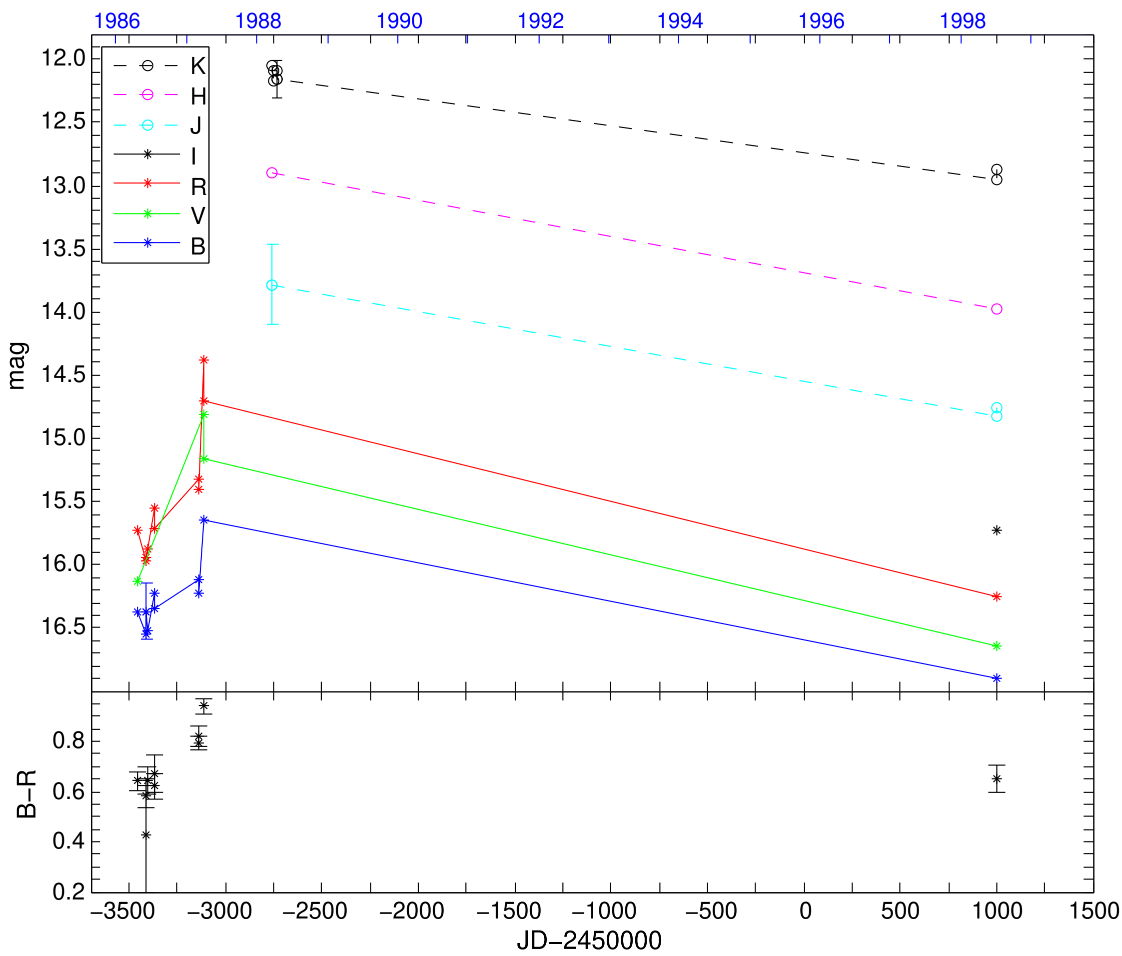

FIGURE 5.23— Light curves in the BVRI bands (top panel) and temporal evolution of the B-R color (bottom panel) of PKS 1510-08.

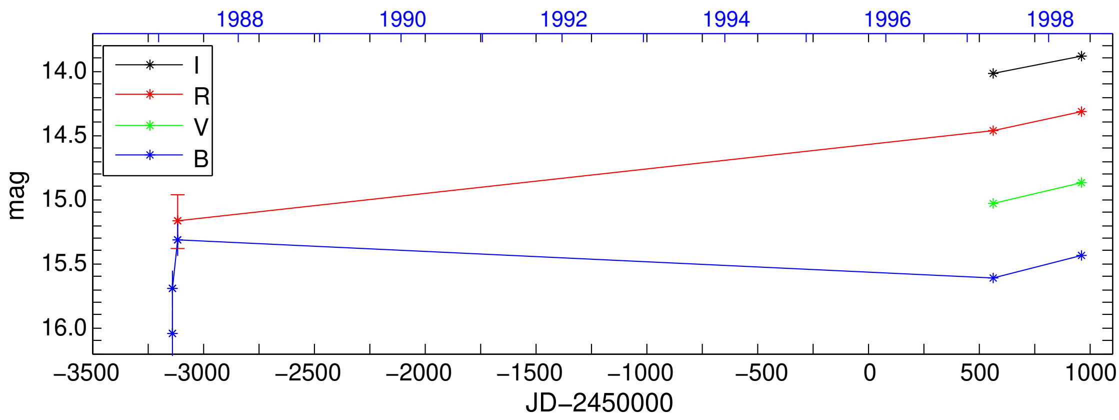

FIGURE 5.24— Light curves in the BVRI bands of AP Lib.

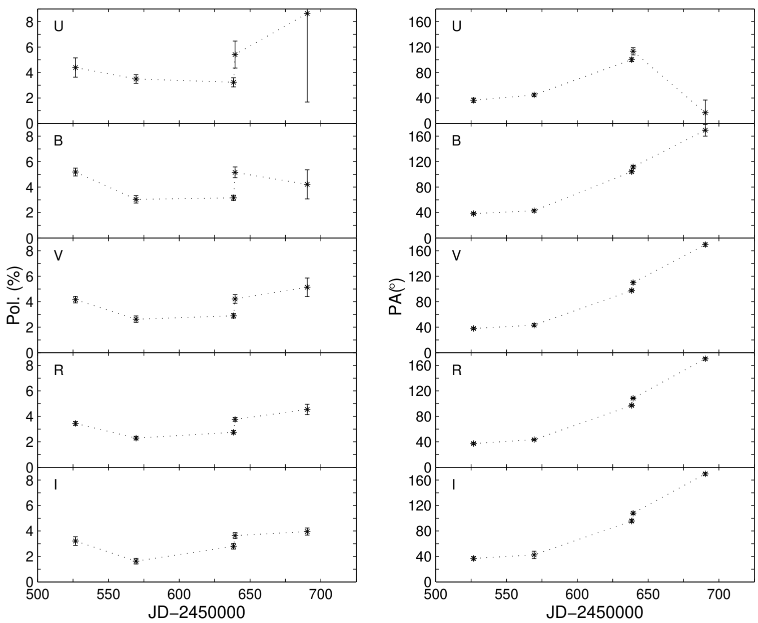

FIGURE 5.25— Polarization value and position angle vs time of AP Lib in the UBVRI bands.

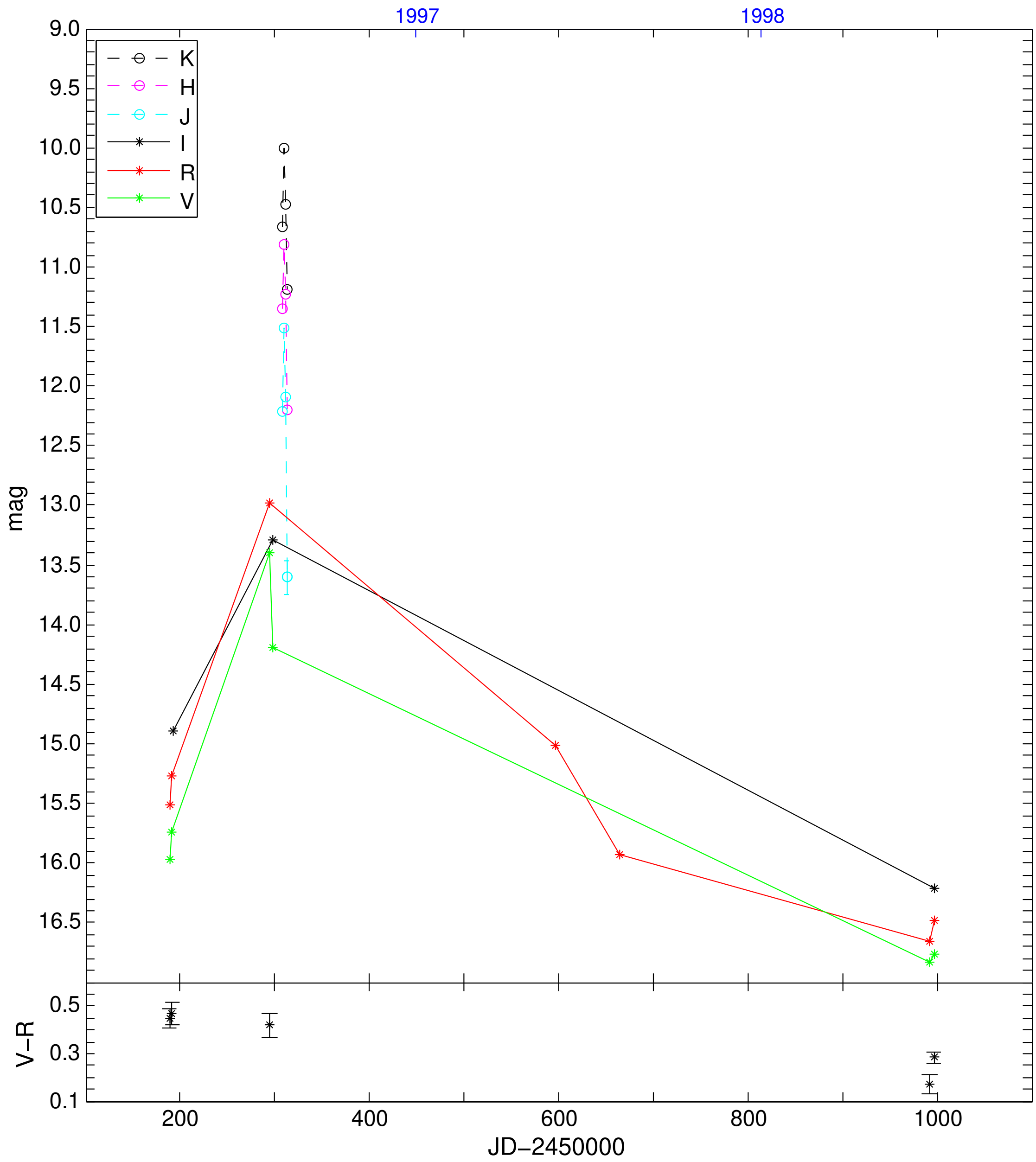

FIGURE 5.26— Light curves in the BVRIJHK bands (top panel) and temporal evolution of the V-R color (bottom panel) of PKS 1622-29.

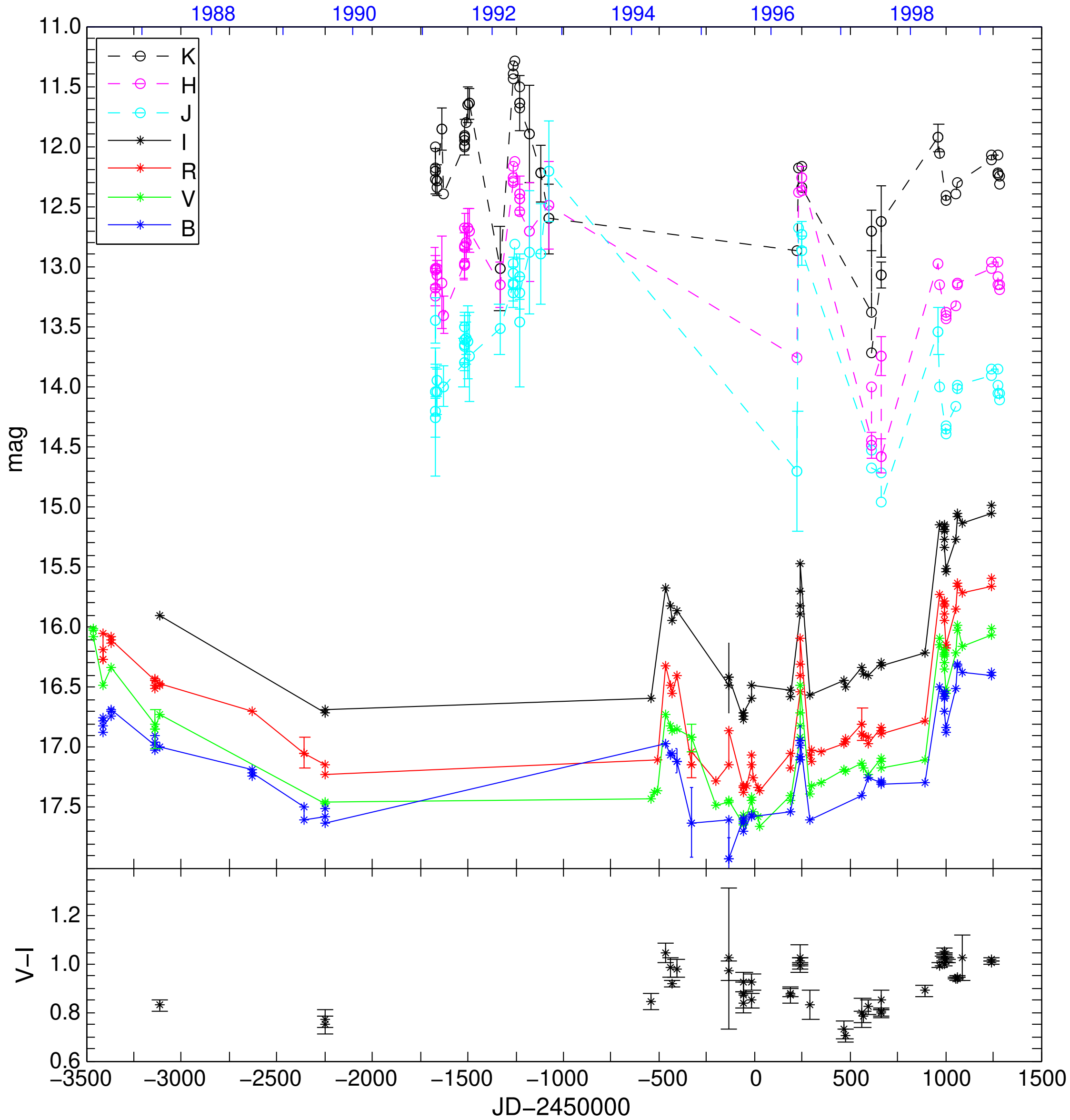

FIGURE 5.27— Light curves in the BVRIJHK bands (top panel) and temporal evolution of the V-I color (bottom panel) of 3C 345.

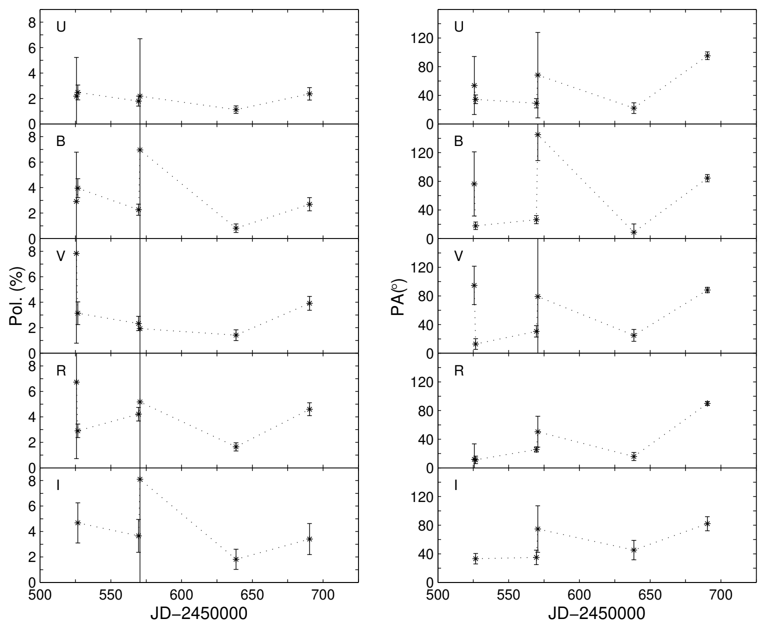

FIGURE 5.28— Polarization value and position angle vs time of 3C 345 in the UBVRI bands.

3C 454.3

Figure 5.34 shows the light curves of this blazar. It is an active source whose amplitude of variability seems small, but the object never remains stable. It also shows color variability (Fig. 5.34) without any obvious relationship with flux, but with large variations. In our five nights of polarimetric observations over a full year (Fig. 5.35), 3C 454.3 displayed a low degree of polarization ($p \lesssim 3\%$), although with a strong and variable frequency dependent position angle.

5.3 Global statistical properties

From the light curves, we can derive the statistical properties of the AGNs, namely, the average magnitudes and colors, the spectral energy distribution in the optical-NIR and the average polarimetry.

5.3.1 Average magnitudes and colors

Table 5.1 shows the median observed magnitudes (not corrected from Galactic extinction) in each of the observed optical and NIR filters. Most of the values lie in the range V$\sim 14-16$. Sources with these magnitudes can be observed with a good S/N ratio using the IAC80 telescope with exposure times of 5 min. Some objects (e.g., PKS 0528+134, GB 0738+54, and PKS 1622-29) are much fainter and accordingly, their exposure times were larger (typically, around 15 min). The brightest object in our sample is 3C 273.

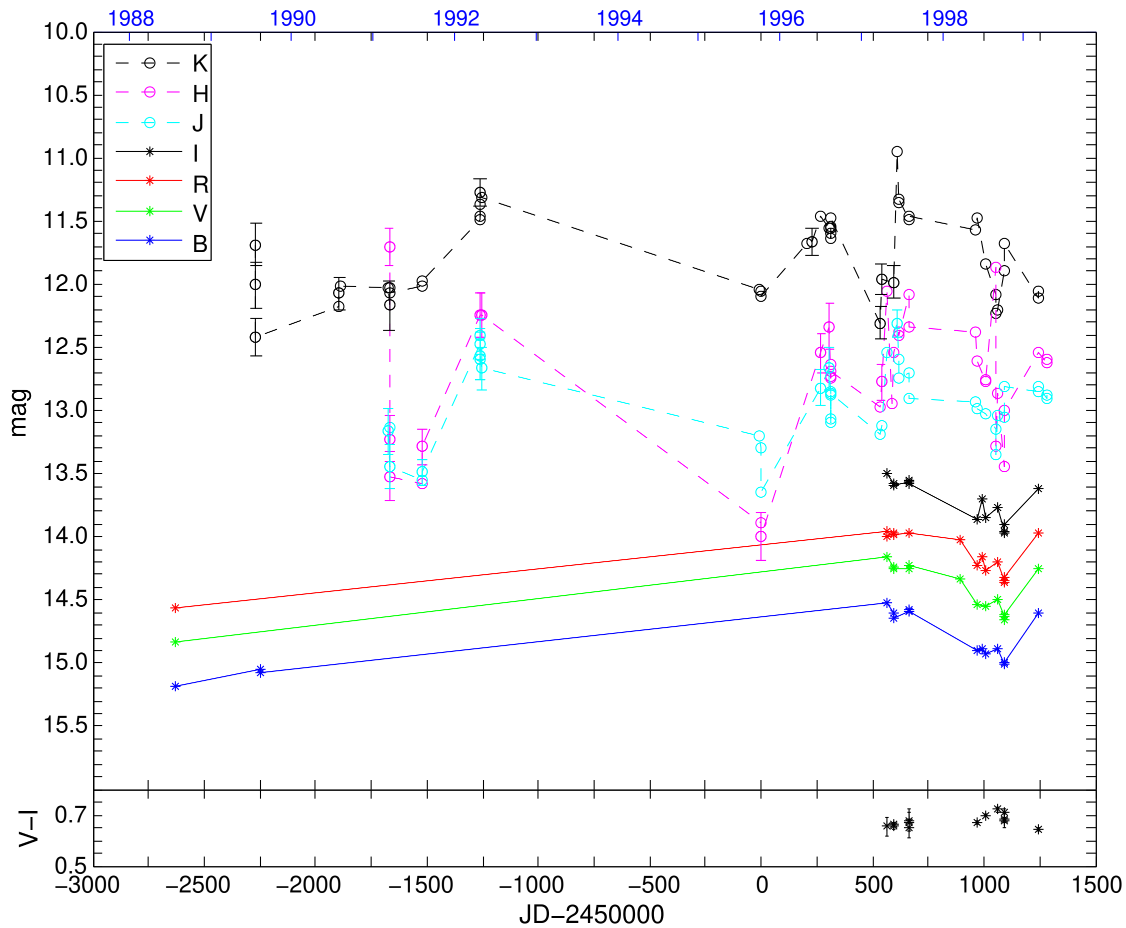

FIGURE 5.29— Light curves in the BVRIJHK bands (top panel) and temporal evolution of the V-I color (bottom panel) of Mkn 501.

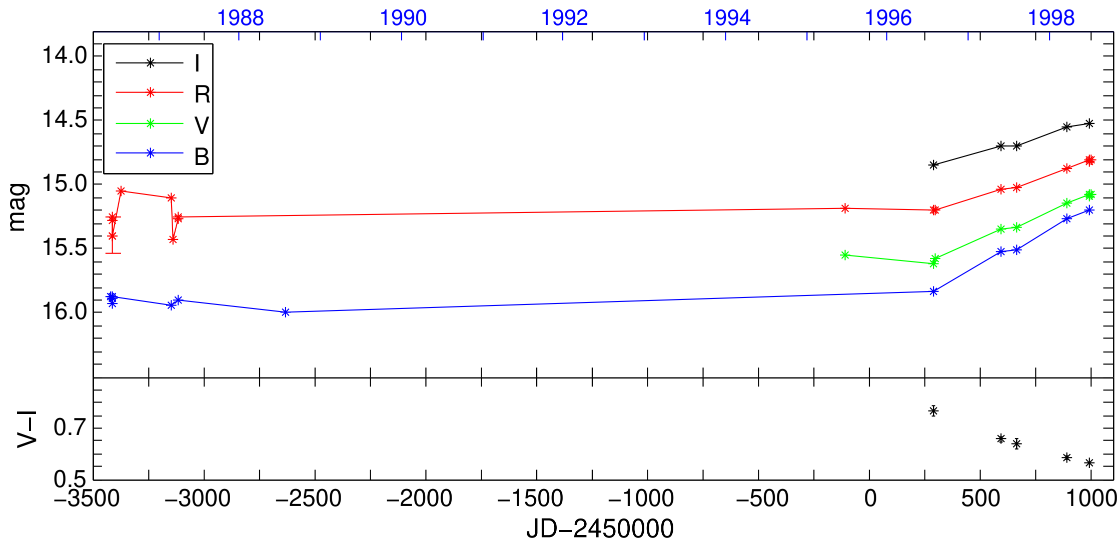

FIGURE 5.30— Light curves in the BVRI bands (top panel) and temporal evolution of the V-I color (bottom panel) of 3C 351.

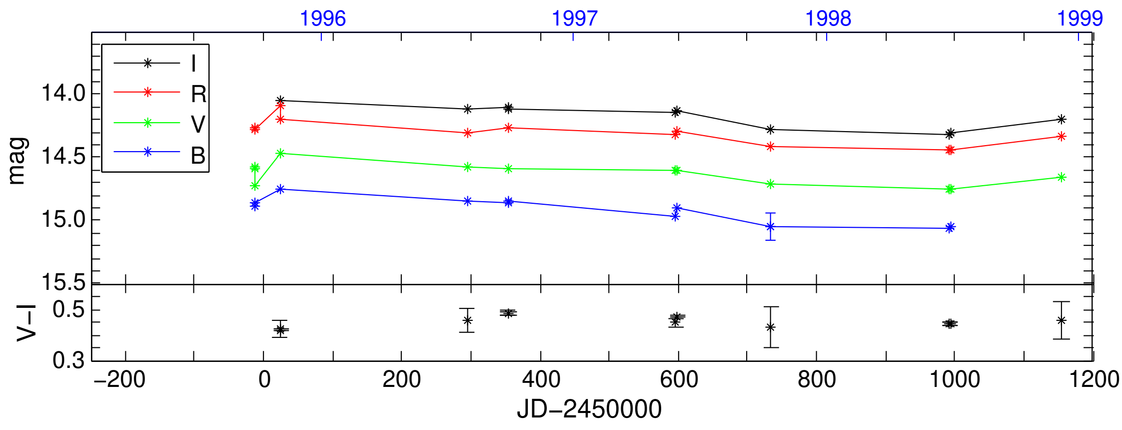

FIGURE 5.31— Light curves in the BVRI bands (top panel) and temporal evolution of the V-I color (bottom panel) of II Zw 136.

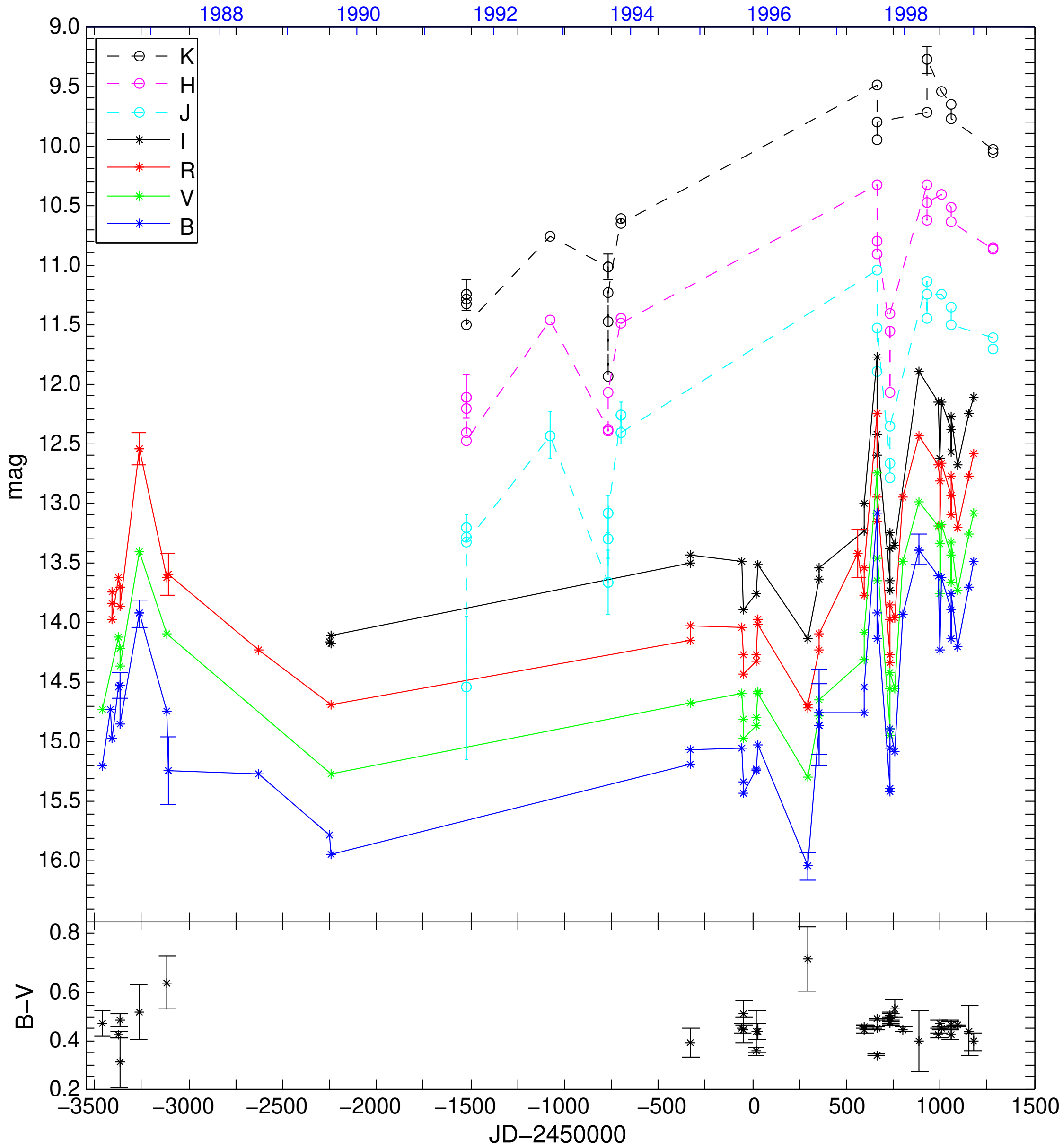

FIGURE 5.32— Light curves in the BVRIJHK bands (top panel) and temporal evolution of the B-V color (bottom panel) of BL Lac.

TABLE 5.1— Median of the observed magnitudes of the objects. These data have not been corrected for Galactic extinction.

Object	B	V	R	I	J	H	K
III Zw 2	15.89	15.55	15.21	14.88	-	-	-
I Zw 1	15.03	14.58	14.18	14.09	-	-	-
NAB 0205+02	15.47	15.28	15.10	14.67	-	-	-
3C 66A	14.70	14.28	13.88	13.32	12.36	11.69	10.95
AO 0235+16	17.26	16.44	16.23	14.81	13.17	12.26	11.36
PKS 0405-12	14.84	14.63	14.47	14.17	-	-	-
PKS 0528+134	20.87	19.71	18.74	18.02	-	-	-
S5 0716+71	14.30	13.88	13.50	13.00	-	-	-
GB 0738+545	18.34	18.47	18.10	17.59	15.82	14.84	14.01
B2 0742+31	15.74	15.65	15.44	15.08	-	-	-
OJ 287	16.09	15.50	15.01	14.37	13.39	12.56	11.70
PG 1008+133	16.60	16.44	16.10	15.84	-	-	-
Mkn 205	16.03	15.58	15.16	15.22	-	-	-
3C 273	13.08	12.83	12.64	12.25	11.69	10.88	9.79
3C 279	15.73	15.12	14.62	14.21	12.75	11.85	10.89
PG 1351+640	15.01	14.78	14.48	14.11	-	-	-
PKS 1510-08	16.76	15.97	15.98	15.92	14.88	14.04	12.16
AP Lib	16.11	15.41	14.76	14.22	-	-	-
PKS 1622-29	-	17.29	16.67	15.73	12.48	11.54	10.73
3C 345	17.05	17.04	16.56	15.94	13.94	13.01	12.17
Mkn 501	14.97	14.39	14.07	13.70	13.01	12.64	11.68
3C 351	15.97	15.31	15.16	14.73	-	-	-
II Zw 136	15.06	14.74	14.42	14.22	-	-	-
BL Lac	16.29	15.40	14.72	13.99	11.99	11.60	10.45
3C 454.3	16.79	16.22	15.91	15.47	14.23	13.52	12.61

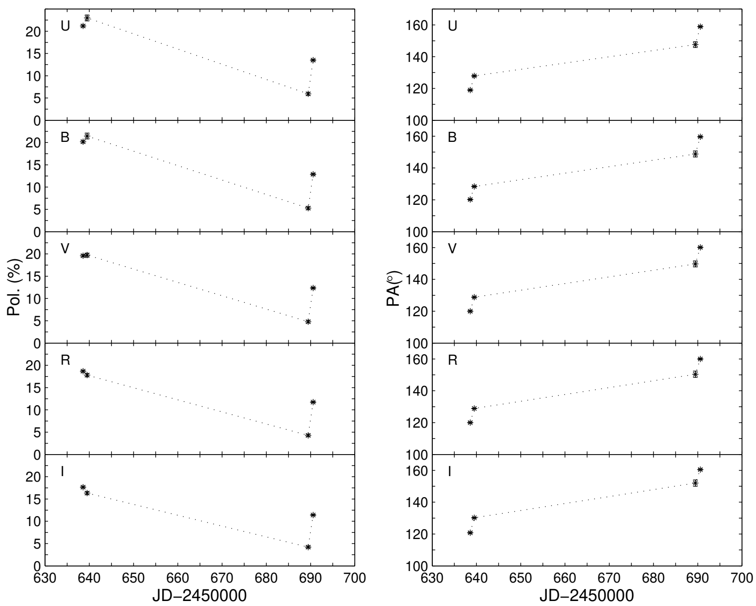

FIGURE 5.33— Polarization value and position angle vs time of BL Lac in the UBVRI bands.

In order to compute the average colors, we selected the nights in which an object was observed in at least two bands. A mean color value for these nights was calculated as the difference between nightly averaged magnitudes. The medians of these color values over all nights are shown in the Table 5.2. The reddest sources are the BL Lac objects, such as AO 0235+164, BL Lac, and OJ 287, with V-I≥1. Also, the FSRQ 3C 279 has an average V-I=1.05. The bluest objects are typically the quasars, with both RLQ and RQQ showing similar average color V-I∼ 0.5. The group of FSRQs, with an average V-I=0.85, are bluer than the BL Lac objects. A more detailed description of the color variability will be provided in Chapter 6.

Here, we prefer to work with spectral indices instead of colors, because spectral indices have a more fundamental physical meaning. The spectral indices (α, where $F_\nu \propto \nu^\alpha$) can be calculated using the colors, the central frequencies of the spectral bands and the fluxes for a zero-magnitude star (from Mead et al. 1990). We can separate the individual types of AGNs by comparing spectral indices calculated from different colors. Fig. 5.36 displays some spectral index diagrams, using different pairs of colors. In this figure, distinct types of objects (BL Lac objects, FSRQ, RLQ, and RQQ) are displayed with different symbols. The top-left panel shows the α_{B-V} vs. α_{V-R} plot. The points are located close to the α_{B-V}=α_{V-R} line, which is partly a consequence of the proximity of the V and R bands. In the top-right panel (α_{B-V} vs. α_{V-I}) the BL Lac objects approximately follow the line $\alpha_{V-I} = \alpha_{B-V}$, while other types of objects show a larger dispersion in α_{V-I} for similar α_{B-V}, indicating that these objects display a higher degree of curvature in the spectrum.

The bottom panels in Fig. 5.36 show the spectral indices calculated from the NIR magnitudes. Because almost no NIR observations of RQQs and RLQs were performed, the plots show mostly

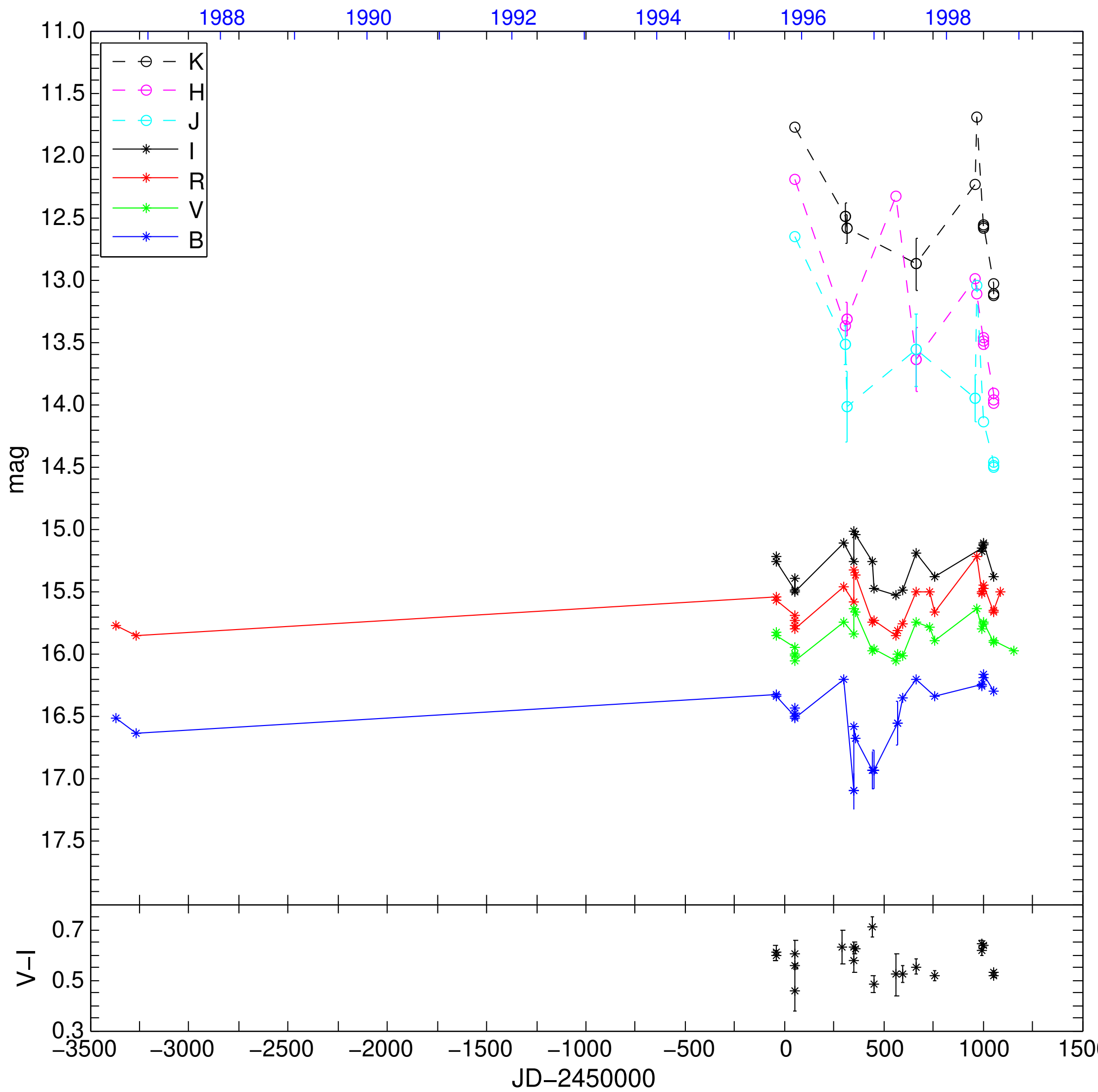

FIGURE 5.34— Light curves in the BVRIJHK bands (top panel) and temporal evolution of the V-I color (bottom panel) of 3C 454.3.

TABLE 5.2— Median colors of the sample objects. To calculate these values, the magnitudes were first corrected of Galactic extincion.

Objects	B-V	V-R	V-I	J-H	H-K	V-H
III Zw 2	0.42	0.26	0.55	-	-	-
I Zw 1	0.27	0.35	0.41	-	-	-
NAB 0205+02	0.18	0.19	0.57	-	-	-
3C 66A	0.36	0.37	0.86	0.71	0.76	2.42
AO 0235+16	0.84	0.70	1.52	0.99	1.00	3.93
PKS 0405-12	0.15	0.12	0.40	-	-	-
PKS 0528+134	0.11	0.18	0.75	-	-	-
S5 0716+71	0.41	0.40	0.84	-	-	-
GB 0738+545	0.36	0.35	0.84	0.86	0.86	-
B2 0742+31	0.02	0.16	0.47	-	-	-
OJ 287	0.53	0.47	1.06	0.85	0.88	3.10
PG 1008+133	0.12	0.30	0.52	-	-	-
Mkn 205	0.24	0.37	0.43	-	-	-
3C 273	0.10	0.23	0.69	0.80	1.09	1.99
3C 279	0.46	0.45	1.05	0.86	0.90	3.05
PG 1351+640	0.18	0.28	0.64	-	-	-
PKS 1510-08	0.26	0.42	0.92	0.85	0.93	2.67
AP Lib	0.57	0.56	1.01	-	-	-
PKS 1622-29	-	0.42	0.86	0.86	0.78	-
3C 345	0.26	0.32	0.93	0.85	0.89	3.02
Mkn 501	0.36	0.28	0.67	0.26	1.01	1.80
3C 351	0.17	0.30	0.64	-	-	-
II Zw 136	0.30	0.31	0.45	-	-	-
BL Lac	0.45	0.55	1.09	0.85	0.86	2.86
3C 454.3	0.46	0.27	0.59	0.54	0.86	2.28

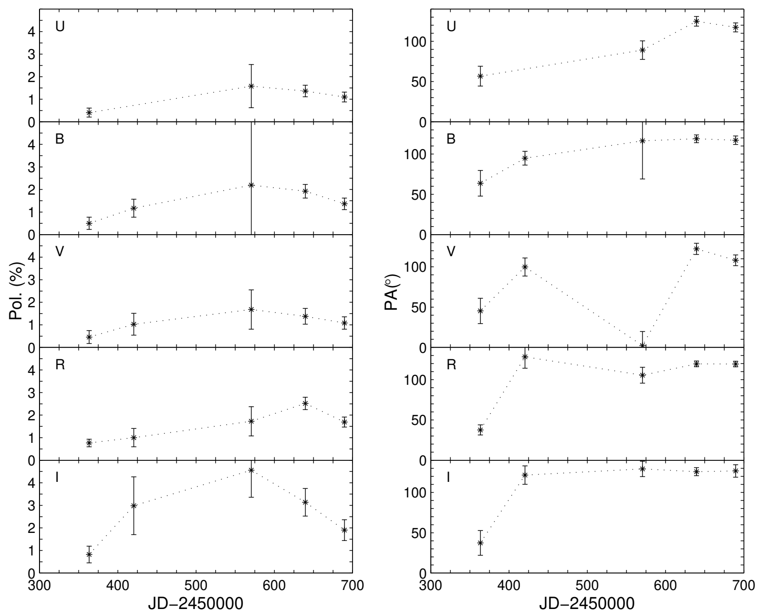

FIGURE 5.35— Polarization value and position angle vs time of 3C 454.3 in the UBVRI bands.

only blazars. There seems to be a linear relationship between the optical and NIR spectral indices, although the points are not distributed along the $\alpha_i = \alpha_j$ line, hinting to the existence of spectral curvature.

This is more clearly seen in Fig. 5.37, where the difference between two spectral indices is plotted as a function of a spectral index. The ordinate can be understood as a measure of the curvature of the spectrum. In our sample, the BL Lac objects and the FSRQs show a smaller curvature, while the RQQs and RLQs display a higher degree of curvature, indicating a possible difference in the physical emission process between these types of objects. It is thought that in BL Lac objects, the optical-NIR emission is dominated by synchrotron emission from the relativistic jet, which in this spectral range can be considered as a power law (except around the frequencies of the maximum synchrotron emission), while in quasars, the emission is dominated by the accretion disk—roughly a thermal process with a shape similar to a combinations of black-bodies (Beckmann & Shrader 2012). Also, strong emission lines, such as the Balmer series or Mg II h and k-lines, may contribute significantly to the fluxes in certain bands. These lines would dilute the variability observed in these bands because the timescales of variation in the emission lines are much larger than those of the continuum.

5.3.2 Spectral energy distribution

The shape of the continuum emission gives insights into the emission processes acting in these objects. We constructed the average rest frame spectral energy distribution (SED) from the continuum broadband fluxes. The main problem in this calculation is that all sources studied are variable. Hence, the different time sampling used for different individual bands prevents

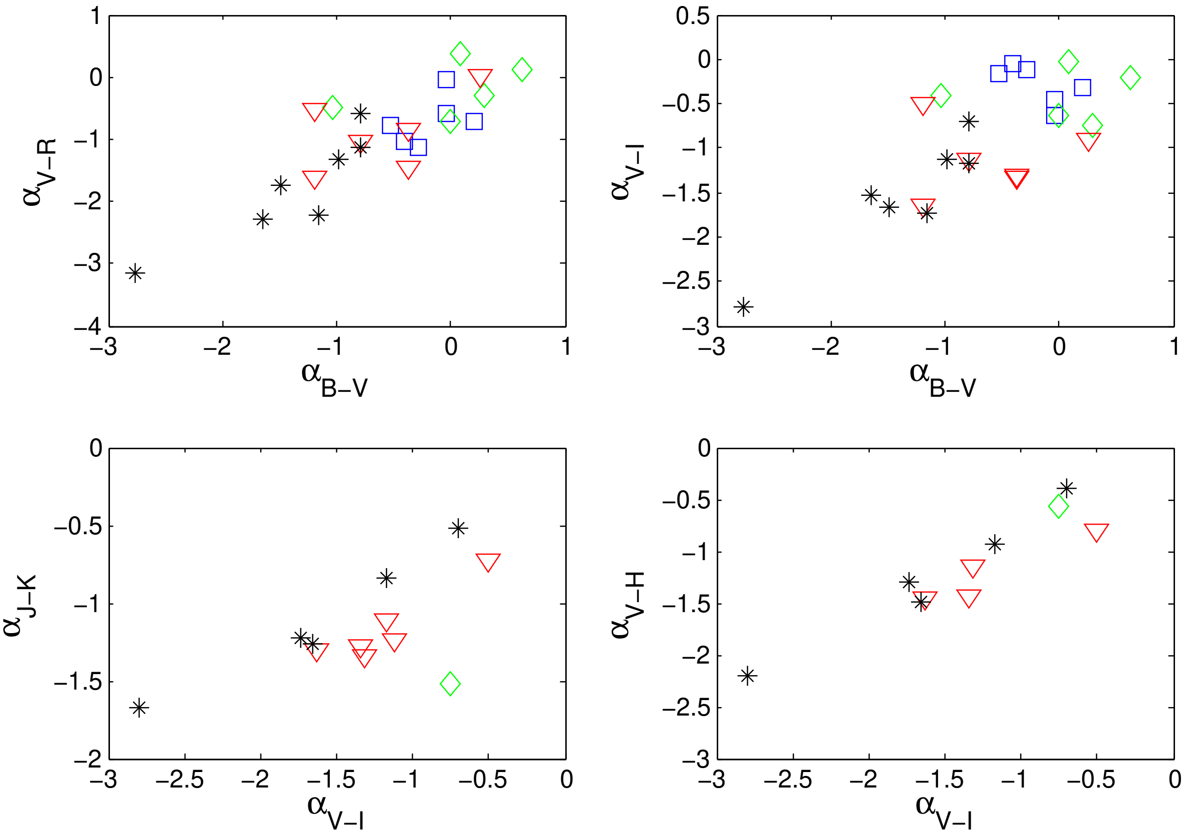

FIGURE 5.36— Spectral index vs spectral index plots computed from different filter pairs. Blue squares are RQQs; green diamonds are RLQs, red triangles are FSRQs and black asterisks are BL Lac objects.

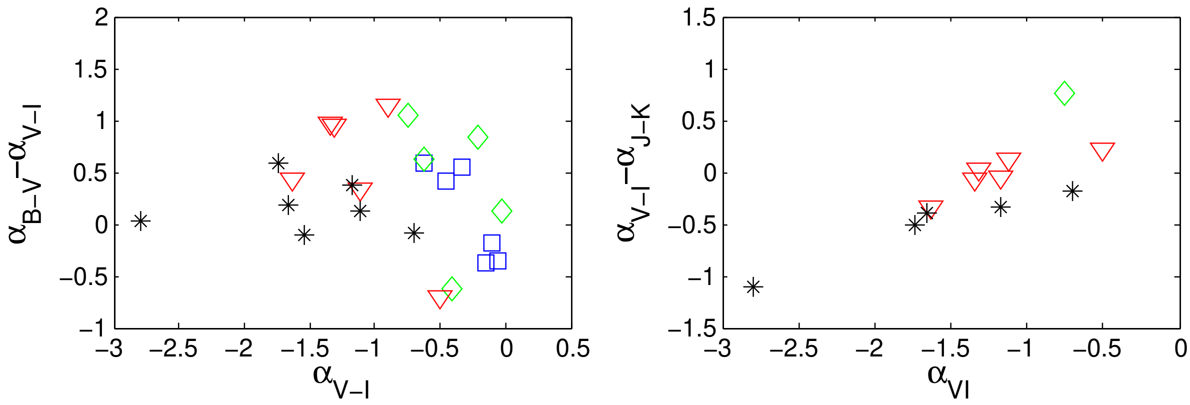

FIGURE 5.37— Differences of optical spectral indices and optical-NIR spectral indices vs the spectral index. They show the curvature of the spectra. Blue squares are quasars; green diamonds are LPQs, red triangles are OVV and black asterisks are BL Lac objects.

from simply using the median magnitude in each band to reconstruct the spectrum.

Our broadband spectral reconstruction begins with the median flux in the V band. For all other bands, we search for all nights in which the object was observed both in V and this other filter. The average flux ratio is calculated using all data from these nights, and the result is assumed to be the flux ratio in the average spectrum. For the H and K bands, the same method was applied, using the observations in J as a reference and, finally, the same was done for V and J to calibrate the scale between the optical and NIR data.

Using this procedure for all objects and correcting the values to the rest frame, the SED is computed and presented in Fig. 5.38. The redshifts of all the objects are known, except for S5 0716+71. For this object, which has a featureless spectrum, we assumed a redshift of $z = 0.3$ (see Wagner et al. 1996). The cosmological constants are assumed here and in the rest of the thesis to be $H_0 = 73$ km s^{-1} Mpc^{-1}, $\Omega_m = 0.27$ and $\Omega_\lambda = 0.73$. In Fig. 5.38 we included a vertical red line indicating the rest-frame location of the Hα emission line. In some objects, the influence of this emission line can clearly be seen, particularly 3C 273 and 3C 454.3. This line also seems to be important in several of the objects from the sample of RQQs and RLQs. Some other lines, such as Hβ and MgII2798 (the latter only for objects with $z > 0.5$) may also contribute to the observed broadband flux, but are less prominent than the Hα line.

The SEDs of the blazars are characterized by two broad components peaking between $10^{13} - 10^{17}$Hz and between $10^{21} - 10^{24}$Hz respectively. The component at lower frequencies is caused by synchrotron emission in the relativistic jet and the high energy component by inverse Compton scattering (Beckmann & Shrader 2012). Fossati et al. (1998) and Donato et al. (2001) found that there is a relationship between the location of the synchrotron peak and the radio luminosity such that the brighter blazars show the peak at lower frequencies. Also, the ratio of the two peak frequencies is constant and the height of the second peak is proportional to the radio luminosity. On the other hand, from observations in X-rays with BeppoSAX, Tavecchio et al. (2001) found that the synchrotron peak of Mkn 501 shifted to higher energies (up to $E > 100$ keV) as the source brightened. This behavior, observed not only during individual flares but also on much longer timescales, is the exact opposite of what Fossati et al. (1998) found for the whole sample. This is explained by Tavecchio et al. (2001) in a general scenario for both types of behavior, in which the variability observed in a single source is due to a change in the Lorentz factor of the particles emitting at the peak.

In our SEDs (Fig. 5.38) the least luminous blazars, Mkn 501 and BL Lac, show their synchrotron peak in the optical and NIR bands respectively. Brighter blazars present the peak at frequencies below the NIR range, although we cannot estimate the exact location of the peak for these objects. This is consistent with the results of Fossati et al. (1998) and Donato et al. (2001). However, there are two exceptions: 3C 66A and 3C 454.3, two of the most luminous blazars in our sample, show their peaks at frequencies higher than the optical bands.

For 13 objects, we have only optical observations, so that the shape of the global SED is not well constrained. Several quasars display a harder SED on the blue side. This may be the start of the blue bump, caused by thermal emission of the accretion disk, or line emission from the broad line regions.

The SED of 3C 273 is particularly interesting. Apart from the emission in Hα, it shows a rise in the frequency on the blue side of the spectrum, that could be due to the emission of the accretion disk. Towards the red, the spectrum rises again; it is likely that in the NIR bands the emission starts to be dominated by the relativistic jet or dust (Soldi et al. 2008).

5.3.3 Polarimetry

A subsample of objects was also observed with the NOT in photopolarimetric mode. The chosen sample contains some well-known blazars and PG 1351+640, a member of the low polarization quasars sample from de Diego (1994b). For these objects, the mean values of the polarization and position angle are displayed in Table 5.3. The three most strongly polarized sources are 3C 66A, OJ 287, and BL Lac, our best-studied objects and also very active sources. Surprisingly, 3C 345, a quite active OVV, shows only a small degree of polarization in our data, although a polarization as large as 35% was seen in this object during the 1983 outburst (Smith et al. 1986b).

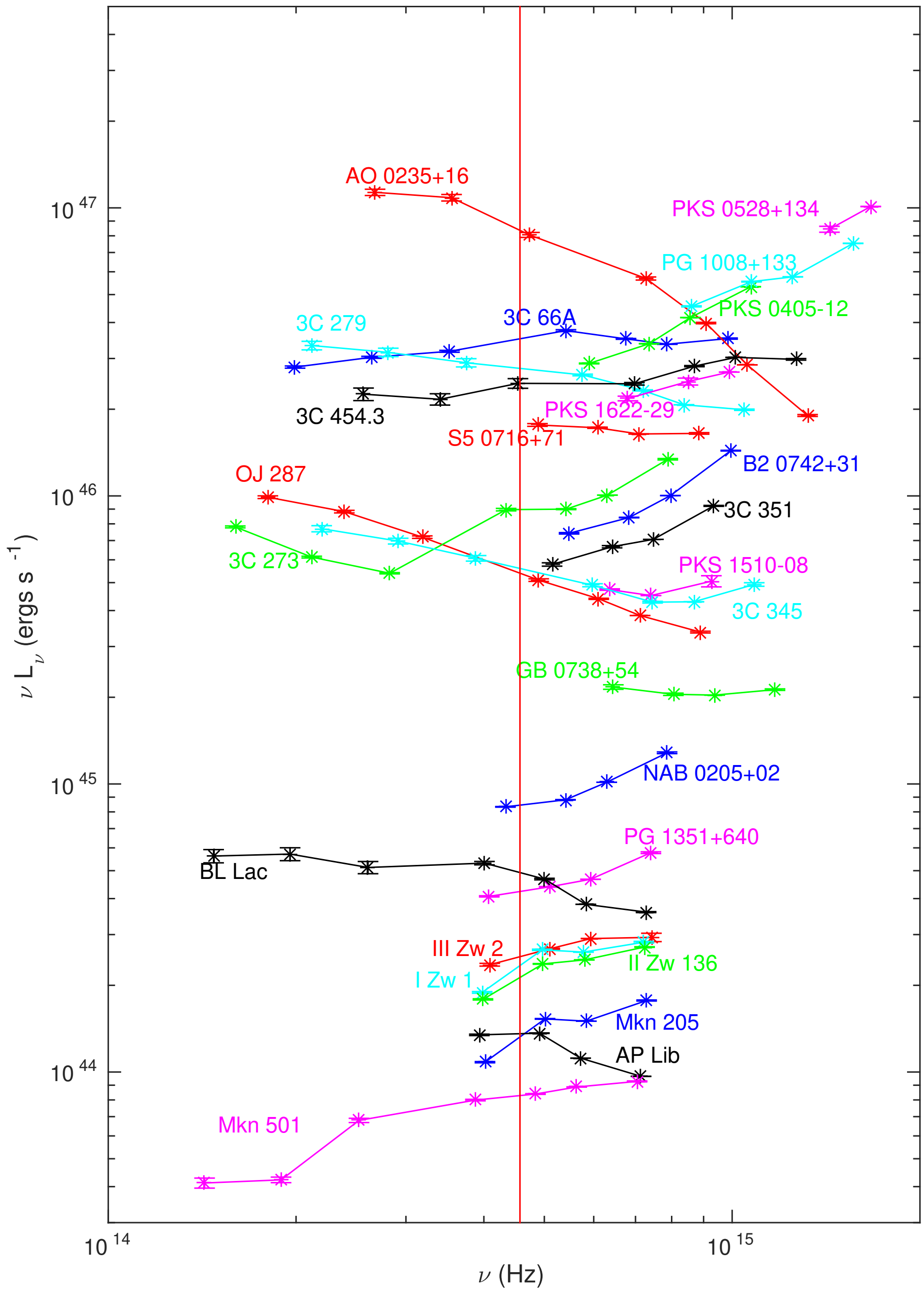

FIGURE 5.38— Rest frame spectral energy distribution of the objects presented in this work. The vertical line shows the location of the Hα line.

TABLE 5.3— Polarization and position angle of the mean polarization of the sample objects. It is shown the average polarization, p, the average position angle, PA, and the number of observation nights (n) for each filter.

Object	U			B			V			R			I		
	p(%)	PA(°)	n	p(%)	PA(°)	n	p(%)	PA(°)	n	p(%)	PA(°)	n	p(%)	PA(°)	n
3C 66A	15.1	27.8	6	15.2	32.3	8	15.0	32.9	8	14.7	32.3	8	14.6	32.4	8
S5 0716+71	5.9	104.3	6	2.8	72.7	6	2.7	72.0	6	2.8	71.3	6	2.9	72.5	6
87GB 0738+545	5.7	171.0	2	7.0	135.6	3	5.1	135.5	3	2.9	118.3	3	5.9	102.3	3
OJ 287	23.4	167.0	6	14.7	170.2	6	14.8	-9.1	6	15.1	173.0	6	13.6	-7.9	6
Mkn 421	3.7	66.9	3	5.4	70.8	4	4.9	71.4	4	4.4	72.1	4	4.2	73.6	4
PG 1351+640	1.2	171.0	4	1.2	168.1	4	0.6	12.9	4	0.7	-1.1	4	0.9	6.0	4
3C 345	1.3	51.9	6	0.4	-3.5	6	1.6	77.0	6	2.5	30.3	6	7.5	19.8	6
AP Lib	1.5	38.2	5	0.3	64.5	5	0.3	46.4	5	0.2	53.2	5	0.2	73.6	5
Mkn 501	4.2	16.9	1	3.0	22.0	1	2.6	23.1	1	2.2	21.9	1	2.2	20.0	1
BL Lac	13.7	132.7	4	12.9	133.5	4	12.1	133.7	4	11.2	133.8	4	10.6	135.0	4
3C 454.3	0.8	105.7	4	1.3	111.4	5	0.4	122.5	5	1.2	116.1	5	2.3	126.1	5

5.4 Characterization of the variability

Two basic numbers are used to quantify the variability of a source: the standard deviation and the total amplitude of the fluctuations. The latter is the most problematic to determine because it is highly dependent on the sampling. The amplitude is always underestimated unless the true absolute maximum and minimum are observed. This is mitigated if the object is well sampled over the characteristic timescales of the variations of the light curves. Many of our objects were observed sparsely.

The standard deviation is more robust to such sampling bias, but it is overestimated when the uncertainty of the data is of the same order of magnitude as the intrinsic variability. For these reason, Turner et al. (2001) and Edelson et al. (2002) defined the *fractional variability parameter* as:

$$F_{var} = \frac{\sqrt{S^2 - \overline{\sigma_{err}^2}}}{\overline{F}}, \tag{5.1}$$

where S^2 is the total variance of the flux observations, $\overline{\sigma_{err}^2}$ is the mean square error and $\overline{F}$ is the mean flux. The fractional variability parameter has the advantage that the effect of the uncertainty in the data is removed by the $\overline{\sigma_{err}^2}$ term in the numerator. The error of F_{var} is (Vaughan et al. 2003):

$$\sigma_{F_{var}} = \sqrt{\left(\sqrt{\frac{1}{2N}}\frac{\overline{\sigma_{err}^2}}{\overline{F}^2 F_{var}}\right)^2 + \left(\sqrt{\frac{\overline{\sigma_{err}^2}}{N}}\frac{1}{\overline{F}}\right)^2} \tag{5.2}$$

where N is the total number of data points. The first term in the right-hand side is dominant when the variations are similar to the measurement errors, while the second dominates when the intrinsic variations are much larger than the measurement errors.

Several authors have developed similar methods for the fractional variability amplitude and the *variance excess* (the part of the variance that is only due to the variability and not to the uncertainty of the data), such as Nandra et al. (1997), Almaini et al. (2000), or Garcia et al. (1999), but we obtain similar results in all cases, and Eq. (5.1) is simpler.

Alternatively, Heidt & Wagner (1996) define the fractional variability amplitude as:

$$Y = \frac{\sqrt{\max((F_i - F_j)^2 - (\sigma_i^2 + \sigma_j^2))}}{\overline{F}} \tag{5.3}$$

where F_i and σ_i are the observed flux and flux error of observation i.

One of the problems in the statistical description of the variability of blazars is that most of the methods assume that the flux time series is a stationary process—which is not the case for these objects—and therefore, the sampling can have a strong influence on the values of all global variability estimators. However, for our purposes, F_{var} accurately quantifies the variability.

TABLE 5.4— Optical Fractional variability parameter. For each filter the fractional variability parameter, its error and the number of points used (nightly averages) in the determinations of the F_{var} are shown. The targets are sorted by the right ascension

Object	$F_{var}(B)$	n(B)	$F_{var}(V)$	n(V)	$F_{var}(R)$	n(R)	$F_{var}(I)$	n(I)
III Zw 2	0.29±0.09	5	0.18±0.04	10	0.17±0.04	11	0.15±0.04	7
I Zw 1	0.17 0.05	7	0.18 0.04	11	0.14 0.03	11	0.15 0.04	9
NAB 0205+02	0.03 0.03	10	0.04 0.01	10	0.04 0.01	10	0.02 0.01	7
3C 66A	0.35 0.03	82	0.35 0.03	87	0.33 0.03	83	0.30 0.02	77
AO 0235+16	0.99 0.14	26	0.97 0.13	27	1.22 0.14	37	0.92 0.14	21
PKS 0405-12	0.26 0.09	4	0.06 0.02	5	0.06 0.03	4	-	-
PKS 0528+134	-	-	0.29 0.12	5	0.40 0.13	5	-	-
S5 0716+71	0.26 0.05	16	0.25 0.04	19	0.24 0.04	19	0.22 0.04	15
GB 0738+545	0.30 0.08	9	0.45 0.08	18	0.43 0.06	25	0.53 0.11	12
B2 0742+31	0.03 0.01	5	0.00 0.00	6	0.02 0.01	5	0.02 0.01	3
OJ 287	0.64 0.05	91	0.58 0.04	100	0.57 0.04	96	0.57 0.05	80
PG 1008+133	-	-	0.06 0.05	4	0.05 0.05	4	0.03 0.04	4
Mkn 205	0.19 0.05	8	0.16 0.03	14	0.14 0.03	14	0.19 0.06	6
3C 273	0.12 0.02	17	0.13 0.02	29	0.15 0.02	23	0.13 0.02	17
3C 279	0.62 0.08	27	0.53 0.06	37	0.53 0.06	34	0.38 0.05	25
PG 1351+640	0.08 0.02	9	0.12 0.02	13	0.12 0.02	12	0.07 0.02	7
PKS 1510-08	0.32 0.07	10	0.69 0.24	4	0.63 0.13	11	-	-
AP Lib	0.22 0.08	5	-	-	-	-	-	-
PKS 1622-29	-	-	1.29 0.37	6	1.61 0.43	7	-	-
3C 345	0.38 0.03	61	0.51 0.04	68	0.51 0.04	76	0.56 0.06	47
Mkn 501	0.20 0.03	17	0.18 0.03	15	0.16 0.03	17	0.15 0.03	14
3C 351	0.28 0.05	13	0.20 0.04	10	0.19 0.03	18	0.12 0.04	5
II Zw 136	0.26 0.08	11	0.08 0.02	14	0.09 0.02	13	0.08 0.02	11
BL Lac	0.72 0.08	45	0.67 0.07	41	0.65 0.07	48	0.68 0.08	33
3C 454.3	0.12 0.02	24	0.12 0.02	26	0.16 0.02	28	0.15 0.02	21

The fractional variability parameter in the optical and NIR bands is displayed in Tables 5.4 and 5.5 respectively. In all objects, variability was detected, except for B2 0742+31 and PG 1008+133, for which the variability could not be confirmed—the number of nights with observations is very small. The blazars are the objects showing the strongest variability, as expected. AO 0235+16, PKS 1622-29, and BL Lac are the most variable blazars in our sample. Typically, F_{var} is higher in the optical than in the NIR; there are several exceptions that could be due to the different sampling of observations (see below).

For the different object types, the average F_{var} in the V filter is as follows: 0.11 for both RQQs and RLQs, 0.55 for FSRQs, and 0.50 for BL Lac objects. We carried out an analysis of the variance (ANOVA) to confirm that the observed differences are significant. Merging the RQQs and RLQs on one side, and FSRQs and BL Lac objects on the other, we find that the difference in F_{var} between these two groups is significant at the 99.9% level. By contrast, the difference between the variability of FSRQs and BL Lac objects is not significant. Therefore, regarding variability, there is no difference between the FSRQs and the BL Lac objects, but both display clearly different variability properties to other types of quasars.

5.4.1 Color dependent fractional variability

We studied the variability amplitude as a function of the frequency of observation in a similar way to what was done to calculate the average spectrum. We begin with the fractional variability

TABLE 5.5— NIR Fractional variability parameters. For each filter the fractional variability parameter, its error and the number of points used (nightly averages) in the determinations of the F_{var} are shown.

Object	$F_{var}(J)$		n(J)	$F_{var}(H)$		n(H)	$F_{var}(K)$		n(K)
3C 66A	0.40	0.04	72	0.42	0.04	72	0.40	0.03	75
AO 0235+16	0.66	0.11	19	0.64	0.10	21	0.60	0.09	23
GB 0738+545	0.29	0.09	5	0.12	0.05	4	0.13	0.05	4
OJ 287	0.69	0.05	99	0.66	0.05	107	0.78	0.05	112
3C 273	0.12	0.01	55	0.15	0.01	58	0.12	0.01	61
3C 279	0.66	0.09	26	0.45	0.07	33	0.46	0.05	37
PKS 1510-08	-		-	-		-	0.29	0.08	7
PKS 1622-29	0.61	0.22	4	0.46	0.16	4	0.44	0.16	4
3C 345	0.54	0.07	51	0.43	0.05	52	0.42	0.04	52
Mkn 501	0.27	0.03	45	0.53	0.06	57	0.30	0.03	54
BL Lac	0.70	0.10	24	0.62	0.09	24	0.66	0.10	21
3C 454.3	0.65	0.14	12	0.62	0.12	13	0.48	0.10	12

parameter in the V filter (since it is the best-observed filter) for all objects. For any other filter in the optical, we searched for all pairs of nights, with observations in V and this other filter, in which the variation between these two nights are larger than 3σ. The flux variation ratio between these two filters is then computed for these nights and its mean over all nights is considered the average variability ratio between the two filters. We carry out this process for the B, R, I and J filters. Since the sampling in the optical and NIR filters may be very different, we used the J data as the reference for the data in H and K. Finally, we multiplied these last values with the variability ratio between J and V to obtain the variability ratio between H/K and V. The ratio of variability amplitudes between two filters was computed after removing the contribution of the uncertainty, using an equation similar to Eq. 5.3.

Fig. 5.39 shows F_{var} as a function of the rest frame frequency, for the objects that had enough data. The error bars are higher in the NIR than in the optical, because the number of nights in common between J and V is lower. The big difference in the $F_{var}(\nu)$ between the optical and NIR for 3C 279 could also be due to this.

Most objects are more variable in the bluer filters, but there are exceptions: 3C 345 is more variable in the I-band, showing other optical and NIR filters lower variability; 3C 454.3 and GB 0738+54 show larger amplitude of variability in the reddest bands. This may be due to the dilution of the variability in the blue bands because of the contribution of the accretion disk—all these objects are FSRQs for which the contributions of the accretion disk may be significant.

5.5 Summary and discussion

We have studied the long-term variability of our sample of 25 AGNs. Some of the objects were observed only in a few nights, but intensively (very oft during the night), because we were searching for rapid variability. Seven objects, namely, 3C 66A, AO 0235+16, OJ 287, 3C 273, 3C 279, 3C 454.3 and BL Lac, were also monitored for a long period of time. We built light

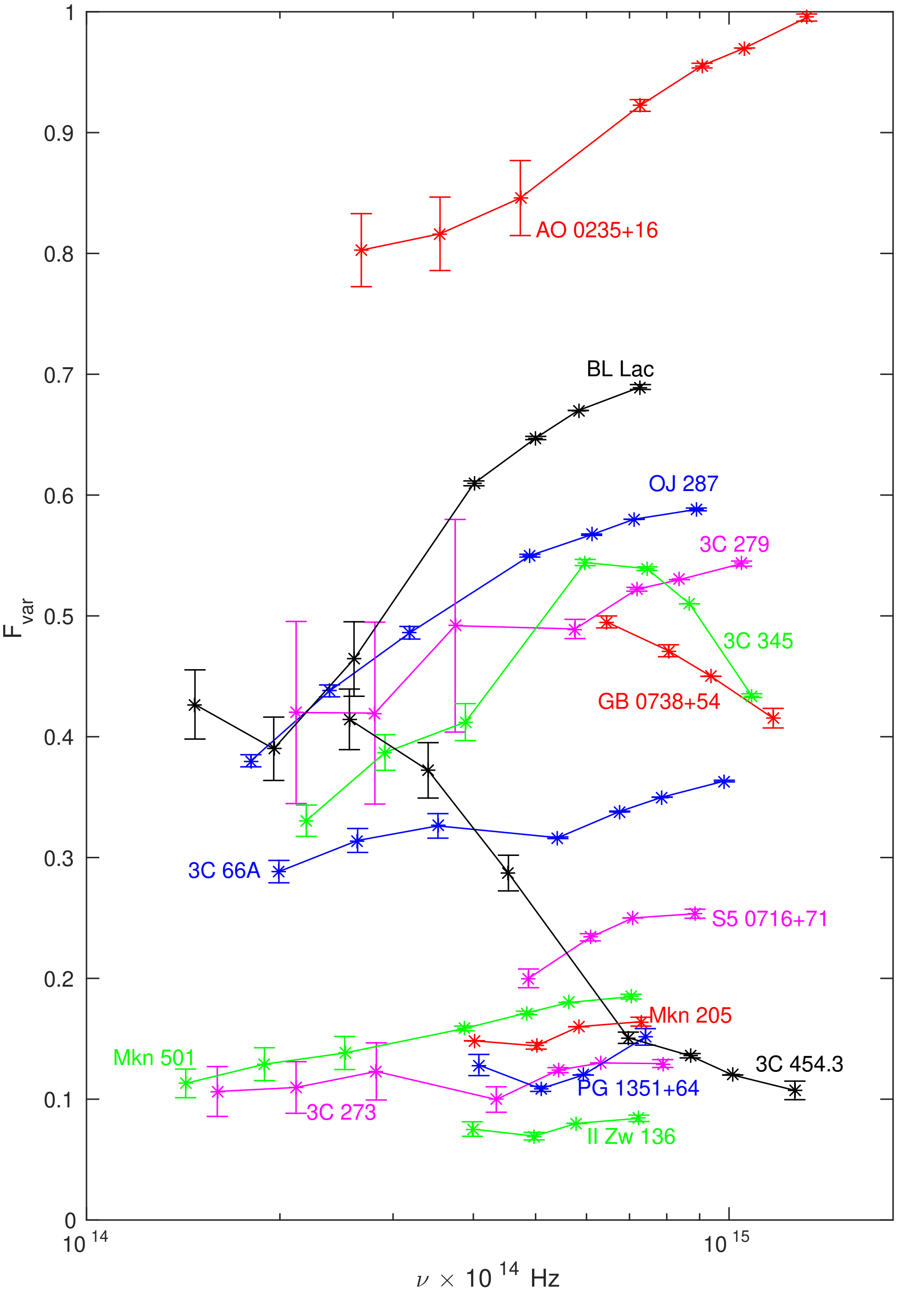

FIGURE 5.39— Fractional variability amplitude vs frequency (see text for an explanation on how it was computed) for the objects in our sample.

curves, color curves and produced plots for the temporal evolution of the polarization. The characteristics of the most interesting objects have been highlighted.

From the light curves, we computed average magnitudes and colors, and we reconstructed the SED of the sample objects. These results were discussed in the framework of current theoretical models of emission for quasars and blazars. In particular, we confirmed the relationship between the peak of the synchrotron component of the emission and luminosity (Fossati et al. 1998).

We computed the amount of variability of each object by means of the fractional variability parameter (F_{var}), which takes into account the uncertainty in the data. We found that blazars (FSRQs and BL Lac objects) show stronger variations than other types of quasars. However, no significant difference in F_{var} is found between FSRQs and BL Lac objects.

The next step in our analysis was to search for correlations between the redshift, luminosity, spectral index, mean polarization and F_{var}. The results are summarized in Fig. 5.40. We used a regression analysis to estimate the significance of the correlations.

We found that for the sample objects the luminosity and redshift are strongly correlated. This a typical selection effect in flux-limited samples. Our sample is not complete in any sense, but it can be considered as a flux-limited sample, because we observed only those AGNs that require relatively short exposure times (<20-30 min.) to reach a good S/N.

Two correlations have a formal significance >95%, both involving the polarization: *Pol* vs. α_{V-I} and F_{var} vs. *Pol* in Fig. 5.40. We found that redder objects show higher polarization, and that objects with higher polarization display a larger variability. This is explained because blazars are those AGNs with the highest polarization and strongest variability—the fact that we have objects of a different type in our sample produces naturally such a correlation.

The most interesting correlation that we have found (at the 99.5% significance) is between the spectral index (α_{V-I}) and F_{var}. If we consider only the BL Lac objects, the significance rises to 99.9%, with the variability being larger for the redder objects. It is known that the synchrotron emission of the jets is more variable at frequencies close to and higher than the maximum in the SED, which is consistent with the relation between the spectral index and the variability. For the other objects, there is no clear relationship between these two parameters. This correlation is not followed by the FSRQs, revealing a possible difference between these two type of objects.

The variability of QSOs is too low and the errors of F_{var} comparable to F_{var}, which does not allow to determine a correlation. However, the fact that they follow the same correlation may indicate that most of the variability is produced by the same mechanism (i.e., process occurring in the relativistic jets). In RQQ and RLQ, the emission of a jet would be completely diluted by the more luminous accretion disk. No difference was found between these two types of objects, although it should be expected that the jet emission is more important in RLQs than in RQQs.

We have repeated this analysis with the published data of BL Lac objects from the monitoring programs of Perugia and Torino (Fiorucci & Tosti 1996, Villata et al. 1997, Raiteri et al. 1998, Villata et al. 2000b) and we find no correlation between the spectral index and F_{var}. This is an important issue to be confirmed or discarded with further analysis (new data for a larger sample of objects, observed in a systematic way are needed).

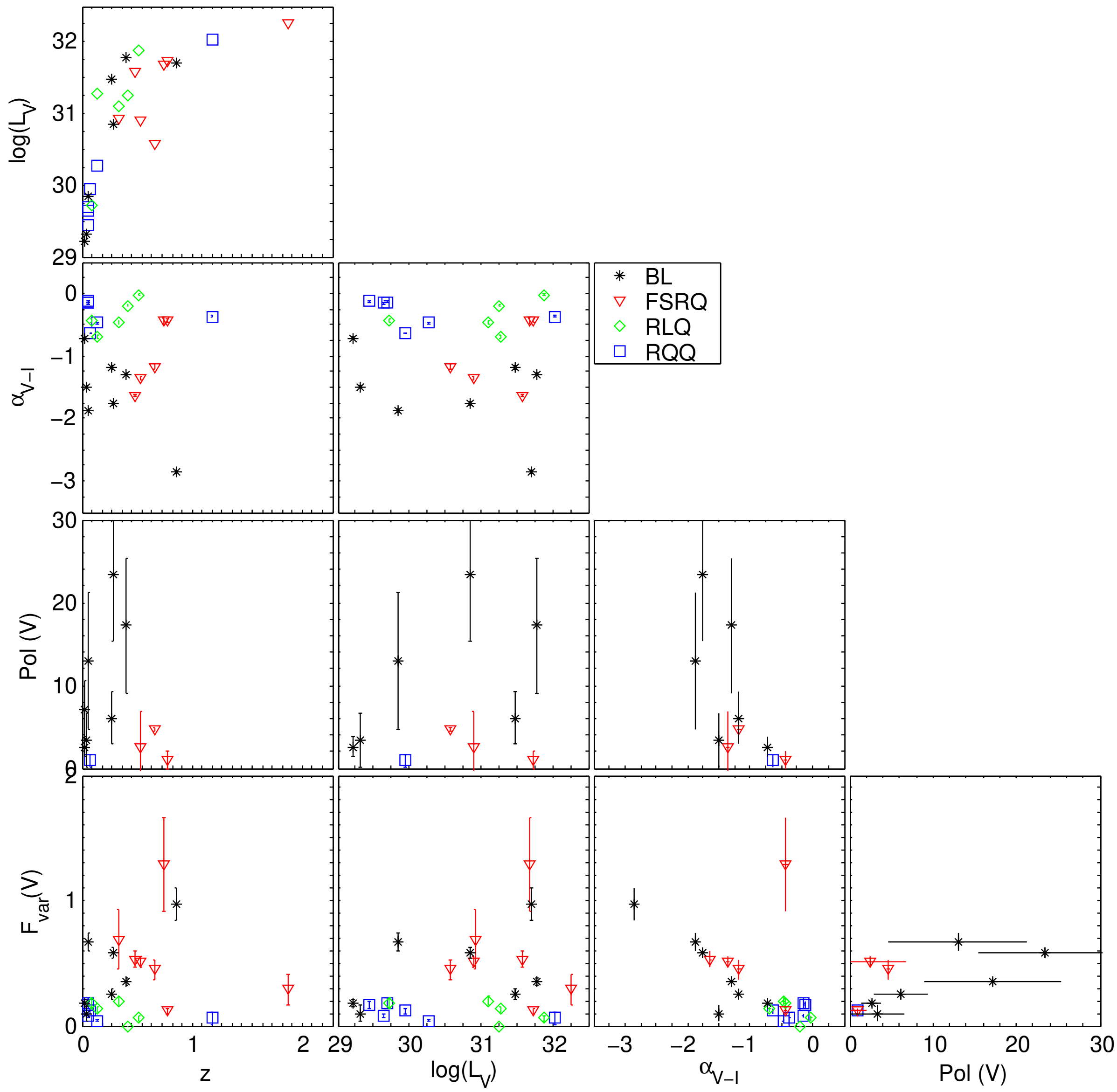

FIGURE 5.40— Plots of the relations between the redshift, luminosity in V, spectral index (from the V-I color), mean polarization and fractional variability parameter. Different symbols are used for the distinct object types (QSOs, LPQs, OVVs and BL Lac objects).

6

Spectral Variability

This chapter presents the analysis of the color long-term variability of the AGNs in our sample and the relation of the color with the flux of the sources. I extracted the spectrum of the variable source applying the method by Hagen-Thorn & Marchenko (1989) and found that, in all objects, except for FSRQs, the variable component is bluer than the observed spectrum of the source. Although the spectral indices of the observed spectrum of BL Lac objects and FSRQs are different, the spectrum of the variable component of FSRQs is similar to that of BL Lac objects. I found that most objects in the sample become bluer when brighter. The only exceptions are FSRQs, whose behavior is explained by a two-component model: the constant blue accretion disk dominates the emission at a lower state, while the variable red relativistic jet dominates the emission at a higher state. In 3C 66A and OJ 287, the best-studied objects in this thesis, I found that the relationship between the flux and the spectral index is notably more significant when some of the outbursts are considered individually. I calculated the spectral variability parameter (SVP), which measures how the spectral index changes for a log-unit change of flux. I found that different object types have different locations in the SVP vs. spectral index diagram and explained the different locations with simple models of variability.

6.1 Introduction

The previous Chapter has been mostly devoted to the study of the long-term flux behavior of the AGNs. Here, we extend this work to include a detailed analysis of the colors of the objects. It has been shown that flux variations alone, although necessary, are not is not enough to thoroughly understand the mechanism of the variability of AGNs, but that to obtain information on several bands, i.e., on the colors of the objects, is essential. Color properties and color variations of AGNs put tighter constraints on the nature of their emission and provide valuable clues about their physics.

Different theoretical models of variability predict different behavior of the colors and different relation of the color variability with respect to the observed flux. Therefore, from color data, we can obtain information about the physics of these objects.

We have usually taken the observations in such a way that we have obtained color information and tried to get a good time sampling. For almost all nights, the observations were performed in all bands, and usually with the strategy VBVRVIVB... which allows us to get spectral data, as well as, to acquire data in V suitable to study the rapid variability. In this chapter, we present the color data (that has also been plotted in the Chapter 5) and its relation with the flux is analyzed.

The color variations properties have been found to be different for distinct types of AGNs (Trèvese & Vagnetti 2002 and Vagnetti et al. 2003). Several shock-in-jet models (e.g. Kirk et al. 1998; Böttcher & Chiang 2002) expect that the spectral index *vs* flux plots show a characteristic loop-like pattern in most cases. This is usually tracked temporally in the clockwise sense. This hysteresis cycle indicates that the spectrum becomes steeper when the source is fainter. That is so, while the spectral slope is completely controlled by the radiative cooling processes so that the information about changes in the injection rate of accelerated particles propagates from high to low energies. For the usually observed clock-wise hysteresis, the non-thermal cooling is effective before acceleration has ceased. This effect has been mostly observed in X-rays (e.g., Takahashi et al. 1996; Kataoka et al. 2000) but some examples have also been detected in the optical (Xilouris et al. 2006; Wu et al. 2007).

The bluer-when-brighter (BWB) behavior has been observed in individual objects of different types (e.g., Xiong et al. 2017; Kaur et al. 2017; Gaur et al. 2015b; Raiteri et al. 2001), and in complete samples of AGNs as in Guo & Gu 2016; Kokubo et al. 2014; Sukanya et al. 2016. However, the opposite behavior, redder-when-brighter, has also been observed, in particular in FSRQs (e.g., Raiteri et al. 2012).

6.2 The determination of color and spectral index

In order to calculate the color and spectral index of the objects in our sample, we have to apply some binning or interpolation of the flux/magnitude data, because the data in the different spectral bands were not simultaneous. This does not apply to the CVF NIR observations: that data were taken quasi-simultaneous and, therefore, colors can be derived simply subtracting the data from the two spectral bands.

In variable objects, this binning (or interpolation) should be done with care to avoid artificial changes of the color if the binning interval (or the time between the points to interpolate) is larger than the variability timescales. We have tested several methods to compute the colors: one involves interpolation and the other one the binning of the magnitudes. We found more reliable results with interpolation.

The main problem when calculating the colors from the magnitudes is that the targets are variable and the observations in the different filters are not strictly simultaneous. Therefore, to avoid large variations, the time difference between the measurement on both bands should not be too long. We applied the following procedure to calculate the colors. First, we computed the typical time interval for the source to have a variation of 0.01 mag. Then, we searched for data in one of the two spectral bands surrounded by two points in the second band whose separation is smaller than the computed typical time for variations of 0.01 mag. Finally, we linearly interpolated between the two points in the second band to the time of measurement in the first band and used the interpolated value to calculate the color.

To compute the typical time interval for variations of 0.01 mag, we used the structure function

(SF) of the magnitudes, m (see Appendix D):

$$SF(\tau) = \left\langle [m(t+\tau) - m(t)]^2 \right\rangle \tag{6.1}$$

where $\langle\rangle$ denotes the average over those pairs for which $t_i < \tau < t_j$ and $[t_i–t_j]$ is the bin interval. For several objects, their typical time of variability for 0.01 mag is too long; for them, we have chosen a maximum time for the separation for the interpolation of 5 hours. For two objects that show very rapid variability, the maximum time for separation was selected to be 0.5 hours. This method provides a good time sampling of the color data for sources with short-term variations (which are the only objects for which rapid color variations are expected) while minimizing the effect of the non-simultaneous observation in the estimation of the colors.

The daily average color data of the objects is computed by subtracting the daily average of the magnitudes.

In principle, to obtain the spectral index, one fits $\log F_\nu$ *vs* $\log \nu$ data to a straight line using more than two spectral bands. However, for the vast majority of our objects, their broadband spectrum cannot be considered as exactly linear in the $\log F_\nu$ vs. $\log \nu$ plot (see Sect. 5.3). Additionally, observations were not always performed in all spectral bands, and the observational errors may be very inhomogeneous. All this makes the computation of the spectral index with such a method unreliable.

We have thus calculated the spectral indices from the colors. This has the drawback that the spectral index estimation is not unique because we get a different spectral index for each pair of photometric bands —as it was noted above, the spectrum of the sources is not strictly linear in the $\log F_\nu$ vs. $\log \nu$ plot. The transformation from colors to spectral indices is straightforward using the middle frequency and the fluxes of zero magnitudes of the spectral bands (Mead et al. 1990).

6.3 Long-term color statistics and curves

The median colors of the objects of our sample and some plots of the spectral indices were already presented in Sect. 5.3. Also, the color time series plots for all sources with enough number of observations were shown in the same chapter in Sect. 5.2.

6.4 Global spectral variations

Apart from the amplitude of color variability, there are no many estimators of color/spectral variability in the literature; one of them is the spectral variability parameter, defined by Trèvese & Vagnetti (2002), which relates the changes of color with the changes of flux. This will be presented later in this chapter.

We have quantified the amount of color variability through the intrinsic standard deviation of the spectral indices of the objects. This is defined, similarly to the variance excess or the fractional variability amplitude (see Sect. 5.4), as the standard deviation after removing the contribution of the measurement errors. Before estimating the intrinsic standard deviation of

TABLE 6.1— Intrinsic standard deviation, σ, of the spectral indices for the objects of the sample, and number of measurements, n.

Object	$\sigma(\alpha_{B-R})$	n	$\sigma(\alpha_{V-I})$	n	$\sigma(\alpha_{J-K})$	n
III Zw 2	0.20±0.04	5	0.00	7	-	0
I Zw 1	0.15±0.04	7	0.15±0.07	9	-	0
NAB 0205+02	0.06±0.02	8	0.00	7	-	0
3C 66A	0.17±0.02	67	0.13±0.01	72	0.00	68
AO 0235+16	0.28±0.05	23	0.17±0.02	18	0.13±0.19	18
S5 0716+71	0.09±0.02	16	0.12±0.02	15	-	0
GB 0738+54	0.10±0.03	5	0.00	12	-	4
B2 0742+31	0.00	5	-	3	-	0
OJ 287	0.22±0.02	73	0.20±0.02	73	0.46±0.11	94
Mkn 205	0.10±0.02	9	0.00	6	-	0
3C 273	0.16±0.05	15	0.09±0.01	15	0.14±0.02	54
3C 279	0.10±0.03	23	0.12±0.02	22	0.22±0.04	24
PG 1351+640	0.06±0.02	9	0.02±0.01	7	-	0
PKS 1510-08	0.24±0.07	9	-	1	-	2
3C 345	0.34±0.03	53	0.23±0.02	46	0.73±0.15	49
Mkn 501	0.10±0.03	15	0.05±0.03	12	0.26±0.05	40
3C 351	0.31±0.06	10	0.17±0.05	5	-	0
II Zw 136	0.05±0.02	9	0.05±0.01	8	-	0
BL Lac	0.18±0.04	35	0.17±0.02	26	0.23±0.05	19
3C 454.3	0.42±0.13	20	0.12±0.02	21	0.34±0.12	8

the spectral indices, we removed from the dataset those values with large measurement errors (those data whose measurement errors are larger than four times the median of the errors). This removal is necessary because the spectral index measurements are more inhomogeneous than the magnitude data due to their calculation process (see Sect. 6.2). The intrinsic standard deviation was finally calculated for the objects with more than four color measurements.

We show in Table 6.1 the intrinsic standard deviation of the spectral indices computed from the B-R, V-I, and J-K colors. For some objects, σ vanishes, which means that the observed variability is solely due to measurement errors. Two of the objects (NAB 0205+02 and PG 1351+640) show only barely detected spectral variations. The strongest spectral variations correspond to 3C 454.3, 3C 345, OJ 287, 3C 351 and AO 0235+16, all blazars, except 3C 351—a low polarization quasar with a moderate amplitude of flux variability.

The average values of the intrinsic standard deviation for the different types of sources are presented in Table 6.2: FSRQ and BL Lac objects display the highest color variability. From the analysis of the sample averages using the statistical t-test, we conclude that the difference in color variability of the blazars and the other quasars is significant to a $p \sim 98\%$. No other differences between the tabulated groups of objects were found to be significant.

Typically, the intrinsic standard deviation of the spectral indices is greater in the NIR bands than in the optical. Also, the spectral variations are higher using the B-R colors than using the

TABLE 6.2— Average values of the intrinsic standard deviation of α_{V-I} for the different types of AGNs.

Type	RQQ	RLQ	FSRQ	BLL	RQQ+RLQ	FSRQ+BLL
$\overline{\alpha}_{V-I}$	0.037	0.056	0.166	0.120	0.045	0.139
n	6	5	5	7	11	12

V-I colors, which may be due to the more significant influence of the accretion disk in the B band.

6.5 Spectrum of the variable component of the source

A relationship between the color and the flux of the source has been established for many AGNs (e.g., Xiong et al. 2017; Guo & Gu 2016; Raiteri et al. 2001, 2012). It is possible that this change in color is due to the combination of a variable component with a steady spectral shape, and a constant component with a different color. When the constant component is redder than the variable, as the object brightens, it becomes bluer.

In fact, there is evidence of a constant component in the emission from AGNs (apart from the host galaxy). Large contributions, e.g., parts of the jet far away from the black hole or the external section of the accretion disk, are supposed to be constant in the probed timescales.

The assumption that the AGN emission has two components was first proposed by Sandage (1971) and then refined by other authors. Choloniewski (1981) proposed a method to separate both components using the whole photometric dataset. Hagen-Thorn et al. (1985) and Hagen-Thorn & Marchenko (1989) further developed this method. Also, Winkler et al. (1992) used a similar method to separate the components of the emission of AGNs.

Here, we will separate the constant and variable components in our AGNs. Following Choloniewski (1981) and Hagen-Thorn & Marchenko (1989), we assume that the variable component has a constant spectral shape. Therefore in each plot F_i-F_j, where F_i is the flux in the photometric band "i", the data points would be located on a straight line. In order to completely disentangle the contributions of the constant and variable components, we must make some assumptions on the constant component (e.g., the color). The constant component should also be located in the fitted straight line in the F_i-F_j plot. If no assumption is made, only the spectral shape of the variable component can be obtained.

If we assume that the emission in one band can be decomposed in two components, one variable (F^v) and another constant (F^c), and that the spectral shape of the variable component is constant ($F_j^v = C_{ji}F_i^v$), then,

$$F_j = F_j^c + F_j^v = C_{ji}F_i + (F_j^c - C_{ji}F_i^c). \tag{6.2}$$

Therefore, by fitting the data F_i vs. F_j to a straight line, the slope of the line is the ratio of the fluxes of the variable component in the bands j and i, C_{ji}. We have made the linear fits using the orthogonal bivariate correlated errors and intrinsic scatter (BCES) method (Akritas & Bershady 1996), considering the measurement errors in both photometric bands.

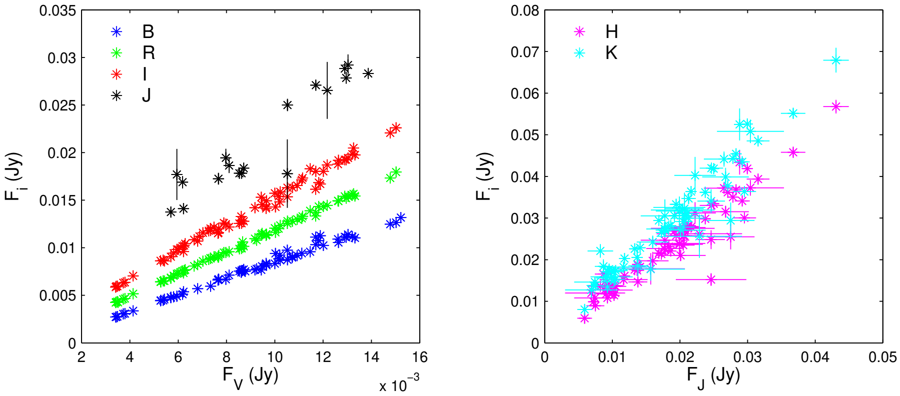

FIGURE 6.1— Flux-flux plots for 3C 66A.

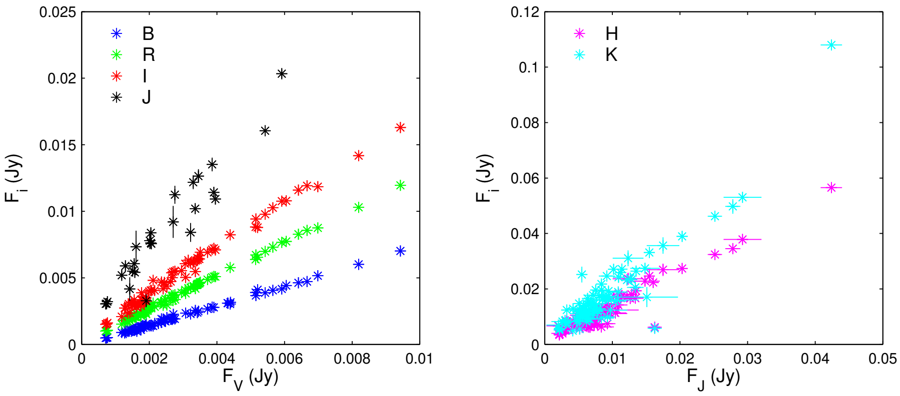

FIGURE 6.2— Flux-flux plots for OJ 287.

We used for this analysis the daily averaged magnitudes after converted to fluxes. The fluxes in B, R, I and J are fitted against the flux in V, and the fluxes in H and K against the flux in J. The fit F_J-F_V meets the spectrum in the optical and NIR.

We show in Fig. 6.1 and Fig. 6.2 two examples of the F_i-F_j plots for 3C 66A and OJ 287, respectively. For 3C 66A, both the optical and the NIR data, are distributed on a straight line. The NIR data have a higher dispersion than the optical due to the observational errors, but no curvature can be seen in the correlation. For OJ 287, the optical data are located on a straight line, but in the NIR, there are two different linear regimes for low and high fluxes, the limit between both regimes being at $F_J = 15$ mJy. As Hagen-Thorn (1997) has noted, this changes of the slope can be the result of two different mechanisms of variability or that it is incorrect the assumption of the stability of the spectral shape of the variable source.

The slopes of the fits of $F_i - F_j$ are used to compute the shape of the spectrum of the variable component (SVC). With these slopes, we have subsequently fitted the variable spectrum by a straight line to calculate its spectral index in the optical, NIR and the whole spectrum. Table 6.3 display the values of the spectral indices of the SVC.

TABLE 6.3— Spectral slopes of the SVC calculated using the method of Hagen-Thorn.

Object	α_{tot}	α_{opt}	α_{nir}
III Zw 2	-	0.15±0.12	-
I Zw 1	-	0.10±0.07	-
NAB 0205+02	-	0.51±0.19	-
3C 66A	-0.78±0.01	-0.83±0.04	-0.80±0.03
AO 0235+16	-1.92±0.10	-2.60±0.04	-1.45±0.08
PKS 0405-12	-	1.51±0.67	-
S5 0716+71	-	-0.89±0.01	-
GB 0738+54	-	-1.41±0.04	-1.21±0.05
B2 0742+31	-	0.82±0.13	-
OJ 287	-1.40±0.03	-1.46±0.02	-1.48±0.09
Mkn 205	-	0.06±0.03	-
3C 273	-0.85±0.13	0.04±0.11	-1.59±0.09
3C 279	-1.29±0.04	-1.47±0.10	-1.07±0.03
PG 1351+640	-	-0.13±0.27	-
PKS 1510-08	-	-1.76±0.36	-
PKS 1622-29	-	-1.33±0.22	-0.52±0.13
3C 345	-1.14±0.05	-1.53±0.08	-1.04±0.10
Mkn 501	-0.46±0.13	-0.52±0.02	-0.68±0.20
3C 351	-	0.69±0.04	-
II Zw 136	-	-0.10±0.10	-
BL Lac	-0.93±0.04	-1.30±0.07	-1.07±0.02
3C 454.3	-1.21±0.15	-1.33±0.11	0.02±0.05

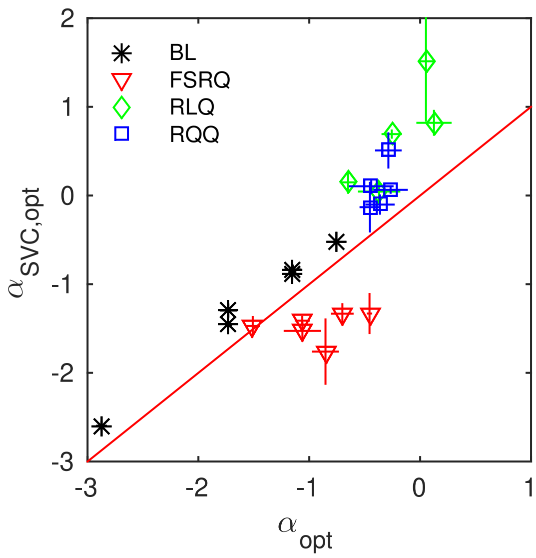

FIGURE 6.3— Relation between the optical total spectral index (α_{opt}) and the spectral index of the variable component ($\alpha_{SVC,opt}$). The red line marks the position where both spectral indices are equal.

We compare both, the spectral index of the SVC, and the spectral index of the average total spectrum (See Chapter 5). The relation between both spectral indices is shown in Fig. 6.3. If the FSRQ data are excluded, there is a good correlation between both spectral indices. This correlation indicates that the constant component and the variable component are related, and that the variations are produced by changes in the conditions of the emitting source, rather than by an unrelated emitting region. In general the SVC is bluer than the average spectrum. For BL Lac objects this difference is small ($\alpha_{SVC,opt} - \alpha_{opt} \sim 0.2 - 0.4$), while for RQQs and in particular for RLQs is larger ($\sim 0.5 - 1.0$).

The FSRQs, on the contrary, have a different behavior: although their average spectral indices span quite a wide range (between -1.5 and 0.5), a value of around -1.5 is found for the spectral indices of their variable component, in the middle of the range occupied by the BL Lac objects.

6.6 Relation between the spectral index and the flux

The intrinsic standard deviation discussed in previous Sections gives clues about the absolute spectral variability but provides no information on how the spectrum varies with the flux. A quantity that relates the spectral variations with the flux changes is essential to discern between the possible models. Most of the accepted models for quasars variability predict that the sources become bluer as they are brighter, but not all of them predict a linear correlation between color and flux. Both microlensing (in the case that the observed size of the AGN depends on the frequency of observation) and the accretion disk models display spectral variations. Synchrotron emission from a shock front in a relativistic jet, accounting from the acceleration of electrons and the cooling due to radiation, exhibits a hysteresis cycle in the α vs. flux diagram (e.g., Kirk et al. 1998); in this model, this diagram shows a clockwise or a counter-clockwise loop depending on the frequency of observation.

The spectral indices change with the brightness of the source in some AGNs. This has been observed in X-rays (Morini et al. 1986; George et al. 1988), in the visible (Bertaud et al. 1973; Fan & Lin 2000), and in NIR (Brown et al. 1989; Fan & Lin 1999). Usually, the spectrum becomes harder while the source brightens. However, in several cases, also the opposite behavior was found (see de Diego et al. 1997 for 3C 66A, Fan & Lin 1999, and Fan & Lin 2000 for a few objects in a sample of BL Lacs). Even conflicting results have even been found for the same object: while Gear et al. (1986), Kidger et al. (1994b), and Zhang & Xie (1996) found a correlation in the NIR bands between spectral index and flux of OJ 287, Lorenzetti et al. (1989) did not found a significant correlation for the same object observing between February 1986 and December 1987.

Massaro & Trevese (1996) have reported that the dependence of the color index with the magnitude introduces a statistical bias in the correlation coefficient if the filter for the magnitude coincides with one of the used for the color calculation. This bias increments artificially the significance of the correlation. For this reason, recent studies search for the correlations by comparing the spectral indices (or color) with the fluxes (or magnitudes) from a band that is not used to compute the color (e.g. V-I vs R), or with the sum of the flux of both bands (e.g. α_{V-I} vs $F_V + F_I$).

In most cases, we show the spectral index calculated from V-I against F_R, but in some cases, where more data with more quality are available, we choose to plot α_{B-R} (or α_{B-I}) vs. F_V (Fig. 6.4). In the NIR, we have looked for correlations between α_{J-K} and the flux in H (Fig. 6.5). Different objects exhibit a wide range of behaviors in these figures.

To quantify the correlations, we computed the Spearman rank correlation coefficient. To do that, first both datasets are sorted, and the rank order is used instead of the data. The Spearman correlation coefficient method is a non-parametric test, and it is better than the Pearson correlation coefficient in the case of non-normality of the sample and for non-linear relationships.

We have estimated the significance of the correlations, and the results are displayed in Table 6.4. The first column shows the name of the source; the second and third columns present the sense of the correlation and its significance, respectively and the last two columns show the same values for the correlations in the NIR. In the second and fourth column, a "0" means that the flux and spectral index are not correlated, a "–" means that the correlation is negative, i.e., the object becomes redder when it is brighter, while "+" means that the object is bluer when brighter. For GB 0738+54 a point with large error bars at low flux levels was removed before the correlation coefficient was computed.

Most of the objects exhibit a significant correlation in the optical. By contrast, only 3C 345 shows a significant correlation in the NIR, with a significance of p>98%. The difference results in optical and NIR is perhaps due to the larger errors of the NIR data.

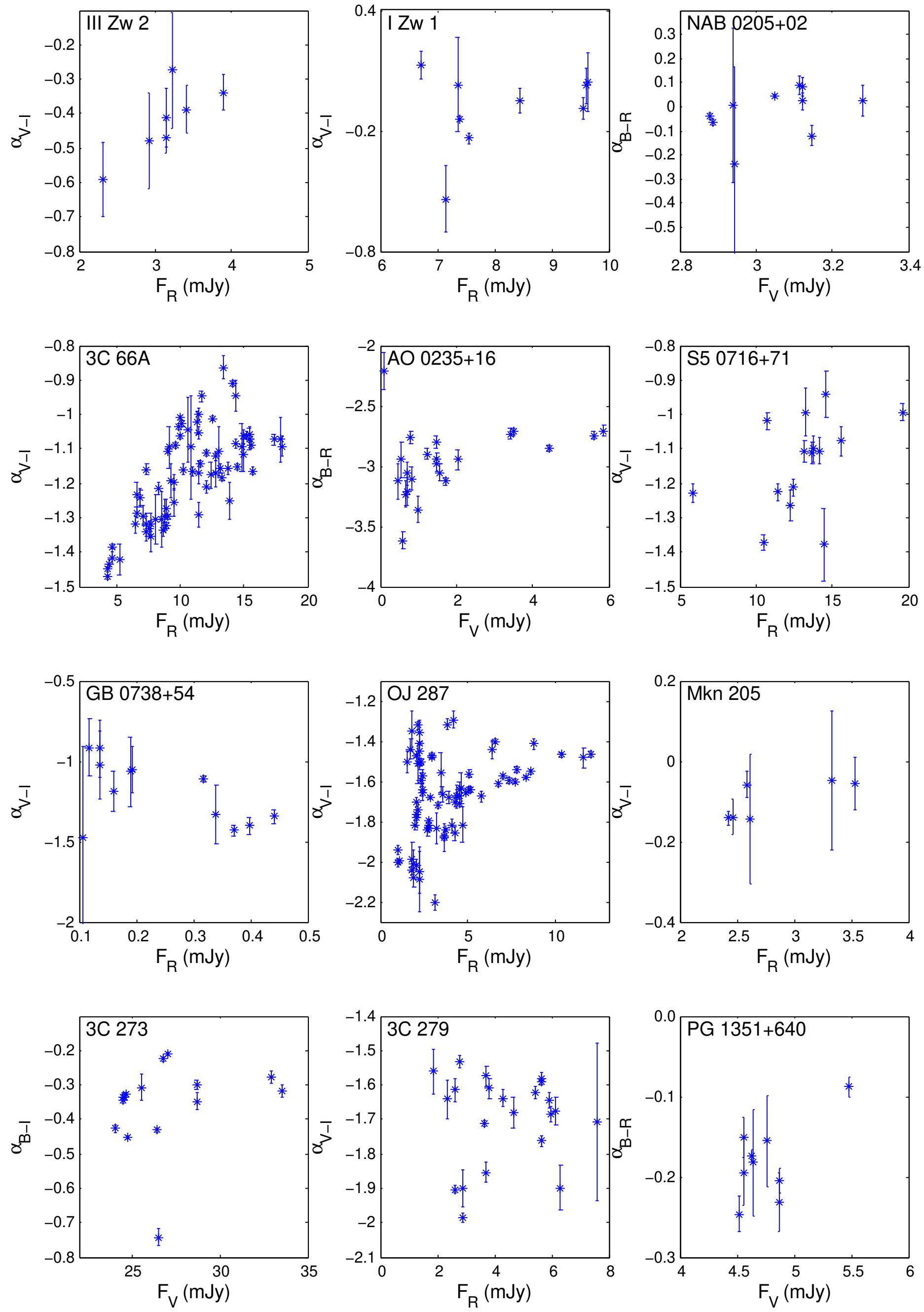

FIGURE 6.4— Relations between flux and spectral index in the optical bands.

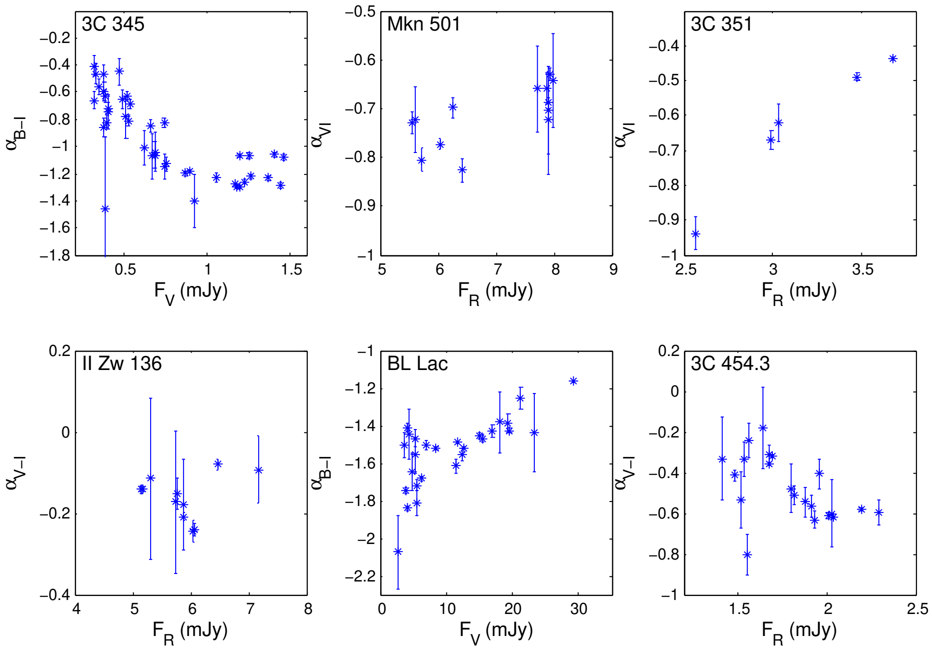

FIGURE 6.4— (cont) Relations between flux and spectral index in the optical bands.

TABLE 6.4— Flux-spectral index correlation observed in our sample. For each source, it is listed the type of the correlation and the significance in the optical and the NIR. If the object shows a bluer when brighter behavior a "+" is displayed, the opposite behavior is showed as a "–" and a "0" means that no significant correlation was found.

Object	Opt.	Sig.(%)	NIR	Sig.(%)
III Zw 2	+	99		
I Zw 1	0			
NAB 0205+02	0			
3C 66A	+	99.9	0	
AO 0235+16	+	99.9	0	
S5 0716+71	+	98		
GB 0738+54	–	99.9		
OJ 287	+	99	0	
Mkn 205	0			
3C 273	0		0	
3C 279	0		0	
PG 1351+640	0		0	
3C 345	–	99.9	+	98
Mkn 501	+	98		
3C 351	+	99.9		
II Zw 136	0			
BL Lac	+	99.9	0	
3C 454.3	–	99		

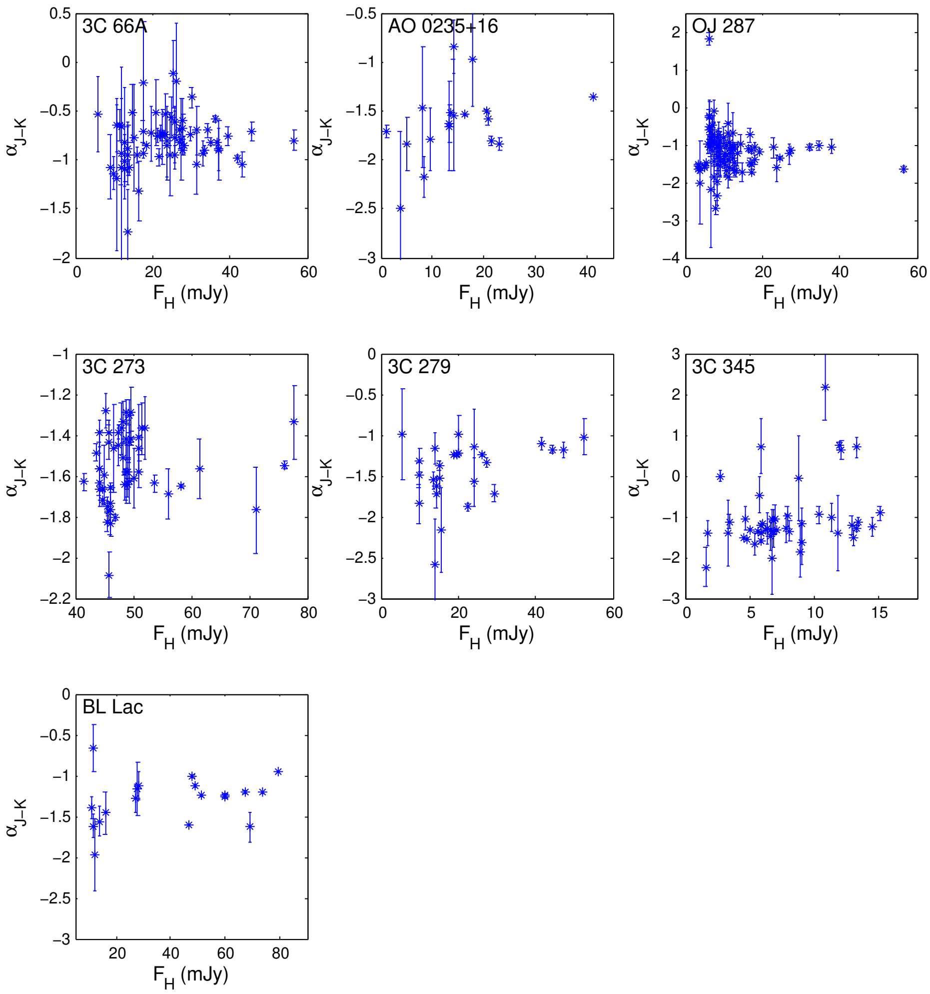

FIGURE 6.5— Relations between flux and spectral index in the NIR bands.

Most of the objects that exhibit a significant correlation between the flux and spectral index (8 from 11) present the usually observed behavior: these objects decrease its color indices while they brighten. The other three that show a negative correlation belong to the FSRQ group. In fact, there is only one other FSRQ quasar with enough observations, 3C 279, for which no significant color-magnitude correlation was found. Summarizing, from the six BL Lac objects in our sample, five display a positive correlation; three from four FSRQs show a negative correlation and 37% of the RQQs and RLQs group (three from eight) show a positive correlation.

The smaller percentage of objects with correlation in the RQQ+RLQ group does not reflect a real difference. These objects present a smaller variability both in flux and in color and, consequently, it is more difficult to find a correlation between both parameters, even if it exists.

The source S5 0716+71 is the only BL Lac object for which a significant correlation was not found. However, if we remove the point with the biggest errorbar, the significance of a positive correlation rises to 99%.

Some flux-spectral index relations are worth to be described in detail. Three FSRQs, GB 0738+54, 3C 345 and 3C 454.3, have very similar plots with a negative correlation. 3C 345 shows the clearest behavior. When the object is brighter than magnitude 16.5, the color is consistent with a constant value of B-I$\sim$1.3. For V>16.5, the object becomes bluer as it is fainter. This transition is not abrupt but gradual. The plots of GB 0738+54 and 3C 454.3 look very similar to the one of 3C 345. This is precisely the expected behavior when a variable red source is superposed over a constant (or mildly variable) blue one: when the object is bright, and the variable component dominates the emission, its spectral index is similar to the spectral index of the variable component, while at lower brightness, the spectral index changes to bluer values as the bluer constant component starts to dominate.

The two most observed sources, 3C 66A and OJ 287, have similar color-magnitude plots in the optical bands. Both objects show a tendency to be bluer when brighter. This relation between spectral index and flux is far from simple. The plot α_{V-I} vs. F_R (Fig. 6.4) of 3C 66A have two branches; in both the color index increases with the magnitude, but with a different slope and they meet at low brightness. When this BL Lac object is in a low state, its color V-I is around 0.95, but in a high state, the color ranges between V-I=0.7 and V-I=0.85.

The complexity of these plots reveals the contradictory reports about the relationship between colors and magnitudes for some objects, with contradictory claims of positive and negative correlations. Since the relationship is not exactly linear, with larger dispersion on the bright or the dim side of the plot, false correlations could be found with different observational sampling.

6.6.1 Relation flux-spectral index at different periods of time

The high number of observations of OJ 287 and 3C 66A allows us to split the time series into different periods of time and to make the same analysis of the correlation between the flux and the spectral index in each of these periods.

We have divided the light curve of these objects according to outbursts or active periods. Figures 6.6 and Fig. 6.7 show the light curves in the top panels, and the different colors and

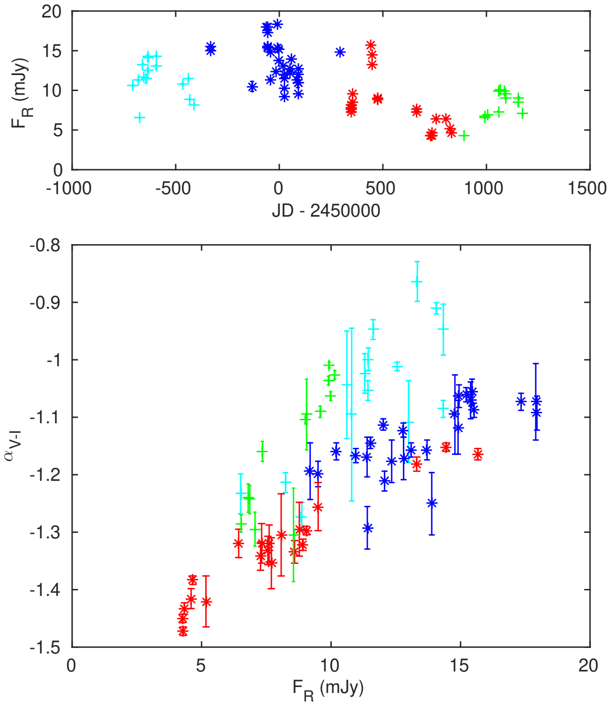

FIGURE 6.6— Comparison of the relation between the flux and the spectral index at different periods of time for 3C 66A. The top panel shows the light curve, with different colors and symbols for the periods of time. The bottom panel displays the plot of the spectral index (calculated from the V-I color) against the flux (in the R band).

symbols represent the time intervals. The bottom panels present the plots with the relation between flux and spectral index, using the same symbols and colors for the same intervals as in the top panels.

For 3C 66A, the splitting of the light curve in periods improves the correlation between the flux and the spectral index. The dispersion of the linear correlations in the distinct periods is lower than the scatter using the whole dataset. In particular, the rms of a linear fit decrease from 0.09, with the entire dataset, to 0.04, using the data from 1995-1996 (blue stars, 26 measurements) and to 0.02, using the data from 1997-1998 (red stars, 21 measurements).

In the case of OJ 287 (see Fig. 6.7) the data contain the double outburst of 1995-1996 (Sillanpaa et al. 1996a; Pursimo et al. 2002). This outburst was predicted using a model of a binary black hole (e.g., Sillanpaa et al. 1988; Valtonen et al. 2006), in which the double outburst (Sillanpaa et al. 1996b) is explained as passages of the secondary black hole through the accretion disk of the primary black hole. The rms of the linear fit in both periods is also lower than the rms of the linear fit using the whole dataset (0.19), being 0.16 for the first outburst (blue points, 19 measurements) and 0.12 for the second outburst (red stars, 26 measurements).

To assess the significance of these results, we randomly selected a subset with a number of points equal to the number of measurements presented in each period and calculated how many

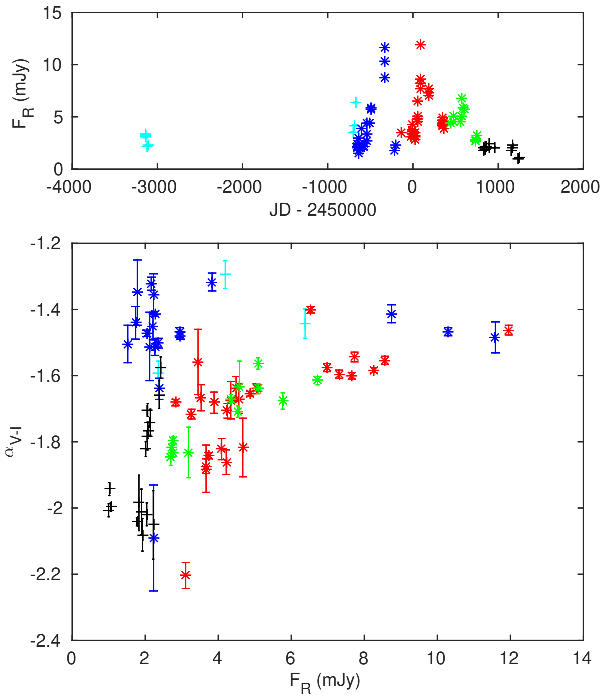

FIGURE 6.7— Comparison of the relation between the flux and the spectral index at different periods of time for OJ 287. The top panel shows the light curve, with different colors and symbols for the periods of time. The bottom panel displays the plot of the spectral index (calculated from the V-I color) against the flux (in the R band).

of the randomly chosen subsets present a dispersion lower than what we have obtained in the period of study. In the case of 3C 66A, only 0.01% of the subsets (with 26 and 21 measurements) have an rms equal or lower than what we have found in the period represented by the blue and red stars (1995-1996 and 1997-1998, respectively). For OJ 287, only 0.28% and 0.02% of the randomly selected 19/26 measurements have an rms lower than what was obtained in the periods of the first and second outbursts respectively.

Besides, the slopes of the linear fits between the spectral index vs. flux using the different subsets are different. We have found that the slopes in the periods plotted with blue and red stars in 3C 66A are 0.018 and 0.026, respectively. The null hypothesis that both datasets have the same slope is rejected with a significance p>99%. The significance is even higher (p>99.99%) if we compare each of these two periods with the last one shown with green stars in Fig. 6.6.

For OJ 287, during the first outburst in 1995 the spectral index did not change, while the flux variates by a factor five (see Fig. 6.7); during the second outburst in 1996 (red stars), OJ 287 displayed a bluer-when-brighter behavior. The slopes found in these two epochs are different with a significance p>99.9%.

6.7 Spectral variability parameter (SVP)

In order to quantify the spectral variations relating them to the flux changes, Trèvese & Vagnetti (2002) define the *spectral variability parameter* (SVP) as:

$$SVP = \frac{\alpha(t+\tau) - \alpha(t)}{\log F(t+\tau) - \log F(t)}, \tag{6.3}$$

which represents the change of the spectral slope per unit log-luminosity change.

We have used the flux and color daily averages (those presented in Chapter 5) to compute the SVP. We have employed only the data with small measurement errors and only those data pairs for which the fluxes have changed by an amount greater than twice the measurement errors. Finally, the individual SVPs were averaged for all data pairs with $\tau < 2$ months and $\tau < 3$ years. Table 6.5 presents the final averages. The errors of the SVPs shown in the table were calculated as the error of the mean. For the optical SVPs presented in the Table, the spectral index was computed from the V-I colors and the fluxes used in the denominator of Eq. 6.3 are the R fluxes. The estimation of the SVP in the NIR (columns 4 and 5) uses the spectral index calculated from the color J-K and the H band fluxes.

Most of the objects have a positive SVP. This means that the objects display the typical behavior of the source being bluer when it is brighter, as it has been observed in most of the quasars and blazars by many authors. However, four of our objects show the opposite behavior, according to the values of the SVP_{3year}. These are the three FSRQs that display a strange behavior in the α vs. flux plot (as was described in the last section) and II Zw 136, for which the negative value of the SVP_{3year} is not significant.

In fact, there is a clear separation in the values of the SVP for the different types of objects, at least in our small sample of AGNs. RQQs and RLQs have a higher SVP than blazars, which

TABLE 6.5— Average values of the spectral variability parameters (SVP) in the optical and NIR. The averages are computed using those data pairs in which the time difference is less than two months and less than three years.

Object	SVP_{2month} (V-I)	SVP_{3year} (V-I)	SVP_{2month} (J-K)	SVP_{3year} (J-K)
III Zw 2	-	1.15±0.30	-	-
I Zw 1	-	0.64±0.35	-	-
NAB 0205+02	-	2.02±0.76	-	-
3C 66A	0.71±0.03	0.64±0.01	1.05±0.06	0.34±0.03
AO 0235+16	0.20±0.03	0.36±0.03	0.38±0.02	0.32±0.03
S5 0716+71	0.67±0.37	0.35±0.07	-	-
GB 0738+54	-1.37±0.41	-0.77±0.09	0.33±0.43	0.33±0.43
OJ 287	0.42±0.05	0.25±0.01	0.14±0.05	0.12±0.02
Mkn 205	-	0.53±0.25	-	-
3C 273	-	0.56±0.34	1.06±0.08	0.41±0.04
3C 279	-0.07±0.11	0.44±0.06	0.11±0.18	0.43±0.12
PG 1351+640	-	0.01±0.27	-	-
PKS 1622-29	-	-	2.32±0.54	2.32±0.54
3C 345	0.16±0.09	-0.67±0.03	1.50±0.16	1.27±0.09
Mkn 501	-1.08±0.64	0.75±0.08	0.21±0.29	-0.06±0.08
3C 351	-	2.89±0.18	-	-
II Zw 136	-	-0.02±0.26	-	-
BL Lac	0.55±0.05	0.70±0.01	2.42±0.27	1.65±0.17
3C 454.3	-3.41±0.15	-1.93±0.10	1.45±0.13	-0.43±0.27

TABLE 6.6— Average values of the spectral variability parameter (SVP) using the V-I color and the flux in R for the different types of AGNs.

Type	RQQ	RLQ	FSRQ	BLL	RQQ+RLQ	FSRQ+BLL
$\overline{\mathrm{SVP}}_{V-I}$	0.64	1.53	-0.74	0.51	0.97	0.02
n	5	3	4	6	8	10

means that they display stronger color variations for the same change in flux, being the sources bluer as they are brighter. On the contrary, BL Lac objects and FSRQs have SVP closer to zero, having the SVP of FSRQ oft negative values. Unfortunately, we have no NIR observation for RQQs and RLQs, and we can not check if the behavior of the SVP observed in the optical is similar in the NIR. Table 6.6 presents the average values of the SVP for all types of objects in our sample. Using the two-sample t-test analysis of averages, we have found that the difference observed between the RQQs+RLQs and the FSRQs+BLLs is significant to $p > 95\%$. Also, FSRQs are found to show a smaller SVP than BL Lac objects with a significance $p > 98\%$. All these data confirm the results of Trèvese & Vagnetti (2002) and Vagnetti et al. (2003).

We display in the top panels of Fig. 6.8 how the SVP is related to the average spectral index in our sources in the optical (top left) and in the NIR (top right). Although the average values of the optical SVP of RQQs and BL Lac objects are similar, they are located in this plot at clearly different regions because BL Lac objects exhibit redder colors. Besides, despite BL Lac objects and FSRQs are situated in distinct places in the optical plot (top left panel), in the NIR plot (top right) they occupy approximately the same location. Unfortunately, from the group of RQQs+RLQs, we have only one object observed in the NIR, 3C 273. Its SVP is, however, similar to the blazars. The bottom panel shows the relation between the optical and NIR SVP. Our optical plot is similar to the one shown by Trèvese & Vagnetti (2002) and Vagnetti et al. (2003). However, our data were estimated using V-I instead of B-R, as was done by these authors and, therefore, there are small differences between both figures.

6.7.1 SVP for several models of variability

In Fig. 6.8 we also plot different models of variability. Some of these models assume that the color variations are originated by the superposition of two components, one of which is constant and the other variable, but whose spectral shapes remain constant; others, that the color variations are intrinsic to the variable process. The models displayed in Fig. 6.8 comprise:

- A black body of fixed area, in which the variations are originated by changes in the temperature (blue line).
- A superposition of a typical host galaxy and a variable source with a spectrum of a typical quasar (cyan lines).
- An accretion disk in which variations are produced by a change in the accretion rate (red lines).

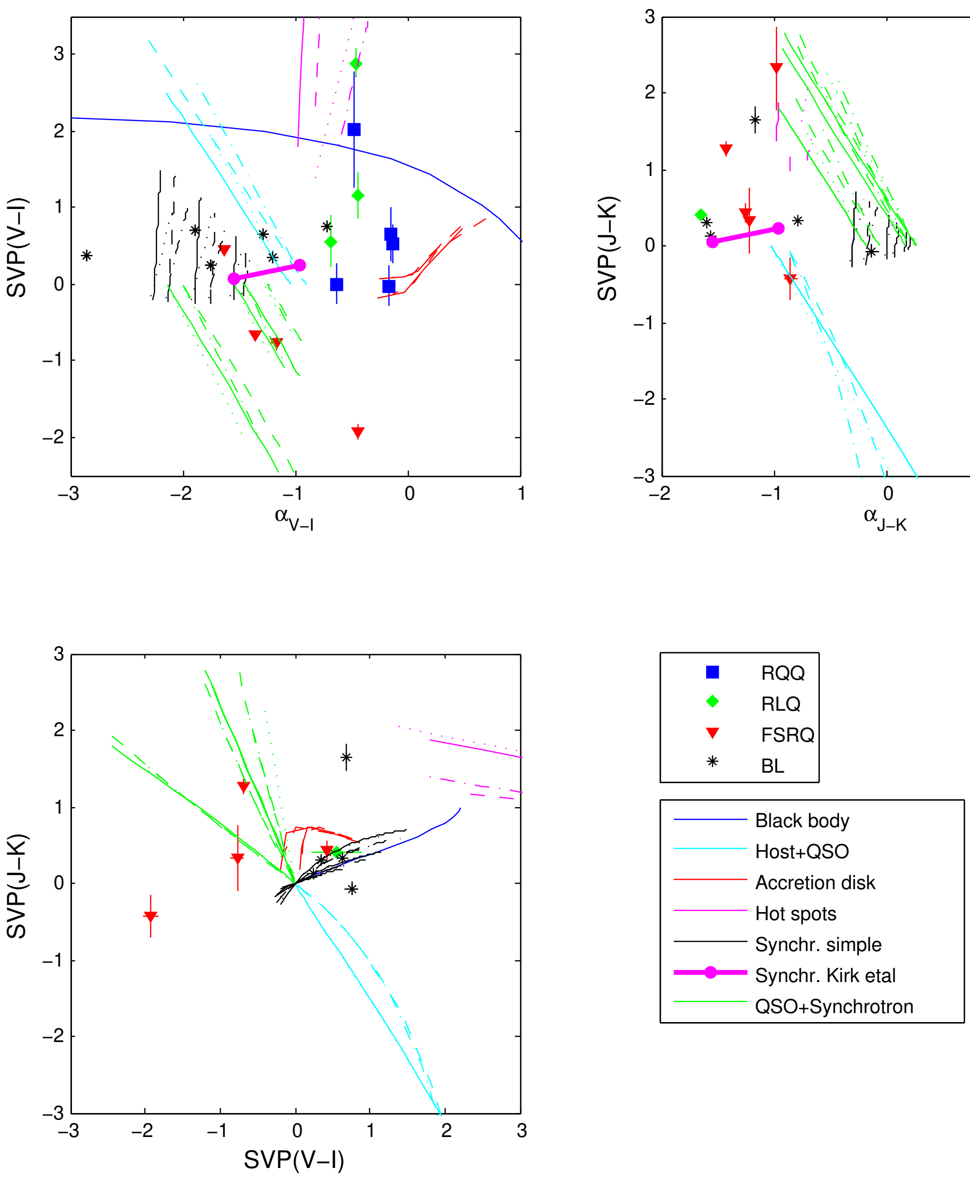

FIGURE 6.8— Top left panel: optical (V-I) SVP vs. spectral index. The top right panel shows the relation between near infrared SVP and spectral index. Finally, in the bottom panel, it is shown the optical vs. NIR SVP plot. In all cases, the SVP is computed by averaging for all $\tau < 3years$ (see Eq. 6.3). The different types of objects are plotted using: blue squares for the RQQs; green diamonds for the RLQs; red triangles for the FSRQs and black asterisks for the BL Lac objects. The lines are the results of several simple models of variability (see the text for details).

- Hot spots in the accretion disk, modeled as small blobs of material whose spectrum can be represented as a black body (magenta lines).

- A synchrotron model represented by two broken power laws, one of which constant and another variable, both with the same analytical form, but different peak frequency (black lines).

- A more detailed numerical synchrotron model from Kirk et al. (1998) (big magenta points joined by a thick line) that accounts for the acceleration of particles in shock fronts inside the jet.

- A model in which the color variations are produced by the superposition of a constant typical quasar spectrum plus a variable synchrotron spectrum (green lines).

The first five models were also used by Trèvese & Vagnetti (2002) and Vagnetti et al. (2003). We have added the last two models, extended the application of the models to the NIR, and adapted them in the optical to consider the new filters used here (V-I instead of B-R).

Next, we explain in detail all these models:

The Black body model

The blue line of Fig. 6.8 represents a black body of fixed area in which a change in temperature produces a change in flux and color. This model has only one free parameter: the temperature of the black body. The spectral variability parameter is computed analytically as $SVP = (\ln 10)[1 - x/(e^x - 1)]$ and $x = h\nu/kT$.

The Host galaxy+quasar model

Several authors have claimed that the color variations are not intrinsic to the variable source, but are the result of the superposition of a constant source and a variable source, whose spectrum remains constant. One obvious possibility for the constant source is the host galaxy, which was considered, e.g., by Romano & Peterson (1999). As Trèvese & Vagnetti (2002), we make use of the templates of the quasars and host galaxies spectral energy distribution (SED) presented by Elvis et al. (1994). The numerical simulations were created by adding a variable quasar SED to the host galaxy SED, in such a way that the average ratio between both components ranges from 10^{-3} to 10^3. In each case, the variable component changes such an amount that the total variability is $F_{var} = 0.12$ and $F_{var} = 0.5$, the typical variations of the RQQs+RLQs and FSRQ+BL groups, respectively. In Fig. 6.8, the cyan lines display the results of these simulations. The solid line represents the simulation for an object at redshift z=0.0 and with a variability of $F_{var} = 0.12$, the dotted line for $z = 0.0$ and $F_{var} = 0.5$, the dashed line for $z = 0.3$ and $F_{var} = 0.12$, and the dot-dashed line for $z = 0.3$ and $F_{var} = 0.5$.

Changes of accretion rate

It is supposed that the emission of the quasars is dominated by the accretion disk, at least in the optical-UV region. We have used, as Trèvese & Vagnetti (2002), the accretion disk models of Siemiginowska et al. (1995) to estimate the expected color variations of an accretion disk when the accretion rate changes. These authors consider a standard α-disk in Schwarzschild and Kerr geometries. The model includes the modification caused by electron scattering and comptomization of soft photons in the disk atmosphere. We have employed the models in the Kerr geometry and with an inclination angle $\theta = 0°$ (face on) and we have computed the expected spectral variability parameters and spectral indices in the optical and NIR for different changes in the accretion rate: from $\dot{m} = \dot{M}/\dot{M}_{Edd} = 0.1$ to $\dot{m} = 0.3$ and from $\dot{m} = 0.3$ to $\dot{m} = 0.8$. The red lines in Fig. 6.8 show the spectral behavior of our simulations for accretion disks around black holes of masses varying from $M = 10^7 M_\odot$ to $M = 10^{10} M_\odot$ (right to left) at z=0 for accretion rates $\dot{m} = 0.1 - 0.3$ (solid line) and $\dot{m} = 0.3 - 0.8$ (dotted line) and at z=0.3 (dashed line and dot-dashed line for $\dot{m}$ from 0.1 to 0.3 and from 0.3 to 0.8, respectively). This model does not represent the observational data adequately since the expected spectral variability is much smaller than observed. Also, it is expected that the timescales of variability for such a model are much larger than observed.

Hot spots in the accretion disk

Another option proposed for the variability of AGNs originated in the accretion disk are the hot spots produced by disk instabilities (e.g., Kawaguchi et al. 1998, Wiita et al. 1992). We assume that the observed total spectrum is the superposition of the quasar SED template presented by Elvis et al. (1994) and a variable component that corresponds to the hot spots. The hot spots are modeled as a black body of a certain temperature. The temperature is assumed to be constant, and the total emission of the hot spot region is parametrized to such a degree that the output variability is $F_{var} = 0.1$ or $F_{var} = 0.5$. The magenta lines show the location of the results of this model for a temperature of the hot spot region from $T = 10^4 K$ (lower part of the lines) to $T = 10^6 K$ (upper part of the lines) for different combinations of redshift and variability: solid line for $F_{var} = 0.12$ and $z = 0.0$, dotted line for $F_{var} = 0.5$ and $z = 0.0$, dashed line for $F_{var} = 0.12$ and $z = 0.3$ and dot-dashed line for $F_{var} = 0.5$ and $z = 0.3$. In the optical plot the results of this model occupy quite a big region, and is consistent with at least part of the RQQs and RLQs; in the NIR the location of the results of the simulations is much smaller.

Two synchrotron components model

It is accepted that the bulk of the optical/NIR radiation of blazars arises from a relativistic jet pointing almost directly toward us and emitting synchrotron radiation. Many models assume that the variability is generated by shock fronts traveling along the jet. The stationary emission of the jet can be simplified as a broken power law, characterized by the two asymptotic spectral slopes α_1 and α_2 below and above the peak frequency, ν_p (Vagnetti et al. 2003, Tavecchio et al. 1998) and with a luminosity of L_p:

$$L_\nu = L_p 2 \left[\left(\frac{\nu}{\nu_p}\right)^{-\alpha_1} + \left(\frac{\nu}{\nu_p}\right)^{-\alpha_2} \right]^{-1} \tag{6.4}$$

We consider here that the variable emission has the same spectral shape but the luminosity and the peak frequency are different. This second component is similar to the one obtained when the shock front crosses the shell of material due to newly accelerated electrons.

We carried out these simulations for three peak frequencies of the stationary emission, $\log\nu_p$ =14.4, 14.7 and 15.0. The three groups of black lines in Fig. 6.8 are the results of the models for these three frequencies, growing from left to right. Inside each line the peak frequency ratio between both components varies from 0.8 to 4 and the four lines in each group are the possible combinations of redshift ($z = 0.0$ and $z = 0.3$) and variability ($F_{var} = 0.12$ and $F_{var} = 0.5$). In the optical plot, these simulations seem to have the same spectral variability and spectral indices as the BL Lac objects; however, in the NIR, although the spectral variability of the simulations is similar to the one of the BL Lac objects, the spectral indices of the simulations are around zero, while these sources present a redder color.

Synchrotron model of Kirk et al. (1998)

Kirk et al. (1998) described a more detailed model of the relativistic jet in blazars, which shows the emitted fluxes and spectral behavior. They model the acceleration of electrons at a shock front and compute the emission of the post-shock region which contains a homogeneous magnetic field in a time-dependent way. Since the magnetic field is assumed to be constant, each observed frequency band can be identified with electrons of a particular energy. They show that the relationship between the flux and the spectral index depends on the frequency of observation. The output spectrum has several regions which are regulated by the different timescales. In the region between the spectral break and the maximum flux, where the particles have had time to cool, but the cooling rate is always much slower than the acceleration rate, the plot spectral index (α) vs. flux shows a clockwise loop, and synchrotron cooling controls the spectral slope. On the other hand, in the region around and above the maximum fluxes, where the acceleration rate is comparable to the cooling rate, the α vs. flux plot displays an anticlockwise loop; in this last case, the information propagates from lower to higher energies as particles are accelerated into the radiative window.

Kirk et al. (1998) present two examples with emitted flux and spectral index in their Fig. 3 and Fig. 4. Using these examples, we have computed the average spectral index and the spectral variability parameter for the flare modeled there. The results are plotted in Fig. 6.8 as the two big magenta points connected by a thick line. It should be noted that, unlike the other simulations in which the SVP vs. α data were computed for our optical and NIR observing windows, here this is not the case. The two points represent two observing bands one around $0.03\nu_{max}$ and the other around $0.5\nu_{max}$, where ν_{max} is the frequency where the maximum synchrotron radiation is located. However, these points should be representative of the location of the results of this model in the SVP vs. α plot.

The Quasar+Synchrotron model

Finally, the last considered simulation try to model the behavior of FSRQs. BL Lac objects and FSRQs display many characteristics in common. However, the spectrum of FSRQs shows the signature of the accretion disk and emission lines. Therefore, we assume here that the spectral variability of FSRQs can be computed as a combination of a stationary emission, that of a typical quasar represented here with the quasar SED template of Elvis et al. (1994), and a variable component, due to synchrotron emission and calculated as in Eq. 6.4.

The green lines of Fig. 6.8 show the results of these simulations. There are three groups of data, one for each peak frequency of the synchrotron emission ($\log \nu_p$ =14.4, 14.7 and 15.0, from left to right). In each group, the four lines represent the four usual combinations of redshift and variability (z =0.0, 0.3 and F_{var} =0.12, 0.5). Through each line, the logarithm of the average ratio between variable emission (synchrotron) and the constant emission (typical quasar) ranges from -3 to 3.

6.7.2 Comparison of the SVP of our objects with the models

Our data and the results of our simulations are consistent with the conclusions of Trèvese & Vagnetti (2002) and Vagnetti et al. (2003), but some difference exists. They are partly due to the different filters used in the optical—these authors compute the relevant parameters using observations in B and R, while we make the analysis using the filters V and I. Also we present results in the NIR.

In general, we have found that the group of RQQs+RLQs have a slightly smaller SVP than the data of QSOs presented by Trèvese & Vagnetti (2002). This is partly because these authors used the flux in the B band to calculate the SVP (Eq. 6.3) and to compute the spectral index. When the variability is not much higher than the measurement errors, as is the case in these objects, this procedure introduces a spurious correlation between the spectral index and the flux (Massaro & Trevese 1996) that translates here to higher positive values of the SVP.

Because of this, we can not conclude, as Trèvese & Vagnetti (2002), that the spectral variability of QSOs is due to the hot spots in an accretion disk. Trèvese & Vagnetti (2002) reported that the results of the simulations of hot spots in an accretion disk agree with the observed SVP vs. spectral index data for quasars. However, while in the optical these simulations span a large range of positions in the plot, in the NIR they are grouped around SVP=1.5 and $\alpha = 0.8$. As noted before, we have no NIR data for the group of RQQs+RLQs, and consequently, no comparison can be made between simulations and observations in these bands.

We have plotted the results for the black body models for comparison with Trèvese & Vagnetti (2002), but it is known that this model is not the origin of the emission of AGNs, because of the high luminosity of the sources and its rapid variability. This is seen in our plots: while in the optical, the data of some objects in the diagram SVP-α are in agreement with blackbodies of a certain temperature, in the NIR, they are totally incompatible.

A similar argument can be employed against the model of accretion disks, in which the variability is originated by changes in the accretion rate (Siemiginowska et al. 1995). The time required for the disk to reach a new stationary state after a change in the accretion rate is much longer than the typical timescales of the variability of AGNs. The simulations with this model predict that the SVP would be around zero, smaller than what is observed, and that the color of the sources is much bluer.

The effect of the host galaxy in the spectral variations is not expected to be significant in our data because, for those objects that show a prominent host galaxy, the fluxes coming from the galaxy was removed as it explained in Chapter 4. The simulations show that, while in the optical, the expected SVP should be positive (the AGN becomes bluer as it is brighter), in the NIR, the reverse should be correct, if the spectral variability is due to the superposition of a host galaxy and a variable source. Only Mkn 501 displays this behavior, and it should be remembered that for this object, the removal of the host galaxy in the NIR is not optimal.

The simulations with the simple model (the sum of two broken power laws) and the model of emission of a relativistic jet described by Kirk et al. (1998) give results in agreement with what is observed in the BL Lac objects in the optical bands, although the distribution of the observed points is broader than the simulations. In the NIR range, the simple model of a jet emission gives an SVP similar to the observations of BL Lac objects, but the simulated spectra are harder.

FSRQs do not seem to be explained alone with these models of a relativistic jet. The simulations, created with a stationary QSO template plus a variable synchrotron component are, however, compatible with the observations of FSRQs. In the optical plot of Fig. 6.8, the FSRQs occupy a region of smaller SVPs and bluer colors than the region of BL Lac objects, as is expected from the simulations. In the NIR, on the contrary, although the range of SVP values of the simulations are similar to the observation in this type of sources, the simulated colors are bluer than the observations. However, as a proof of the idea that FSRQs have both components, those of quasars and those of BL Lac objects, the simulations predict that, while in the optical, FSRQs show smaller SVP and bluer colors than BL Lac objects in the NIR the reverse is expected. The observations seem to favor this scenario.

6.8 Discussion and conclusions

In this chapter, we have presented the analysis of the color long-term variations of the AGNs in our sample and the relation of the color with the flux of the sources. From our analysis we highlight the following conclusions:

Most of the objects in our sample exhibited color variations, having blazars higher amplitudes than quasars. This effect is probably due to the stronger flux variability in blazars: if the source shows flux variability of low amplitude, it is difficult to detect color variability.

We applied the method of Hagen-Thorn & Marchenko (1989) to extract the spectrum of the variable source. This method assumes that the observed flux is the addition of a component with constant flux and a variable component with a constant spectral shape. Although the assumption that the variable component has a constant spectral shape may not be physically correct, using this method we can extract the typical spectrum of the emission region that originates the variability.

In all objects of our sample, except for FSRQs, the variable component is bluer than the observed spectrum of the source. In BL Lac objects, this implies that variability is produced by the injection or acceleration of electrons in the jet with an energy distribution that is harder than that of the previously cooled electrons. In quasars (RQQs+RLQs), if the dominant region is the accretion disk, then the variability may be produced by regions that are hotter than their surroundings, producing a harder spectrum.

FSRQs are supposed to have two components, the accretion disk and the jet. After applying the method of Hagen-Thorn & Marchenko (1989), the spectrum of the variable component of these objects has a spectral index similar to those of BL Lac objects and is redder than the observed spectrum. The similarity of the spectral indices of the variable component in FSRQs and BL Lac objects confirms that the jet is the responsible for at least most of the variability in FSRQs.

Most of the objects in our sample show a bluer-when-brighter behavior. All of them are BL Lac objects and RLQs. We have not found any correlation between the flux and the spectral index in any of the RQQs in our sample. Considering the RLQs, except for 3C 273, which is sometimes considered an FSRQ, the two objects with enough data, III Zw 2 and 3C 351, seem to have large changes in the spectral index compared with the flux changes, which are small.

Several of the FSRQs exhibit a negative correlation. In these cases, the sources are redder when the brightness increases, or show no correlation. The diagrams flux-spectral index of 3C 454.3, GB 0738+54, and 3C 345 are particularly interesting. At lower flux levels, the sources display a strong redder-when-brighter (RWB) behavior. These relationships disappear when the sources are brighter. This behavior is naturally explained by the two-component model of FSRQs, the combination of a constant (or slowly variable) blue accretion disk and the variable red relativistic jet. Although intrinsically both the accretion disk and the relativistic jet may present a BWB behavior, the combination of the two components has a stronger influence in the color changes than the intrinsic color variability of the relativistic jet.

For 3C 66A and OJ 287, the large amount of data allows us to split the data into different periods according to events observable in the light curve. We estimated the correlation separately in each of the periods and found that the dispersion in the relationship is smaller during prominent outburst than in the whole dataset. Also, we found that the slopes of the linear regression flux vs. spectral index in some periods are significantly different from each other.

These differences between the slopes for several outbursts in OJ 287 and 3C 66A can be explained if the physical conditions of the emitting region (e.g., magnetic field, bulk Lorentz factor or the shape of the energy distribution of the injected electrons) are different, or the emission region is located at different places along the jet. This also explains why there are inconsistent results of this relation, with some authors finding a BWB behavior and others the opposite in the same object (e.g., Lorenzetti et al. 1989; Gear et al. 1986; Kidger et al. 1994b). If the data analyzed are from several flares, from emitting regions with different physical conditions, the possible correlation between the flux and the spectral index varies from flare to flare. It is also possible that several flares are present at the same time, which further complicates the analysis of the correlations.

In OJ 287, we found that the outburst in the Fall of 1994 was achromatic as was also found by Sillanpaa et al. (1996b). This was the first of the double-peak outburst predicted by the binary SMBH in this blazar (Sillanpaa et al. 1988; Lehto & Valtonen 1996; Pietilä 1998). These outbursts, with a period of approximately 12 years, has been observed in the last $\sim$ 120 years (see, e.g., Sillanpaa et al. 1988; Hudec et al. 2013). While the second outburst at the start of 1996 was mildly chromatic, in the first outburst, the spectral index remained constant. The reason for this may be a different origin of the emission during the outburst. Valtonen et al. (2012) and Valtonen et al. (2016) modeled the observed emission of the next two outbursts of OJ 287 in April 2005 and December 2015, respectively, as bremsstrahlung radiation. This bremsstrahlung radiation was generated by expanding hot bubbles of gas ejected from the accretion disk of the primary black hole due to the impact of the secondary. After this first outburst, OJ 287 exhibits a series of synchrotron flares, one of which is the outburst observed by us in 2006.

The spectral variability parameter defined by Trèvese & Vagnetti (2002) (Eq. 6.3) measures how the spectral index varies when the flux changes. The diagram of Fig. 6.8, which represent the values of the spectral variability parameter against the spectral index, separates the different object types. While the RQQs and RLQs have a spectral index around $\alpha_{V-I} \sim -0.5$ and the SVP ranges between 0 and 3, BL Lac objects display all a similar $SVP \sim 0.5$, with spectral indices between -0.5 and -3. This wide range of spectral indices arises from the fact that the synchrotron peaks of the BL Lac objects presented here lay at frequencies between 10^{13} and 10^{16} Hz (Ackermann et al. 2015). The approximate location of the different object types in this diagram in the optical can be calculated using simple models.

Hot spots superposed to the typical spectrum of a quasar simulates the position of quasars, although for some objects the SVP is lower than the model. The lower SVP of the quasars may be due to a lower temperature ($< 10^4$ K) of the hot spots.

BL Lac objects, with low but positive SVP and a red spectrumm can be simulated with the combination of two synchrotron components, one constant and one variable. The spectrum of each has a shape of a broken power law with different peak frequencies. Also, the numerical model of a synchrotron flare described by Kirk et al. (1998) gives the approximate location of BL Lac objects in the diagram.

Finally, the blauer spectra of FSRQs, in comparison with BL Lac objects, and negative SVPs are best interpreted as the combination of a constant quasar template and a variable broken power law spectrum. This combination recreates the emission of the accretion disk and the jet, respectively.

All the simulations predict a harder spectrum for both the FSRQs and BL Lac objects in the NIR, though a similar SVP, compared with the observations. A possible explanation could be that there is another component in the NIR that makes these objects redder. The obvious component would be dust. However, in these case, the averaged spectrum of these object should display this component, and there is no indication of an additional component in Fig. 5.38. Besides, another component, presumably constant, not only would change the color of the objects but also would modify the behavior of the SVP and decreases the amount of variability.

7

Rapid Variability

The study of the microvariability, variability on timescales of hours, in blazars puts constraints on the physics of these intriguing objects. I characterized the microvariability of blazars by means of the duty cycle and the fractional variability parameter, and compare it with other types of quasars. Here, I introduce a new definition of the duty cycle that considers both the length of the observations and the different detection level of the variability arising from different observing conditions. I determined the time lags between the variability of different optical bands to be less than 20 min. In the best-studied objects, the microvariability amplitude is correlated with the average flux, similarly to the rms-flux relation that has been found in the X-rays variations of many accreting objects. Assuming that the variability is produced by synchrotron processes, I estimated the magnetic field in the jet of BL Lac to be ~ 4 G. In the objects with the largest microvariability, the intra-night variations are more chromatic than on longer timescales. I propose that all these characteristics can be explained by an inhomogeneous jet, in which the different sub-regions of the jet produce a chromatic flare with different onset times.

7.1 Introduction

One remarkable characteristic of the AGNs is its variability. These variations can be very fast, with timescales even shorter than hours, in particular in blazars (e.g., Heidt & Wagner 1996). Blazars are radio loud AGNs whose relativistic jet is pointed out in a direction close to the line of sight. Due to this orientation, relativistic effects increase the apparent brightness of blazars and its intrinsic variations, and reduce the observed variability timescales. As a result of the finite light travel time, variability on such short timescales probes emission regions that are smaller than those that can be observed with very-long-baseline interferometry (VLBI). Therefore, the study of rapid variability is particularly informative on the physical conditions and processes operating in the emission regions of the jets: acceleration and cooling mechanisms, turbulence, magnetic field, etc.

Following by Agarwal et al. (2016), we call intra-day variability (IDV) or microvariability to those variations with timescales of hours and amplitudes up to a few tenths of a magnitude, while short-term variability has timescales from days to month and amplitudes up to one magnitude. Finally, long-term variability has timescales of years and several magnitudes of amplitude. However, this distinction is arbitrary, and it is not clear if there is a different physical mechanism that is responsible of this classification, or it is just the consequence of the time sampling of the observations and the red-noise nature of the power spectral density of the variability.

The spectral energy distribution (SED) of blazars is characterized by two humps, the first extends from radio to X-rays, and the second at higher energies, reaching TeV energies. The low-energy hump is believed to be caused by synchrotron emission in the jet. The high-energy component can be due to inverse Compton scattering from the same electrons producing the synchrotron emission: the source of low-energy photons that are upscattered can be the same synchrotron emission of the jet (synchrotron self-Compton emission), or an external source, like the dust torus, the accretion disk, or the broad line regions. Other authors favor hadronic models for the origin of the high-energy component, in which the high-energy radiation is originated by the protons accelerated to relativistic energies and the subsequent cascading (e.g., Böttcher 2007 and references therein). With such broadband components, it is expected that the IDV is not only constrained to the optical frequencies but in all electromagnetic spectrum.

7.1.1 Rapid variability at high energies and radio frequencies

Using the EGRET instrument onboard the Compton Gamma Ray Observatory, Kniffen et al. (1993) observed a strong flare of 3C 279 at energies larger than 100 MeV, with an increase of factor two in less than two days and a subsequent decay in a single day. PKS 0528+134 and 3C 454.3 displayed also rapid variability in γ-rays (Hunter et al. 1993, Hartman et al. 1993). Nevertheless, it was the operation of the Fermi satellite that changed the high-energy view of blazars. For example, Foschini et al. (2011) reported e-folding timescales of variations shorter than a few hours in 3C 454.3, 3C 273 and PKS 1222+216 at energies larger than 100 MeV. Kushwaha et al. (2014) found asymmetric profiles in the γ-ray light curve of two flares of PKS 1222+216 with similar rise times but a rapid decline in one flare. Also, PKS 1510-089 displayed a flare with a doubling timescale of 1.3 hours in the rise and a halving timescale of 1.2 h during the following the decay.

Rapid variability in blazars has also been detected at even higher energies with Cherenkov telescopes. For example, Aharonian et al. (2007) described an outburst observed with HESS in July 2006 at energies of hundreds of GeV with timescales of variations of a few tens of minutes.

Giommi et al. (1990) described the X-ray rapid variability in BL Lac objects as a low level flickering with occasional flares. Later, observing with XMM-Newton, Edelson et al. (2001) reported variations in PKS 2155-304 at $\sim 10\%$ level in a few hours with no lags between the different energy bands. Gupta et al. (2016) studied a sample of 12 low energy peaked blazars. These authors found that the duty cycle of IDV in their sample is only of 5%, much lower than it is observed in the optical bands for the same objects. Also, the duty cycle is lower than what was observed in X-rays in high energy peaked blazars (Gaur et al. 2010, Kalita et al. 2015). Gupta et al. (2016) also argued that this difference in the variability properties is due to the peak position of the synchrotron broad component of the spectral energy distribution: in low-energy peaked blazars, the X-ray band lies at the end of the synchrotron component or at the start of the inverse Compton component, while it is located close to, or just above the peak of the synchrotron component in high energy peaked blazars.

Not only blazars show IDV. Seyfert galaxies also exhibit rapid variations in X-rays with timescales from hours to days (e.g., Mushotzky et al. 1993, Nandra et al. 1997, Turner et al. 1997). The X-ray emission mechanisms in Seyfert galaxies is probably related to the combination of processes in the corona of the accretion disk and absorption by intervening material (Parker et al. 2015, Uttley et al. 2005, and references therein).

IDV events observed in radio have two possible origins. Some of these events, in particular in centimeter and meter wavelengths, are due to the scintillation of radio waves originated by the turbulent interstellar medium of the Milky Way (e.g., Lovell et al. 2008, Rickett et al. 2001, Jauncey & Macquart 2001). In other cases, the IDV is intrinsic to the source. Examples of the latter were presented by Wagner et al. (1990), which observed a small sample of six BL Lac objects in radio and optical bands and found simultaneous microvariability in three of the sources. Also, Quirrenbach et al. 1991 showed for the first time a correlation in the IDV pattern of S5 0716+71 in optical and radio frequencies. The same BL Lac object was observed simultaneously in X-rays, optical and radio for a week by Gupta et al. (2012) and it was found that there was a delay of about one day in the variability at 2.8 cm and longer wavelengths, which suggests an intrinsic origin of the rapid variability.

7.1.2 Rapid variability in the optical

Optical IDV in a blazar was reported for the first time by Matthews & Sandage (1963). However the variations observed were not considered intrinsic to the source, but due to instrumental errors. Only with the advent of CCDs in the eighties, the optical microvariability of blazars was confirmed (e.g., Miller et al. 1989).

Many publications have been devoted to the study and characterization of the optical IDV of blazars. Heidt & Wagner (1996) and Heidt & Wagner (1998) studied the microvariability in two samples of radio-selected and X-ray selected BL Lacs, respectively. They found microvariability in the 82% of the complete sample of radio-selected BL Lacs with typical timescales between 0.5 and 3 days. In the X-ray selected sample, they observed microvariability in only 40% of the sources with amplitudes smaller than what was found in the radio-selected sample.

Often microvariability has larger amplitudes and are more frequent in the bluer filters (e.g. Nesci et al. 1998; Ghisellini et al. 1997; Bonning et al. 2012, Gaur et al. 2015a). Besides, the rises and decays are also faster at these frequencies (Papadakis et al. 2003). The amplitude of IDV may depend on the relative position of the filter of the observation and the frequency of the synchrotron peak of the SED (Giommi et al. 1999; Zhang 2010). The peak of the synchrotron hump can also shift its position and, therefore, the characteristics of the variability may also change.

Gaur et al. (2015a) reported that the microvariability amplitudes of BL Lac between 2010 and 2012 decreased when the source was brighter. This anticorrelation was explained by a two-component model, in which one of the components, responsible for slower variations, dominates the emission in the bright phases of the light curve.

Similar to the long-term variability (see Chapter 6), contradictory results were found in the analysis of the relationship between the flux and the color of the IDV. Many authors find a bluer-when-brighter behavior in the microvariability (Gaur et al. 2015a, Villata et al. 2002a, Raiteri et al. 2003), but the opposite behavior has been also observed in some cases (Ghosh et al. 2000; Ramírez et al. 2004).

The comparison of the color-flux behavior between intra-day and longer timescales has shown that in many cases, the correlation between the flux and color in IDV is stronger than in long-term flux variations. This is the case in S5 0716+71 as described by Ghisellini et al. (1997) and Raiteri et al. (2003). Also, Villata et al. (2002a), from an extensive campaign of optical observations, found that the spectral index of BL Lac is only mildly sensitive to the long-term flux variations, while it is strongly dependent on the short-term variations. A two-component model explains this behavior. The first component, responsible for the long-term variations has a weak color-flux correlation as is expected if it is due to changes in the jet Doppler factor. The second component is due to intrinsic processes related to the jet mechanism (see also Raiteri et al. 2013, Villata et al. 2004, Hu et al. 2006, Agarwal & Gupta 2015).

Several authors have studied the time lags between the optical bands. In many reports, no lags were found, due in part to the proximity of the frequencies of the different filters. For example, for S5+0716+71, Poon et al. (2009) reported time lags < 20 min between the B and I bands in observations obtained in 2008 and 2009. Also, Villata et al. (2000a) constrained the possible lag to < 10 min between the same bands from observations taken in 1999. Other authors detected some lags, although small. Papadakis et al. (2003) claimed the detection of a time lag in BL Lac, where the variations in the I filter were delayed by ~ 12 min with respect to the variations in the B band. Stalin et al. (2006) found indications that the V flux of S5 0716+71 leads that of the R band by 6 and 13 min on two different nights in 1996.

Optical microvariability has also been studied in non-blazar AGNs. Gupta & Joshi (2005) found IDV in two out seven radio quiet quasars, and evidence of microvariability in a third. The authors compared the IDV statistic of different types of AGNs: blazars may show microvariations up to 100%, other radio loud AGNs may have flux variations up to 50% while RQQs may show IDV up to a level of 10%. Ramírez et al. (2009), Goyal et al. (2013) and Kumar & Gopal-Krishna (2015) studied the incidence of microvariability in RQQs and compared it with other types of objects. They conclude that the duty cycle of IDV in RQQs is lower than in blazars or RQQs. Some authors explain the origin of IDV in RQQs as a weak blazar component (e.g., Czerny et al. 2008, Gupta & Joshi 2005), while other favor mechanisms related to the accretion disk (e.g., Joshi et al. 2012).

Several models have been proposed to explain the microvariability in blazars. Many of them are related to the relativistic jet because the timescales are shortened, and the amplitude of variations are enhanced by the relativistic Doppler beaming (e.g., Wagner & Witzel 1995). Microvariability may be related to processes intrinsic to the jet, such as the jet power: changes in the evolution of the energy spectrum or energy gains of the emitting particles. Shock-in-jet models have also been proposed, for which it is expected that the amplitudes of variability decrease toward longer wavelengths (Wagner & Witzel 1995), as has been observed by Fan & Lin (2000), Nesci et al. (1998) and others. Other models assume a turbulent magnetic field in the jet (Jones et al. 1985; Jones 1988), or the interaction of the relativistic shock with the inhomogeneous jet (Qian et al. 1991). Geometric changes can also lead to variability because the change of the viewing angle of the relativistic jet leads to variations in the Doppler factor (Gopal-Krishna & Wiita 1992).

Not related to the relativistic jet, there are models that explain the IDV due to instabilities and perturbations in the accretion disk (Mangalam & Wiita 1993, Fan et al. 2008). This processes may be important in RQQs, objects for which the relativistic jet is assumed not to be dominant. Also, external processes, as microlensing, have been proposed as the origin of microvariability (Gopal-Krishna & Subramanian 1991, Paczynski 1996)

In this chapter, we present the analysis of the microvariability in our sample. The light curve of several events of IDV are first introduced. Then we study the incidence of the microvariability and how the microvariability is related to the flux and color of the source. It is also shown the analysis of the possible time lags between different optical bands.

7.2 Analysis and Results

One of the primary goals of this thesis is to analyze and characterize the rapid variability in blazars. For this purpose, we observed some of the AGNs continuously for several hours on many different nights in order to detect and measure the variability on short timescales. Usually, during these nights we have observed more intensively in one (or two) of the optical filters, and more sparsely in the others. The series of observations were typically VBVRVIVB... (or VRBVRIVRB...), so that we could probe shorter timescales in the V (or V and R) filter, while also getting color information on longer timescales.

Figures 7.1-7.6 show different examples of IDV observed in the blazars 3C 66A, OJ 287, BL Lac, and 3C 454.3. The objects display a wide range of shapes of the light curves and amplitudes of variability. At some periods the AGNs are more active than at others. In some cases, the source showed only a linear increase or decay (for example, BL Lac on Oct. 13/14, 1997; Fig. 7.4), while in other cases flickering was observed (e.g., 3C 454.3 on Aug. 31/Sep. 1, 1998; Fig. 7.6). In the latter case, the color V-H also displayed variations, but these seemed to be not strongly correlated with the flux variations.

Blazars flared at several times with different amplitudes. During these flares, the object usually shows the characteristic bluer-when-brighter behavior. An example of this is BL Lac, which showed flares lasting for a few hours. Figure 7.3 displays a strong flare with an amplitude of ~ 0.6 mag in V, with a fast rise of 0.5 mag in ~ 1 hour at the start of the flare; then, some slower variations were observed and at the end of our time-series, the shallower decay of the flare started. The V-I color shows a clear anticorrelation between the color and the magnitude, being bluer when brighter. A similar flare in BL Lac, although with a smaller amplitude (0.17 mag. in V), was observed in Aug 28/29 1998 (Fig. 7.5). Unlike the flare in Fig. 7.3, the decay was slower than the rise in this case. The possible relation between the color and the magnitude is not as evident in the flare of Aug. 28/29 1998 due to the smaller amplitude of the variations.

More complex variations were observed on Aug. 1/2 1997 when BL Lac displayed a series of flares with a total amplitude of variability of 0.65 mag (Fig. 7.2). In this example, the most prominent feature of the light curve was a fast decay of 0.45 mag in only 27 minutes.

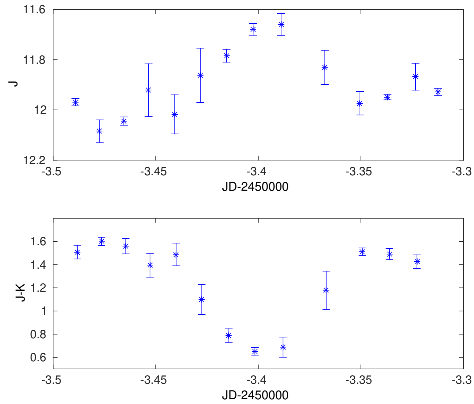

FIGURE 7.1— Short-term magnitude (J) and color (J-K) variations of 3C 66A in the night of Oct. 5/6 1995.

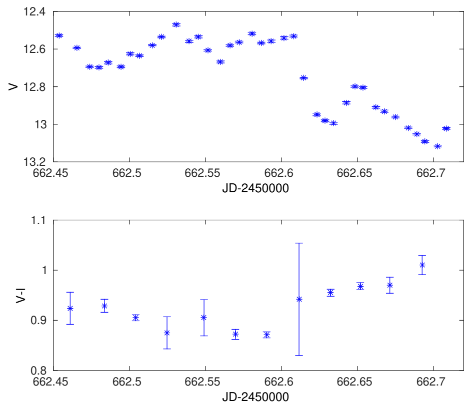

FIGURE 7.2— Short-term magnitude (V) and color (V-I) variations of BL Lac in the night of Aug. 1/2 1997.

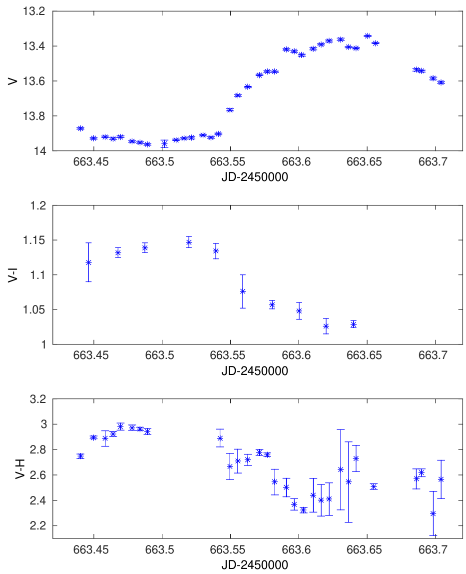

FIGURE 7.3— Short-term magnitude (V) and color (V-I and V-H) variations of BL Lac in the night of Aug. 2/3 1997.

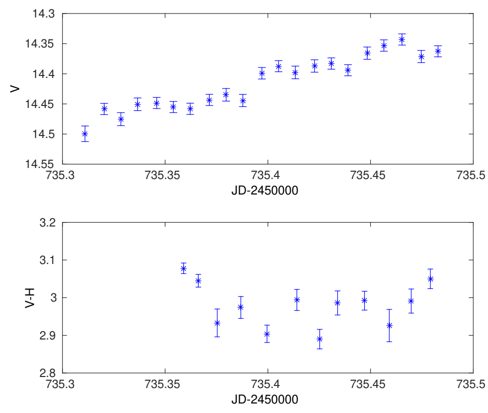

FIGURE 7.4— Short-term magnitude (V) and color (V-H) variations of BL Lac in the night of Oct. 13/14 1997

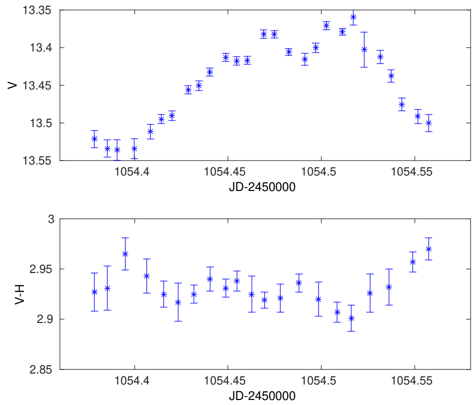

FIGURE 7.5— Short-term magnitude (V) and color variations of BL Lac in the night of Aug. 28/29 1998.

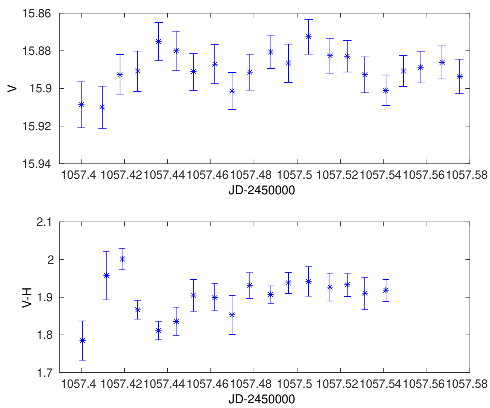

FIGURE 7.6— Short-term magnitude (V) and color (V-H) variations of 3C 454.3 in the night of Aug. 31/Sep. 1 1998.

The case of 3C 66A on Oct. 5/6 1995 is also noteworthy and the analysis of this night was presented in Kidger et al. (1996). In the optical and H filters, the object displayed low-amplitude variations ($\sim 10\%$). In the other two NIR filters, the behavior was peculiar. While in J the 3C 66A showed a flare in the middle of our time-series with an amplitude of ~ 0.4 mag, in the K filter, on the contrary, it dimmed with by ~ 0.6 mag. The evolution of the continuum spectrum shows first a flattening in H and K filters, and eventually, the spectrum was inverted for ~ 1 hour (see Kidger et al. 1996 for more details).

7.2.1 Detection of microvariability

We have applied a χ^2 test to test the presence of the microvariability in the light curves. The χ^2 is defined as (e.g., Agarwal & Gupta 2015, Gupta et al. 2017):

$$\chi^2 = \sum_{i=1}^{N} \frac{m_i - \overline{m}}{\sigma_i}, \tag{7.1}$$

where m_i are the individual magnitude measurements, σ_i their measurement error, and $\overline{m}$ is the average of the magnitudes during the night.

This test was applied to those nights when the length of the observations in a filter was longer than one hour, and the number of measurements, N, was at least 5. The χ^2 obtained for each night is then compared with the critical value $\chi^2_{\alpha,\nu}$ corresponding for a significance level of $\alpha = 0.01$ and $\nu = N - 1$ degrees of freedom. We consider that the source exhibits IDV in a night if $\chi^2 > \chi^2_{\alpha,\nu}$.

Essential for the application of this test is an accurate estimation of the individual errors of the measurements. As many authors have shown, the magnitude errors given by the package APPHOT in IRAF (and probably by other programs) underestimate the actual values (see, e.g., Gopal-Krishna et al. 1995, Garcia et al. 1999, Stalin et al. 2004, and references therein). One of the reasons may be that the routines do not consider the contribution of the calibration errors (e.g., flat fielding) in the error budget. Some authors multiply by a factor to the errors given by the programs to calculate the final measurement errors (e.g., Meng et al. 2017, Goyal et al. 2017). In our case, we extract the magnitude of all stars present in each frame. This information is used to estimate the actual measurement errors by quadratically adding a value to the errors given by IRAF. This procedure has been explained in more detail in Sect. 3.3.4.

Table 7.1 shows, for each object and filter, the number of nights with detected microvariability together with the total number of nights when the object was observed longer than one hour. There are significant differences between the objects. Even objects of the same type do not have the same rate detected microvariability.

The difference between filters arises from the fact that the object was observed more frequently in the V filter than in others and by the accuracy reached in the different filters. With our optical instruments, the best accuracy is obtained in R and the worst in B.

The source with the highest rate of IDV is BL Lac, for which microvariability was detected

TABLE 7.1— For each object and filter it is shown the total number of nights observed with $n_{dat} > 4$ and those with $P_{var} > 99\%$

Object	B	V	R	I	J	H	K
III Zw 2	-	0/1	0/2	-	-	-	1/1
I Zw 1	1/1	0/3	0/3	0/1	-	-	-
NAB 0205+02	0/2	0/4	0/4	0/2	-	-	-
3C 66A	4/21	15/50	8/33	3/21	6/19	10/19	7/20
AO 0235+16	1/3	2/6	3/5	2/3	2/6	5/7	2/9
PKS 0405-12	0/1	0/1	1/1	0/1	-	-	-
S5 0716+71	0/1	0/1	1/1	-	-	-	-
87GB 073840.5+545138	1/1	1/1	1/2	1/1	-	-	-
B2 0742+31	0/2	0/3	0/3	0/1	-	-	-
OJ 287	6/17	18/46	15/32	5/15	10/21	6/24	7/28
PG 1008+133	0/1	0/2	0/2	0/1	-	-	-
Mkn 205	0/2	0/8	1/7	0/2	-	-	-
3C 273	1/3	0/11	0/4	1/2	2/7	3/7	2/8
3C 279	0/1	0/3	0/2	0/1	1/3	0/4	1/3
PG 1351+640	0/4	0/7	0/7	0/4	-	-	-
PKS 1510-08	-	-	-	-	0/1	0/1	-
AP Lib	-	-	0/1	-	-	-	-
3C 345	0/3	2/14	1/13	1/2	6/10	5/10	1/9
Mkn 501	2/5	1/7	0/6	0/3	5/7	13/16	0/3
3C 351	0/1	0/7	1/7	0/1	-	-	-
II Zw 136	1/4	0/7	0/7	0/4	-	-	-
BL Lac	7/8	10/13	9/12	9/9	7/8	8/9	3/5
3C 454.3	0/5	1/5	3/8	1/5	2/4	4/4	1/4

in most of the nights. Also, OJ 287 and 3C 66A present IDV in many nights, although the detection rate in 3C 66A is much lower. Another object with a high rate of detection of IDV is AO 0235+164, although this source was observed not so often due to its faintness.

Generally, the objects with the highest detection rate are blazars, but we have also detected microvariability in RQQs. Two out of the three of these cases were detected in the filter B. Although this is not a significant result, it may be because the microvariability in RQQs is originated in the accretion disk, which has bluer colors than the synchrotron emission of the jet and the amplitudes of variability may be also higher in the bluer filters.

For the FSRQs in our sample, in particular, 3C 345 and 3C 454.3, the detection rate is higher in the NIR filters than in the optical filters, although the quality of the data is better in the optical. Also, 3C 273, which is sometimes considered an RLQ and sometimes an FSRQ, exhibits higher detection rates in the NIR. In FSRQs, the accretion disk and the relativistic jets are both dominant emitters in the optical and NIR frequencies. Since the synchrotron emission is redder than the thermal emission of the accretion disk, the dominance of the synchrotron emission is higher in the NIR bands. For this reason, if the IDV is originated in the relativistic jet, it is expected that the IDV is higher in the NIR bands where the synchrotron emission is less diluted by the accretion disk.

7.2.2 Measurement of the amplitude of microvariability: fractional variability parameter

The detection of microvariability does not give all information possible, because it depends on the precision of the measurements. In the case of a non-detection, it is of course not known whether the object does not show any variability at all, what is unlikely in these objects, or the precision of the measurements is not good enough to detect the existent variations. Therefore, it is more valuable and of more physical meaning to quantify the amplitude of the fluctuations.

We have calculated the F_{var} (see Eq. 5.1) in each filter for each night of observation with enough data. Almaini et al. (2000) pointed out that, because of the red noise nature of the variability, the F_{var} depends on the length of the observations in such a way that longer observations tend to have higher variability. We have corrected our results of the F_{var} using the following relation (Middei et al. 2016):

$$F_{var} \propto \Delta T^{\beta/2}, \tag{7.2}$$

where ΔT is the duration of the observation and β is the slope of the structure function of the flux variations (see Appendix. D). All F_{var} values were corrected to a common duration of the observation of 0.1 days.

In Table 7.2, we present the weighted average of the F_{var} for each object in the optical bands V and R, which are those with the most number of nights and detections. The last four lines show the weighted average of the different types of AGNs in our sample. Blazars (BL Lac objects and FSRQs) display the highest amplitude of IDV, typically around 2% (for a duration of the observation of 0.1d) while RLQs and RQQs show much lower amplitudes of microvariability, less

TABLE 7.2— For each object and filter, the table lists the total average of the nightly F_{var} with the number of nights in the filters V and R. The last four lines show the average for each type of object.

Object	$\langle F_{var}(V)\rangle$	n_V	$\langle F_{var}(R)\rangle$	n_R
III Zw 2	0.0000 –	1	0.0069±0.0035	2
I Zw 1	0.0079±0.0031	3	0.0057±0.0025	3
NAB 0205+02	0.0033±0.0014	4	0.0024±0.0007	4
3C 66A	0.0056±0.0007	50	0.0061±0.0013	33
AO 0235+16	0.0212±0.0073	6	0.0866±0.0386	5
PKS 0405-12	0.0049 –	1	0.0077 –	1
S5 0716+71	0.0204 –	1	0.0151 –	1
87GB 073840.5+545138	0.0285 –	1	0.0087±0.0043	2
B2 0742+31	0.0008±0.0004	3	0.0027±0.0013	3
OJ 287	0.0208±0.0054	46	0.0142±0.0019	32
PG 1008+133	0.0037±0.0007	2	0.0032±0.0007	2
Mkn 205	0.0045±0.0021	8	0.0033±0.0011	7
3C 273	0.0011±0.0003	11	0.0044±0.0015	4
3C 279	0.0031±0.0016	3	0.0000 –	2
PG 1351+640	0.0015±0.0007	7	0.0049±0.0021	7
AP Lib	– –	-	0.0000 –	1
3C 345	0.0277±0.0111	14	0.0181±0.0059	13
Mkn 501	0.0073±0.0036	7	0.0088±0.0029	6
3C 351	0.0044±0.0022	7	0.0080±0.0040	7
II Zw 136	0.0000 –	7	0.0000 –	7
BL Lac	0.0444±0.0114	13	0.0441±0.0111	12
3C 454.3	0.0086±0.0041	5	0.0226±0.0081	8
BLLacs	0.0203±0.0035	123	0.0279±0.0073	89
FSRQs	0.0228±0.0082	23	0.0185±0.0043	25
RLQs	0.0013±0.0004	23	0.0039±0.0009	17
RQQs	0.0043±0.0009	31	0.0053±0.0015	30

than 0.5%.

We have applied the Wilcoxon-Mann-Whitney U test for two samples (e.g., Wall & Jenkins 2003) to determine if the differences obtained between the object types are significant. This test is a non-parametric test to check if two samples have the same parent population. It is preferred to the χ^2 two-sample test because it does not require sample binning. Since it is a non-parametric test, it does not assume any type of distribution. We find that both BL Lac objects and FLRQs have significant larger IDV amplitudes than RLQs and RQQs (with a significance level of $p > 99\%$), while the differences between BL Lac objects and FLRQs, and between RLQs and RQQs are not found to be significant.

7.2.3 Duty cycle of microvariability

The duty cycle (DC) of microvariability, or the percentage of the time that the object shows microvariability, has also been used as a measurement of the IDV in AGNs. Some authors calculate the duty cycle for a sample of objects as the number of objects for which microvariability was detected divided by the total number of objects in the sample (e.g., Heidt & Wagner 1996, 1998).

Others authors use the procedure described in Romero et al. (1999): in order to correct for the different duration of the observations, the duty cycle (DC) is calculated as,

$$DC = 100\frac{\sum_{i=1}^{n} N_i(1/\Delta t_i)}{\sum_{i=1}^{n}(1/\Delta t_i)}\ \%, \tag{7.3}$$

where n is the number of nights, and the duration of the monitoring in each night i is Δt_i. N_i is set to 1 if the object was found to be variable in the night and 0 otherwise. In this way, the detection is weighted by the inverse of the duration of the light curve. This procedure has been used in many publications (e.g., Gaur et al. 2015a, Agarwal et al. 2016 and Xiong et al. 2017).

However, this procedure has several drawbacks. First, it does not consider that the light curves can have different detection levels of IDV. Also, to simply weight each detection with $1/\Delta t_i$ is not entirely correct because different sources may have different slopes of the power spectral density (PSD). Therefore, we used a different method to estimate the duty cycle of microvariability. Selecting a minimum threshold of microvariability 0.01, we define the duty cycle as,

$$DC = \frac{N(F_{var} \geq 0.01)}{N(det) + N(F_{var,upp} \leq 0.01)}. \tag{7.4}$$

DC is the number of nights when the source shows a level of IDV higher or equal than our threshold, $N(F_{var} \geq 0.01)$, divided by the sum of the number of nights with a detection of microvariability, $N(det)$, plus the number of nights with an upper limit of F_{var} lower or equal than our threshold, $N(F_{var,upp} \leq 0.01)$. In this way, the duty cycle defined by us gives the probability that a source exhibits IDV with a $F_{var} \geq 0.01$ for a duration of the monitoring of 0.1 days.

Apart from the duty cycle, we introduce the typical level of microvariability, $F_{var,50\%}$, to quantify IDV. This is defined so that the source display at least this level of IDV in 50% of the time (for a length of a time-series of 0.1 days).

To calculate the $F_{var,50\%}$, we first created the plots of the probability for a specific F_{var} shown in Fig. 7.7 and Fig. 7.8. For each night with detected microvariability ($F_{var,i}$), we calculated the probability that the source displayed at least this level of microvariability, as N_i/N_{tot}, where N_i is the number of nights with $F_{var} \geq F_{var,i}$ and N_{tot} is the total number of nights with detected F_{var} plus the number of nights whose upper limit of F_{var} is less than $F_{var,i}$. Fig. 7.7 shows the probability plots for our three best-monitored objects, 3C 66A, OJ 287 and BL Lac and Fig. 7.8 shows the probability plot for quasars (RQQ+RLQ) and blazars (FSRQ and BL Lac objects).

TABLE 7.3— Duty cycle (for a $F_{var} = 0.01$) and F_{var} in the R filter for a probability of 50% for different objects or groups of objects

Object(s)	Duty cycle	$F_{var,50\%}(R)$
3C 66A	0.16	0.005
OJ 287	0.50	0.011
BL Lac	0.90	0.029
BL Lac objects	0.43	0.008
FSRQs	0.31	0.009
blazars	0.41	0.008
RQQs+RLQs	0.03	-

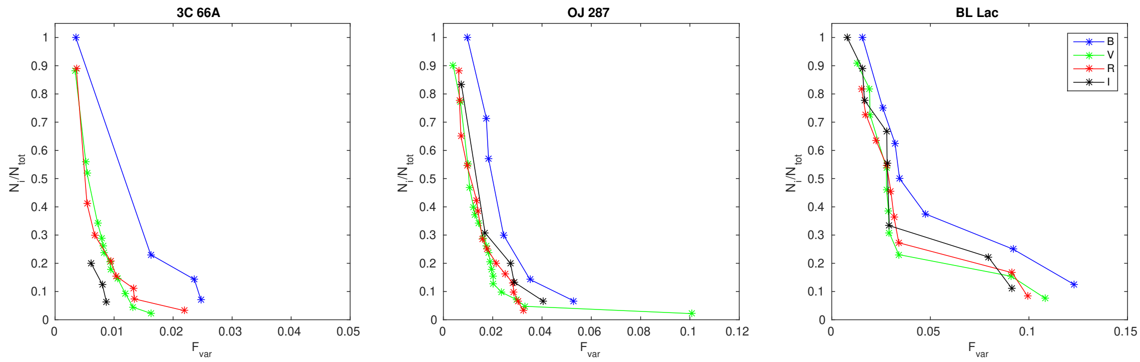

FIGURE 7.7— Probability that the microvariability of the sources 3C 66A, OJ 287 and BL Lac have a certain F_{var} in each optical bands.

Interpolating the N_i/N_{tot} vs F_{var} for a probability of 50% we obtain the $F_{var,50\%}$. These values, together with the duty cycles, are tabulated in Table 7.3 for our three best-observed objects, 3C 66A, OJ 287 and BL Lac, as well as for blazars (together and separated in BL Lac objects and FSRQs) and quasars (RQQ+RLQ).

BL Lac shows a very high duty cycle, close to 100%. 3C 66A, on the contrary, has a much smaller duty cycle, although it is also a BL Lac object. Unfortunately, the small number of detections in quasars does not allow us to calculate the duty cycle of RQQs and RLQ separately.

Although our method to calculate the duty cycle is different from other authors, we obtain similar results. Our result on BL Lac is one of the highest found in a blazar, identical to S5 0716+71 reported by Agarwal et al. (2016) (also $\sim$ 90%). However, Gaur et al. (2015a) found only a duty cycle of 44% in BL Lac in 38 nights between 2010 and 2012. For 3C 66A, different results are found in the literature: Kaur et al. (2017) reported a DC of 16% from observations of 89 nights between 2005 and 2016; Rani et al. (2011) found IDV in two from seven nights (28%); Gopal-Krishna et al. (2011) and Sagar et al. (2004) reported higher values, 47% and 85% respectively, but with a small number of nights.

Goyal et al. (2013) summarized the results obtained from an extensive program of observation with telescopes in India for 77 AGNs of different types. It is found that the DC of RQQs is 10% from 68 light curves. This value is higher than what was obtained from our sample of

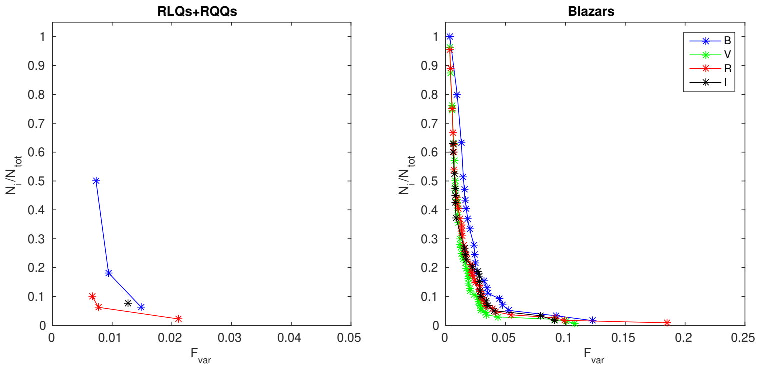

FIGURE 7.8— Probability that the microvariability of quasars (LPQ+QSO) and blazars have a certain F_{var} in each optical bands.

RQQs+RLQs, but consistent with our results, considering that our number of sources and light curves are relatively small. For blazars, they determined a duty cycle of $\sim 45\%$, comparable to what we found.

7.2.4 Comparison between microvariability and long-term variability

The amplitude of the microvariability, measured with the average of the F_{var} (table 7.2), is higher for the objects that exhibit higher long-term variability. Figure 7.9(a) shows how the weighted averages of the $F_{var,}$ of microvariability, $\langle F_{var,mic} \rangle$, relate to the fractional variability parameter of the long-term variability ($F_{var,tot}$) in the V filter—the values of $F_{var,tot}$ were presented and analyzed in Sect. 5.4. The accuracy of the data and the small size of the sample do not allow us to differentiate between the types of AGNs, apart from the fact that RQQs and RLQs show lower amplitudes of variability.

Figure. 7.9(b) shows the averaged F_{var} of microvariability against the average spectral index between the filters V and I from Chapter 5. It was found that the microvariability has larger amplitudes in redder objects. However, this is biased by the fact that the blazars have on average redder colors because its SED is dominated by the synchrotron emission of the jet and not by the accretion disk, as in normal quasars.

7.2.5 Wavelength dependence of the microvariability

AGNs exhibit larger amplitudes of long-term variability in the bluer filters. We observed the same behavior in the microvariability. For BL Lac, we show in Fig. 7.10 the ratio between the fractional variability parameters in each filter and V, $F_{var}(V)$, and how this ratio relates with $F_{var}(V)$. This ratio was calculated for those nights when there are measurements in the two filters. We do not find any evidence that the ratio of the F_{var} in different filters depends on the level of microvariability. The fractional variability parameter at higher frequencies is on average larger than at lower frequencies. Between V and H we have fewer measurements, and the dispersion is much larger.

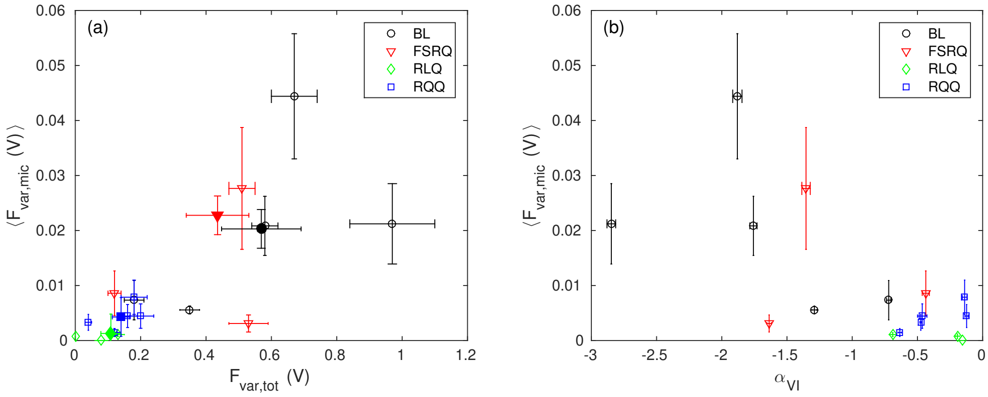

FIGURE 7.9— On the left, it is shown the fractional variability parameter of the IDV against the F_{var} on the long-term variability. On the right, it is displayed the relation of the F_{var} of the microvariability vs. the average spectral index.

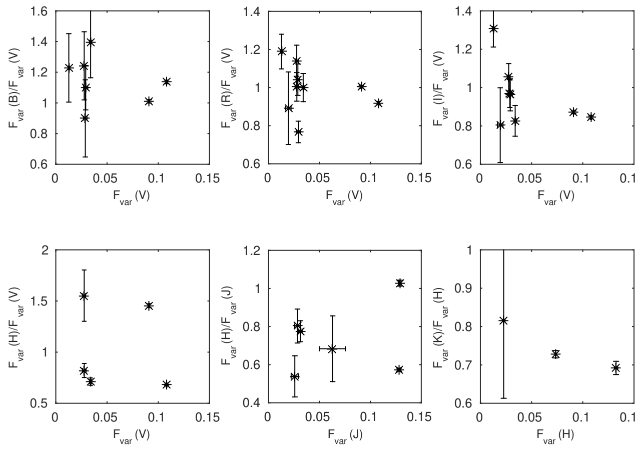

FIGURE 7.10— Ratio of the fractional variability parameters of two filters against the fractional variability parameter in V and J for BL Lac

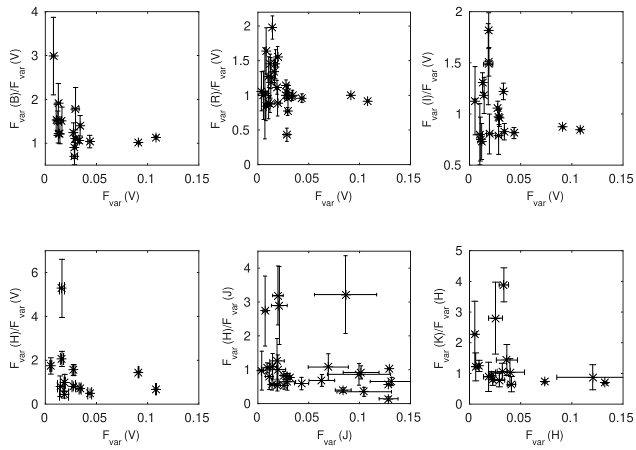

FIGURE 7.11— Ratio of the fractional variability parameters of two filters against the fractional variability parameter in Vand J for all objects

TABLE 7.4—

Filters	Ratio
B/V	1.17
R/V	1.00
I/V	0.87
H/V	0.82
H/J	0.79
K/H	0.89

We have estimated the typical ratio between the fractional variability parameters at different frequencies using the measurements of all blazars (Fig. 7.11). First, we removed those measurements with very large measurement errors and the outliers. After that, the median of the F_{var} ratios was calculated, and they are tabulated in table 7.4. It is found that the F_{var} of microvariability tends to be higher in the bluer filters. This effect has been usually found by other authors in BL Lac objects (e.g., Ghisellini et al. 1997; Bonning et al. 2012)

7.2.6 Relation of microvariability with the average flux and spectral index

How the amplitude of the microvariability is related to the average flux or spectral index gives hints about the process that are producing the IDV. Fig. 7.12-7.14, show the relation between the fractional variability parameter in the V filter with the nightly-averages of the flux and the spectral index for the best-observed objects, 3C 66A, OJ 287, and BL Lac, respectively. There is no apparent correlation with the flux or the spectral index.

In order to quantify this relation, we applied the Kendall's *Tau-b* correlation test, with the generalization for left censored data and with correction of ties (Feigelson & Babu 2012; Helsel

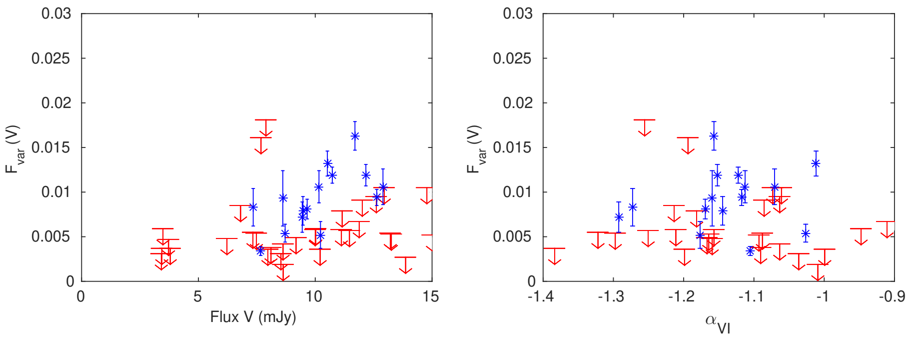

FIGURE 7.12— Left: IDV fractional variability parameter versus average flux in the V filter for 3C 66A. Right: fractional variability parameter of IDV versus spectral index for the same object. Blue asterisks represent the detections of IDV, and red arrows show the upper limits of F_{var} for nights without detection of microvariability.

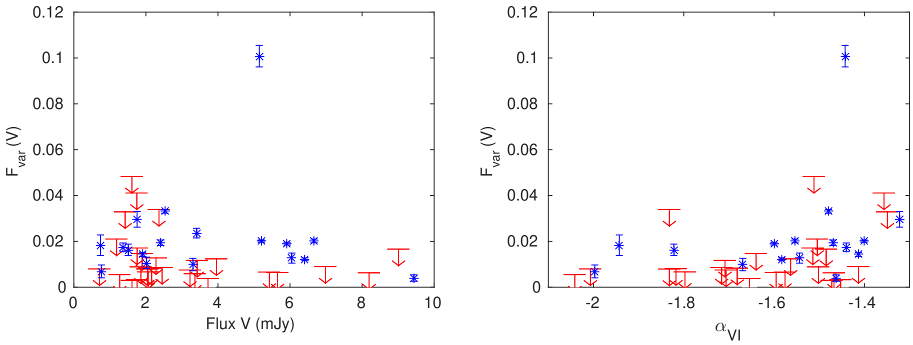

FIGURE 7.13— Left: IDV fractional variability parameter versus average flux in the V filter for OJ 287. Right: fractional variability parameter of IDV versus spectral index for the same object. Blue asterisks represent the detections of IDV, and red arrows show the upper limits of F_{var} for nights without detection of microvariability.

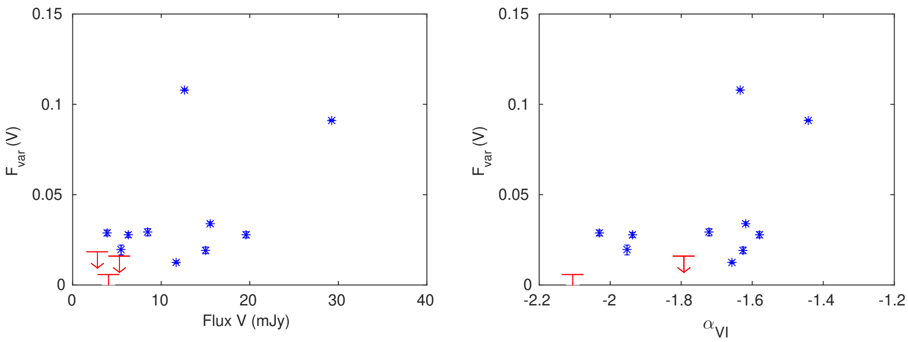

FIGURE 7.14— Left: IDV fractional variability parameter versus average flux in the V filter for BL Lac. Right: fractional variability parameter of IDV versus spectral index for the same object. Blue asterisks represent the detections of IDV, and red arrows show the upper limits of F_{var} for nights without detection of microvariability.

2011; Beal 2016).

The most significant correlation found is between the F_{var} and the flux in BL Lac with a $p > 95\%$ (Fig. 7.14). However, if the points with the highest microvariability are removed, no correlation is found. The data on 3C 66A seem to show a correlation between the fractional variability parameter of IDV and the flux, at least considering only the detected IDV: if we apply a Spearman rank correlation test to the data with detected IDV, we found that the correlation is significant to the $p > 99\%$ level. However, if one considers the non-detections and applies the generalized Kendall's $tau - b$ test, the significance of the correlations disappears. Therefore, our data do not support the claim that the F_{var} of microvariability is higher at higher flux levels. Also, no relation between the IDV and the spectral index was found.

If the value of F_{var} does not depend on the flux, it means that the amplitude of variability grows linearly with the average flux. This is the so-called rms-flux relation observed in X-rays in many radio-quiet AGNs and other accreting compact objects, such as X-ray binaries (Uttley et al. 2005, Heil et al. 2012, and references therein). If we now use only the numerator in the fractional variability parameter, i.e., the intrinsic standard deviation (see Eq. 5.1), as the measure of the IDV, we could test the hypothesis that the microvariability amplitude does not depend on the average flux. Applying again the Kendall's *Tau-b* correlation test, we obtain probability values of $p > 99.9\%$, 99% and 97% for BL Lac, OJ 287, and 3C 66A, respectively that the intrinsic standard deviation of microvariability is correlated with the average flux in the night.

7.2.7 Change rate and asymmetry of light curves

The concept timescale is ambiguous and often not well-defined. Sometimes, it refers to the length of the observations, as when we talk about intra-day variability. Several definitions exist; some use the breaks in the PSD or the structure function. Other consider the slopes of the structure function (e.g., Goyal et al. 2018, Dobrotka et al. 2017, Vovk & Neronov 2013).

One definition that is independent on the length of the observation and can be calculated directly from the light curve is the *doubling timescale* or, equivalently, the *e-folding timescale*, which is the time needed for the source to double its flux, or to increase it by a factor of e. From the change rate of the magnitude, we compute the e-folding timescale of flux variations as

$$\tau = \frac{1.086}{|dm/dt|}. \tag{7.5}$$

Note that positive change rates give decay timescales and negative rates, rise timescales.

In order to calculate the change rates, we divided the nightly light curves into intervals of five data points, with a maximum length of the interval of 0.2 days; the last interval of the night could have between five and nine points; we did not include in the analysis intervals with less than five points. Then, we calculated the change rate of each interval as the slope of the linear regression between the magnitude and the time of the observation. Intervals, for which the error of the change rate was larger than 0.2 mag/h were excluded. This method is similar to the one used by Montagni et al. (2006) or Hu et al. (2014). In the first of these publications the authors

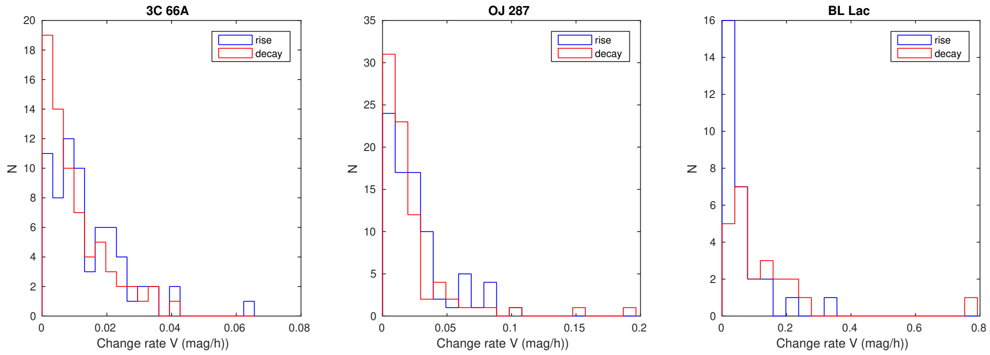

FIGURE 7.15— Distribution of the rises (blue line) and decays (red line) magnitude change rates of IDV variations in the V filter for 3C 66a, OJ 287 and BL Lac.

TABLE 7.5— Median values of the change rates (mag/h) of rises and decays.

	3C 66A	OJ 287	BL Lac
rises	0.011	0.020	0.028
decays	0.007	0.014	0.069

interactively select the intervals by dividing the light curve into a series of monotonic linear portions, while in the second publication, the intervals have a fixed length of about 25 minutes.

No relationship was found between the change rate and the flux in the light curve for any of the sources, although the number of data points does not allow us to give statistically significant results. Figure 7.15 displays the distribution of positive (decays) and negative (rises) change rates for the blazars 3C 66A, OJ 287, and BL Lac. The values are typically larger for BL Lac because this is the source with higher levels of microvariability. Although the sampling of the light curves cannot be considered complete, we can determine whether the light curves are asymmetric, i.e., whether the rises are faster or slower than decays. Asymmetry in the light curves provides hints about the variability mechanism operating in these objects (Montagni et al. 2006, Bachev et al. 2012).

The medians of the change rates of rises and decays obtained for these objects are listed in Table 7.5. To test if the distributions of rises and decays change rates have different underlying populations, we applied the Wilcoxon-Mann-Whitney U test, which examines if the two populations have different medians, and the two-sample Kolmogorov-Smirnov test, which evaluates the difference of the cumulative distribution functions of the distribution of the two samples. We found that none of the differences between the rises and decays are significant with $p > 0.99$, but all of them are significant to a level of $p > 0.95$, with the Wilcoxon-Mann-Whitney U test and $p > 0.90$, with the two-sample Kolmogorov-Smirnov test.

The fastest variability found was a decay at 0.79 ± 0.01 mag/h in BL Lac on Aug. 1/2 1997 (see Fig. 7.2). Even faster variability was reported by Zhang et al. (2012), with a decline of 0.9 mag/h in S5 0716+71 over a period of 6 minutes. Also, Chandra et al. (2011) informed about a change rate of 0.38 mag/h in March 2010 in the same object, and Sandrinelli et al. (2014) found an event of variability with a change rate of 0.43 mag/h in PKS 2155-304.

If we consider together the change rates of all blazars in our sample, we find there is $\sim 5\%$ probability of a change rate larger than 0.1 mag/h; Bachev et al. (2012) found a probability of $\sim 2\%$ for the same change rate in a sample of six blazars.

Although Montagni et al. (2006), Zhang et al. (2012), and Bhatta et al. (2013) found similar rising and declining rates, Bachev et al. (2012) and Hu et al. (2014) found significative differences in the distribution of change rates of rises and decays. Hu et al. (2014) reported that the increases are typically faster than the declines.

7.2.8 Time lag between different bands

We searched for lags between the different bands applying a cross-correlation analysis based on the Z-transformed discrete correlation function (ZDCF; Alexander 1997). ZDCF is a variant of the discrete correlation function (DCF) described in Edelson & Krolik (1988). The DCF estimates the correlation function of discrete unevenly sampled time series. The DCF uses all points available and does not introduce interpolation artifacts. The ZDCF uses the Fisher's Z-transform and equal-population binning to correct for several biases of the DCF introduced by sparse unevenly sampled time series (Alexander 2013). The number of data pairs in each binning is at least 11, which is the minimum number required for the convergence of the Z-transform (Alexander 1997).

We calculated the time lag between the light curves with the centroid of the peak of the ZDCF. For the estimation of the centroid, we use only those points of the ZDCF with correlation coefficients larger than 80% of the maximum of the ZDCF, as recommended by Peterson et al. (2004). The estimation of the lag error was performed with the flux-randomization/random-subset-selection (FR/RSS) approach described in Peterson et al. (1998, 2004). We performed 1000 realizations of the light curve as follows. For each realization, the flux was randomized according to the Gaussian distribution of the photometric errors (FR). Then, a randomly chosen subset of the realization (RSS) was selected, excluding redundant data points. Then, the time lag was calculated and the statistics of the time lags gives our estimate of the error.

We calculated the ZDCF of the light curves of several consecutive days to increase the sensitivity for the detection of time lags if maxima or minima appear in the light curve of the different nights. The data of each night and filter were subtracted from their average, to filter out the slow variations. This detrending of the time series has been proposed in the analysis of time delays by Peterson et al. (2004) to increase the accuracy.

We have not detected any significant time lag between the optical/NIR filters in our data of BL Lac, OJ 287 or 3C 66A. Figures 7.16 and 7.17 show the light curves in the V and I filters of BL Lac on several nights in August and October 1997, respectively (top panels), and the ZDCF between the data in both filters (bottom panels). The time lags found for the two datasets are 4 ± 7 min for the two nights in August 1997 and 10 ± 7 min for the three nights in October of the same year, in both cases consistent with no delay. This result is also consistent with what other authors have found in blazars. Most of the studies did not detect any delay between the optical bands (e.g., Hao et al. 2010; Carini et al. 2011; Zhang et al. 2016; Agarwal & Gupta

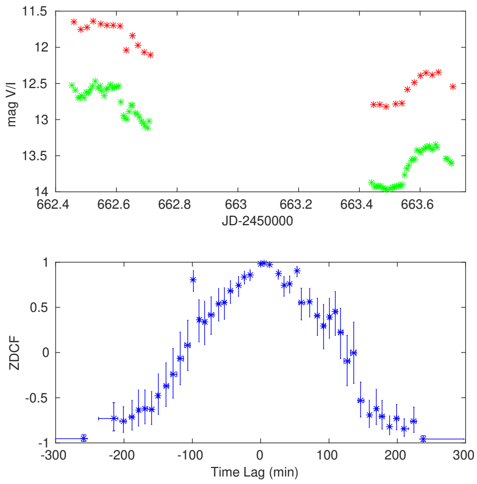

FIGURE 7.16— Top panel: light curves of BL Lac in the V (green) and I (red) filters on Aug. 1997. Botton panel: ZDCF plots between V and I for the light curves displayed in the top panel. A positive lag means that V is leading.

2015; Bachev et al. 2017). This non-detection of the lag is explained because the different optical bands are close to each other. However, several publications report the detection of time lags between the optical bands in blazars, although the possible lags appear only in few nights.

In BL Lac, Papadakis et al. (2003) found that the variations in the I band were delayed with respect to the B fluxes by 13 min. Wu et al. (2012) claimed the detection of a delay of 30 min between B and R. However, that detection, at the 3σ level, occurs in a night with small variations, while in other nights with larger variability, no time lag was detected. Possible detection of a delay of $\sim$ 11 min in one night in S5 0716+71 was presented by Poon et al. (2009), although no proper errors were given. Finally, Meng et al. (2017) found a possible delay in BL Lac of $\sim$ 10 min in one night between the filters V and R.

In other frequency ranges, delays have been oft found. For instance, Urry et al. (1997) observed an X-ray flare in PKS 2155-304 that was followed by broader and lower amplitude flares in the extreme-UV and UV, one and two days later, respectively. In Mrk 421, Takahashi et al. (1996) detected a flare in X-rays following the onset of a TeV flare. The authors report that the soft X-ray lags behind the hard X-rays by 1 hr. Also, a soft lag of $\sim$ 1000 s was detected in the same object with XMM-Newton in 2007 (Zhang 2010).

7.2.9 Temporal characterization of the color-flux relation

We investigated how the color variations are related to the flux variations on short timescales in a way similar to our analysis of the long-term variability presented in Sect. 6.6 and 6.7. We computed the SVP (Eq. 6.3; Trèvese & Vagnetti 2002) of several sources using the nightly averages of the light curves and also the whole database. The SVP was averaged on timescales from 1 to 12 hours, and from 0.5 to 5 days, using the original dataset. With the nightly-average

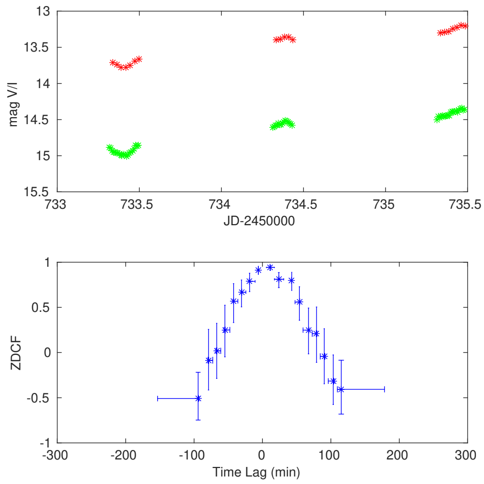

FIGURE 7.17— Top panel: light curves of BL Lac in the V (green) and I (red) filters on Oct. 1997. Botton panel: ZDCF plots between V and I for the light curves displayed in the top panel. A positive lag means that V is leading.

fluxes, we have computed the SVP on different timescales between 0.5 days and 5 years. Between 12 hours and 5 days, we have estimated the SVP using both datasets, the nightly averages and the complete dataset, which allowed us to check for differences produced by the sampling.

Figure 7.18 shows the dependence of the SVP with the timescale for six blazars. In every object, there is a local maximum at timescales of several months. The maximum is located at $\sim$ 5 months in 3C 66A, AO 0235+164, OJ 287, and BL Lac; at $\sim$ 1 year in 3C 279; and $\sim$ 2 months in 3C 345. The SVP at the maximum is always positive, which means that the object is bluer when it is brighter.

On intra-day timescales, the SVP of AO 0235+164 and BL Lac is higher than on longer timescales. These are the blazars with the stronger IDV in our sample (see Table 7.2). In these two objects, the bluer-when-brighter behavior (BWB) is stronger on intra-day timescales. In the other objects, the measurement errors do not allow reaching a definitive conclusion, although there is some evidence for the IDV of OJ 287 exhibiting a redder-when-brighter behavior.

Villata et al. (2004) analyzed an extensive collection of optical photometric data on BL Lac from 1994 to 2002. They found that the fast variability is strongly-chromatic, while the long-term variability is only "mildly-chromatic". This behavior was explained in terms of two components, one responsible for the long-term variability with a shallow color dependence and another one that origines the IDV, with a strong BWB behavior.

7.3 Discussion and conclusions

Intra-day variability is a common feature of blazars (e.g., Wagner & Witzel 1995 and references therein). We have used data from our sample of AGNs to compare the rapid variability

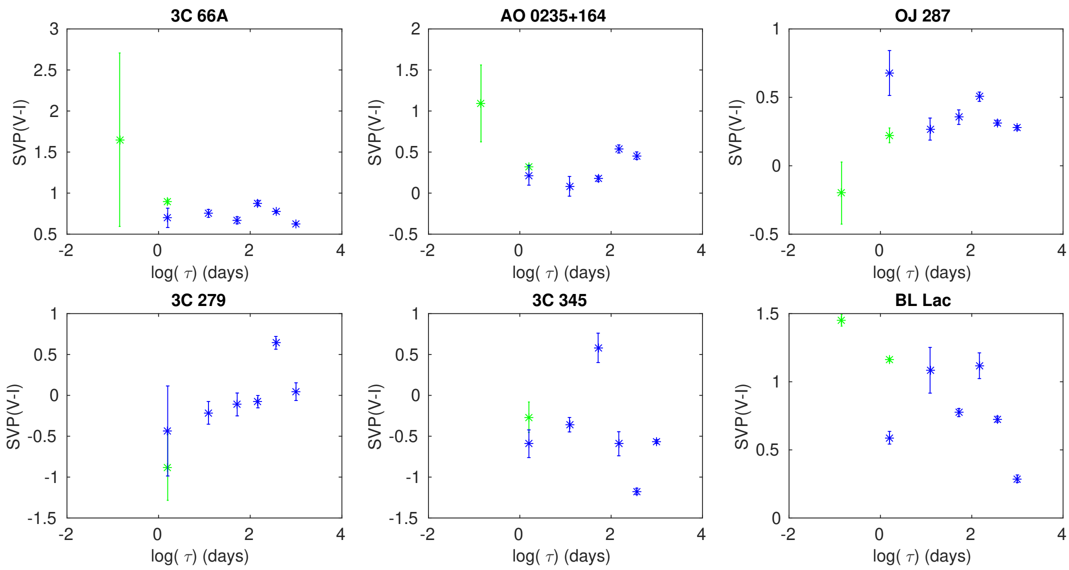

FIGURE 7.18— Spectral variability parameter of the color V-I at different timescales from hours to 5 years for six blazars in our sample. Blue points were calculated using the nightly average data and gree points using the whole dataset.

properties between different types of objects and to characterize their IDV. We have detected microvariability in most objects belonging to all the types present in our sample, including radio-loud and radio-quiet quasars.

The duty cycle, the fraction of time that an object exhibits microvariability, depends strongly on the object type. Romero et al. (1999) defined the duty cycle taking into account whether the IDV was detected or not and the length of the observations. Many authors follow this definition (e.g., Goyal et al. 2013; Gaur et al. 2015a). However, this definition does not consider the possible differences in the detection level between the nights, i.e., the fact that photometric accuracy and the number of measurements differ from night to night. We have introduced a new definition of the duty cycle that accounts for these differences. Our definition (given in Eq. 7.4) uses the fractional variability parameter of each night, corrected to a common duration of the nightly time series and considers the number of nights with detected variability, their amplitudes, and the upper limit of the amplitudes for the nights without a detection.

The three BL Lac objects with the highest number of observations exhibited very different duty cycles. BL Lac showed microvariability most of the nights (DC=0.90), while the duty of OJ 287 was 0.5, and the duty cycle of 3C 66A was much lower, 0.16. Kaur et al. (2017) found that 3C 66A showed IDV in 8% of 76 nights with observations between 2005 and 2006; other authors (e.g., Sagar et al. 2004; Rani et al. 2011) found higher values of the duty cycle for this source, but with a much lower number of nights. For OJ 287, Gupta et al. (2017) found microvariability in six out of ten nights. BL Lac, together with S5 0716+71, is one of the objects with more studies devoted to its microvariability. One of the reasons for this is that both are very active and displays variations in many nights. BL Lac has some periods with higher activity than others: while we obtained a duty cycle of 90% from our observations between 1986 and 1998, Gaur et al. (2015a) found a duty cycle of 44% between 2010 and 2012 and the same group reported only a 12% of nights with microvariability between 2014 and 2016 (Gaur et al. 2017).

The difference between these three objects tells us that some BL Lac objects are more active than others. Heidt & Wagner (1996) and Gopal-Krishna et al. (2011) found that the duty cycle of LBLs is around 60-70%. On the other hand, the duty cycle of HBLs has been found to be between 30% and 50% (Romero et al. 2002; Gopal-Krishna et al. 2011). This difference and observations of rapid variability in X-rays with XMM-Newton lead Gupta et al. (2016) to claim that the wavelength of the synchrotron peak of the SED has strong importance in the detection of IDV, which is more common at frequencies close to and just above the peak.

The synchrotron peak of OJ 287 and BL Lac lies in the IR (around 4×10^{13} Hz) and the UV for 3C 66A (around 10^{15} Hz; Ackermann et al. 2015). This may be one of the reasons why the amplitude of microvariability in 3C 66A is lower than in OJ 287 or BL Lac. Averaging the data of all objects, the IDV is larger in the bluer bands (see Table 7.4). This average uses mostly data from BL Lac and OJ 287 due to the higher number of detections and because the amplitudes are larger in these two objects. Therefore, the amplitude of IDV grows with the frequency at least until frequencies one order of magnitude larger than the synchrotron peak. The electrons responsible for the synchrotron emission at higher frequencies cool faster (from Eq. 1.9), which means that the variations at higher frequencies are faster and of higher amplitude. This remains true at least up to frequencies corresponding to the maximal energy of the electron distribution.

We found that the amplitude of microvariability, measured with the intrinsic standard deviation, is correlated with the nightly average flux. This implies that the object is more variable in flux when it is brighter. This is similar to the rms-flux relation observed in X-rays and the optical in many types of accreting objects, such as X-ray binary systems, or radio-quiet quasars (Uttley et al. 2005; Heil et al. 2012; Scaringi et al. 2012 and references therein). In these objects, the short-term root-mean-square (rms) variability amplitude and the flux measured on longer timescales are linearly correlated.

An important characteristic of the rms-flux relation is that it occurs at all observed timescales (Uttley et al. 2005). This means that, for example, this relation is seen when the rms is measured in short segments of 1 s and the flux in 10 s, and also when the rms is measured in segments of 10 s and the flux in intervals of minutes. Therefore, the rms-flux relation in these objects cannot be explained by a model that invokes a simple modulation of the short-term variations by a single slower process. As pointed out by Uttley et al. (2017), this simple model could not produce the broad timescale dependence of the rms-flux relation. One model that explains the rms-flux relation was discussed by Lyubarskii (1997) and Vaughan & Uttley (2008). In this model, fluctuations in the accretion rate are originated at all radii in the disk and propagate inwards. In the inner region of the disk, where the X-ray emission is produced, the accretion rate is the product of all fluctuations propagating from all radii. In this way, long-term fluctuations are originated in the outer regions and propagate inwards modulating the more rapid fluctuations that are generated in the inner radii.

This effect has been less studied in blazars. Studies using ground-based telescopes have yielded inconclusive reports. No correlation between the amplitude of microvariability and the flux was found in CTA 102 (Bachev et al. 2017), in S5 0716+71 (Mocanu & Marcu 2012), or in OJ 287 (González-Pérez et al. 1996). Gaur et al. (2015a) found that the amplitude of variability of BL Lac is lower when the object is brighter. However, this study did not correct the time series of the nights for the different durations of the observations. The analysis of the best time series in the optical was performed by Edelson et al. (2013) and Mohan et al. (2016) using the well-sampled light curve of the blazar W2R 1926+42 taken by the Kepler telescope. They reported a clear linear correlation rms-flux, although there could be a deviation from linearity at higher brightness. In blazars, this behavior has been explained using the "minijet-in-a-jet" model of Biteau & Giebels (2012). In this model, smaller regions within the relativistic jet, are boosted with random orientations in the rest frame. The effective relativistic Lorentz factor of these regions (minijet) is then proportional to the product of the Lorentz factor of both the jet and the minijet, and the flux of a single minijet is proportional to its rms.

Analysing the magnitude change rate on short timescales, we found that there evidence that the light curves of 3C 66A, OJ 287, and BL Lac are asymmetric. The rises are faster than the declines in 3C 66A and OJ 287, while the opposite is true in BL Lac. Hu et al. (2014) reported that the rises in the rapid variations of S5 0716+71 are faster than the declines, although other authors found no difference between the rises and decays timescales (Montagni et al. 2006; Zhang et al. 2012; Bhatta et al. 2013).

In the standard model of variability in blazars (e.g., Marscher & Gear 1985), the rises are governed by the mechanism that accelerates or injects the high-energy electrons, which is poorly known; the decays are related to the radiative cooling of the electrons (see Eq. 1.9). Therefore, some asymmetry in the light curves is expected. However, since the emitting regions have a finite size, the light travel time effects may dilute the asymmetry of the light curve. In this case, the rises and decays timescales are not governed by the physics of acceleration and cooling of the electrons but by the geometry of the emitting region. In the model of the helical jet (e.g., Villata et al. 2004; Raiteri et al. 2017), it is expected that the light curve is symmetric; in this model, the variations are produced by a change of viewing angle of the jet that yields to a change in the Doppler beaming.

Using the cross-correlation, we found no significant time lags between the different bands; if a delay between the variations in the V and the I filter exists, it is shorter than 20 min. This result is in agreement with observations by other authors: some authors find a detection of a delay between the optical bands of ~ 10 min (Papadakis et al. (2003); Poon et al. (2009); Meng et al. (2017)).

From the delay between different bands, it is possible to estimate the magnetic field in the emitting region. Assuming that the emission of the two bands is dominated by synchrotron emission and that the time delay is caused by synchrotron cooling of the high energy electrons, the time lag, Δt, in hours is (Böttcher 2007; Bachev et al. 2017):

$$\Delta t \simeq 5B^{-3/2}\delta_{10}^{-1/2}\left(1+\frac{u_{ph}}{u_B}\right)^{-1}\left(\sqrt{\lambda_{2,5000}}-\sqrt{\lambda_{1,5000}}\right) \tag{7.6}$$

where B is the magnetic field in gauss, $\delta_{10}=\delta/10$, δ is the Doppler factor, u_{ph} and u_B are the photon and magnetic field energies, respectively, and $\lambda_{1,5000}$ and $\lambda_{2,5000}$ are central wavelength of the two bands in units of 5000Å. For BL Lac, using $\delta = 7$ (Hovatta et al. 2009), we found that the magnetic field should be $B \gtrsim 2.5$ G to be consistent with our upper limit of the lag.

Alternatively, the magnetic field in the emitting region can also be estimated from a strong decay in the light curve, like the one in BL Lac on Aug. 1/2 1997 (Fig. 7.2). The halving-timescale for this event is ~ 1 h. If this decay is produced by synchrotron cooling of the electrons, then Eq. 1.9 applies. In the case of synchrotron emission, it can be considered that an electron with a Lorentz factor γ emits most of its power at the observed frequency (e.g., Pandey et al. 2017; Paliya et al. 2015):

$$\nu \simeq 4.2 \times 10^6 \frac{\delta}{1+z} B\gamma^2, \tag{7.7}$$

where z is the redshift. Combining this equation with Eq. 1.9, the magnetic field of the emitting region is:

$$B \simeq 1.4 \times 10^8 t_{cool}^{-2/3} (1+z)^{1/3} \delta^{-1/3} \nu^{-1/3} \text{ G} \tag{7.8}$$

where t_{cool} is the cooling time in seconds. Applying this equation, we obtain $B \simeq 3.9$ G. Note, that this value is a lower limit because the observed decay time has to be larger than or equal to the synchrotron cooling time t_{cool}. This value is larger than values reported for this object by other authors, which range between 0.3 and 2.5 G (e.g., Gaur et al. 2018; Baring et al. 2017; Yan et al. 2014; Potter & Cotter 2012), but not atypical in blazars (e.g., Celotti & Ghisellini 2008)

We studied the temporal evolution of the SVP in Sect. 7.2.9. In BL Lac, and probably also in AO 0235+16, the SVP is higher on IDV timescales than on longer timescales, which implies that IDV shows a stronger BWB behavior. The same behavior was found in BL Lac by Villata et al. (2004). They explained this behavior with a two-component model, in which one component is responsible for the rapid variations and is strongly chromatic, while the other, responsible for the long-term variations, is only "mildly-chromatic".

Here we propose an alternative explanation for this observed behavior. The variability of blazars may be dictated by an inhomogeneous model, like the turbulent, extreme multi-zone model (Marscher 2014) or the "minijet-in-a-jet" model (Biteau & Giebels 2012). In this model, the jet can be divided into many cells with different physical conditions and the flares produced by the individual cells are strongly chromatic. When one of the cells dominates the emission, the BWB behavior is stronger. This is the case in IDV flares like those shown in Figs. 7.2 and 7.3. On longer timescales, several regions, with different onset times, may all substantially contribute to the emission and the chromatism is diluted. This explanation is supported by the fact that the relation between the spectral index and the flux in 3C 66A and OJ 287 is more significant when some prominent outbursts are considered individually. In these cases, the outburst may be regulated by a single emission region. Also, the plots of the temporal dependence of the SVP (Fig. 7.18) show a maximum at timescales of a few months. If this feature is real and not an effect of the sampling, it may reflect the influence of individual prominent outbursts in the chromatism, whose typical duration is a few months.

8

Conclusions

The main purpose of this work has been to investigate the variability of blazars and other AGNs, with special emphasis on the rapid variability of blazars (timescales ranging from hours to a few days). To this aim, we have carried out for 14 years an extensive optical/NIR observing program, the Canary Islands Blazar Monitoring Program. The sample consists of 25 objects (15 blazars and other 10 quasars), which guaranteed a good light curve coverage for all of them. Photometric data were taken for a total of 393 observing nights. The 25 AGNs were observed in at least four optical bands ($BVRI$), while for 11 out the 14 blazars also NIR (JHK) observations were collected. Additional polarimetric observations were done for 7 blazars. Because my goal was to measure short-term variability in blazars (with amplitudes of a few tenths of a magnitude or less), the photometry had to be extremely precise. This demanded a very careful data reduction and the introduction of improved photometric techniques.

From my work, the following results and conclusions can be highlighted:

- I have developed a new algorithm to extract the brightness of the source by using a variable number of stars for comparison. This method is superior to other approaches because: i) it can be used with images taken at different photometric conditions, ii) it can be also applied in those cases when not all comparison stars are in the field. This approach can then be used for photometry of the same object in different telescopes.

  Using this *ensemble-based differential photometry* method, I reached a precision of ≈0.5% for stars of magnitudes 15—this is an improvement of up to 40% with respect to standard methods.

- Some AGNs in the sample are hosted by a prominent galaxy. The presence of the host galaxy affects the photometry in two ways: on the one hand, it dilutes the intrinsic variations of the AGN because the contribution of the brightness of the host galaxy can be substantial (up to 70% of the light); on the other hand, the host galaxy is not a point source and seeing fluctuations produce spurious variations in the aparent photometry. I have developed a technique for accurate photometry of these AGNs. The method assumes that the AGN has two components: a point source and an extended host. The surface brightness profile of the host galaxy was fitted by a Sersic function using the 2D fitting algorithm GALFIT. As a result, I provided a correction factor for the photometry of eight objects in up to seven filters for different observing conditions that can be used by other observers.

- To investigate the long-term variability properties of the AGNs, I built light curves, color curves and produced plots of the temporal evolution of the polarization. From the light curves, I derived average magnitudes, colors and spectral energy distributions, and discussed these results in the framework of current theoretical models. I listed the mean polarization and polarization angle. I quantified the AGNs variability through the fractional variability parameter and found that blazars show stronger variations than other types of quasars. I searched for correlations between the redshift, luminosity, spectral index, mean polarization, and the fractional variability parameter. I found a remarkable correlation between spectral index and the fractional variability parameter, particularly significant for BL Lac objects: redder BL Lac objects display stronger variability.

- I analyzed the color long-term variability of the AGNs in our sample and the relation of the color with the flux of the sources. The spectrum of the variable source was extracted applying the method by Hagen-Thorn & Marchenko (1989), and I found that the variable component is bluer than the observed spectrum in all objects, except FSRQs. The spectral indices of the observed spectrum of BL Lac objects and FSRQs are different but the spectrum of their variable component are similar. I found that most objects in the sample become bluer when brighter. The only exception are FSRQs, whose behavior is explained by a two-component model: the constant blue accretion disk dominates the emission at a lower state, while the variable red relativistic jet dominates the emission at a higher state. In 3C 66A and OJ 287, the best-studied objects in this thesis, I found that the relationship between the flux and the spectral index is notably more significant when some of the outbursts are considered individually. I computed the spectral variability parameter (SVP) and found that different object types have different locations in the SVP vs. spectral index diagram. The different locations in this diagram are interpreted in terms of simple models of variability: the variability of RQQs and RLQs is better explained with hot spots in the accretion disk; for BL Lac objects, the best model is a synchrotron flare; and for FSRQs, a combination of a typical constant quasar spectrum and a synchrotron flare.

- I characterized the microvariability of blazars by means of the duty cycle and the fractional variability parameter, and compared it with other types of quasars. To do that, I introduced a new definition of the duty cycle that considers both the length of the observations and the different detection level of the variability arising from different observing conditions. The time lags between the rapid variability of different optical bands in BL Lac are less than 20 min. The microvariability amplitude of the best studied objects, 3C 66A, OJ 287, and BL Lac, is correlated with the average flux. This relation is similar to the rms-flux relation found in the X-rays variations of many accreting objects. Assuming that the variability is produced by synchrotron processes, I estimated the magnetic field in the jet of BL Lac to be ~ 4 G. In the sources with the largest microvariability, the intra-day variations are more chromatic than variations on longer timescales. I proposed a model that explains these findings: an inhomogeneous jet, in which the different sub-regions of the jet produce a chromatic flare with different onset times.

8.1 Outlook

I have learnt from this work that, in order to maximize the scientific output of future observations, the observational strategy should be redefined. Since the variations between the different optical bands are strongly correlated, the monitoring should be carried out in only a pair of well-separated filters (e.g., V and I, B and I) for as many hours in each night as possible. In this way, the monitoring rate increases and the measurements of microvariability and color changes is maximized. Additionally, the delays of the flux variations between bands can be determined with higher accuracy. Because changes of the curvature in the spectrum are very rare or of a very low level, more than two filters do not increase the amount of information obtained from the data.

The microvariability of RQQs has not been precisely charaterized until now—mainly due to its low amplitude. The microvariability of blazars is generally believed to be originated by the relativistic jet. However, there is not a general concensus about the origin of the rapid variability in RQQs. Some authors claim that it comes from small perturbations in the accretion disk, while others favor the precense of a low-luminosity jet. Hence, high-precision data in more than one filter are required to constraints the models of microvariability of these objects.

The linear correlation between the amplitude of microvariability and the average flux has been determined only in a few individual blazars. In accreting objects, another type of sources, this is a well-known relation that has been observed at all timescales, and is particularly informative on the origin of the variability. It would be of the much interest to confirm this behavior also in blazars. This program can be already pursued using the existing large database of well-sampled light curves of blazars, like Yale / SMARTS optical/NIR monitoring of Fermi blazars (Sect. A.2).

A

Other monitoring programs in the optical

Here we will describe some of the monitoring programs of variability in the optical (and NIR) that are currently operating or have operated in the past. It is by no means a complete list of programs but intends to focus on the most important related to this work.

A.1 Hamburg Quasar Monitoring program (HQM)

The main goal of this program was the search for indications of microlensing in a sample of ~ 100 quasars. To this end, CCD photometry was taken with the MPIA 1.2m telescope at the Calar Alto observatory in the filters BVR of the Johnson system between 1988 and 1993. The results were published in Borgeest & Schramm (1994) and Schramm et al. (1994a,b)

A.2 Yale / SMARTS optical/NIR monitoring of Fermi blazars

SMARTS (small & moderate aperture research telescope system) is a set of four 1m class telescopes located on the Cerro Tololo Inter-American Observatory, Chile. An overview of the SMARTS can be found in Subasavage et al. (2010). It contains two telescopes with a CCD as instrumentation (0.4 m and 1.0 m), one telescope of 1.3 m diameter with a dual channel imager in the optical and NIR (Andicam), which is the one mostly used by this monitoring program, and a 1.5 m telescope with a high-resolution spectrograph.

The primary goal is the photometric monitoring of a subset of the Fermi-LAT monitored blazars to search for correlations and delays between the γ-ray and optical brightness. The observations started in 2008 and continued until the present. This monitoring program does not search for microvariability (variability on timescales shorter than ~ 1 day).

For example, Chatterjee et al. (2013) reported the detection of three optical flares in PKS 0208-512. Two of them were also observed at GeV energies with Fermi-LAT, while the third did not have a γ-ray counterpart. This was explained by the fact that in the last flare, there was only a change of the magnetic field, while the total number of emitting electrons or the Doppler factor remained constant. Alternatively, the locations of the flares were different.

In a sample of 12 blazars, Bonning et al. (2012) found a good correlation between the optical and NIR fluxes. In FSRQs, the variability amplitudes increase toward the NIR wavelengths. This is consistent with the presence of a constant (or slowing variable) accretion disk, which has a luminosity similar to the more variable (and redder) jet.

A.3 Institute of Astronomy of the Bulgarian Academy of Science

Here some telescopes of Bulgarian observatories were used to monitor several blazars, in particular, the 60cm telescope in the Belogradchik Observatory, the 50/70cm Schmidt Telescope and the 2m RCC reflector in the Rozhen National Observatory and the 30cm Ritchey Chretien Astrograph of the Irida Observatory.

They are centered in the study of microvariability of a small group of blazars, e.g., CTA 102 (Bachev et al. 2017) or S4 0954+65 (Bachev 2015, Bachev et al. 2016).

A.4 Aryabhatta Research Institute of Observational Sciences (ARIES)

Researchers of the ARIES uses several 1m class telescopes in Nainital, India. They also have collaborations with the group at the Bulgarian Academy of Science (e.g., Gopal-Krishna & Wiita 2018, and references therein).

Their research is centered in the systematic characterization of the microvariability of AGNs of all types (including RQQs, RLQs, and blazars). For example, they found microvariability events in several RQQs, although at low levels (e.g., Goyal et al. 2013 and references therein). They also reported that all quasars seem to show microvariability with duty cycles between 5 and 20%. In blazars, the duty cycle estimated is larger than 40% (Gopal-Krishna & Wiita 2018 and references therein).

A.5 Tuorla observatory blazar monitoring

This monitoring program, lead from the Tuorla Observatory in Finland, follows the light curves of a sample of about 80 AGNs, most of them blazars, including some Fermi bright AGNs [1] (e.g., Katajainen et al. 2000). For this, they use several telescopes in Finland, Chile, New Mexico, Bulgaria, and La Palma.

A.6 Blazar monitoring at the SpbSU

The monitoring program of the Saint Petersburg State University (SpbSU) observes since 2002 a sample of $\sim$45 quasars, simultaneously with the observations of Fermi[2].

[1] http://users.utu.fi/kani/1m/
[2] http://vo.astro.spbu.ru/en/node/17

A.7 Whole Earth Blazar Telescope (WEBT)

The WEBT is a network of optical, NIR and radio observers that coordinates multi-wavelength simultaneous monitoring campaigns of several blazars since 1997. In particular, many of these campaigns are simultaneous with high-energy satellite-borne telescopes, like Fermi. The continuous high-density monitoring uses telescopes of 42 observatories spread around the world, which allow obtaining gap-less light curves of blazars.

After 2007, most of the observing activity of WEBT is devoted to the GASP project (GLAST-AGILE support program) to provide optical-to-radio long-term continuous monitoring of a list of selected γ-ray-loud blazars during the operations of AGILE and Fermi γ-ray space telescopes.

Around 200 papers have been published using data of WEBT. An example is Bhatta et al. (2013), which reported three days of intensive monitoring of the microvariability of S5 0716+71 in February 2009. These observations were used to fit the light curve as a series of pulses due to cells in a turbulent jet.

B

Photometric issues

B.1 Photometric error

An estimate of the photometric error, σ_m, can be calculated as

$$\sigma_m \simeq \frac{1.0857}{S/N} \tag{B.1}$$

where S/N is the signal to noise ratio of the object. In the particular case of aperture photometry, the S/N has been usually evaluated simply as:

$$\frac{S}{N} = \frac{N_{obj}}{\sqrt{N_{obj} + n_{pix}(N_{sky} + RN^2)}} \tag{B.2}$$

N_{obj} is the total number of electrons or detected photons of the object inside the aperture that has a total of n_{pix} pixels. N_{sky} is the number of electrons per pixel of the sky background, and finally RN denotes the readout noise of the CCD in electrons.

The first term of the noise budget arises from the Poissonian noise of the observed photons of the object. The second term, $n_{pix}N_{sky}$ is the contribution of the Poissonian noise of the background inside the aperture. The final term in the equation, $n_{pix}RN^2$ accounts for the error due to readout noise.

The standard deviation of the background in an ideal situation can be computed as:

$$\sigma_{sky} = \sqrt{N_{sky} + RN^2} \tag{B.3}$$

although usually, the approximation $\sigma_{sky} = \sqrt{N_{sky}}$ is valid, except for very short exposures or narrow filters.

The use of σ^2_{sky} instead of $N_{sky} + RN^2$ in Eq. B.2 has the advantage of also considering other terms than those mentioned that may affect the dispersion of the sky background and should be included.

Nevertheless, real situations are a bit more complicated. Equation B.2 only considers the influence of the dispersion of the sky inside the aperture, but it does not take into account the error in the computation of the sky value. This depends on the number of pixels of the aperture and the number of pixels used to compute the sky (n_{bkg}) and can be included in the equation by substituting n_{pix} by $n_{pix}(1 + n_{pix}/n_{bkg})$. Finally we have:

$$\frac{S}{N} = \frac{N_{obj}}{\sqrt{N_{obj} + n_{pix}\left(1 + \frac{n_{pix}}{n_{bkg}}\right)\sigma_{sky}}} \qquad \text{(B.4)}$$

Besides this, there are more effects that could be included in this equation. However, they are difficult to compute. We can mention in this group: centering errors that will have a significant influence in the photometry (when using small apertures) in undersampled images (Kjeldsen & Frandsen 1992). Also, errors in the flat fields have a strong influence on the photometry (both Poissonian noise and of other types) if they are not well measured. The gain (number of electrons per ADU), the pixelization of the image and subpixel sensitivity variations (see for example Penny & Leese 1996b, Lauer 1999) may also introduce a factor in the error budget of the photometry. These and other topics are explained in more detail in Appendix B.2, where some tests are presented.

From Eq. B.4, it can be shown that, under the same circumstances (sky, seeing), the aperture for largest S/N depends sensitively on the flux of the object (see Fig. B.10). For small apertures, the S/N is low because of the low number of counts included in the aperture; while for big apertures the influence of the sky, which dominates the error, also reduces the S/N. The aperture of the largest S/N is called the optimal aperture. Faint objects have smaller optimal apertures than bright objects because the influence of the sky in the error budget for faint objects dominates at smaller apertures.

This definition is used by Howell (1989, 1992, 1993) to introduce the optimal data extraction technique. The photometry of the objects is performed with different apertures. In faint objects, only the optimal aperture is used. To compare this instrumental magnitude of different objects, growth curves (the instrumental magnitude obtained at different apertures) are constructed for bright objects in the frame. With the growth curves, it is straightforward to "extrapolate" the instrumental magnitude derived with the optimal aperture to any other aperture that could be used for all the stars. With this algorithm, the photometric errors of faint objects are significantly diminished.

A different approach to optimal extraction techniques is described by Naylor (1998), in which each pixel is weighted optimally by a quantity related to its variance. The author claims that this technique provides a gain of around 10% in S/N over normal aperture photometry.

These optimal techniques assume that the seeing profile is the same for every star in the frame. However, in many cases, this assumption cannot be applied due to variations in the PSF across the image caused by a misalignment of the optical elements and the detector or some aberrations (for example coma) from the telescope optic. This is the reason why we have not applied these techniques to our data.

Lastly, there is another contribution to the error budget that is extrinsic to the instrument and comes from the atmosphere. This is the scintillation noise, that is the major source of variance in time for the brightest stars. The scintillation noise is usually estimated as (Young 1967, Gilliland et al. 1993):

$$S = 0.09 D^{-2/3} X^{1.8} \exp(-h/h_0)(2t_{exp})^{-1/2}, \tag{B.5}$$

where D is the diameter of the telescope in cm, X is the airmass, h is the observatory altitude, $h_0 = 8000m$ is an atmospheric scale height and t_{exp} is the exposure time in seconds. For our typical observations in which the exposure time is ∼5 min and the airmass ranges between 1 and 2.2, the largest scintillation noise expected is below 1 mmag and does not contribute significantly in the error budget of our data.

Another extrinsic source of error is the differential extinction, caused by the different extinction of objects placed at different positions in the detector. At our highest airmass observations (X=2.2) the highest differential extinction of two objects at opposite extremes of the CCD of the IAC-80 is ∼4 and 2 mmag in B and V filters, respectively, and smaller in the redder filters.

Since these last two noise factors are small, we have not taken them into account in the analysis of our photometry.

B.2 Practical issues

In this Appendix certain aspects that can affect the CCD photometry are reviewed in detail. Many of the topics discussed here describe how some characteristics of the CCDs or the observations affect the photometry. Other topics are related to the possible algorithms used in the different steps of the photometry. In the latter cases, we have used IRAF to test which are the best algorithm for our purposes, although the discussion is in principle general to any photometric package.

B.2.1 Flat fielding

Each pixel in a CCD behaves like an individual detector with its quantum efficiency (QE). In order to correct the differences in the QE of the distinct pixels, images of a blank field are taken. However, it is not easy to find a uniformly illuminated field to be imaged. The illuminated field should also be of the same color of the object to be observed because the QE of each pixel is strongly related to the wavelength. Three kinds of flat field are typically used for this correction: the illuminated dome, the twilight sky, and the night sky.

Dome flats have the advantage over the other two methods that they can attain a better S/N because the brightness level can be adjusted for an efficient exposure time and a large number of frames can be taken in daytime. However, its main drawbacks are: first, the observed field is not uniformly enough illuminated; and second, the difference in color between the dome and the objects to be measured; and finally, the stray light that can fall into the detector if the telescope is not properly baffled. This last problem also affects the other methods for taking flat fields and the science observations although to a less extent. Even the NOT, a carefully designed telescope, had this problem. Grundahl & Sorensen (1996) observed that the flat fields taken with the telescope pointed to the east were different than those with the telescope pointed to the west. They could almost correct this undesirable effect with an appropriate baffling.

Twilight flats are difficult to obtain because the sky is highly variable at dawn and dusk and usually the time available to take the exposures needed to create of high-quality flat field is not long enough. Massey et al. (1989) pointed out that twilight flat fields should be taken pointing the telescope to the direction opposite to the Sun, in order to reduce any possible polarization effects. Other authors recommend however an area near the zenith but offset toward the antisolar horizon by $\sim 20°$considering the gradients of the sky background (Chromey & Hasselbacher 1996). The differences between twilight and dome flats are usually attributed to be due to the color difference between them (see for example Stetson 1987, Massey et al. 1989, Buffington et al. 1991).

Night sky flats are built using all the images taken during the night. They are combined with a clipping algorithm to remove the objects from the images. These flat fields are regarded as being the best to use because the conditions in which they are taken match those of the science frames. However, it is very difficult to obtain a high S/N flat field in this way, especially in the blue colors, due to the low surface brightness of the sky on nights without Moon. When the Moon is bright and over the horizon, great care should be taken in obtaining the night sky flat fields. If the Moon is close to the observed field or its light falls directly on the telescope, detector or even inside the dome, this can yield large spatial variations in the background of the frame. Apart from the gradients in the background, it is not clear that the response of the detector to oblique and direct light are similar, so flat fields should be taken in the same conditions as the science frames, i.e., through the optical axis of the telescope. In any case, this kind of flat field can be utilized to check the validity of the other flats by comparing the large-scale structure of the images.

A different method for building a flat field would be to combine dome flats with the flat obtained by one of the other methods. Dome flats, with their higher S/N can be used to correct the pixel-to-pixel sensitivity variations, while the large-scale structures are corrected using the night sky, or twilight flats.

Generally, we have taken twilight flat fields. On some occasions, these have been combined with dome flat fields in the way mentioned above. On other occasions we have combined the twilight images obtained on consecutive nights, after checking they are similar, to build a higher S/N final master flat field.

Flat fielding, as for any of the steps of the reduction process, adds noise to the photometric measurements. Furthermore, it is quite difficult to obtain a flat field good to the level of 0.1%, not only due to photon statistics but also to the difficulty in finding a good flat source. It needs typically > 25 flat frames each with a high level of counts in each filter to reach this level on a pixel-to-pixel basis and there is rarely, if ever, time for doing this for the whole set of filters, even when dome flats are taken during the day. In the twilight, it is totally impossible. Thus, flat fielding imposes a stringent limit on the photometry.

B.2.2 Centering

In order to compute the center of an object, it is necessary to know, as input parameters, an initial estimate of the center and the width of the box of pixels to be used to calculate the center. This box needs to be big enough to include sufficient number of pixels from the star, but not so large as to include excessive noise or other objects. In IRAF all of the three available algorithms compute the center position separately in x and y coordinates by summing the counts of all the rows and columns respectively, included in the box. This is called the marginal distribution. The three techniques are the *centroid*, a Gaussian fit to the marginals (*gauss*) and the optimal filter of the marginals (*ofilter*).

The *centroid* algorithm computes the mean of the marginal distribution in x and y weighted by the intensity. This is the only centering algorithm that is independent on an input estimate of the FWHM of the object. The *gauss* technique fits a 1-D Gaussian function to the x and y marginal distribution, using the initial estimate of the center and FWHM as inputs. This routine is iterated until a best fit solution is achieved. The last algorithm, *ofilter*, uses a triangle function for the optimal filter technique to compute the center of the marginal distribution. A full description of the algorithms can be found in the IRAF document "Specifications for the Aperture Photometry Package".

The *centroid* algorithm seems to be the best option for our data because it does not assume any shape for the objects, as the other two routines do. That could be an important point when the telescope is not carefully aligned and cannot be perfectly focused, so the profile obtained was not a good Gaussian or any other simple function.

We created artificial images with the *ARTDATA* package of IRAF. The shape of the object was a circular Moffat function with an FWHM of 1, 2,..., 8 pixels. The number of stars per frame was one hundred distributed randomly; the background ranged between 10 and 10000 counts, and the range of magnitudes was chosen to give a range from very bright stars (m=14) to very faint stars (m=20).

In Fig. B.1, a sample histogram of the distance between the nominal center location and the computed center position of the objects (Δpos) is shown for the case of m=14, FWHM=4 pixels and sky=1000 counts. For this plot, the algorithm used is *centroid*. The distribution peaks around 0.1 pixels and, in the majority of the stars, the distance between the nominal and the computed position is less than 0.2 pixels. However, even in these favorable conditions, a small number of objects have $\Delta pos > 0.5$ pixels. These outliers are caused by the presence of a second object very close to the star for which the center is computed.

For each simulation, the mean and the standard deviation of the distance (Δpos) between the nominal and computed center position was calculated. Figure B.2 shows the average of the Δpos, while Fig. B.3 plots the standard deviation of Δpos for each test. At small FWHM, *ofilter* and *centroid* behave quite well for bright objects and low sky background. Although the center is better for the *ofilter* algorithm in almost all cases, for the most unfavorable cases

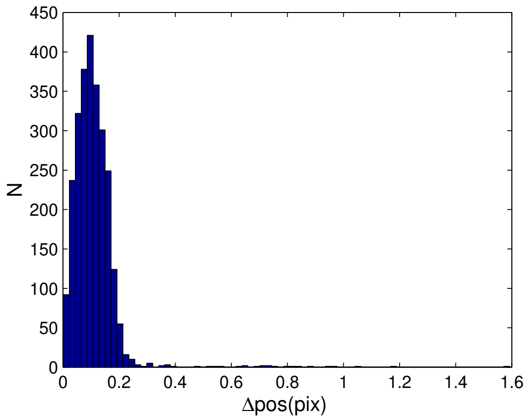

FIGURE B.1— Example histogram of the centering error for the simulation with m=14, FWHM=4 pixels and sky=1000 counts with the centroid algorithm (see text for details). There are around 0.04% of outliers with $\Delta pos > 0.5$ pixels.

(higher background and faint stars) the *centroid* algorithm works reasonably well, unlike the other two techniques (Fig. B.2) at least for FWHM>3 pixels, which is the case for most of our data. Furthermore, the standard deviation of the distance between the initial position and the calculated position is smaller for the *centroid* routine, except for very small FWHM. As the standard deviation is quite sensitive to outliers, Fig. B.3 shows that the *centroid* algorithm is the safest option for computing the center position of an object.

Apart from this, the *centroid* routine always gives a value of the center position, while the other two methods sometimes fail to estimate of the center position (0.6% in all conditions and 5% in the worst case, of high sky background and faint objects).

We have also tested the influence of the centering on the photometry. We have created artificial images with zero background and a circular Moffat profile with FWHM of 10 pixels in order to avoid the effects of sky noise and the aperture in the photometry (see below). Although the exact results of this test depend on the actual shape of the PSF, the Moffat profile should approximate quite well to real situations. Photometry is performed for each star using distinct apertures, fixing the center of the aperture with a certain offset from the nominal center of the star. A total of 2500 artificial stars have been measured for each aperture and each offset. Figure B.4 shows the magnitude difference in the photometry with and without the displacement of the center of the aperture. The curves are displayed for distinct offsets (0.03, 0.05, 0.1, 0.2, 0.5, 0.9) in units of the FWHM. The aperture radius is also shown in units of the FWHM. The plot indicates that the error in the photometry is higher for smaller apertures and greater centering offsets, as expected.

For a representative example of a star with FWHM of 5 pixels (close to our typical case in the visible), the errors in the centering are typically less than 0.3 pixels (see Figs. B.2 and B.3) which gives an error in the photometry below 10^{-3} mag for aperture sizes of 6.5 pixels (1.3 times the FWHM). Except for bright stars with small FWHM (~1-2 pixels) and small apertures, the

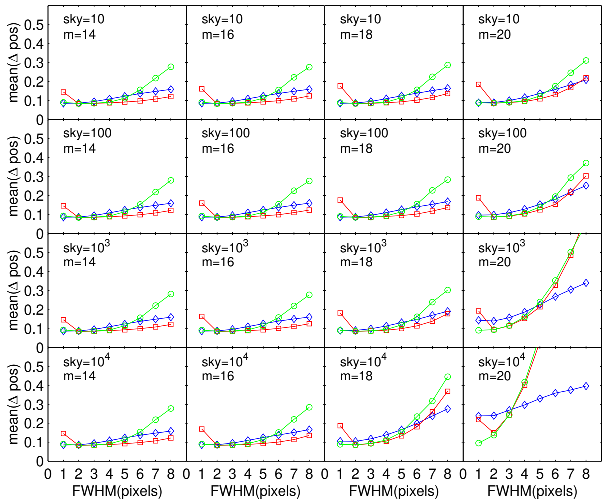

FIGURE B.2— Mean of the location errors for all centering tests. Blue diamonds show the results of *centroid* algorithm, red squares are the average error for the *gauss* algorithm and green circles represents the results of the *ofilter* routine. Although it does not always give the smallest errors, note that the *centroid* algorithm is the most robust, since even in the worst cases it gives reliable results.

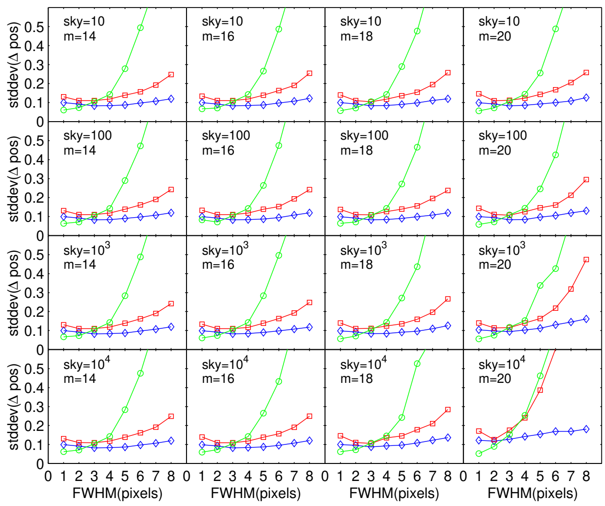

FIGURE B.3— Standard deviation of the location errors for all centering tests. Symbols are the same of Fig. B.2. Once again, the *centroid* routine is the most robust because it gives the more reliable results in all cases.

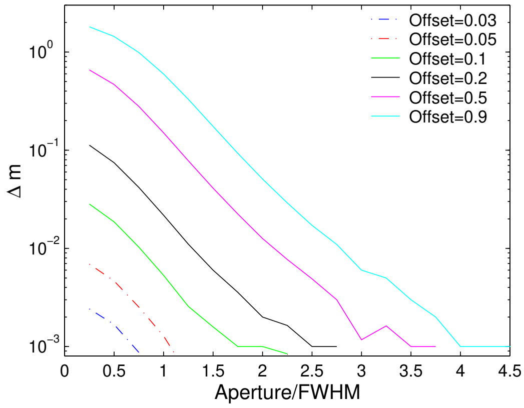

FIGURE B.4— Magnitude error after centering the photometric aperture with a certain offset with different aperture radius. The offsets shown in the legend are in units of the FWHM of the PSF.

photometric errors induced by centering errors are of no importance compared to the overall photometric error.

B.2.3 Sky fitting

As stated above, the sky fitting process is very important when performing the photometry. Even a small error in the sky will have a considerable influence on the photometry of faint objects. On the other hand, the effect of the determination of the sky in the photometry of a bright object is negligible, unless the sky background is very high and the photometry is performed with a very large aperture.

In IRAF, the sky is computed using the values of the pixels enclosed in an annulus around the object. The radius of the annulus should be large enough not to contain any signal from the object, but not so large that the assumptions in a local determination of the sky are not valid, and so that the annulus includes other stars. The width of the annulus should be selected in such a way that the number of pixels included in the sky annulus is large enough to give good statistics.

In any case, it is possible that the sky annulus would contain also contaminating objects or cosmic rays. Thus a good pixel rejection algorithm is needed. We have selected a 3σ-clipping rejection in which those pixels whose values are larger or smaller than three times the standard deviation of the computed sky are removed from the list of sky pixels in an iterative process.

There are several routines available in IRAF for the task of sky determination. These techniques fall into three categories: those that compute the sky by using the actual values of the sky pixels; those that make use of the histogram of sky values and those interactive methods in which the user chooses the sky after being shown the histogram of sky values, or a radial plot. Since we have a great number of images and each image has several dozen stars that are to be measured, and the interactive methods are not very reliable and repeatable, only

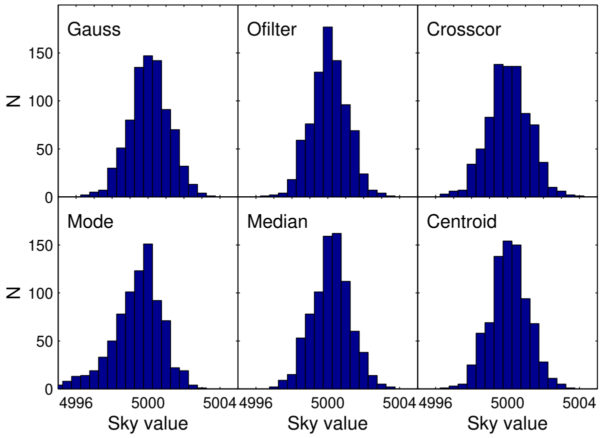

FIGURE B.5— Histograms of the sky values obtained with each IRAF algorithm. The artificial images were created with a sky level of 5,000 counts, $n_s = 50$ and $n_c = 50$.

the first two groups are considered.

The *median* and the *mode* compose the first group of techniques. The median is calculated in the usual way. The *mode*, the most probable value in the distribution, is theoretically the actual value of the sky. However IRAF makes the following approximation:

$$I_{mode} = 3 \times I_{median} - 2 \times I_{mean}. \tag{B.6}$$

Newberry (1992) has stated that this mode approximation is biased toward higher values.

In the histogram methods, the routines construct the histogram with a user-defined bin size (we have chosen 0.2 times the standard deviation of the sky, a value which we have tested and that works quite well). Four methods can be selected for computing the peak of the distribution of sky pixels: *centroid*, a Gaussian fit (*gauss*) and the Optimal Filter (*ofilter*), which use the same techniques described for the centering algorithms, and finally the cross correlation (*crosscor*) in which the noise function is estimated using the standard deviation of the sky pixels and is cross-correlated with the histogram. The peak of the cross correlation gives the sky value.

To decide which is the best algorithm for sky fitting our data, we created a set of artificial images. These have different values of the background (from 10 to 10,000), and in them, we have included a number of stars n_s and cosmic rays n_c, from 0 to 500 each. In each image, the sky was computed centering the annulus in 81 random location using each algorithm.

In Fig. B.5 we display the histogram of the sky values obtained by each algorithm for images with sky background of 5,000 counts and for 50 stars and 50 cosmic rays. The distributions of values are similar for all algorithms, except for the *mode*, which is quite skewed to lower values in contradiction to Newberry (1992). We also see that the *crosscor* routine seems to give a distribution slightly wider than the others.

The effect of the number of stars in the distribution of sky values is, as expected, stronger

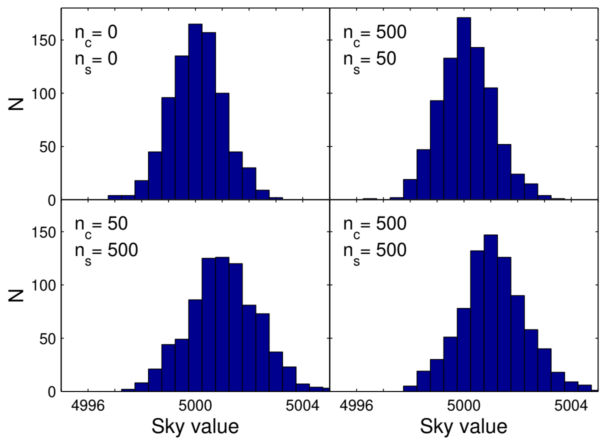

FIGURE B.6— Histograms of the sky values obtained with the *ofilter* algorithm for images with distinct number of stars and cosmic rays and a nominal background of 5000 counts.

than for the number of cosmic rays, since stars spread the counts over more pixels than cosmic rays and thus the rejection algorithm is more efficient in removing pixel values affected by cosmic rays than by stars. Figure B.6 shows the distribution of sky estimates with the optimal filter algorithm for images with a background of 5000 counts and with different quantities of cosmic rays, or stars. Increasing the number of stars makes the histogram shift to higher values and widens it. On the contrary, increasing the number of cosmic rays only makes the histogram somewhat skewed.

The *mode* algorithm gives lower values of the sky than the other routines. Figure B.7 shows the mean sky value computed by each algorithm minus the nominal sky value (solid lines) and the standard deviation of the computed sky values (dashed lines) with a number of cosmic rays and stars of 50 (top panel), 500 (middle panel) and all conditions (bottom panel). For sky values in the range of 10-100 with a small number of stars and cosmic rays, the mode algorithm gives values consistently below nominal (~ 0.1 count). For higher backgrounds, the difference is even greater, reaching almost 1 count with a sky level of 10,000 counts. Nevertheless, for images with a higher number of stars and cosmic rays, all routines but the mode gives sky values higher than nominal. This is due to the fact that with this large number of stars, a large fraction of the sky pixels is contaminated by stars. In these conditions, these algorithms fail to give a correct sky value and the stars should be removed before computing the sky background (for example with a PSF fitting photometric package). Also, with this large number of stars, the pixels inside the object apertures should also be affected by other stars. In any case, with such a degree of crowding, PSF fitting photometry is recommended. We note that the optimal filter gives less deviant values (the standard deviation is smaller) than the other routines. As a result of these tests, we have decanted for the use of the *ofilter* algorithm.

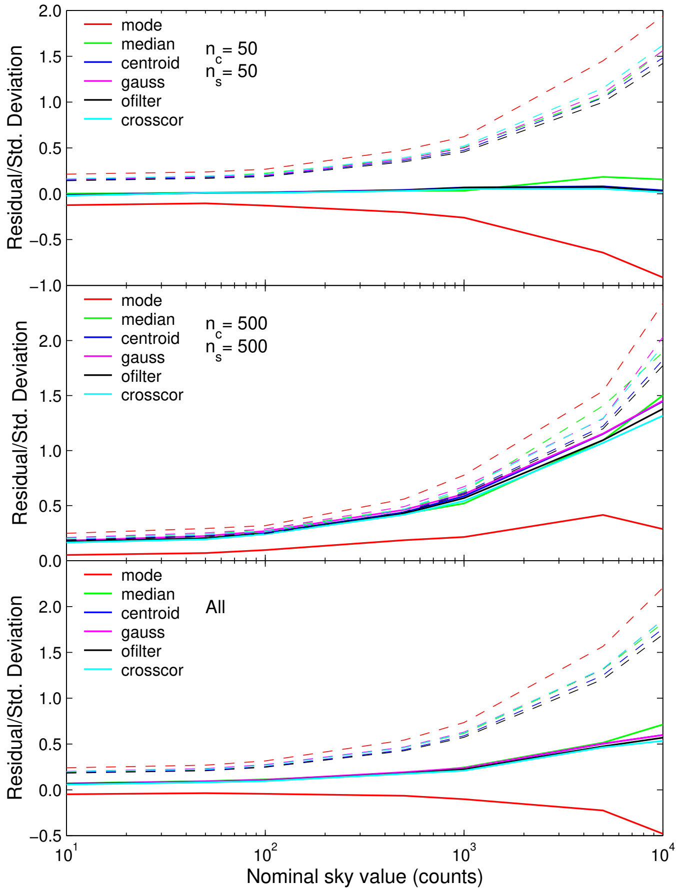

FIGURE B.7— Mean of sky residuals (solid lines) and standard deviations (dashed lines) of the sky values obtained from each algorithm. The top panel shows the results with images with a number of stars and cosmic rays of 50; the middle panel displays the results of images with $n_s = n_c = 500$ and in the bottom panel the results using all the simulations are presented.

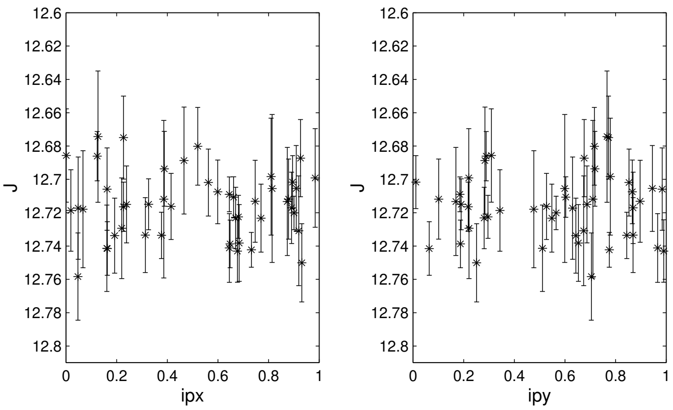

FIGURE B.8— Relation between the J magnitude and the intrapixel position *ipx* and *ipy* for a star in the field of BL Lac the night of August 29, 1998. The average of the seeing during the night was around 2.5 pixels.

B.2.4 Subpixel response variations

After performing the flat field correction, images are free from the effects of the difference in response of each pixel. However, the complex microstructure of a CCD or any other solid-state detector may cause its sensitivity to vary substantially within a pixel, and this can lead to errors in stellar photometry under certain conditions. Jorden et al. (1994) measured the intrapixel sensitivity variations of several CCDs of the ING at the Roque de los Muchachos Observatory. They show that the response varies more than 20% with the intrapixel position, both in x and y direction. They also present results that show that this variation is strongly dependent on wavelength and that the subpixel structure is stable and repeatable from one pixel to another. Penny & Leese (1996a) show that this subpixel structure may cause photometric errors of the order of a few percent for undersampled images.

We do not expect to detect this effect in our optical images, because the FWHM was much larger than one pixel with all the telescopes and instruments that we have used for the optical photometry. In all but two of our nights of observation, the seeing of the optical images is FWHM$\gtrsim$3 pixels, so in principle, the possible subpixel response variation does not affect our photometry. For some nights with good seeing, we have searched for any possible relationship between the magnitude of a bright star and the location of the star inside the pixel and we have not found any evidence that subpixel response variations affect our photometry.

The new wide-field optics of the near-infrared camera (CAIN) mounted on the CST since 1998 gives a pixel size of $1''$. We have only found marginal evidence of the effect of response variations at intrapixel scales (see Fig. B.8), although the amplitude of the magnitude variations is at the level of the photometric error.

Even in this case, the subpixel response variations do not affect significantly our data (apart from a slight increase in the errors) because in these observations the autoguiding of the telescope was turned off, so the photometric variations are diluted by the randomizing of the center locations of the sources and the objects are widened, making the images less undersampled.

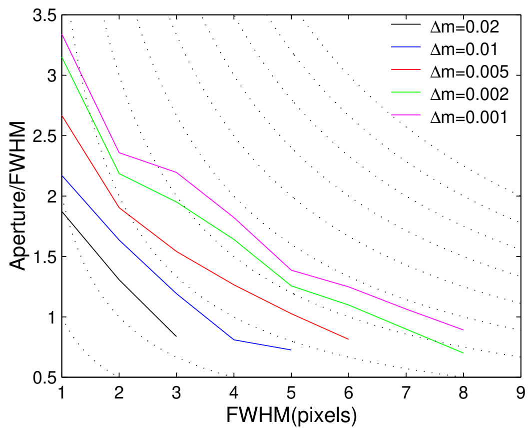

FIGURE B.9— The ratio of minimum aperture to FWHM necessary to obtain a certain systematic photometric error against the FWHM. Dotted lines represent aperture radii of equal number of pixels.

B.2.5 Pixelization

The division of the images in pixels can introduce noise and systematic photometric errors in the aperture photometry (Mighell & Leese 1999). Usually, photometric packages compute the total counts enclosed in the aperture by fractional pixel techniques. If a pixel is completely within the aperture, the whole of its counts are added to the flux of the objects, but for those pixels that are partially within the aperture, only a fraction of the counts are included. Thus, IRAF and other packages approximate the circular aperture by an irregular polygon and assume that the PSF is nearly flat at the edges of the aperture. These assumptions are generally appropriate for larger apertures, but wherever the PSF changes rapidly with radius, there will be large systematic photometric errors. Thus, this method is unsuitable for small aperture photometry with the adopted aperture less than a very few times of the FWHM.

We have created artificial images with distinct FWHM of the PSF from 1 to 10 pixels. These images are noiseless and have a background of zero counts in order to avoid any noise error in the photometry. Aperture photometry was then performed for the stars included in the images, fixing the center of the apertures to the nominal location center of the objects. The aperture radii range from 0.5×FWHM to 5×FWHM. Finally, the average of the magnitude of the objects with different FWHM at each aperture was calculated. Figure B.9 shows the aperture necessary to obtain a certain systematic photometric error defined as the difference between the mean magnitude of objects for each FWHM minus the magnitude of objects with FWHM=10 pixels. These magnitudes are obtained with the same aperture to FWHM ratio. The effect of pixelization in the photometry is more important with small apertures and the FWHM of the PSF. For a typical image in our observations, which has FWHM$\gtrsim$ 3 pixels, we need an aperture of $\sim$ 6 pixels to obtain a systematic error less than 0.002 mag from this effect.

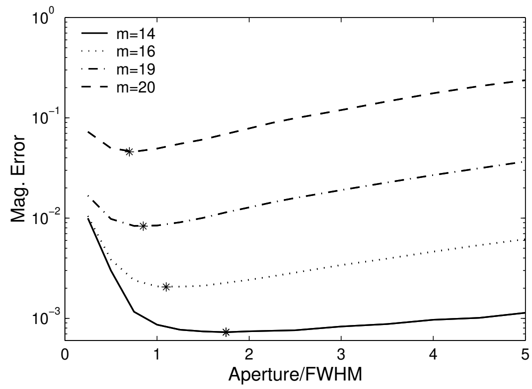

FIGURE B.10— Photometric error plotted as function of aperture radius for four stars of different magnitudes. At a certain radius of the aperture, marked by an asterisk, the objects has a maximal S/N. See text for more detais.

B.2.6 Maximal S/N

In Sect. B.1, we have outlined the principles of optimal photometry. Here, we show the results of some simulations to study the relationship between the optimal aperture and the magnitude of the object, the sky background, and the seeing. Several artificial images with different seeing, sky and object magnitudes were created. The PSF profiles were determined using a Moffat function. Finally, photometry was performed using distinct apertures, leaving IRAF to center the object, fit the sky and compute the magnitude. Thus, these simulations take into account the influence of the center task and the sky background fitting in the photometry, but it does not consider either the influence of crowding or of seeing variations.

We have computed the standard deviation (which should be equal to the photometric error) for each aperture and each set of initial conditions, and finally, the aperture of minimum standard deviation was estimated.

Figure B.10 shows the magnitude error with different apertures for four stars with magnitudes from 14, a very bright star, to 20, which is quite a faint star. The aperture of maximal S/N for each magnitude is indicated by an asterisk. The sky in these simulations was of 1000 counts, and the FWHM of the PSF was 5 pixels.

The aperture of maximal S/N and the standard deviation for this aperture are shown in Fig. B.11. Each panel represents the result for an object of a different magnitude. The optimal aperture radius to FWHM ratio is larger for brighter objects, smaller FWHM of the star profile and smaller sky background. This is mainly due to the different contributions of the sky background in the error budget.

Taking into consideration only the Poissonian noise of the sky and the source, the aperture of maximal S/N ranges from 0.8 to 3 FWHM, depending on the brightness of the source and the sky. These results have led to some authors to define optimal data extraction techniques, through which, a different aperture (the optimal) is used for each star. Then, the effect of using different

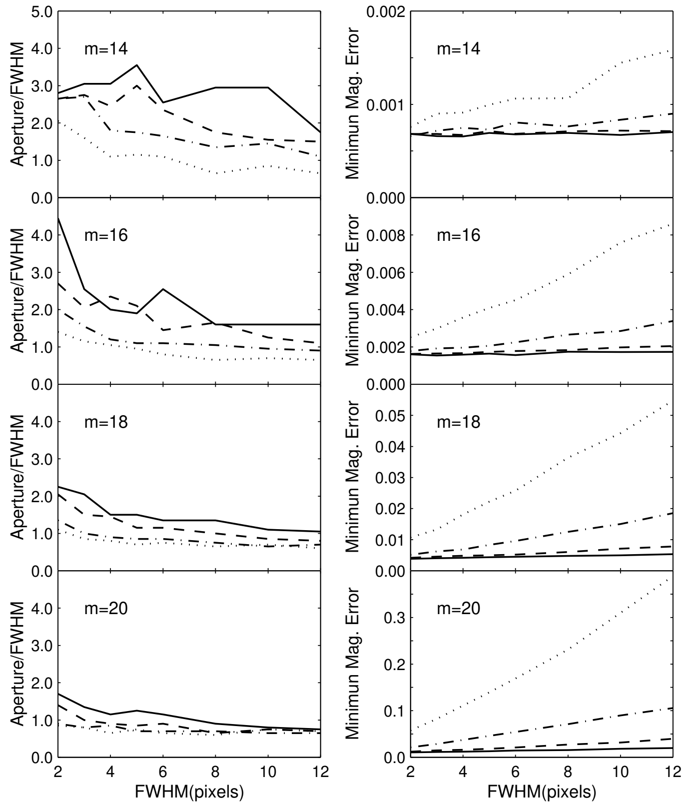

FIGURE B.11— Apertures of maximal S/N to FWHM ratio (left panels) and minimum photometric error (right panels) for point sources of different magnitudes and sky values, as a function of the FWHM. Sky backgrounds are 10 counts (solid lines), 100 counts (dashed lines), 1000 counts (dash-dot lines) and 10,000 counts (dotted lines).

apertures, that implies to add a distinct amount of photons for any star, is corrected by using a bright star in the field, for which the photometry is computed using supplementary apertures. Nevertheless, in these simulations, we have not considered the effect that any variation of the FWHM of the point sources across the frame has on the photometry (see next section), nor the influence of crowding.

B.2.7 FWHM variations

We try to quantify how seeing/FWHM variations influence the photometry. As the seeing varies, the photometry of an object should vary while maintaining the aperture fixed, since the number of photons that fall outside the aperture changes with the seeing. It is important to take this into consideration when the PSF varies across the image, as it usually does in our observations and in performing absolute photometry. In both cases, the aperture should be chosen so that for any FWHM variation the photometry remains quasi-stable. Of course, the FWHM variations across the images, usually a few percent at most, are much smaller than the seeing variations that normally occur during a night of observations.

As in Sect. B.2.5, a set of noiseless artificial images were created. The simulated variation of the FWHM of the Moffat function used to model the stars in our images ranges between 1% and 100%. Photometry was then performed with different apertures centering them in the nominal location of the objects. The FWHM of the profiles was always chosen to be big enough (in pixels) so as not to have problems with pixelization. Figure B.12 shows the results of our simulations. It displays the aperture radius needed to limit the highest magnitude variation to 0.02, 0.01, 0.005, 0.002 and 0.001 mag for different changes in the FWHM of the profile. It should be noted that the apertures are in units of the minimum FWHM. For a typical night in which the seeing varies around 50-80%, it is necessary to have an aperture radius 4-6 times the FWHM of the star profiles to obtain a good absolute photometry. Besides, in differential photometry an aperture radius of at least 2 times the FWHM is required to obtain a photometric precision of 0.005 mag for possible changes of FWHM of $\sim 5\%$.

These results advise us against using the optimal apertures algorithm, for which a typical aperture radius/FWHM is 1.2, as this can give systematic photometric errors of the order of 0.01 mag in our images.

B.2.8 Scattered light

In Sect. B.2.1, we have referred to some of the effects of stray light, mainly gradients in the background that will also affect science frames. Scattered light can arise from the inside of the secondary mirror baffle, the inside of the primary mirror baffle, the collar used to support the primary mirror baffle, and from the instrument itself, which may be prone to scatter light (Grundahl & Sorensen 1996). Nevertheless, in principle, this effect is of no importance in the case of science images because on performing the photometry, the local background is removed. However, apart from this, scattered light from a nearby very bright object produces ghosts which could be a problem if the location of the ghost is close to an object of interest.

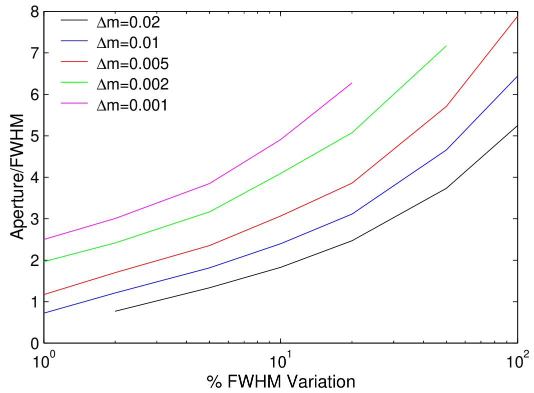

FIGURE B.12— Aperture radius to minimum FWHM ratio needed to attain certain systematic photometric error (Δm) as function of the variation of the FWHM of the profile.

B.2.9 Dust

Usually, both the filter and the window of the CCD are "dirty" with dust or filaments. The effect of such dust spots can be seen easily in the flat fields as diffraction rings. If they are in the window of the CCD, the rings are smaller than if they are on the filter. Although this can be corrected quite well with the flat field, there is always a remnant, especially in nights with bright Moon, since its light falls obliquely on the detector and the shadow of the dust spot is displaced from its position in the flat field. If the dust spot is close to an object, this shadow can affect the background light that falls inside the aperture and, consequently, yields a misestimate of the photometry of the object.

B.2.10 Other effects

Here we include some effects that could have an influence on photometry, such as cosmic rays, interference fringes or electrons spread from saturated objects. These effects will cause spurious photometric measurements which are not necessarily reflected in the photometric uncertainty. There is no solution to them apart from avoiding them completely.

There are several algorithms available for removing cosmic rays hits, but none of them is safe in the sense that they can also remove real information and hence we have not used them.

In addition to this, the characteristics of the instrument must be known before the observations take place. For example, there is a minimum of the exposure time for the shutter movement to be an insignificant fraction of the exposure time and thus the exposure time recorded in the header to be accurate. The difference between the real and the nominal exposure time can be too large to be acceptable for exposures shorter than this shortest exposure time. The IAC-80 CCD camera has a shortest exposure time of 12 seconds for a relative error of $\sim$1%.

Moreover, CCDs have a limited range of linear response. The typical linearity curves of the CCDs available at the telescopes claim that the CCD behaves linearly along a certain range of brightness. However, this range usually is computed for a maximal deviation of ∼1% which is much larger than the theoretical accuracy that we can obtain. It is necessary, therefore, to maintain the exposure time of the science frames adjusted so that the count levels of the object and sky remain well within the linear range, although modern CCDs are now very nearly linear up to saturation.

B.2.11 Summary

Taking into account the Poissonian noise of the sky and the source, the best aperture to be used depends on the brightness of the object but ranges between 0.8 and 2 FWHM of the profile (Sect.B.2.6). For larger apertures, the magnitude error increases, although slowly.

In the later sections of this Appendix, we have detailed several other aspects that affect the photometry. The results are somewhat contradictory in the sense that some effects favor using a small aperture in order to obtain accurate results, while other effects can only be suppressed with a large aperture.

As seen in Sect. B.2.2, errors in the centering of a source make the measured magnitude fainter. For objects with an FWHM of 4 pixels or larger, as the majority of our optical images, with a typical centering error of 0.2 pixels or smaller, the error in the photometry is smaller than 10^{-3} mag for apertures ∼1.2 FWHM of the seeing (5 pixels in this particular case). Due to the different scale of the NIR camera, the FWHM of the seeing in the NIR images can be as small as 2 pixels. So we expect magnitude errors induced by the centering below 0.001 mag for apertures of 1.7 FWHM (∼3.5 pixels).

The pixelization of the images (Sect. B.2.5) also has a significant effect on photometry. For a FWHM of the profile of the source of 4 pixels or greater the photometric error induced by the pixelization has an upper limit of 2 mmag if the aperture is of approximately 1.8 FWHM (∼ 7 pixels, for an FWHM of 4 pixels) while if the FWHM is in the range of 2 pixels, the required aperture to obtain a photometric error smaller than 2 mmag is 2.4 FWHM (∼ 4.8 pixels).

Finally, in our images, there are variations of the FWHM of the profile of point sources across the images (Sect. B.2.7). These variations are usually of the order of 2-5%. This gives a photometric error of 0.005 mag if the aperture is of only 1.8 FWHM. The use of the optimal aperture (∼ 1.2 FWHM) can give magnitude errors up to 0.01 mag.

In short, with smaller apertures better photometric precision is obtained, but there is a limit imposed principally by the pixelization of the image and the FWHM variations across the frame. We have performed photometry with an aperture of 1.8-2.0 FWHM, which is a compromise between these factors and have chosen a lower limit of 5 pixels for the aperture when the images are not well sampled (FWHM<3pix).

C

Host galaxy correction for the aperture photometry

This appendix presents the tables with the correction of the photometry of the AGNs in our sample. See Chapter 4 describes how the host galaxy profiles and the photometric correction were calculated. The surface brightness profiles of the AGNs in all filters are presented in Fig. C.1-C.8, together with the models of the host galaxy, nuclear point source, and other possible components. Tables C.1-C.38 present the magnitude of the host galaxies inside different apertures given the seeing of the observations.

TABLE C.1— Magnitude of the fitted galaxy of IIIZw2 inside the aperture in the B filter.

Apert.	Seeing (arcsec)							
(arcsec)	1.0	2.0	3.0	4.0	5.0	6.0	7.0	8.0
1.0	20.49±0.72	20.04±0.73	19.67±0.74	19.38±0.75	19.17±0.76	18.99±0.77	18.85±0.78	18.74±0.79
1.5	20.03±0.61	19.80±0.62	19.54±0.63	19.30±0.65	19.11±0.66	18.95±0.67	18.81±0.69	18.70±0.70
2.0	19.65±0.54	19.56±0.55	19.40±0.56	19.22±0.57	19.05±0.59	18.91±0.60	18.79±0.62	18.69±0.63
2.5	19.36±0.48	19.34±0.49	19.25±0.51	19.12±0.53	18.99±0.54	18.87±0.56	18.76±0.57	18.67±0.58
3.0	19.14±0.45	19.14±0.47	19.10±0.48	19.02±0.50	18.91±0.51	18.81±0.53	18.72±0.54	18.63±0.56
3.5	18.96±0.45	18.97±0.46	18.96±0.48	18.91±0.49	18.84±0.51	18.76±0.53	18.68±0.54	18.60±0.56
4.0	18.82±0.43	18.82±0.44	18.83±0.46	18.81±0.47	18.76±0.49	18.70±0.50	18.63±0.52	18.56±0.53
4.5	18.70±0.41	18.70±0.42	18.72±0.44	18.71±0.45	18.68±0.47	18.64±0.49	18.58±0.50	18.53±0.52
5.0	18.60±0.40	18.59±0.41	18.62±0.42	18.62±0.44	18.61±0.46	18.58±0.47	18.53±0.49	18.49±0.50
5.5	18.51±0.39	18.50±0.40	18.53±0.42	18.54±0.43	18.54±0.45	18.51±0.46	18.48±0.48	18.45±0.50
6.0	18.44±0.39	18.42±0.39	18.45±0.41	18.47±0.42	18.47±0.44	18.46±0.46	18.43±0.47	18.41±0.49
6.5	18.37±0.39	18.35±0.40	18.38±0.41	18.40±0.43	18.41±0.44	18.40±0.46	18.39±0.47	18.36±0.49
7.0	18.31±0.40	18.29±0.41	18.31±0.42	18.33±0.43	18.35±0.45	18.35±0.46	18.34±0.48	18.32±0.49
7.5	18.26±0.41	18.24±0.41	18.26±0.42	18.28±0.43	18.29±0.45	18.30±0.46	18.30±0.48	18.29±0.49
8.0	18.21±0.41	18.19±0.42	18.21±0.42	18.23±0.44	18.24±0.45	18.25±0.46	18.25±0.48	18.25±0.49
8.5	18.17±0.41	18.15±0.42	18.16±0.43	18.18±0.44	18.20±0.45	18.21±0.46	18.21±0.48	18.21±0.49
9.0	18.13±0.42	18.11±0.42	18.12±0.43	18.14±0.44	18.16±0.45	18.17±0.47	18.18±0.48	18.18±0.49
9.5	18.10±0.43	18.07±0.43	18.09±0.44	18.10±0.45	18.12±0.46	18.13±0.47	18.14±0.48	18.14±0.49
10.0	18.07±0.43	18.04±0.43	18.05±0.44	18.07±0.45	18.08±0.46	18.10±0.47	18.11±0.48	18.11±0.49

TABLE C.2— Magnitude of the fitted galaxy of IIIZw2 inside the aperture in the V filter.

Apert.	Seeing (arcsec)							
(arcsec)	1.0	2.0	3.0	4.0	5.0	6.0	7.0	8.0
1.0	19.09±0.34	18.63±0.34	18.28±0.34	18.01±0.34	17.80±0.34	17.63±0.34	17.50±0.34	17.39±0.34
1.5	18.63±0.19	18.40±0.19	18.15±0.19	17.92±0.19	17.74±0.19	17.59±0.19	17.46±0.19	17.36±0.19
2.0	18.27±0.11	18.18±0.11	18.02±0.11	17.85±0.11	17.69±0.11	17.56±0.11	17.45±0.11	17.35±0.11
2.5	17.99±0.08	17.96±0.08	17.88±0.08	17.75±0.08	17.63±0.08	17.51±0.08	17.41±0.08	17.32±0.08
3.0	17.78±0.06	17.76±0.06	17.73±0.06	17.65±0.06	17.56±0.06	17.46±0.06	17.37±0.06	17.29±0.06
3.5	17.61±0.05	17.60±0.05	17.60±0.05	17.55±0.05	17.49±0.05	17.41±0.05	17.33±0.05	17.26±0.05
4.0	17.47±0.04	17.46±0.04	17.48±0.04	17.46±0.04	17.41±0.04	17.35±0.04	17.29±0.04	17.23±0.05
4.5	17.36±0.03	17.34±0.03	17.37±0.03	17.36±0.04	17.34±0.04	17.29±0.04	17.24±0.04	17.19±0.04
5.0	17.26±0.03	17.24±0.03	17.27±0.03	17.28±0.03	17.26±0.03	17.24±0.03	17.20±0.03	17.15±0.04
5.5	17.18±0.03	17.16±0.03	17.18±0.03	17.20±0.03	17.20±0.03	17.18±0.03	17.15±0.03	17.11±0.04
6.0	17.11±0.03	17.08±0.03	17.11±0.03	17.13±0.03	17.13±0.03	17.12±0.03	17.10±0.03	17.08±0.04
6.5	17.05±0.03	17.02±0.03	17.04±0.03	17.06±0.03	17.07±0.03	17.07±0.03	17.06±0.04	17.04±0.04
7.0	16.99±0.04	16.96±0.04	16.98±0.04	17.01±0.04	17.02±0.04	17.02±0.04	17.02±0.04	17.00±0.04
7.5	16.94±0.04	16.91±0.04	16.93±0.04	16.95±0.04	16.97±0.04	16.98±0.04	16.97±0.04	16.96±0.04
8.0	16.90±0.04	16.87±0.04	16.89±0.04	16.91±0.05	16.92±0.05	16.93±0.05	16.93±0.05	16.93±0.05
8.5	16.86±0.05	16.83±0.05	16.84±0.05	16.86±0.05	16.88±0.05	16.89±0.05	16.90±0.05	16.89±0.05
9.0	16.83±0.05	16.79±0.05	16.81±0.05	16.82±0.05	16.84±0.05	16.85±0.05	16.86±0.05	16.86±0.05
9.5	16.80±0.05	16.76±0.05	16.77±0.05	16.79±0.05	16.81±0.05	16.82±0.05	16.83±0.05	16.83±0.05
10.0	16.77±0.04	16.73±0.04	16.74±0.04	16.76±0.04	16.77±0.04	16.79±0.04	16.80±0.04	16.80±0.05

Table C.3— Magnitude of the fitted galaxy of IIIZw2 inside the aperture in the R filter.

Apert.	Seeing (arcsec)							
(arcsec)	1.0	2.0	3.0	4.0	5.0	6.0	7.0	8.0
1.0	18.55±0.08	18.07±0.08	17.69±0.08	17.39±0.08	17.16±0.08	16.98±0.09	16.83±0.09	16.71±0.09
1.5	18.09±0.04	17.85±0.04	17.58±0.04	17.34±0.04	17.13±0.04	16.97±0.04	16.83±0.04	16.71±0.04
2.0	17.69±0.02	17.60±0.02	17.43±0.02	17.24±0.03	17.07±0.03	16.92±0.03	16.79±0.03	16.68±0.03
2.5	17.39±0.02	17.37±0.02	17.28±0.02	17.14±0.02	17.00±0.03	16.87±0.03	16.76±0.03	16.66±0.03
3.0	17.17±0.02	17.17±0.02	17.13±0.02	17.04±0.02	16.93±0.03	16.82±0.03	16.72±0.03	16.63±0.03
3.5	16.98±0.02	16.99±0.02	16.98±0.02	16.92±0.02	16.85±0.03	16.76±0.03	16.67±0.03	16.59±0.03
4.0	16.83±0.02	16.83±0.03	16.85±0.03	16.82±0.03	16.76±0.03	16.70±0.03	16.63±0.03	16.55±0.03
4.5	16.70±0.03	16.71±0.03	16.73±0.03	16.72±0.03	16.68±0.03	16.63±0.03	16.57±0.03	16.51±0.04
5.0	16.59±0.03	16.59±0.03	16.62±0.03	16.62±0.03	16.60±0.04	16.57±0.04	16.52±0.04	16.47±0.04
5.5	16.50±0.03	16.50±0.03	16.52±0.03	16.54±0.03	16.53±0.04	16.51±0.04	16.47±0.04	16.43±0.04
6.0	16.42±0.03	16.41±0.03	16.44±0.03	16.46±0.03	16.46±0.04	16.44±0.04	16.42±0.04	16.39±0.04
6.5	16.35±0.03	16.34±0.03	16.36±0.03	16.38±0.03	16.39±0.03	16.38±0.04	16.37±0.04	16.34±0.04
7.0	16.29±0.03	16.28±0.03	16.30±0.03	16.32±0.03	16.33±0.03	16.33±0.03	16.32±0.03	16.30±0.04
7.5	16.23±0.03	16.22±0.03	16.24±0.03	16.26±0.03	16.27±0.03	16.28±0.03	16.27±0.03	16.26±0.03
8.0	16.18±0.03	16.17±0.03	16.18±0.03	16.20±0.03	16.22±0.03	16.23±0.03	16.23±0.03	16.22±0.03
8.5	16.14±0.03	16.12±0.03	16.14±0.03	16.15±0.03	16.17±0.03	16.18±0.03	16.18±0.03	16.18±0.03
9.0	16.10±0.03	16.08±0.03	16.09±0.03	16.11±0.03	16.12±0.03	16.14±0.04	16.14±0.04	16.14±0.04
9.5	16.06±0.04	16.04±0.04	16.05±0.04	16.07±0.04	16.08±0.04	16.10±0.04	16.10±0.04	16.11±0.04
10.0	16.03±0.05	16.00±0.05	16.02±0.05	16.03±0.05	16.05±0.06	16.06±0.06	16.07±0.06	16.07±0.06

Table C.4— Magnitude of the fitted galaxy of IIIZw2 inside the aperture in the I filter.

Apert.	Seeing (arcsec)							
(arcsec)	1.0	2.0	3.0	4.0	5.0	6.0	7.0	8.0
1.0	17.76±0.22	17.31±0.22	16.95±0.22	16.67±0.22	16.46±0.22	16.29±0.22	16.15±0.22	16.04±0.22
1.5	17.32±0.09	17.10±0.09	16.84±0.09	16.61±0.09	16.42±0.09	16.27±0.09	16.14±0.09	16.03±0.09
2.0	16.94±0.05	16.86±0.05	16.70±0.05	16.53±0.05	16.37±0.05	16.23±0.05	16.11±0.05	16.01±0.05
2.5	16.66±0.05	16.64±0.05	16.55±0.05	16.43±0.05	16.30±0.05	16.18±0.04	16.08±0.04	15.99±0.04
3.0	16.44±0.05	16.44±0.05	16.41±0.05	16.33±0.05	16.23±0.04	16.13±0.04	16.04±0.04	15.96±0.04
3.5	16.26±0.05	16.27±0.05	16.27±0.04	16.23±0.04	16.16±0.04	16.08±0.04	16.00±0.04	15.93±0.04
4.0	16.13±0.04	16.13±0.04	16.15±0.04	16.13±0.04	16.08±0.04	16.02±0.04	15.95±0.04	15.89±0.04
4.5	16.01±0.04	16.01±0.04	16.04±0.04	16.03±0.04	16.00±0.04	15.96±0.04	15.91±0.04	15.86±0.04
5.0	15.91±0.04	15.91±0.04	15.94±0.04	15.95±0.04	15.93±0.04	15.90±0.04	15.86±0.04	15.82±0.04
5.5	15.83±0.04	15.82±0.04	15.85±0.04	15.87±0.04	15.86±0.04	15.84±0.04	15.81±0.04	15.78±0.04
6.0	15.76±0.04	15.75±0.04	15.77±0.04	15.79±0.04	15.80±0.04	15.79±0.04	15.77±0.04	15.74±0.04
6.5	15.69±0.04	15.68±0.04	15.71±0.04	15.73±0.04	15.74±0.04	15.73±0.04	15.72±0.04	15.70±0.04
7.0	15.64±0.04	15.63±0.04	15.65±0.04	15.67±0.04	15.68±0.04	15.68±0.04	15.68±0.04	15.66±0.04
7.5	15.59±0.05	15.57±0.05	15.59±0.05	15.61±0.05	15.63±0.05	15.64±0.05	15.63±0.05	15.62±0.05
8.0	15.54±0.05	15.53±0.05	15.55±0.05	15.56±0.05	15.58±0.05	15.59±0.05	15.59±0.05	15.59±0.05
8.5	15.50±0.05	15.49±0.05	15.50±0.05	15.52±0.05	15.54±0.05	15.55±0.05	15.55±0.05	15.55±0.05
9.0	15.47±0.05	15.45±0.05	15.46±0.05	15.48±0.05	15.50±0.05	15.51±0.05	15.52±0.05	15.52±0.05
9.5	15.44±0.05	15.42±0.05	15.43±0.05	15.45±0.05	15.46±0.05	15.48±0.05	15.48±0.05	15.49±0.05
10.0	15.41±0.05	15.39±0.05	15.40±0.05	15.41±0.05	15.43±0.05	15.44±0.05	15.45±0.05	15.46±0.05

TABLE C.5— Magnitude of the fitted galaxy of IZw1 inside the aperture in the B filter.

Apert.	Seeing (arcsec)							
(arcsec)	1.0	2.0	3.0	4.0	5.0	6.0	7.0	8.0
1.0	17.96±0.13	17.67±0.12	17.40±0.11	17.20±0.10	17.05±0.09	16.93±0.09	16.84±0.09	16.76±0.08
1.5	17.56±0.12	17.49±0.11	17.31±0.11	17.15±0.10	17.02±0.09	16.91±0.09	16.82±0.09	16.75±0.08
2.0	17.29±0.13	17.31±0.12	17.21±0.12	17.09±0.11	16.98±0.11	16.89±0.11	16.80±0.10	16.73±0.10
2.5	17.10±0.12	17.14±0.12	17.10±0.11	17.02±0.11	16.93±0.11	16.85±0.10	16.78±0.10	16.71±0.10
3.0	16.96±0.10	17.00±0.10	16.99±0.10	16.95±0.10	16.88±0.10	16.81±0.10	16.75±0.09	16.69±0.09
3.5	16.84±0.09	16.89±0.09	16.90±0.09	16.87±0.09	16.83±0.09	16.77±0.09	16.72±0.08	16.67±0.08
4.0	16.75±0.08	16.79±0.08	16.81±0.08	16.80±0.08	16.77±0.08	16.73±0.08	16.69±0.08	16.64±0.08
4.5	16.67±0.07	16.71±0.07	16.73±0.07	16.73±0.07	16.72±0.07	16.69±0.07	16.65±0.07	16.61±0.07
5.0	16.61±0.07	16.64±0.07	16.66±0.07	16.67±0.07	16.66±0.07	16.65±0.07	16.62±0.06	16.59±0.06
5.5	16.55±0.06	16.58±0.06	16.60±0.06	16.61±0.06	16.61±0.06	16.60±0.06	16.58±0.06	16.56±0.06
6.0	16.50±0.06	16.53±0.06	16.55±0.06	16.56±0.06	16.57±0.06	16.56±0.06	16.55±0.06	16.53±0.06
6.5	16.46±0.06	16.48±0.06	16.50±0.06	16.51±0.06	16.52±0.06	16.52±0.06	16.51±0.06	16.50±0.06
7.0	16.42±0.06	16.44±0.06	16.45±0.06	16.47±0.06	16.48±0.06	16.48±0.06	16.48±0.06	16.47±0.06
7.5	16.38±0.06	16.40±0.06	16.42±0.06	16.43±0.06	16.44±0.06	16.45±0.06	16.45±0.06	16.44±0.06
8.0	16.35±0.06	16.37±0.06	16.38±0.06	16.40±0.06	16.41±0.06	16.42±0.06	16.42±0.06	16.41±0.06
8.5	16.32±0.06	16.34±0.06	16.35±0.06	16.36±0.06	16.38±0.06	16.38±0.06	16.39±0.06	16.39±0.06
9.0	16.30±0.06	16.31±0.06	16.32±0.06	16.33±0.06	16.34±0.06	16.35±0.06	16.36±0.06	16.36±0.06
9.5	16.27±0.07	16.28±0.07	16.29±0.07	16.31±0.07	16.32±0.07	16.33±0.07	16.33±0.07	16.34±0.07
10.0	16.25±0.07	16.26±0.07	16.27±0.07	16.28±0.07	16.29±0.07	16.30±0.07	16.31±0.07	16.31±0.07

TABLE C.6— Magnitude of the fitted galaxy of IZw1 inside the aperture in the V filter.

Apert.	Seeing (arcsec)							
(arcsec)	1.0	2.0	3.0	4.0	5.0	6.0	7.0	8.0
1.0	17.00±0.13	16.75±0.11	16.52±0.09	16.36±0.08	16.25±0.07	16.17±0.07	16.11±0.06	16.07±0.05
1.5	16.63±0.11	16.54±0.10	16.37±0.09	16.22±0.08	16.09±0.07	15.98±0.07	15.89±0.06	15.81±0.05
2.0	16.37±0.10	16.36±0.09	16.27±0.09	16.15±0.08	16.04±0.07	15.94±0.06	15.85±0.06	15.77±0.05
2.5	16.19±0.08	16.21±0.08	16.17±0.08	16.09±0.07	16.00±0.07	15.91±0.06	15.83±0.06	15.76±0.05
3.0	16.05±0.08	16.08±0.08	16.07±0.07	16.02±0.07	15.95±0.06	15.88±0.06	15.81±0.05	15.74±0.05
3.5	15.95±0.07	15.97±0.07	15.98±0.07	15.96±0.06	15.91±0.06	15.85±0.06	15.79±0.05	15.73±0.05
4.0	15.86±0.06	15.88±0.06	15.90±0.06	15.89±0.06	15.86±0.06	15.82±0.05	15.77±0.05	15.72±0.05
4.5	15.80±0.06	15.81±0.06	15.83±0.06	15.84±0.06	15.82±0.05	15.79±0.05	15.75±0.05	15.71±0.05
5.0	15.74±0.05	15.75±0.05	15.78±0.05	15.78±0.05	15.78±0.05	15.76±0.05	15.73±0.05	15.69±0.05
5.5	15.69±0.05	15.70±0.05	15.72±0.05	15.74±0.05	15.74±0.05	15.72±0.05	15.70±0.05	15.67±0.05
6.0	15.65±0.05	15.66±0.05	15.68±0.05	15.69±0.05	15.70±0.05	15.69±0.05	15.67±0.05	15.65±0.05
6.5	15.61±0.05	15.62±0.05	15.63±0.05	15.65±0.05	15.66±0.05	15.65±0.05	15.64±0.05	15.63±0.05
7.0	15.57±0.05	15.58±0.05	15.59±0.05	15.61±0.05	15.62±0.05	15.62±0.05	15.61±0.05	15.60±0.05
7.5	15.54±0.05	15.54±0.05	15.56±0.05	15.57±0.05	15.58±0.05	15.58±0.05	15.58±0.05	15.57±0.05
8.0	15.51±0.04	15.51±0.04	15.52±0.04	15.53±0.05	15.54±0.05	15.54±0.05	15.54±0.04	15.53±0.04
8.5	15.47±0.04	15.47±0.04	15.48±0.04	15.49±0.04	15.50±0.04	15.51±0.04	15.51±0.04	15.50±0.04
9.0	15.44±0.04	15.44±0.04	15.45±0.04	15.46±0.04	15.46±0.04	15.47±0.04	15.47±0.04	15.47±0.04
9.5	15.41±0.04	15.41±0.04	15.42±0.04	15.42±0.04	15.43±0.04	15.43±0.04	15.43±0.04	15.43±0.04
10.0	15.38±0.03	15.38±0.03	15.38±0.03	15.39±0.03	15.39±0.03	15.40±0.03	15.40±0.03	15.40±0.03

Table C.7— Magnitude of the fitted galaxy of IZw1 inside the aperture in the R filter.

Apert.	Seeing (arcsec)							
(arcsec)	1.0	2.0	3.0	4.0	5.0	6.0	7.0	8.0
1.0	16.40±0.07	16.15±0.06	15.92±0.05	15.75±0.05	15.61±0.04	15.51±0.04	15.42±0.04	15.35±0.03
1.5	16.08±0.06	16.00±0.05	15.85±0.05	15.71±0.04	15.59±0.04	15.49±0.04	15.41±0.03	15.35±0.03
2.0	15.85±0.05	15.84±0.05	15.76±0.04	15.66±0.04	15.56±0.04	15.47±0.03	15.40±0.03	15.34±0.03
2.5	15.68±0.04	15.70±0.04	15.66±0.04	15.59±0.04	15.52±0.03	15.45±0.03	15.38±0.03	15.32±0.03
3.0	15.55±0.04	15.58±0.04	15.57±0.04	15.53±0.03	15.47±0.03	15.41±0.03	15.36±0.03	15.31±0.02
3.5	15.45±0.03	15.47±0.03	15.48±0.03	15.46±0.03	15.42±0.03	15.38±0.03	15.33±0.02	15.28±0.02
4.0	15.37±0.03	15.39±0.03	15.40±0.03	15.40±0.03	15.37±0.03	15.34±0.03	15.30±0.02	15.26±0.02
4.5	15.30±0.03	15.31±0.03	15.33±0.03	15.34±0.03	15.32±0.03	15.30±0.02	15.27±0.02	15.24±0.02
5.0	15.24±0.02	15.25±0.02	15.27±0.02	15.28±0.02	15.28±0.02	15.26±0.02	15.24±0.02	15.21±0.02
5.5	15.19±0.02	15.20±0.02	15.22±0.02	15.23±0.02	15.23±0.02	15.22±0.02	15.21±0.02	15.18±0.02
6.0	15.15±0.02	15.15±0.02	15.17±0.02	15.19±0.02	15.19±0.02	15.19±0.02	15.18±0.02	15.16±0.02
6.5	15.11±0.02	15.11±0.02	15.13±0.02	15.14±0.02	15.15±0.02	15.15±0.02	15.15±0.02	15.13±0.02
7.0	15.07±0.02	15.08±0.02	15.09±0.02	15.11±0.02	15.12±0.02	15.12±0.02	15.12±0.02	15.11±0.01
7.5	15.04±0.01	15.04±0.01	15.06±0.01	15.07±0.01	15.08±0.01	15.09±0.01	15.09±0.01	15.08±0.01
8.0	15.02±0.01	15.01±0.01	15.03±0.01	15.04±0.01	15.05±0.01	15.06±0.01	15.06±0.01	15.06±0.01
8.5	14.99±0.01	14.99±0.01	15.00±0.01	15.01±0.01	15.02±0.01	15.03±0.01	15.04±0.01	15.04±0.01
9.0	14.97±0.01	14.96±0.01	14.97±0.01	14.98±0.01	15.00±0.01	15.01±0.01	15.01±0.01	15.01±0.01
9.5	14.95±0.02	14.94±0.02	14.95±0.02	14.96±0.02	14.97±0.02	14.98±0.02	14.99±0.02	14.99±0.02
10.0	14.93±0.02	14.92±0.02	14.93±0.02	14.94±0.02	14.95±0.02	14.96±0.02	14.97±0.02	14.97±0.02

Table C.8— Magnitude of the fitted galaxy of IZw1 inside the aperture in the I filter.

Apert.	Seeing (arcsec)							
(arcsec)	1.0	2.0	3.0	4.0	5.0	6.0	7.0	8.0
1.0	15.38±0.05	15.16±0.04	14.96±0.03	14.81±0.03	14.70±0.03	14.61±0.02	14.53±0.02	14.47±0.02
1.5	15.10±0.04	15.02±0.04	14.89±0.03	14.77±0.03	14.67±0.03	14.59±0.02	14.52±0.02	14.46±0.02
2.0	14.89±0.03	14.88±0.03	14.81±0.03	14.72±0.03	14.64±0.02	14.57±0.02	14.51±0.02	14.45±0.02
2.5	14.74±0.03	14.75±0.03	14.73±0.03	14.67±0.02	14.60±0.02	14.54±0.02	14.49±0.02	14.44±0.02
3.0	14.63±0.02	14.65±0.02	14.64±0.02	14.61±0.02	14.56±0.02	14.51±0.02	14.46±0.02	14.42±0.01
3.5	14.54±0.02	14.56±0.02	14.57±0.02	14.55±0.02	14.52±0.02	14.48±0.01	14.44±0.01	14.40±0.01
4.0	14.47±0.01	14.48±0.01	14.50±0.01	14.50±0.01	14.48±0.01	14.45±0.01	14.42±0.01	14.38±0.01
4.5	14.41±0.01	14.42±0.01	14.44±0.01	14.45±0.01	14.44±0.01	14.42±0.01	14.39±0.01	14.36±0.01
5.0	14.37±0.01	14.37±0.01	14.39±0.01	14.40±0.01	14.40±0.01	14.38±0.01	14.36±0.01	14.34±0.00
5.5	14.32±0.00	14.32±0.01	14.34±0.01	14.35±0.01	14.36±0.00	14.35±0.00	14.34±0.00	14.32±0.00
6.0	14.29±0.00	14.28±0.00	14.30±0.00	14.32±0.00	14.32±0.00	14.32±0.00	14.31±0.00	14.30±0.00
6.5	14.26±0.00	14.25±0.00	14.27±0.00	14.28±0.00	14.29±0.00	14.29±0.00	14.29±0.00	14.28±0.00
7.0	14.23±0.00	14.22±0.00	14.23±0.00	14.25±0.00	14.26±0.00	14.26±0.00	14.26±0.00	14.25±0.00
7.5	14.20±0.01	14.19±0.01	14.21±0.01	14.22±0.01	14.23±0.01	14.24±0.01	14.24±0.01	14.23±0.01
8.0	14.18±0.01	14.17±0.01	14.18±0.01	14.19±0.01	14.20±0.01	14.21±0.01	14.21±0.01	14.21±0.01
8.5	14.16±0.01	14.15±0.01	14.16±0.01	14.17±0.01	14.18±0.01	14.19±0.01	14.19±0.01	14.19±0.01
9.0	14.14±0.02	14.13±0.02	14.14±0.02	14.15±0.02	14.16±0.02	14.17±0.02	14.17±0.02	14.17±0.02
9.5	14.12±0.02	14.11±0.02	14.12±0.02	14.13±0.02	14.14±0.02	14.15±0.02	14.15±0.02	14.16±0.02
10.0	14.11±0.02	14.10±0.02	14.10±0.02	14.11±0.02	14.12±0.02	14.13±0.02	14.14±0.02	14.14±0.02

TABLE C.9— Magnitude of the fitted galaxy of Mkn205 inside the aperture in the B filter.

Apert.	Seeing (arcsec)							
(arcsec)	1.0	2.0	3.0	4.0	5.0	6.0	7.0	8.0
1.0	18.53±0.12	18.27±0.10	18.04±0.09	17.88±0.08	17.75±0.08	17.66±0.08	17.58±0.08	17.52±0.08
1.5	18.20±0.11	18.12±0.10	17.97±0.10	17.84±0.09	17.73±0.09	17.64±0.09	17.57±0.09	17.52±0.09
2.0	17.96±0.10	17.96±0.10	17.88±0.10	17.78±0.09	17.69±0.09	17.62±0.09	17.56±0.09	17.50±0.09
2.5	17.79±0.10	17.81±0.10	17.79±0.10	17.72±0.10	17.66±0.09	17.59±0.09	17.54±0.10	17.49±0.10
3.0	17.66±0.10	17.70±0.10	17.70±0.10	17.66±0.10	17.61±0.10	17.56±0.10	17.52±0.10	17.47±0.10
3.5	17.57±0.11	17.60±0.12	17.61±0.11	17.60±0.11	17.57±0.12	17.53±0.12	17.49±0.12	17.45±0.12
4.0	17.50±0.13	17.52±0.13	17.54±0.13	17.54±0.13	17.52±0.13	17.50±0.13	17.47±0.13	17.44±0.13
4.5	17.44±0.14	17.45±0.14	17.48±0.14	17.49±0.14	17.48±0.14	17.46±0.14	17.44±0.14	17.42±0.15
5.0	17.39±0.15	17.40±0.15	17.43±0.15	17.44±0.15	17.44±0.15	17.43±0.15	17.41±0.16	17.40±0.16
5.5	17.35±0.16	17.36±0.16	17.38±0.16	17.40±0.16	17.40±0.16	17.40±0.16	17.39±0.16	17.37±0.17
6.0	17.32±0.18	17.32±0.17	17.34±0.17	17.36±0.17	17.37±0.17	17.37±0.18	17.36±0.18	17.35±0.18
6.5	17.29±0.19	17.29±0.19	17.31±0.19	17.33±0.19	17.34±0.19	17.34±0.19	17.34±0.19	17.33±0.19
7.0	17.27±0.20	17.27±0.20	17.28±0.20	17.30±0.20	17.31±0.20	17.32±0.20	17.32±0.20	17.31±0.20
7.5	17.25±0.22	17.24±0.22	17.26±0.22	17.27±0.22	17.28±0.22	17.29±0.22	17.30±0.22	17.29±0.22
8.0	17.23±0.23	17.23±0.23	17.24±0.23	17.25±0.23	17.26±0.23	17.27±0.23	17.28±0.23	17.28±0.23
8.5	17.21±0.25	17.21±0.25	17.22±0.25	17.23±0.25	17.24±0.25	17.25±0.25	17.26±0.25	17.26±0.25
9.0	17.20±0.26	17.19±0.26	17.20±0.26	17.21±0.26	17.22±0.26	17.23±0.26	17.24±0.26	17.24±0.26
9.5	17.19±0.28	17.18±0.28	17.19±0.28	17.20±0.28	17.21±0.28	17.22±0.28	17.22±0.28	17.23±0.28
10.0	17.17±0.30	17.17±0.30	17.17±0.30	17.18±0.30	17.19±0.30	17.20±0.29	17.21±0.29	17.21±0.29

TABLE C.10— Magnitude of the fitted galaxy of Mkn205 inside the aperture in the V filter.

Apert.	Seeing (arcsec)							
(arcsec)	1.0	2.0	3.0	4.0	5.0	6.0	7.0	8.0
1.0	17.72±0.07	17.43±0.07	17.16±0.07	16.96±0.07	16.82±0.07	16.70±0.07	16.61±0.07	16.53±0.07
1.5	17.34±0.05	17.25±0.05	17.07±0.05	16.92±0.05	16.79±0.05	16.68±0.05	16.60±0.05	16.52±0.05
2.0	17.07±0.05	17.07±0.05	16.97±0.05	16.86±0.05	16.75±0.05	16.66±0.05	16.58±0.05	16.51±0.05
2.5	16.87±0.05	16.91±0.05	16.87±0.05	16.79±0.05	16.71±0.05	16.63±0.05	16.56±0.05	16.50±0.05
3.0	16.72±0.06	16.77±0.06	16.76±0.06	16.72±0.06	16.65±0.06	16.59±0.06	16.53±0.06	16.48±0.06
3.5	16.61±0.08	16.65±0.08	16.67±0.08	16.64±0.08	16.60±0.08	16.55±0.08	16.50±0.08	16.46±0.08
4.0	16.52±0.10	16.56±0.10	16.58±0.10	16.57±0.10	16.55±0.10	16.51±0.10	16.47±0.10	16.43±0.10
4.5	16.45±0.10	16.48±0.10	16.50±0.10	16.51±0.10	16.50±0.10	16.47±0.10	16.44±0.10	16.41±0.10
5.0	16.39±0.11	16.41±0.11	16.44±0.11	16.45±0.11	16.45±0.11	16.43±0.11	16.41±0.11	16.38±0.11
5.5	16.33±0.12	16.36±0.12	16.38±0.12	16.40±0.12	16.40±0.12	16.39±0.12	16.38±0.12	16.36±0.12
6.0	16.29±0.12	16.31±0.12	16.33±0.12	16.35±0.12	16.36±0.12	16.36±0.12	16.35±0.12	16.33±0.12
6.5	16.25±0.13	16.27±0.13	16.29±0.13	16.31±0.13	16.32±0.13	16.32±0.13	16.31±0.13	16.30±0.13
7.0	16.22±0.14	16.23±0.14	16.25±0.14	16.27±0.14	16.28±0.14	16.29±0.14	16.29±0.14	16.28±0.14
7.5	16.19±0.15	16.20±0.15	16.22±0.15	16.23±0.15	16.25±0.15	16.26±0.15	16.26±0.15	16.25±0.15
8.0	16.16±0.16	16.17±0.16	16.19±0.16	16.20±0.16	16.22±0.16	16.23±0.16	16.23±0.16	16.23±0.16
8.5	16.14±0.17	16.15±0.17	16.16±0.17	16.18±0.17	16.19±0.17	16.20±0.17	16.21±0.17	16.21±0.17
9.0	16.12±0.19	16.13±0.19	16.14±0.19	16.15±0.19	16.17±0.19	16.18±0.19	16.18±0.19	16.19±0.19
9.5	16.10±0.20	16.11±0.20	16.12±0.20	16.13±0.20	16.14±0.20	16.15±0.20	16.16±0.20	16.17±0.20
10.0	16.09±0.21	16.09±0.21	16.10±0.21	16.11±0.21	16.12±0.21	16.13±0.21	16.14±0.21	16.15±0.21

Table C.11— Magnitude of the fitted galaxy of Mkn205 inside the aperture in the R filter.

Apert.	Seeing (arcsec)							
(arcsec)	1.0	2.0	3.0	4.0	5.0	6.0	7.0	8.0
1.0	17.01±0.05	16.74±0.04	16.50±0.04	16.32±0.04	16.18±0.04	16.08±0.04	15.99±0.04	15.93±0.03
1.5	16.66±0.04	16.57±0.04	16.41±0.04	16.27±0.04	16.15±0.03	16.05±0.03	15.98±0.03	15.91±0.03
2.0	16.40±0.04	16.40±0.04	16.31±0.04	16.21±0.04	16.11±0.04	16.03±0.04	15.96±0.04	15.90±0.04
2.5	16.21±0.05	16.25±0.05	16.21±0.05	16.14±0.05	16.07±0.05	15.99±0.05	15.93±0.05	15.88±0.05
3.0	16.08±0.07	16.12±0.07	16.11±0.07	16.07±0.07	16.02±0.07	15.96±0.07	15.91±0.07	15.86±0.07
3.5	15.98±0.09	16.01±0.09	16.03±0.09	16.01±0.09	15.97±0.09	15.93±0.09	15.88±0.09	15.84±0.09
4.0	15.90±0.11	15.92±0.11	15.95±0.11	15.95±0.11	15.92±0.11	15.89±0.11	15.86±0.11	15.82±0.11
4.5	15.83±0.12	15.85±0.12	15.88±0.12	15.89±0.12	15.88±0.12	15.86±0.12	15.83±0.12	15.80±0.12
5.0	15.78±0.13	15.79±0.13	15.82±0.13	15.83±0.13	15.83±0.13	15.82±0.13	15.80±0.13	15.78±0.13
5.5	15.73±0.14	15.74±0.14	15.77±0.14	15.78±0.14	15.79±0.14	15.78±0.14	15.77±0.14	15.75±0.14
6.0	15.69±0.15	15.70±0.15	15.72±0.15	15.74±0.15	15.75±0.15	15.75±0.15	15.74±0.15	15.73±0.15
6.5	15.66±0.16	15.67±0.16	15.69±0.16	15.70±0.16	15.71±0.16	15.72±0.16	15.71±0.16	15.71±0.16
7.0	15.63±0.17	15.64±0.17	15.65±0.17	15.67±0.17	15.68±0.17	15.69±0.17	15.69±0.17	15.68±0.17
7.5	15.61±0.19	15.61±0.19	15.62±0.19	15.64±0.19	15.65±0.19	15.66±0.19	15.67±0.19	15.66±0.19
8.0	15.58±0.20	15.59±0.20	15.60±0.20	15.61±0.20	15.63±0.20	15.64±0.20	15.64±0.20	15.64±0.20
8.5	15.57±0.21	15.57±0.21	15.58±0.21	15.59±0.21	15.60±0.21	15.61±0.21	15.62±0.21	15.62±0.21
9.0	15.55±0.23	15.55±0.23	15.56±0.23	15.57±0.23	15.58±0.23	15.59±0.23	15.60±0.23	15.60±0.23
9.5	15.53±0.24	15.53±0.24	15.54±0.24	15.55±0.24	15.56±0.24	15.57±0.24	15.58±0.24	15.59±0.24
10.0	15.52±0.26	15.52±0.26	15.53±0.26	15.54±0.26	15.55±0.26	15.56±0.26	15.56±0.26	15.57±0.26

Table C.12— Magnitude of the fitted galaxy of Mkn205 inside the aperture in the I filter.

Apert.	Seeing (arcsec)							
(arcsec)	1.0	2.0	3.0	4.0	5.0	6.0	7.0	8.0
1.0	16.04±0.03	15.78±0.03	15.56±0.03	15.39±0.03	15.27±0.03	15.18±0.03	15.11±0.03	15.05±0.03
1.5	15.72±0.03	15.62±0.03	15.48±0.03	15.35±0.03	15.25±0.03	15.16±0.03	15.10±0.03	15.04±0.03
2.0	15.48±0.03	15.47±0.03	15.39±0.03	15.30±0.03	15.21±0.03	15.14±0.03	15.08±0.03	15.03±0.03
2.5	15.32±0.04	15.33±0.04	15.30±0.04	15.24±0.04	15.18±0.04	15.12±0.04	15.06±0.04	15.02±0.04
3.0	15.20±0.05	15.21±0.05	15.21±0.05	15.18±0.05	15.14±0.05	15.09±0.05	15.04±0.05	15.00±0.05
3.5	15.11±0.06	15.12±0.06	15.14±0.06	15.12±0.06	15.09±0.06	15.06±0.06	15.02±0.06	14.99±0.06
4.0	15.04±0.07	15.04±0.07	15.07±0.07	15.07±0.07	15.05±0.07	15.02±0.07	15.00±0.07	14.97±0.07
4.5	14.99±0.08	14.98±0.08	15.01±0.08	15.02±0.08	15.01±0.08	14.99±0.08	14.97±0.08	14.95±0.08
5.0	14.94±0.09	14.93±0.09	14.96±0.09	14.97±0.09	14.97±0.09	14.96±0.09	14.95±0.09	14.93±0.09
5.5	14.90±0.09	14.89±0.09	14.91±0.09	14.93±0.09	14.94±0.09	14.93±0.09	14.92±0.09	14.91±0.09
6.0	14.87±0.11	14.86±0.11	14.88±0.11	14.89±0.11	14.90±0.11	14.90±0.11	14.90±0.11	14.89±0.11
6.5	14.85±0.12	14.83±0.12	14.85±0.12	14.86±0.12	14.87±0.12	14.88±0.12	14.88±0.12	14.87±0.12
7.0	14.82±0.13	14.80±0.13	14.82±0.13	14.83±0.13	14.85±0.13	14.85±0.13	14.85±0.13	14.85±0.13
7.5	14.80±0.14	14.78±0.14	14.80±0.14	14.81±0.14	14.82±0.14	14.83±0.14	14.83±0.14	14.83±0.14
8.0	14.79±0.15	14.77±0.15	14.78±0.15	14.79±0.15	14.80±0.15	14.81±0.15	14.81±0.15	14.82±0.15
8.5	14.77±0.17	14.75±0.17	14.76±0.17	14.77±0.17	14.78±0.17	14.79±0.17	14.80±0.17	14.80±0.17
9.0	14.76±0.18	14.74±0.18	14.74±0.18	14.75±0.18	14.76±0.18	14.77±0.18	14.78±0.18	14.78±0.18
9.5	14.75±0.19	14.72±0.19	14.73±0.19	14.74±0.19	14.75±0.19	14.76±0.19	14.77±0.19	14.77±0.19
10.0	14.74±0.21	14.71±0.21	14.72±0.21	14.73±0.21	14.74±0.21	14.74±0.21	14.75±0.21	14.76±0.21

TABLE C.13— Magnitude of the fitted galaxy of PG1351 inside the aperture in the B filter.

Apert.	Seeing (arcsec)							
(arcsec)	1.0	2.0	3.0	4.0	5.0	6.0	7.0	8.0
1.0	18.01±0.26	17.88±0.22	17.74±0.18	17.64±0.16	17.57±0.14	17.51±0.13	17.46±0.13	17.43±0.12
1.5	17.79±0.18	17.78±0.16	17.69±0.14	17.62±0.11	17.55±0.09	17.50±0.07	17.46±0.06	17.42±0.06
2.0	17.64±0.14	17.68±0.14	17.64±0.12	17.58±0.10	17.53±0.08	17.49±0.07	17.45±0.06	17.42±0.06
2.5	17.54±0.11	17.59±0.11	17.58±0.10	17.55±0.09	17.51±0.07	17.47±0.06	17.44±0.06	17.41±0.05
3.0	17.46±0.09	17.52±0.09	17.53±0.09	17.51±0.08	17.48±0.07	17.45±0.06	17.43±0.05	17.40±0.05
3.5	17.41±0.07	17.46±0.07	17.48±0.07	17.47±0.07	17.45±0.06	17.43±0.05	17.41±0.05	17.39±0.05
4.0	17.37±0.05	17.41±0.06	17.43±0.06	17.44±0.06	17.43±0.05	17.41±0.05	17.40±0.05	17.38±0.05
4.5	17.34±0.05	17.38±0.05	17.40±0.05	17.40±0.05	17.40±0.05	17.39±0.05	17.38±0.05	17.37±0.05
5.0	17.31±0.04	17.35±0.04	17.37±0.04	17.38±0.04	17.38±0.04	17.37±0.04	17.37±0.05	17.35±0.05
5.5	17.29±0.05	17.33±0.04	17.34±0.04	17.35±0.04	17.36±0.04	17.36±0.04	17.35±0.05	17.34±0.05
6.0	17.27±0.05	17.31±0.05	17.32±0.05	17.33±0.05	17.34±0.05	17.34±0.05	17.34±0.05	17.33±0.05
6.5	17.26±0.06	17.29±0.05	17.30±0.05	17.31±0.05	17.32±0.05	17.32±0.05	17.32±0.05	17.32±0.06
7.0	17.25±0.06	17.27±0.06	17.28±0.06	17.29±0.06	17.30±0.06	17.31±0.06	17.31±0.06	17.31±0.06
7.5	17.24±0.07	17.26±0.07	17.27±0.07	17.28±0.06	17.29±0.06	17.29±0.06	17.30±0.06	17.30±0.06
8.0	17.23±0.08	17.25±0.07	17.26±0.07	17.27±0.07	17.27±0.07	17.28±0.07	17.28±0.07	17.29±0.07
8.5	17.22±0.08	17.24±0.08	17.25±0.08	17.26±0.08	17.26±0.07	17.27±0.07	17.27±0.07	17.28±0.07
9.0	17.21±0.09	17.23±0.09	17.24±0.08	17.25±0.08	17.25±0.08	17.26±0.08	17.26±0.08	17.27±0.08
9.5	17.20±0.09	17.23±0.09	17.23±0.09	17.24±0.09	17.24±0.09	17.25±0.09	17.25±0.08	17.26±0.08
10.0	17.20±0.10	17.22±0.10	17.22±0.10	17.23±0.09	17.24±0.09	17.24±0.09	17.25±0.09	17.25±0.09

TABLE C.14— Magnitude of the fitted galaxy of PG1351 inside the aperture in the V filter.

Apert.	Seeing (arcsec)							
(arcsec)	1.0	2.0	3.0	4.0	5.0	6.0	7.0	8.0
1.0	17.29±0.42	17.15±0.37	17.01±0.32	16.91±0.28	16.83±0.25	16.78±0.22	16.73±0.20	16.70±0.19
1.5	17.08±0.36	17.04±0.34	16.96±0.30	16.88±0.27	16.81±0.24	16.76±0.22	16.72±0.20	16.69±0.18
2.0	16.93±0.31	16.94±0.30	16.90±0.28	16.84±0.26	16.79±0.23	16.75±0.21	16.71±0.19	16.68±0.18
2.5	16.82±0.27	16.85±0.27	16.84±0.26	16.80±0.24	16.77±0.22	16.73±0.21	16.70±0.19	16.67±0.17
3.0	16.75±0.24	16.78±0.25	16.78±0.24	16.77±0.23	16.74±0.21	16.71±0.20	16.68±0.18	16.66±0.17
3.5	16.70±0.22	16.72±0.22	16.73±0.22	16.73±0.21	16.71±0.20	16.69±0.19	16.67±0.18	16.65±0.17
4.0	16.66±0.20	16.67±0.20	16.69±0.20	16.70±0.20	16.69±0.19	16.67±0.18	16.66±0.17	16.64±0.16
4.5	16.63±0.18	16.64±0.18	16.66±0.19	16.66±0.18	16.66±0.18	16.65±0.17	16.64±0.16	16.63±0.15
5.0	16.60±0.16	16.61±0.17	16.63±0.17	16.64±0.17	16.64±0.17	16.63±0.16	16.63±0.16	16.61±0.15
5.5	16.58±0.15	16.59±0.15	16.60±0.16	16.61±0.16	16.62±0.16	16.61±0.15	16.61±0.15	16.60±0.14
6.0	16.56±0.14	16.57±0.14	16.58±0.14	16.59±0.15	16.60±0.15	16.60±0.14	16.60±0.14	16.59±0.14
6.5	16.55±0.13	16.55±0.13	16.56±0.13	16.57±0.14	16.58±0.14	16.58±0.14	16.58±0.13	16.58±0.13
7.0	16.53±0.12	16.53±0.12	16.54±0.13	16.55±0.13	16.56±0.13	16.57±0.13	16.57±0.13	16.57±0.12
7.5	16.52±0.11	16.52±0.11	16.53±0.12	16.54±0.12	16.55±0.12	16.55±0.12	16.56±0.12	16.56±0.12
8.0	16.51±0.11	16.51±0.11	16.52±0.11	16.53±0.11	16.53±0.11	16.54±0.11	16.54±0.11	16.55±0.11
8.5	16.51±0.10	16.50±0.10	16.51±0.10	16.52±0.11	16.52±0.11	16.53±0.11	16.53±0.11	16.54±0.11
9.0	16.50±0.10	16.50±0.10	16.50±0.10	16.51±0.10	16.51±0.10	16.52±0.10	16.52±0.10	16.53±0.10
9.5	16.49±0.09	16.49±0.09	16.49±0.09	16.50±0.09	16.50±0.10	16.51±0.10	16.51±0.10	16.52±0.10
10.0	16.49±0.09	16.48±0.09	16.49±0.09	16.49±0.09	16.50±0.09	16.50±0.09	16.51±0.09	16.51±0.09

TABLE C.15— Magnitude of the fitted galaxy of PG1351 inside the aperture in the R filter.

Apert.	Seeing (arcsec)							
(arcsec)	1.0	2.0	3.0	4.0	5.0	6.0	7.0	8.0
1.0	17.32±0.16	17.08±0.14	16.90±0.12	16.75±0.11	16.65±0.10	16.56±0.09	16.50±0.09	16.44±0.08
1.5	17.05±0.14	16.97±0.13	16.84±0.12	16.73±0.11	16.63±0.10	16.56±0.09	16.49±0.08	16.44±0.08
2.0	16.85±0.12	16.84±0.12	16.77±0.11	16.69±0.10	16.61±0.09	16.55±0.09	16.49±0.08	16.44±0.07
2.5	16.71±0.11	16.72±0.11	16.69±0.10	16.64±0.10	16.58±0.09	16.53±0.08	16.48±0.08	16.43±0.07
3.0	16.61±0.10	16.62±0.10	16.62±0.10	16.59±0.09	16.55±0.09	16.50±0.08	16.46±0.07	16.42±0.07
3.5	16.53±0.09	16.53±0.09	16.55±0.09	16.53±0.09	16.51±0.08	16.47±0.08	16.44±0.07	16.40±0.07
4.0	16.47±0.08	16.46±0.08	16.48±0.08	16.48±0.08	16.47±0.08	16.44±0.07	16.41±0.07	16.38±0.07
4.5	16.41±0.07	16.41±0.07	16.43±0.08	16.43±0.07	16.43±0.07	16.41±0.07	16.39±0.07	16.36±0.06
5.0	16.37±0.07	16.36±0.07	16.38±0.07	16.39±0.07	16.39±0.07	16.38±0.07	16.36±0.07	16.34±0.06
5.5	16.34±0.06	16.32±0.06	16.34±0.07	16.35±0.07	16.36±0.07	16.35±0.06	16.34±0.06	16.33±0.06
6.0	16.30±0.06	16.29±0.06	16.30±0.06	16.32±0.06	16.32±0.06	16.32±0.06	16.32±0.06	16.31±0.06
6.5	16.28±0.06	16.26±0.06	16.27±0.06	16.29±0.06	16.30±0.06	16.30±0.06	16.30±0.06	16.29±0.06
7.0	16.25±0.05	16.23±0.05	16.25±0.05	16.26±0.06	16.27±0.06	16.27±0.06	16.27±0.06	16.27±0.05
7.5	16.23±0.05	16.21±0.05	16.22±0.05	16.23±0.05	16.24±0.05	16.25±0.05	16.25±0.05	16.25±0.05
8.0	16.21±0.05	16.19±0.05	16.20±0.05	16.21±0.05	16.22±0.05	16.23±0.05	16.23±0.05	16.23±0.05
8.5	16.20±0.05	16.17±0.05	16.18±0.05	16.19±0.05	16.20±0.05	16.21±0.05	16.21±0.05	16.22±0.05
9.0	16.18±0.04	16.16±0.04	16.17±0.05	16.17±0.05	16.18±0.05	16.19±0.05	16.20±0.05	16.20±0.05
9.5	16.17±0.04	16.14±0.04	16.15±0.04	16.16±0.04	16.17±0.05	16.18±0.05	16.18±0.05	16.19±0.05
10.0	16.16±0.04	16.13±0.04	16.14±0.04	16.14±0.04	16.15±0.04	16.16±0.04	16.17±0.04	16.17±0.04

TABLE C.16— Magnitude of the fitted galaxy of PG1351 inside the aperture in the I filter.

Apert.	Seeing (arcsec)							
(arcsec)	1.0	2.0	3.0	4.0	5.0	6.0	7.0	8.0
1.0	16.69±0.11	16.46±0.09	16.27±0.08	16.13±0.06	16.02±0.05	15.93±0.05	15.86±0.04	15.81±0.04
1.5	16.41±0.09	16.33±0.08	16.20±0.07	16.09±0.06	15.99±0.05	15.91±0.05	15.85±0.04	15.79±0.04
2.0	16.20±0.08	16.19±0.07	16.12±0.07	16.04±0.06	15.96±0.05	15.89±0.05	15.83±0.04	15.78±0.04
2.5	16.05±0.07	16.06±0.06	16.04±0.06	15.98±0.06	15.92±0.05	15.86±0.04	15.81±0.04	15.77±0.04
3.0	15.94±0.06	15.96±0.06	15.96±0.05	15.93±0.05	15.88±0.05	15.83±0.04	15.79±0.04	15.75±0.04
3.5	15.86±0.05	15.87±0.05	15.89±0.05	15.87±0.05	15.84±0.04	15.81±0.04	15.77±0.04	15.73±0.03
4.0	15.80±0.04	15.80±0.04	15.82±0.04	15.82±0.04	15.80±0.04	15.78±0.04	15.75±0.03	15.72±0.03
4.5	15.74±0.04	15.74±0.04	15.76±0.04	15.77±0.04	15.76±0.04	15.75±0.03	15.72±0.03	15.70±0.03
5.0	15.70±0.03	15.69±0.03	15.71±0.03	15.73±0.03	15.73±0.03	15.71±0.03	15.70±0.03	15.68±0.03
5.5	15.66±0.03	15.65±0.03	15.67±0.03	15.69±0.03	15.69±0.03	15.69±0.03	15.67±0.03	15.66±0.03
6.0	15.63±0.03	15.62±0.03	15.63±0.03	15.65±0.03	15.66±0.03	15.66±0.03	15.65±0.03	15.64±0.03
6.5	15.60±0.03	15.59±0.03	15.60±0.03	15.62±0.03	15.63±0.03	15.63±0.03	15.63±0.03	15.62±0.03
7.0	15.57±0.03	15.56±0.03	15.57±0.03	15.59±0.03	15.60±0.03	15.60±0.03	15.60±0.03	15.60±0.03
7.5	15.55±0.03	15.54±0.03	15.55±0.03	15.56±0.03	15.57±0.03	15.58±0.03	15.58±0.03	15.58±0.03
8.0	15.53±0.03	15.52±0.03	15.53±0.03	15.54±0.03	15.55±0.03	15.56±0.03	15.56±0.03	15.56±0.03
8.5	15.51±0.04	15.50±0.03	15.51±0.03	15.52±0.03	15.53±0.03	15.54±0.03	15.54±0.03	15.54±0.03
9.0	15.50±0.04	15.48±0.04	15.49±0.04	15.50±0.04	15.51±0.04	15.52±0.04	15.52±0.04	15.53±0.04
9.5	15.48±0.04	15.47±0.04	15.47±0.04	15.48±0.04	15.49±0.04	15.50±0.04	15.51±0.04	15.51±0.04
10.0	15.47±0.04	15.45±0.04	15.46±0.04	15.47±0.04	15.48±0.04	15.48±0.04	15.49±0.04	15.50±0.04

TABLE C.17— Magnitude of the fitted galaxy of APLib inside the aperture in the B filter.

Apert.	Seeing (arcsec)							
(arcsec)	1.0	2.0	3.0	4.0	5.0	6.0	7.0	8.0
1.0	17.86±0.32	17.54±0.33	17.26±0.37	17.05±0.41	16.88±0.44	16.74±0.48	16.62±0.51	16.52±0.54
1.5	17.53±0.32	17.37±0.34	17.17±0.37	16.99±0.41	16.84±0.44	16.71±0.48	16.60±0.51	16.51±0.54
2.0	17.24±0.34	17.18±0.35	17.06±0.38	16.93±0.41	16.80±0.45	16.68±0.48	16.58±0.51	16.49±0.53
2.5	17.02±0.36	17.01±0.37	16.95±0.39	16.85±0.42	16.74±0.45	16.64±0.48	16.55±0.51	16.47±0.53
3.0	16.85±0.40	16.86±0.40	16.83±0.41	16.77±0.44	16.68±0.46	16.60±0.49	16.52±0.51	16.44±0.54
3.5	16.72±0.43	16.72±0.43	16.72±0.44	16.68±0.46	16.62±0.48	16.55±0.50	16.48±0.52	16.41±0.55
4.0	16.60±0.46	16.60±0.46	16.62±0.47	16.60±0.48	16.56±0.50	16.50±0.51	16.44±0.53	16.38±0.55
4.5	16.51±0.49	16.50±0.49	16.52±0.49	16.52±0.50	16.49±0.51	16.45±0.53	16.40±0.55	16.35±0.56
5.0	16.42±0.52	16.42±0.52	16.44±0.52	16.44±0.52	16.42±0.53	16.39±0.54	16.36±0.56	16.31±0.57
5.5	16.35±0.54	16.34±0.54	16.36±0.54	16.37±0.54	16.36±0.55	16.34±0.56	16.31±0.57	16.28±0.59
6.0	16.28±0.57	16.27±0.56	16.29±0.56	16.30±0.56	16.30±0.57	16.29±0.57	16.27±0.58	16.24±0.60
6.5	16.22±0.58	16.21±0.58	16.23±0.58	16.24±0.58	16.25±0.58	16.24±0.59	16.22±0.60	16.20±0.61
7.0	16.17±0.60	16.15±0.60	16.17±0.60	16.19±0.60	16.19±0.60	16.19±0.60	16.18±0.61	16.16±0.62
7.5	16.12±0.62	16.10±0.62	16.12±0.62	16.13±0.61	16.14±0.61	16.15±0.62	16.14±0.62	16.13±0.63
8.0	16.08±0.63	16.06±0.63	16.07±0.63	16.08±0.63	16.10±0.63	16.10±0.63	16.10±0.64	16.09±0.64
8.5	16.03±0.65	16.01±0.65	16.03±0.65	16.04±0.64	16.05±0.64	16.06±0.64	16.06±0.65	16.06±0.65
9.0	16.00±0.66	15.97±0.66	15.99±0.66	16.00±0.66	16.01±0.66	16.02±0.66	16.02±0.66	16.02±0.66
9.5	15.96±0.67	15.94±0.67	15.95±0.67	15.96±0.67	15.97±0.67	15.98±0.67	15.99±0.67	15.99±0.67
10.0	15.93±0.69	15.91±0.68	15.91±0.68	15.93±0.68	15.94±0.68	15.95±0.68	15.95±0.68	15.96±0.68

TABLE C.18— Magnitude of the fitted galaxy of APLib inside the aperture in the V filter.

Apert.	Seeing (arcsec)							
(arcsec)	1.0	2.0	3.0	4.0	5.0	6.0	7.0	8.0
1.0	16.39±0.48	16.17±0.41	16.01±0.35	15.88±0.31	15.78±0.28	15.70±0.25	15.64±0.23	15.58±0.21
1.5	16.16±0.41	16.06±0.38	15.94±0.33	15.84±0.29	15.75±0.28	15.68±0.25	15.62±0.22	15.57±0.21
2.0	15.98±0.35	15.94±0.34	15.88±0.31	15.80±0.29	15.73±0.27	15.66±0.24	15.61±0.22	15.56±0.20
2.5	15.84±0.30	15.83±0.30	15.81±0.29	15.76±0.27	15.70±0.25	15.64±0.23	15.59±0.21	15.55±0.19
3.0	15.74±0.27	15.74±0.27	15.73±0.26	15.70±0.25	15.66±0.24	15.61±0.22	15.57±0.21	15.53±0.19
3.5	15.66±0.24	15.66±0.25	15.67±0.25	15.65±0.24	15.62±0.23	15.59±0.21	15.55±0.20	15.52±0.18
4.0	15.60±0.22	15.59±0.23	15.61±0.23	15.60±0.22	15.58±0.21	15.56±0.20	15.53±0.19	15.50±0.18
4.5	15.55±0.21	15.53±0.21	15.55±0.21	15.56±0.21	15.55±0.20	15.53±0.19	15.51±0.18	15.48±0.16
5.0	15.50±0.19	15.48±0.19	15.50±0.19	15.51±0.20	15.51±0.19	15.50±0.18	15.48±0.16	15.46±0.15
5.5	15.47±0.17	15.44±0.17	15.46±0.18	15.47±0.18	15.48±0.17	15.47±0.17	15.46±0.15	15.44±0.14
6.0	15.43±0.16	15.41±0.16	15.43±0.16	15.44±0.16	15.44±0.15	15.44±0.15	15.43±0.14	15.42±0.13
6.5	15.40±0.15	15.38±0.14	15.39±0.14	15.41±0.14	15.41±0.14	15.42±0.14	15.41±0.13	15.40±0.13
7.0	15.38±0.11	15.35±0.12	15.36±0.13	15.38±0.13	15.39±0.13	15.39±0.13	15.39±0.13	15.38±0.12
7.5	15.36±0.10	15.33±0.10	15.34±0.11	15.35±0.11	15.36±0.11	15.37±0.11	15.37±0.11	15.36±0.10
8.0	15.34±0.09	15.31±0.09	15.32±0.09	15.33±0.10	15.34±0.10	15.34±0.10	15.35±0.10	15.34±0.09
8.5	15.32±0.08	15.29±0.08	15.30±0.08	15.31±0.09	15.32±0.09	15.32±0.09	15.33±0.09	15.33±0.08
9.0	15.30±0.07	15.27±0.07	15.28±0.07	15.29±0.07	15.30±0.08	15.30±0.08	15.31±0.08	15.31±0.08
9.5	15.28±0.06	15.25±0.06	15.26±0.07	15.27±0.07	15.28±0.07	15.29±0.07	15.29±0.07	15.29±0.07
10.0	15.27±0.06	15.24±0.06	15.24±0.06	15.25±0.06	15.26±0.07	15.27±0.07	15.27±0.07	15.28±0.07

Table C.19— Magnitude of the fitted galaxy of APLib inside the aperture in the R filter.

Apert.	Seeing (arcsec)							
(arcsec)	1.0	2.0	3.0	4.0	5.0	6.0	7.0	8.0
1.0	15.97±0.05	15.73±0.05	15.54±0.05	15.40±0.06	15.28±0.06	15.19±0.06	15.11±0.06	15.05±0.07
1.5	15.72±0.03	15.61±0.04	15.47±0.04	15.35±0.04	15.25±0.04	15.17±0.04	15.10±0.04	15.03±0.05
2.0	15.51±0.03	15.47±0.03	15.40±0.03	15.31±0.03	15.22±0.03	15.15±0.04	15.08±0.03	15.02±0.05
2.5	15.36±0.03	15.35±0.03	15.32±0.03	15.25±0.03	15.19±0.03	15.12±0.03	15.06±0.05	15.01±0.05
3.0	15.24±0.03	15.24±0.03	15.23±0.03	15.19±0.03	15.14±0.04	15.09±0.03	15.04±0.05	14.99±0.05
3.5	15.15±0.03	15.15±0.03	15.16±0.03	15.14±0.03	15.10±0.03	15.06±0.05	15.02±0.05	14.97±0.05
4.0	15.07±0.03	15.07±0.03	15.09±0.03	15.08±0.03	15.06±0.03	15.03±0.05	14.99±0.05	14.95±0.05
4.5	15.01±0.05	15.00±0.03	15.02±0.03	15.03±0.05	15.01±0.05	14.99±0.05	14.96±0.05	14.93±0.05
5.0	14.96±0.05	14.95±0.05	14.97±0.05	14.98±0.05	14.97±0.05	14.96±0.05	14.93±0.05	14.91±0.05
5.5	14.91±0.05	14.90±0.05	14.92±0.05	14.93±0.05	14.93±0.05	14.92±0.05	14.91±0.05	14.89±0.05
6.0	14.87±0.05	14.86±0.05	14.87±0.05	14.89±0.05	14.89±0.05	14.89±0.05	14.88±0.05	14.86±0.05
6.5	14.84±0.06	14.82±0.06	14.83±0.06	14.85±0.06	14.86±0.06	14.86±0.06	14.85±0.05	14.84±0.05
7.0	14.81±0.05	14.79±0.05	14.80±0.05	14.81±0.05	14.82±0.05	14.83±0.05	14.82±0.05	14.82±0.05
7.5	14.78±0.06	14.76±0.06	14.77±0.06	14.78±0.06	14.79±0.06	14.80±0.06	14.80±0.06	14.79±0.06
8.0	14.75±0.06	14.73±0.06	14.74±0.06	14.75±0.06	14.76±0.06	14.77±0.06	14.77±0.06	14.77±0.06
8.5	14.73±0.07	14.71±0.07	14.72±0.07	14.73±0.07	14.74±0.07	14.75±0.07	14.75±0.07	14.75±0.07
9.0	14.71±0.07	14.68±0.07	14.69±0.07	14.70±0.07	14.71±0.07	14.72±0.07	14.73±0.07	14.73±0.07
9.5	14.69±0.08	14.66±0.08	14.67±0.08	14.68±0.08	14.69±0.08	14.70±0.08	14.71±0.08	14.71±0.08
10.0	14.67±0.09	14.64±0.09	14.65±0.08	14.66±0.08	14.67±0.08	14.68±0.08	14.69±0.08	14.69±0.08

Table C.20— Magnitude of the fitted galaxy of APLib inside the aperture in the I filter.

Apert.	Seeing (arcsec)							
(arcsec)	1.0	2.0	3.0	4.0	5.0	6.0	7.0	8.0
1.0	15.32±0.40	15.06±0.34	14.85±0.29	14.70±0.24	14.57±0.21	14.47±0.18	14.39±0.15	14.32±0.11
1.5	15.05±0.34	14.92±0.31	14.78±0.27	14.64±0.23	14.53±0.20	14.44±0.17	14.37±0.14	14.30±0.11
2.0	14.83±0.29	14.78±0.28	14.70±0.25	14.60±0.22	14.51±0.19	14.43±0.16	14.36±0.14	14.29±0.10
2.5	14.66±0.25	14.65±0.24	14.61±0.23	14.54±0.20	14.47±0.18	14.40±0.16	14.34±0.13	14.28±0.10
3.0	14.54±0.21	14.53±0.21	14.52±0.20	14.48±0.19	14.42±0.17	14.36±0.14	14.31±0.11	14.25±0.10
3.5	14.44±0.18	14.43±0.19	14.44±0.18	14.42±0.17	14.38±0.15	14.33±0.14	14.28±0.10	14.24±0.09
4.0	14.36±0.16	14.35±0.16	14.36±0.16	14.36±0.15	14.33±0.14	14.29±0.11	14.25±0.10	14.22±0.09
4.5	14.29±0.13	14.27±0.14	14.29±0.14	14.30±0.13	14.28±0.11	14.26±0.10	14.22±0.09	14.19±0.08
5.0	14.23±0.12	14.21±0.12	14.23±0.10	14.24±0.10	14.24±0.10	14.22±0.09	14.20±0.08	14.17±0.08
5.5	14.18±0.08	14.16±0.08	14.18±0.08	14.19±0.08	14.19±0.09	14.18±0.08	14.16±0.08	14.14±0.07
6.0	14.14±0.07	14.11±0.07	14.13±0.07	14.14±0.08	14.15±0.08	14.15±0.08	14.13±0.07	14.11±0.07
6.5	14.10±0.07	14.07±0.07	14.09±0.07	14.10±0.07	14.11±0.07	14.11±0.07	14.10±0.07	14.09±0.07
7.0	14.06±0.06	14.04±0.06	14.05±0.06	14.06±0.06	14.07±0.07	14.08±0.06	14.07±0.06	14.06±0.06
7.5	14.03±0.05	14.00±0.05	14.02±0.06	14.03±0.06	14.04±0.06	14.05±0.06	14.04±0.06	14.04±0.05
8.0	14.01±0.04	13.97±0.04	13.98±0.07	14.00±0.07	14.01±0.07	14.02±0.07	14.02±0.05	14.01±0.07
8.5	13.98±0.07	13.95±0.07	13.96±0.07	13.97±0.07	13.98±0.07	13.99±0.07	13.99±0.07	13.99±0.07
9.0	13.96±0.07	13.92±0.07	13.93±0.07	13.94±0.07	13.95±0.07	13.96±0.07	13.97±0.07	13.97±0.07
9.5	13.93±0.05	13.90±0.07	13.91±0.05	13.92±0.05	13.93±0.07	13.94±0.07	13.94±0.07	13.94±0.07
10.0	13.91±0.06	13.88±0.06	13.89±0.06	13.89±0.06	13.90±0.07	13.91±0.05	13.92±0.05	13.92±0.05

TABLE C.21— Magnitude of the fitted galaxy of Mkn501 inside the aperture in the B filter.

Apert.	Seeing (arcsec)							
(arcsec)	1.0	2.0	3.0	4.0	5.0	6.0	7.0	8.0
1.0	16.84±0.09	16.53±0.08	16.29±0.07	16.11±0.07	15.96±0.06	15.84±0.05	15.74±0.05	15.65±0.05
1.5	16.56±0.08	16.39±0.08	16.22±0.07	16.07±0.06	15.94±0.06	15.83±0.05	15.74±0.05	15.66±0.04
2.0	16.32±0.07	16.23±0.07	16.12±0.07	16.00±0.06	15.89±0.06	15.79±0.05	15.70±0.05	15.63±0.04
2.5	16.13±0.07	16.08±0.07	16.02±0.06	15.93±0.06	15.84±0.05	15.76±0.05	15.68±0.05	15.61±0.04
3.0	15.98±0.06	15.95±0.06	15.92±0.06	15.86±0.06	15.79±0.05	15.72±0.05	15.65±0.05	15.59±0.04
3.5	15.86±0.06	15.84±0.06	15.82±0.05	15.78±0.05	15.73±0.05	15.67±0.05	15.61±0.04	15.56±0.04
4.0	15.76±0.05	15.74±0.05	15.74±0.05	15.71±0.05	15.67±0.05	15.63±0.05	15.58±0.04	15.53±0.04
4.5	15.67±0.05	15.65±0.05	15.66±0.05	15.65±0.05	15.62±0.05	15.58±0.04	15.54±0.04	15.50±0.04
5.0	15.60±0.04	15.58±0.04	15.59±0.04	15.58±0.04	15.56±0.04	15.54±0.04	15.50±0.04	15.47±0.04
5.5	15.53±0.04	15.51±0.04	15.53±0.04	15.53±0.04	15.51±0.04	15.49±0.04	15.47±0.04	15.44±0.04
6.0	15.48±0.04	15.45±0.04	15.47±0.04	15.47±0.04	15.47±0.04	15.45±0.04	15.43±0.04	15.41±0.04
6.5	15.43±0.04	15.40±0.04	15.42±0.04	15.42±0.04	15.42±0.04	15.41±0.04	15.40±0.04	15.38±0.03
7.0	15.38±0.04	15.36±0.04	15.37±0.04	15.38±0.04	15.38±0.04	15.37±0.04	15.36±0.03	15.35±0.03
7.5	15.34±0.03	15.31±0.03	15.33±0.03	15.34±0.03	15.34±0.03	15.34±0.03	15.33±0.03	15.32±0.03
8.0	15.30±0.03	15.27±0.03	15.29±0.03	15.30±0.03	15.30±0.03	15.30±0.03	15.30±0.03	15.29±0.03
8.5	15.27±0.03	15.24±0.03	15.25±0.03	15.26±0.03	15.27±0.03	15.27±0.03	15.27±0.03	15.26±0.03
9.0	15.24±0.03	15.21±0.03	15.22±0.03	15.23±0.03	15.24±0.03	15.24±0.03	15.24±0.03	15.24±0.03
9.5	15.21±0.03	15.18±0.03	15.19±0.03	15.20±0.03	15.21±0.03	15.21±0.03	15.21±0.03	15.21±0.03
10.0	15.18±0.03	15.15±0.03	15.16±0.03	15.17±0.03	15.18±0.03	15.19±0.03	15.19±0.03	15.19±0.03

TABLE C.22— Magnitude of the fitted galaxy of Mkn501 inside the aperture in the V filter.

Apert.	Seeing (arcsec)							
(arcsec)	1.0	2.0	3.0	4.0	5.0	6.0	7.0	8.0
1.0	15.78±0.05	15.49±0.05	15.26±0.04	15.07±0.04	14.92±0.04	14.80±0.04	14.69±0.04	14.61±0.04
1.5	15.47±0.04	15.33±0.04	15.16±0.04	15.00±0.04	14.87±0.03	14.76±0.03	14.66±0.03	14.58±0.03
2.0	15.22±0.03	15.17±0.03	15.07±0.03	14.95±0.03	14.84±0.03	14.74±0.02	14.65±0.02	14.57±0.02
2.5	15.03±0.03	15.02±0.03	14.96±0.03	14.88±0.03	14.79±0.03	14.70±0.02	14.62±0.02	14.55±0.02
3.0	14.88±0.03	14.88±0.03	14.86±0.03	14.81±0.03	14.73±0.03	14.66±0.03	14.59±0.02	14.53±0.02
3.5	14.76±0.03	14.76±0.03	14.76±0.03	14.73±0.03	14.68±0.03	14.62±0.03	14.56±0.02	14.50±0.02
4.0	14.66±0.03	14.66±0.03	14.67±0.03	14.66±0.03	14.62±0.03	14.58±0.03	14.53±0.02	14.48±0.02
4.5	14.58±0.03	14.57±0.03	14.59±0.03	14.59±0.03	14.56±0.02	14.53±0.02	14.49±0.02	14.45±0.02
5.0	14.50±0.02	14.49±0.02	14.51±0.02	14.52±0.02	14.51±0.02	14.48±0.02	14.45±0.02	14.42±0.02
5.5	14.44±0.02	14.43±0.02	14.45±0.02	14.46±0.02	14.45±0.02	14.44±0.02	14.41±0.02	14.38±0.02
6.0	14.38±0.02	14.37±0.02	14.39±0.02	14.40±0.02	14.40±0.02	14.39±0.02	14.38±0.02	14.35±0.02
6.5	14.33±0.02	14.32±0.02	14.33±0.02	14.35±0.02	14.35±0.02	14.35±0.02	14.34±0.02	14.32±0.02
7.0	14.29±0.02	14.27±0.02	14.28±0.02	14.30±0.02	14.31±0.02	14.31±0.02	14.30±0.02	14.29±0.02
7.5	14.25±0.02	14.23±0.02	14.24±0.02	14.26±0.02	14.27±0.02	14.27±0.02	14.27±0.02	14.26±0.02
8.0	14.21±0.02	14.19±0.02	14.20±0.02	14.22±0.02	14.23±0.02	14.23±0.02	14.23±0.02	14.23±0.02
8.5	14.18±0.02	14.15±0.02	14.17±0.02	14.18±0.02	14.19±0.02	14.20±0.02	14.20±0.02	14.20±0.02
9.0	14.15±0.02	14.12±0.02	14.13±0.02	14.14±0.02	14.16±0.02	14.17±0.02	14.17±0.02	14.17±0.02
9.5	14.12±0.02	14.09±0.02	14.10±0.02	14.11±0.02	14.13±0.02	14.13±0.02	14.14±0.02	14.14±0.02
10.0	14.09±0.02	14.07±0.02	14.07±0.02	14.09±0.02	14.10±0.02	14.11±0.02	14.11±0.02	14.12±0.02

TABLE C.23— Magnitude of the fitted galaxy of Mkn501 inside the aperture in the R filter.

Apert. (arcsec)	Seeing (arcsec) 1.0	2.0	3.0	4.0	5.0	6.0	7.0	8.0
1.0	15.00±0.01	14.72±0.01	14.51±0.01	14.34±0.01	14.20±0.01	14.08±0.01	13.99±0.01	13.90±0.01
1.5	14.78±0.01	14.59±0.01	14.43±0.01	14.29±0.01	14.16±0.01	14.05±0.01	13.96±0.01	13.88±0.01
2.0	14.55±0.01	14.46±0.01	14.36±0.01	14.24±0.01	14.13±0.01	14.04±0.01	13.95±0.01	13.87±0.01
2.5	14.36±0.01	14.32±0.01	14.26±0.01	14.17±0.01	14.08±0.01	14.00±0.01	13.92±0.01	13.85±0.01
3.0	14.21±0.01	14.18±0.01	14.16±0.01	14.10±0.01	14.03±0.01	13.96±0.01	13.89±0.01	13.83±0.01
3.5	14.09±0.01	14.07±0.01	14.07±0.01	14.03±0.01	13.98±0.01	13.92±0.01	13.86±0.01	13.81±0.01
4.0	13.99±0.01	13.97±0.01	13.98±0.01	13.96±0.01	13.93±0.01	13.88±0.01	13.83±0.01	13.78±0.01
4.5	13.90±0.01	13.88±0.01	13.90±0.01	13.89±0.01	13.87±0.01	13.83±0.01	13.79±0.01	13.75±0.01
5.0	13.83±0.01	13.80±0.01	13.82±0.01	13.83±0.01	13.82±0.01	13.79±0.01	13.76±0.01	13.72±0.01
5.5	13.77±0.01	13.74±0.01	13.76±0.01	13.77±0.01	13.76±0.01	13.75±0.01	13.72±0.01	13.69±0.01
6.0	13.71±0.01	13.68±0.01	13.70±0.01	13.71±0.01	13.71±0.01	13.70±0.01	13.68±0.01	13.66±0.01
6.5	13.66±0.01	13.63±0.01	13.65±0.01	13.66±0.01	13.66±0.01	13.66±0.01	13.65±0.01	13.63±0.01
7.0	13.62±0.01	13.58±0.01	13.60±0.01	13.61±0.01	13.62±0.01	13.62±0.01	13.61±0.01	13.60±0.01
7.5	13.58±0.01	13.54±0.01	13.55±0.01	13.57±0.01	13.58±0.01	13.58±0.01	13.58±0.01	13.57±0.01
8.0	13.54±0.01	13.50±0.01	13.51±0.01	13.53±0.01	13.54±0.01	13.54±0.01	13.54±0.01	13.54±0.01
8.5	13.51±0.01	13.47±0.01	13.48±0.01	13.49±0.01	13.50±0.01	13.51±0.01	13.51±0.01	13.51±0.01
9.0	13.48±0.01	13.44±0.01	13.45±0.01	13.46±0.01	13.47±0.01	13.48±0.01	13.48±0.01	13.48±0.01
9.5	13.45±0.01	13.41±0.01	13.42±0.01	13.43±0.01	13.44±0.01	13.45±0.01	13.45±0.01	13.45±0.01
10.0	13.42±0.01	13.38±0.01	13.39±0.01	13.40±0.01	13.41±0.01	13.42±0.01	13.43±0.01	13.43±0.01

TABLE C.24— Magnitude of the fitted galaxy of Mkn501 inside the aperture in the I filter.

Apert. (arcsec)	Seeing (arcsec) 1.0	2.0	3.0	4.0	5.0	6.0	7.0	8.0
1.0	14.24±0.07	13.97±0.06	13.76±0.05	13.59±0.05	13.46±0.04	13.35±0.04	13.26±0.04	13.18±0.03
1.5	13.98±0.06	13.84±0.06	13.70±0.05	13.56±0.05	13.44±0.04	13.35±0.04	13.26±0.04	13.19±0.03
2.0	13.76±0.05	13.69±0.05	13.60±0.05	13.49±0.04	13.39±0.04	13.31±0.04	13.23±0.04	13.16±0.03
2.5	13.59±0.05	13.56±0.05	13.51±0.05	13.43±0.04	13.35±0.04	13.27±0.04	13.21±0.04	13.14±0.03
3.0	13.46±0.04	13.45±0.04	13.42±0.04	13.37±0.04	13.30±0.04	13.24±0.04	13.18±0.03	13.12±0.03
3.5	13.35±0.04	13.34±0.04	13.33±0.04	13.30±0.04	13.25±0.04	13.20±0.04	13.14±0.03	13.09±0.03
4.0	13.26±0.04	13.26±0.04	13.26±0.04	13.23±0.04	13.20±0.04	13.16±0.03	13.11±0.03	13.07±0.03
4.5	13.18±0.04	13.18±0.04	13.19±0.04	13.17±0.04	13.15±0.03	13.12±0.03	13.08±0.03	13.04±0.03
5.0	13.12±0.03	13.11±0.03	13.12±0.03	13.12±0.03	13.10±0.03	13.07±0.03	13.04±0.03	13.01±0.03
5.5	13.06±0.03	13.05±0.03	13.06±0.03	13.06±0.03	13.05±0.03	13.04±0.03	13.01±0.03	12.99±0.03
6.0	13.01±0.03	13.00±0.03	13.01±0.03	13.01±0.03	13.01±0.03	13.00±0.03	12.98±0.03	12.96±0.03
6.5	12.96±0.03	12.95±0.03	12.96±0.03	12.97±0.03	12.97±0.03	12.96±0.03	12.95±0.03	12.93±0.03
7.0	12.92±0.03	12.91±0.03	12.92±0.03	12.93±0.03	12.93±0.03	12.92±0.03	12.91±0.03	12.90±0.03
7.5	12.88±0.03	12.87±0.03	12.88±0.03	12.89±0.03	12.89±0.03	12.89±0.03	12.88±0.03	12.87±0.03
8.0	12.85±0.03	12.83±0.03	12.85±0.03	12.85±0.03	12.86±0.03	12.86±0.03	12.86±0.03	12.85±0.03
8.5	12.81±0.02	12.80±0.02	12.81±0.02	12.82±0.02	12.83±0.02	12.83±0.02	12.83±0.02	12.82±0.02
9.0	12.79±0.02	12.77±0.02	12.78±0.02	12.79±0.02	12.80±0.02	12.80±0.02	12.80±0.02	12.80±0.02
9.5	12.76±0.02	12.74±0.02	12.75±0.02	12.76±0.02	12.77±0.02	12.78±0.02	12.78±0.02	12.78±0.02
10.0	12.73±0.02	12.72±0.02	12.73±0.02	12.74±0.02	12.75±0.02	12.75±0.02	12.75±0.02	12.75±0.02

TABLE C.25— Magnitude of the fitted galaxy of Mkn501 inside the aperture in the J filter.

Apert.	Seeing (arcsec)							
(arcsec)	1.0	2.0	3.0	4.0	5.0	6.0	7.0	8.0
1.0	12.90±0.49	12.71±0.49	12.49±0.49	12.29±0.49	12.17±0.49	12.06±0.49	11.98±0.49	11.91±0.49
1.5	12.79±0.45	12.66±0.45	12.48±0.45	12.30±0.45	12.19±0.45	12.09±0.45	12.01±0.45	11.94±0.45
2.0	12.55±0.35	12.50±0.35	12.38±0.35	12.24±0.35	12.15±0.35	12.06±0.35	11.99±0.35	11.92±0.35
2.5	12.32±0.27	12.35±0.27	12.28±0.27	12.17±0.27	12.09±0.27	12.02±0.27	11.95±0.27	11.89±0.27
3.0	12.18±0.21	12.22±0.21	12.18±0.21	12.10±0.21	12.04±0.21	11.98±0.21	11.92±0.21	11.87±0.21
3.5	12.08±0.15	12.12±0.15	12.10±0.15	12.04±0.15	12.00±0.15	11.95±0.15	11.90±0.15	11.85±0.15
4.0	11.98±0.11	12.03±0.11	12.02±0.11	11.98±0.11	11.95±0.11	11.91±0.11	11.87±0.11	11.83±0.11
4.5	11.90±0.08	11.95±0.08	11.94±0.08	11.92±0.08	11.90±0.08	11.87±0.08	11.84±0.08	11.80±0.08
5.0	11.84±0.06	11.88±0.06	11.88±0.06	11.86±0.06	11.85±0.06	11.83±0.06	11.81±0.06	11.78±0.06
5.5	11.79±0.04	11.82±0.04	11.82±0.04	11.80±0.04	11.80±0.04	11.79±0.04	11.77±0.04	11.75±0.04
6.0	11.75±0.04	11.77±0.04	11.77±0.04	11.76±0.04	11.76±0.04	11.75±0.04	11.74±0.03	11.72±0.03
6.5	11.71±0.03	11.73±0.03	11.72±0.03	11.71±0.03	11.72±0.03	11.72±0.03	11.71±0.03	11.69±0.03
7.0	11.67±0.02	11.69±0.02	11.68±0.02	11.67±0.02	11.68±0.02	11.68±0.02	11.68±0.02	11.67±0.02
7.5	11.63±0.02	11.65±0.02	11.65±0.02	11.63±0.02	11.64±0.02	11.65±0.02	11.65±0.02	11.64±0.02
8.0	11.60±0.02	11.62±0.02	11.61±0.02	11.60±0.02	11.61±0.02	11.62±0.02	11.62±0.02	11.61±0.02
8.5	11.58±0.02	11.59±0.02	11.58±0.02	11.57±0.02	11.58±0.02	11.59±0.02	11.59±0.02	11.59±0.02
9.0	11.55±0.01	11.57±0.01	11.56±0.02	11.54±0.02	11.55±0.02	11.56±0.02	11.56±0.02	11.57±0.02
9.5	11.53±0.01	11.54±0.02	11.53±0.02	11.51±0.02	11.52±0.02	11.53±0.02	11.54±0.02	11.54±0.02
10.0	11.51±0.01	11.52±0.01	11.51±0.02	11.49±0.02	11.50±0.02	11.51±0.02	11.52±0.02	11.52±0.02

TABLE C.26— Magnitude of the fitted galaxy of Mkn501 inside the aperture in the H filter.

Apert.	Seeing (arcsec)							
(arcsec)	1.0	2.0	3.0	4.0	5.0	6.0	7.0	8.0
1.0	12.13±0.10	11.92±0.10	11.69±0.09	11.48±0.09	11.35±0.08	11.25±0.08	11.16±0.08	11.08±0.08
1.5	12.01±0.09	11.88±0.09	11.69±0.08	11.50±0.08	11.38±0.07	11.27±0.07	11.19±0.07	11.11±0.07
2.0	11.76±0.08	11.70±0.08	11.58±0.07	11.43±0.07	11.34±0.06	11.25±0.06	11.17±0.06	11.11±0.06
2.5	11.51±0.07	11.54±0.07	11.47±0.06	11.36±0.06	11.28±0.06	11.20±0.05	11.13±0.05	11.07±0.05
3.0	11.37±0.06	11.41±0.06	11.37±0.06	11.29±0.05	11.22±0.05	11.16±0.05	11.10±0.05	11.04±0.04
3.5	11.26±0.05	11.30±0.05	11.28±0.05	11.23±0.05	11.18±0.05	11.13±0.05	11.08±0.04	11.03±0.04
4.0	11.16±0.05	11.20±0.05	11.20±0.05	11.16±0.05	11.13±0.05	11.09±0.04	11.05±0.04	11.00±0.04
4.5	11.08±0.04	11.12±0.04	11.12±0.04	11.09±0.04	11.08±0.04	11.05±0.04	11.01±0.04	10.97±0.04
5.0	11.02±0.04	11.05±0.04	11.05±0.04	11.04±0.04	11.03±0.04	11.01±0.04	10.98±0.04	10.95±0.04
5.5	10.97±0.04	11.00±0.04	11.00±0.04	10.98±0.04	10.98±0.04	10.97±0.04	10.95±0.04	10.93±0.03
6.0	10.92±0.04	10.95±0.04	10.94±0.04	10.93±0.04	10.93±0.04	10.93±0.04	10.92±0.03	10.90±0.03
6.5	10.88±0.03	10.90±0.03	10.90±0.03	10.88±0.03	10.89±0.03	10.89±0.03	10.88±0.03	10.87±0.03
7.0	10.84±0.03	10.86±0.03	10.86±0.03	10.84±0.03	10.85±0.03	10.86±0.03	10.85±0.03	10.84±0.03
7.5	10.81±0.03	10.83±0.03	10.82±0.03	10.80±0.03	10.82±0.03	10.82±0.03	10.82±0.03	10.82±0.03
8.0	10.78±0.03	10.79±0.03	10.79±0.03	10.77±0.03	10.78±0.03	10.79±0.03	10.79±0.03	10.79±0.03
8.5	10.75±0.03	10.77±0.03	10.76±0.03	10.74±0.03	10.75±0.03	10.76±0.03	10.77±0.03	10.77±0.03
9.0	10.72±0.03	10.74±0.03	10.73±0.03	10.71±0.03	10.72±0.03	10.73±0.03	10.74±0.03	10.74±0.03
9.5	10.70±0.02	10.72±0.02	10.71±0.02	10.69±0.02	10.70±0.02	10.71±0.03	10.72±0.03	10.72±0.03
10.0	10.68±0.02	10.70±0.02	10.68±0.02	10.66±0.02	10.67±0.02	10.69±0.02	10.69±0.02	10.70±0.02

Table C.27— Magnitude of the fitted galaxy of Mkn501 inside the aperture in the K filter.

Apert. (arcsec)	Seeing (arcsec) 1.0	2.0	3.0	4.0	5.0	6.0	7.0	8.0
1.0	11.55±0.09	11.40±0.08	11.23±0.08	11.07±0.07	10.97±0.07	10.88±0.06	10.81±0.06	10.75±0.05
1.5	11.46±0.09	11.35±0.08	11.19±0.07	11.04±0.07	10.94±0.06	10.86±0.06	10.79±0.06	10.73±0.05
2.0	11.25±0.08	11.21±0.08	11.10±0.07	10.99±0.07	10.90±0.07	10.83±0.06	10.77±0.06	10.72±0.06
2.5	11.06±0.08	11.09±0.08	11.04±0.07	10.95±0.07	10.88±0.07	10.82±0.06	10.76±0.06	10.71±0.06
3.0	10.94±0.07	10.99±0.07	10.96±0.07	10.89±0.07	10.84±0.07	10.79±0.06	10.74±0.06	10.70±0.06
3.5	10.86±0.07	10.90±0.07	10.88±0.07	10.84±0.07	10.80±0.06	10.76±0.06	10.72±0.06	10.68±0.06
4.0	10.78±0.06	10.82±0.06	10.81±0.06	10.78±0.06	10.76±0.06	10.73±0.06	10.70±0.06	10.66±0.06
4.5	10.71±0.06	10.75±0.06	10.75±0.06	10.73±0.06	10.72±0.06	10.70±0.06	10.67±0.06	10.64±0.06
5.0	10.66±0.06	10.70±0.06	10.70±0.06	10.68±0.06	10.67±0.06	10.66±0.06	10.64±0.06	10.61±0.06
5.5	10.62±0.06	10.65±0.06	10.65±0.06	10.63±0.06	10.64±0.06	10.63±0.06	10.61±0.06	10.59±0.06
6.0	10.58±0.06	10.61±0.06	10.61±0.06	10.59±0.06	10.60±0.06	10.59±0.06	10.58±0.06	10.57±0.06
6.5	10.55±0.06	10.57±0.06	10.57±0.06	10.56±0.06	10.56±0.06	10.57±0.06	10.56±0.06	10.55±0.06
7.0	10.52±0.06	10.54±0.06	10.53±0.06	10.52±0.06	10.53±0.06	10.54±0.06	10.53±0.06	10.52±0.06
7.5	10.49±0.06	10.51±0.06	10.51±0.06	10.49±0.06	10.50±0.06	10.51±0.06	10.51±0.06	10.50±0.06
8.0	10.47±0.06	10.49±0.06	10.48±0.06	10.46±0.06	10.47±0.06	10.48±0.06	10.48±0.06	10.48±0.06
8.5	10.45±0.06	10.46±0.06	10.45±0.06	10.44±0.06	10.45±0.06	10.46±0.06	10.46±0.06	10.46±0.06
9.0	10.43±0.06	10.44±0.06	10.43±0.06	10.42±0.06	10.43±0.06	10.43±0.06	10.44±0.06	10.44±0.06
9.5	10.41±0.05	10.42±0.05	10.41±0.05	10.39±0.05	10.40±0.06	10.41±0.06	10.42±0.06	10.42±0.06
10.0	10.39±0.05	10.41±0.05	10.39±0.05	10.38±0.05	10.38±0.05	10.39±0.05	10.40±0.05	10.40±0.05

Table C.28— Magnitude of the fitted galaxy of IIZw136 inside the aperture in the B filter.

Apert. (arcsec)	Seeing (arcsec) 1.0	2.0	3.0	4.0	5.0	6.0	7.0	8.0
1.0	19.90±0.94	19.58±0.94	19.25±0.94	18.97±0.94	18.75±0.94	18.56±0.94	18.41±0.94	18.28±0.94
1.5	19.35±0.56	19.25±0.56	19.06±0.56	18.85±0.56	18.67±0.56	18.51±0.56	18.37±0.56	18.25±0.56
2.0	18.96±0.43	18.93±0.43	18.85±0.43	18.71±0.43	18.57±0.43	18.44±0.43	18.31±0.43	18.20±0.44
2.5	18.67±0.35	18.67±0.35	18.64±0.35	18.56±0.35	18.46±0.35	18.35±0.36	18.25±0.36	18.15±0.36
3.0	18.45±0.29	18.45±0.29	18.45±0.29	18.41±0.29	18.35±0.29	18.27±0.29	18.18±0.30	18.10±0.30
3.5	18.27±0.24	18.27±0.25	18.28±0.25	18.27±0.25	18.23±0.25	18.18±0.25	18.11±0.26	18.04±0.26
4.0	18.12±0.21	18.12±0.22	18.14±0.22	18.14±0.22	18.12±0.22	18.09±0.22	18.04±0.23	17.98±0.23
4.5	18.00±0.19	17.99±0.19	18.01±0.19	18.03±0.20	18.02±0.20	18.00±0.20	17.96±0.20	17.92±0.21
5.0	17.90±0.17	17.88±0.17	17.90±0.18	17.92±0.18	17.92±0.18	17.91±0.18	17.89±0.19	17.86±0.19
5.5	17.80±0.16	17.79±0.16	17.81±0.16	17.82±0.17	17.83±0.17	17.83±0.17	17.82±0.18	17.80±0.18
6.0	17.72±0.15	17.70±0.15	17.72±0.16	17.74±0.16	17.75±0.16	17.75±0.17	17.75±0.17	17.73±0.17
6.5	17.65±0.15	17.63±0.15	17.65±0.15	17.66±0.15	17.68±0.16	17.68±0.16	17.68±0.16	17.68±0.17
7.0	17.59±0.15	17.57±0.15	17.58±0.15	17.59±0.15	17.61±0.16	17.62±0.16	17.62±0.16	17.62±0.16
7.5	17.53±0.15	17.51±0.15	17.52±0.15	17.53±0.15	17.55±0.16	17.56±0.16	17.57±0.16	17.57±0.16
8.0	17.48±0.15	17.45±0.15	17.46±0.15	17.48±0.15	17.49±0.16	17.50±0.16	17.51±0.16	17.51±0.16
8.5	17.43±0.15	17.40±0.15	17.41±0.15	17.43±0.16	17.44±0.16	17.45±0.16	17.46±0.16	17.47±0.17
9.0	17.38±0.15	17.36±0.15	17.37±0.16	17.38±0.16	17.39±0.16	17.40±0.16	17.41±0.16	17.42±0.17
9.5	17.34±0.16	17.32±0.16	17.33±0.16	17.34±0.16	17.35±0.16	17.36±0.17	17.37±0.17	17.38±0.17
10.0	17.31±0.16	17.28±0.16	17.29±0.16	17.30±0.16	17.31±0.16	17.32±0.17	17.33±0.17	17.34±0.17

TABLE C.29— Magnitude of the fitted galaxy of IIZw136 inside the aperture in the V filter.

Apert.	Seeing (arcsec)							
(arcsec)	1.0	2.0	3.0	4.0	5.0	6.0	7.0	8.0
1.0	18.74±0.16	18.44±0.16	18.14±0.15	17.88±0.15	17.67±0.15	17.50±0.15	17.36±0.15	17.24±0.15
1.5	18.22±0.15	18.12±0.15	17.95±0.15	17.77±0.14	17.60±0.14	17.45±0.14	17.32±0.14	17.21±0.14
2.0	17.85±0.15	17.83±0.14	17.76±0.14	17.63±0.14	17.50±0.13	17.38±0.13	17.27±0.13	17.17±0.13
2.5	17.58±0.14	17.58±0.14	17.56±0.13	17.49±0.13	17.40±0.13	17.31±0.13	17.21±0.13	17.13±0.13
3.0	17.38±0.13	17.38±0.12	17.39±0.12	17.36±0.12	17.30±0.12	17.23±0.12	17.15±0.11	17.08±0.11
3.5	17.21±0.12	17.21±0.11	17.23±0.11	17.23±0.11	17.19±0.11	17.14±0.11	17.09±0.10	17.03±0.10
4.0	17.08±0.11	17.08±0.11	17.10±0.10	17.11±0.10	17.09±0.10	17.06±0.10	17.02±0.10	16.97±0.10
4.5	16.97±0.10	16.96±0.10	16.99±0.10	17.00±0.10	17.00±0.09	16.98±0.09	16.95±0.09	16.92±0.09
5.0	16.88±0.10	16.86±0.10	16.89±0.10	16.90±0.09	16.91±0.09	16.90±0.09	16.88±0.09	16.86±0.09
5.5	16.80±0.10	16.78±0.10	16.80±0.09	16.82±0.09	16.83±0.09	16.83±0.09	16.82±0.09	16.80±0.09
6.0	16.73±0.10	16.71±0.10	16.72±0.09	16.74±0.09	16.75±0.09	16.76±0.09	16.76±0.09	16.75±0.09
6.5	16.66±0.10	16.64±0.10	16.66±0.09	16.67±0.09	16.69±0.09	16.70±0.09	16.70±0.09	16.69±0.09
7.0	16.61±0.10	16.58±0.09	16.60±0.09	16.61±0.09	16.63±0.09	16.64±0.09	16.64±0.09	16.64±0.09
7.5	16.56±0.09	16.53±0.09	16.55±0.09	16.56±0.09	16.57±0.09	16.59±0.09	16.59±0.09	16.60±0.09
8.0	16.51±0.09	16.49±0.09	16.50±0.09	16.51±0.09	16.52±0.09	16.54±0.09	16.55±0.09	16.55±0.09
8.5	16.47±0.09	16.45±0.09	16.46±0.09	16.47±0.09	16.48±0.09	16.49±0.09	16.50±0.09	16.51±0.09
9.0	16.43±0.09	16.41±0.09	16.42±0.09	16.43±0.09	16.44±0.09	16.45±0.09	16.46±0.09	16.47±0.09
9.5	16.40±0.09	16.37±0.09	16.38±0.09	16.39±0.09	16.40±0.09	16.41±0.09	16.42±0.09	16.43±0.09
10.0	16.37±0.09	16.34±0.09	16.35±0.09	16.36±0.09	16.37±0.09	16.38±0.09	16.39±0.09	16.40±0.09

Table C.30— Magnitude of the fitted galaxy of IIZw136 inside the aperture in the R filter.

Apert.	Seeing (arcsec)							
(arcsec)	1.0	2.0	3.0	4.0	5.0	6.0	7.0	8.0
1.0	18.07±0.08	17.75±0.08	17.46±0.08	17.21±0.08	17.01±0.08	16.85±0.08	16.71±0.08	16.59±0.08
1.5	17.57±0.05	17.46±0.04	17.29±0.04	17.11±0.04	16.95±0.04	16.80±0.05	16.68±0.05	16.57±0.05
2.0	17.21±0.03	17.18±0.02	17.10±0.02	16.99±0.02	16.86±0.02	16.74±0.03	16.64±0.03	16.54±0.03
2.5	16.95±0.02	16.94±0.02	16.92±0.02	16.85±0.02	16.77±0.02	16.67±0.02	16.58±0.03	16.50±0.03
3.0	16.75±0.02	16.74±0.02	16.75±0.02	16.72±0.02	16.66±0.02	16.60±0.02	16.52±0.03	16.45±0.03
3.5	16.60±0.02	16.58±0.01	16.60±0.01	16.59±0.02	16.56±0.02	16.51±0.02	16.46±0.02	16.40±0.03
4.0	16.47±0.02	16.44±0.02	16.47±0.02	16.47±0.02	16.46±0.02	16.43±0.02	16.39±0.02	16.35±0.03
4.5	16.36±0.02	16.33±0.02	16.35±0.02	16.37±0.02	16.37±0.02	16.35±0.02	16.33±0.03	16.29±0.03
5.0	16.27±0.02	16.24±0.02	16.26±0.02	16.28±0.02	16.28±0.03	16.28±0.03	16.26±0.03	16.24±0.03
5.5	16.19±0.03	16.16±0.03	16.18±0.03	16.19±0.03	16.21±0.03	16.21±0.03	16.20±0.03	16.18±0.03
6.0	16.12±0.03	16.09±0.03	16.10±0.03	16.12±0.03	16.14±0.03	16.14±0.03	16.14±0.03	16.13±0.04
6.5	16.06±0.03	16.03±0.03	16.04±0.03	16.06±0.03	16.07±0.03	16.08±0.03	16.08±0.03	16.08±0.04
7.0	16.01±0.03	15.97±0.03	15.98±0.03	16.00±0.03	16.01±0.03	16.03±0.03	16.03±0.03	16.03±0.04
7.5	15.96±0.02	15.92±0.02	15.93±0.03	15.95±0.03	15.96±0.03	15.97±0.03	15.98±0.03	15.98±0.03
8.0	15.92±0.02	15.88±0.02	15.89±0.02	15.90±0.03	15.91±0.03	15.93±0.03	15.94±0.03	15.94±0.03
8.5	15.88±0.02	15.84±0.02	15.85±0.02	15.86±0.02	15.87±0.02	15.88±0.03	15.89±0.03	15.90±0.03
9.0	15.85±0.02	15.80±0.02	15.81±0.02	15.82±0.02	15.83±0.02	15.84±0.03	15.86±0.03	15.86±0.03
9.5	15.81±0.02	15.77±0.02	15.78±0.02	15.79±0.02	15.80±0.02	15.81±0.02	15.82±0.03	15.83±0.03
10.0	15.79±0.02	15.74±0.02	15.75±0.02	15.75±0.02	15.76±0.02	15.78±0.02	15.79±0.03	15.80±0.03

Table C.31— Magnitude of the fitted galaxy of IIZw136 inside the aperture in the I filter.

Apert.	Seeing (arcsec)							
(arcsec)	1.0	2.0	3.0	4.0	5.0	6.0	7.0	8.0
1.0	17.32±0.29	17.03±0.26	16.73±0.25	16.49±0.24	16.29±0.23	16.13±1.18	15.99±0.23	15.88±0.22
1.5	16.82±0.31	16.73±0.27	16.57±0.25	16.39±0.24	16.22±0.23	16.08±1.17	15.96±0.22	15.86±0.22
2.0	16.46±0.33	16.45±0.28	16.38±0.25	16.26±0.24	16.14±0.23	16.02±1.17	15.92±0.22	15.82±0.22
2.5	16.20±0.34	16.21±0.29	16.19±0.26	16.13±0.25	16.04±0.24	15.95±1.16	15.86±0.23	15.78±0.22
3.0	16.01±0.34	16.01±0.30	16.02±0.27	15.99±0.25	15.94±0.24	15.87±1.15	15.80±0.23	15.73±0.22
3.5	15.85±0.34	15.85±0.30	15.87±0.27	15.87±0.25	15.84±0.24	15.79±1.15	15.74±0.23	15.68±0.22
4.0	15.73±0.34	15.72±0.31	15.75±0.28	15.75±0.26	15.74±0.24	15.71±1.14	15.67±0.23	15.63±0.22
4.5	15.62±0.34	15.61±0.31	15.64±0.28	15.65±0.26	15.65±0.25	15.64±1.13	15.61±0.23	15.58±0.23
5.0	15.53±0.33	15.52±0.31	15.54±0.29	15.56±0.27	15.57±0.25	15.56±1.12	15.55±0.23	15.52±0.23
5.5	15.46±0.33	15.44±0.31	15.46±0.29	15.48±0.27	15.49±0.26	15.49±1.11	15.48±0.24	15.47±0.23
6.0	15.39±0.32	15.37±0.32	15.39±0.30	15.41±0.28	15.42±0.26	15.43±1.10	15.43±0.24	15.42±0.23
6.5	15.33±0.32	15.31±0.31	15.33±0.30	15.34±0.28	15.36±0.26	15.37±1.09	15.37±0.24	15.37±0.23
7.0	15.28±0.32	15.26±0.31	15.27±0.30	15.29±0.28	15.30±0.26	15.31±1.08	15.32±0.24	15.32±0.24
7.5	15.23±0.31	15.21±0.31	15.22±0.30	15.24±0.28	15.25±0.27	15.26±1.07	15.27±0.25	15.27±0.24
8.0	15.19±0.31	15.17±0.31	15.18±0.30	15.19±0.28	15.20±0.27	15.22±1.06	15.23±0.25	15.23±0.24
8.5	15.16±0.31	15.13±0.31	15.14±0.30	15.15±0.28	15.16±0.27	15.18±1.05	15.19±0.25	15.19±0.24
9.0	15.12±0.30	15.09±0.30	15.10±0.30	15.11±0.28	15.12±0.27	15.14±1.04	15.15±0.25	15.15±0.24
9.5	15.09±0.30	15.06±0.30	15.07±0.30	15.08±0.29	15.09±0.27	15.10±1.03	15.11±0.25	15.12±0.24
10.0	15.06±0.30	15.03±0.30	15.04±0.29	15.05±0.29	15.06±0.27	15.07±1.02	15.08±0.25	15.09±0.24

Table C.32— Magnitude of the fitted galaxy of BLLac inside the aperture in the B filter.

Apert.	Seeing (arcsec)							
(arcsec)	1.0	2.0	3.0	4.0	5.0	6.0	7.0	8.0
1.0	20.09±0.10	19.74±0.11	19.48±0.11	19.27±0.11	19.11±0.11	18.97±0.11	18.87±0.11	18.77±0.11
1.5	19.76±0.09	19.59±0.09	19.41±0.08	19.24±0.08	19.09±0.08	18.97±0.09	18.86±0.09	18.78±0.09
2.0	19.48±0.08	19.41±0.08	19.29±0.08	19.16±0.08	19.04±0.08	18.93±0.08	18.84±0.08	18.75±0.08
2.5	19.27±0.07	19.24±0.07	19.18±0.07	19.09±0.07	18.99±0.08	18.90±0.08	18.81±0.08	18.73±0.08
3.0	19.11±0.07	19.09±0.07	19.07±0.07	19.01±0.07	18.93±0.07	18.86±0.08	18.78±0.08	18.71±0.08
3.5	18.98±0.07	18.96±0.07	18.96±0.07	18.93±0.07	18.87±0.08	18.81±0.08	18.74±0.08	18.68±0.08
4.0	18.87±0.07	18.85±0.07	18.86±0.07	18.85±0.07	18.81±0.08	18.76±0.08	18.71±0.08	18.65±0.08
4.5	18.78±0.08	18.75±0.08	18.78±0.08	18.77±0.08	18.75±0.08	18.71±0.08	18.67±0.08	18.62±0.08
5.0	18.70±0.08	18.67±0.08	18.69±0.08	18.70±0.08	18.69±0.08	18.66±0.08	18.63±0.08	18.59±0.08
5.5	18.63±0.08	18.60±0.08	18.62±0.08	18.64±0.08	18.63±0.08	18.61±0.08	18.59±0.08	18.56±0.08
6.0	18.57±0.08	18.54±0.08	18.56±0.08	18.57±0.08	18.58±0.08	18.57±0.08	18.55±0.08	18.52±0.09
6.5	18.52±0.08	18.48±0.08	18.50±0.08	18.52±0.08	18.52±0.08	18.52±0.08	18.51±0.09	18.49±0.09
7.0	18.47±0.09	18.43±0.09	18.45±0.09	18.47±0.09	18.48±0.09	18.48±0.09	18.47±0.09	18.45±0.09
7.5	18.43±0.09	18.39±0.09	18.40±0.09	18.42±0.09	18.43±0.09	18.43±0.09	18.43±0.09	18.42±0.09
8.0	18.39±0.09	18.35±0.09	18.36±0.09	18.38±0.09	18.39±0.09	18.39±0.09	18.39±0.09	18.39±0.09
8.5	18.35±0.09	18.31±0.09	18.32±0.09	18.34±0.09	18.35±0.09	18.36±0.09	18.36±0.09	18.36±0.09
9.0	18.32±0.10	18.27±0.10	18.29±0.10	18.30±0.10	18.31±0.10	18.32±0.10	18.32±0.10	18.32±0.10
9.5	18.29±0.10	18.24±0.10	18.25±0.10	18.27±0.10	18.28±0.10	18.29±0.10	18.29±0.10	18.29±0.10
10.0	18.26±0.10	18.21±0.10	18.22±0.10	18.23±0.10	18.25±0.10	18.26±0.10	18.26±0.10	18.27±0.10

Table C.33— Magnitude of the fitted galaxy of BLLac inside the aperture in the V filter.

Apert.	Seeing (arcsec)							
(arcsec)	1.0	2.0	3.0	4.0	5.0	6.0	7.0	8.0
1.0	18.63±0.19	18.29±0.19	18.02±0.18	17.81±0.18	17.64±0.18	17.51±0.18	17.39±0.18	17.30±0.18
1.5	18.28±0.06	18.12±0.06	17.92±0.05	17.75±0.05	17.60±0.05	17.47±0.04	17.36±0.04	17.27±0.04
2.0	17.99±0.05	17.94±0.04	17.82±0.04	17.68±0.03	17.56±0.03	17.45±0.03	17.35±0.02	17.26±0.02
2.5	17.78±0.04	17.77±0.04	17.71±0.04	17.61±0.03	17.51±0.03	17.41±0.03	17.32±0.02	17.24±0.02
3.0	17.61±0.04	17.61±0.04	17.59±0.04	17.52±0.03	17.44±0.03	17.36±0.03	17.28±0.03	17.21±0.02
3.5	17.47±0.04	17.48±0.04	17.48±0.03	17.44±0.03	17.38±0.03	17.32±0.03	17.25±0.03	17.19±0.03
4.0	17.36±0.03	17.36±0.03	17.38±0.03	17.36±0.03	17.32±0.03	17.27±0.03	17.21±0.03	17.16±0.03
4.5	17.27±0.03	17.26±0.03	17.28±0.03	17.28±0.03	17.26±0.03	17.22±0.03	17.17±0.03	17.12±0.03
5.0	17.18±0.03	17.18±0.03	17.20±0.03	17.21±0.03	17.19±0.03	17.17±0.03	17.13±0.02	17.09±0.02
5.5	17.11±0.03	17.10±0.03	17.13±0.03	17.14±0.03	17.13±0.03	17.12±0.02	17.09±0.02	17.05±0.02
6.0	17.05±0.03	17.04±0.03	17.06±0.03	17.08±0.03	17.08±0.02	17.07±0.02	17.05±0.02	17.02±0.02
6.5	17.00±0.03	16.98±0.03	17.00±0.03	17.02±0.03	17.02±0.03	17.02±0.03	17.00±0.03	16.98±0.03
7.0	16.95±0.03	16.93±0.03	16.95±0.03	16.96±0.03	16.97±0.03	16.97±0.03	16.96±0.03	16.95±0.03
7.5	16.90±0.03	16.88±0.03	16.90±0.03	16.91±0.03	16.92±0.03	16.93±0.03	16.92±0.03	16.91±0.03
8.0	16.86±0.03	16.84±0.03	16.85±0.03	16.87±0.03	16.88±0.03	16.89±0.03	16.89±0.03	16.88±0.03
8.5	16.82±0.03	16.80±0.03	16.81±0.03	16.83±0.03	16.84±0.03	16.85±0.03	16.85±0.03	16.85±0.03
9.0	16.79±0.03	16.76±0.03	16.78±0.03	16.79±0.03	16.80±0.03	16.81±0.03	16.82±0.03	16.81±0.03
9.5	16.75±0.04	16.73±0.04	16.74±0.04	16.75±0.04	16.77±0.04	16.78±0.04	16.78±0.04	16.78±0.04
10.0	16.72±0.04	16.70±0.04	16.71±0.04	16.72±0.04	16.73±0.04	16.74±0.04	16.75±0.04	16.75±0.04

TABLE C.34— Magnitude of the fitted galaxy of BLLac inside the aperture in the R filter.

Apert.	Seeing (arcsec)							
(arcsec)	1.0	2.0	3.0	4.0	5.0	6.0	7.0	8.0
1.0	17.74±0.10	17.39±0.10	17.12±0.10	16.91±0.10	16.74±0.10	16.61±0.10	16.50±0.10	16.41±0.10
1.5	17.39±0.06	17.22±0.06	17.03±0.06	16.86±0.06	16.71±0.06	16.59±0.06	16.48±0.06	16.39±0.06
2.0	17.10±0.02	17.04±0.02	16.92±0.02	16.79±0.02	16.66±0.03	16.55±0.03	16.46±0.03	16.37±0.03
2.5	16.89±0.02	16.87±0.02	16.81±0.02	16.71±0.02	16.61±0.03	16.52±0.03	16.43±0.03	16.35±0.02
3.0	16.72±0.02	16.71±0.02	16.69±0.02	16.63±0.03	16.55±0.03	16.47±0.03	16.40±0.03	16.33±0.02
3.5	16.59±0.02	16.58±0.02	16.59±0.02	16.55±0.03	16.49±0.03	16.43±0.03	16.36±0.03	16.30±0.03
4.0	16.48±0.02	16.47±0.02	16.49±0.02	16.47±0.03	16.43±0.03	16.38±0.03	16.33±0.03	16.27±0.03
4.5	16.39±0.02	16.37±0.02	16.39±0.02	16.39±0.03	16.37±0.03	16.33±0.03	16.29±0.03	16.24±0.03
5.0	16.31±0.02	16.29±0.02	16.31±0.02	16.32±0.03	16.31±0.03	16.28±0.03	16.25±0.03	16.21±0.03
5.5	16.24±0.02	16.22±0.02	16.24±0.03	16.25±0.03	16.25±0.03	16.23±0.03	16.20±0.03	16.17±0.03
6.0	16.18±0.02	16.15±0.02	16.18±0.03	16.19±0.03	16.19±0.03	16.18±0.03	16.16±0.03	16.14±0.03
6.5	16.13±0.03	16.10±0.03	16.12±0.03	16.13±0.03	16.14±0.03	16.14±0.03	16.12±0.03	16.10±0.03
7.0	16.08±0.03	16.05±0.03	16.07±0.03	16.08±0.03	16.09±0.03	16.09±0.03	16.08±0.03	16.07±0.03
7.5	16.03±0.03	16.00±0.03	16.02±0.03	16.03±0.03	16.04±0.03	16.05±0.03	16.05±0.03	16.03±0.03
8.0	15.99±0.03	15.96±0.03	15.97±0.03	15.99±0.03	16.00±0.03	16.01±0.03	16.01±0.03	16.00±0.03
8.5	15.96±0.04	15.92±0.04	15.94±0.04	15.95±0.04	15.96±0.03	15.97±0.03	15.97±0.03	15.97±0.03
9.0	15.92±0.04	15.89±0.04	15.90±0.04	15.91±0.04	15.92±0.04	15.93±0.04	15.94±0.04	15.94±0.04
9.5	15.89±0.04	15.86±0.04	15.87±0.04	15.88±0.04	15.89±0.04	15.90±0.04	15.91±0.04	15.91±0.04
10.0	15.86±0.05	15.83±0.05	15.83±0.05	15.85±0.05	15.86±0.05	15.87±0.05	15.88±0.05	15.88±0.05

TABLE C.35— Magnitude of the fitted galaxy of BLLac inside the aperture in the I filter.

Apert.	Seeing (arcsec)							
(arcsec)	1.0	2.0	3.0	4.0	5.0	6.0	7.0	8.0
1.0	16.91±0.17	16.58±0.16	16.32±0.16	16.12±0.16	15.96±0.17	15.83±0.18	15.73±0.18	15.64±0.18
1.5	16.58±0.14	16.42±0.12	16.24±0.12	16.08±0.13	15.94±0.13	15.82±0.14	15.72±0.14	15.63±0.15
2.0	16.30±0.12	16.24±0.10	16.13±0.10	16.01±0.11	15.89±0.11	15.78±0.12	15.69±0.13	15.61±0.13
2.5	16.10±0.10	16.08±0.09	16.03±0.09	15.94±0.09	15.84±0.10	15.75±0.10	15.67±0.11	15.60±0.11
3.0	15.94±0.10	15.93±0.09	15.92±0.09	15.86±0.09	15.79±0.09	15.71±0.10	15.64±0.10	15.57±0.11
3.5	15.81±0.09	15.81±0.08	15.81±0.08	15.78±0.08	15.73±0.08	15.67±0.09	15.60±0.09	15.54±0.10
4.0	15.71±0.09	15.70±0.08	15.72±0.08	15.70±0.08	15.67±0.08	15.62±0.08	15.57±0.09	15.52±0.09
4.5	15.62±0.09	15.61±0.08	15.63±0.08	15.63±0.08	15.61±0.08	15.57±0.08	15.53±0.08	15.49±0.09
5.0	15.55±0.09	15.53±0.09	15.55±0.08	15.56±0.08	15.55±0.08	15.52±0.08	15.49±0.08	15.46±0.09
5.5	15.48±0.09	15.46±0.09	15.48±0.09	15.50±0.09	15.49±0.08	15.48±0.08	15.45±0.09	15.42±0.09
6.0	15.43±0.10	15.40±0.09	15.42±0.09	15.44±0.09	15.44±0.09	15.43±0.09	15.41±0.09	15.39±0.09
6.5	15.37±0.10	15.35±0.10	15.37±0.10	15.38±0.10	15.39±0.10	15.39±0.09	15.38±0.10	15.36±0.10
7.0	15.33±0.10	15.30±0.10	15.32±0.10	15.33±0.10	15.34±0.10	15.35±0.10	15.34±0.10	15.32±0.10
7.5	15.29±0.10	15.26±0.10	15.27±0.10	15.29±0.10	15.30±0.10	15.30±0.10	15.30±0.10	15.29±0.10
8.0	15.25±0.11	15.22±0.11	15.23±0.11	15.25±0.10	15.26±0.10	15.27±0.10	15.27±0.10	15.26±0.10
8.5	15.21±0.11	15.18±0.11	15.20±0.11	15.21±0.11	15.22±0.10	15.23±0.10	15.23±0.10	15.23±0.10
9.0	15.18±0.11	15.15±0.11	15.16±0.11	15.17±0.11	15.19±0.11	15.20±0.11	15.20±0.11	15.20±0.11
9.5	15.15±0.11	15.12±0.11	15.13±0.11	15.14±0.11	15.16±0.11	15.16±0.11	15.17±0.11	15.17±0.11
10.0	15.13±0.11	15.09±0.11	15.10±0.11	15.11±0.11	15.12±0.11	15.13±0.11	15.14±0.11	15.14±0.11

TABLE C.36— Magnitude of the fitted galaxy of BLLac inside the aperture in the J filter.

Apert.	Seeing (arcsec)							
(arcsec)	1.0	2.0	3.0	4.0	5.0	6.0	7.0	8.0
1.0	14.61±0.11	14.42±0.10	14.17±0.09	14.04±0.09	13.92±0.08	13.82±0.08	13.75±0.08	13.68±0.08
1.5	14.44±0.10	14.32±0.08	14.11±0.07	14.00±0.07	13.89±0.07	13.81±0.07	13.73±0.07	13.67±0.07
2.0	14.22±0.08	14.18±0.07	14.02±0.06	13.95±0.05	13.86±0.05	13.78±0.05	13.71±0.05	13.65±0.05
2.5	14.02±0.07	14.05±0.06	13.94±0.05	13.89±0.04	13.82±0.04	13.76±0.03	13.70±0.03	13.64±0.03
3.0	13.89±0.06	13.93±0.05	13.85±0.04	13.84±0.04	13.78±0.03	13.72±0.03	13.67±0.03	13.62±0.03
3.5	13.81±0.05	13.83±0.04	13.77±0.04	13.77±0.03	13.73±0.03	13.69±0.02	13.65±0.02	13.60±0.02
4.0	13.73±0.04	13.75±0.04	13.70±0.03	13.71±0.03	13.69±0.02	13.66±0.02	13.62±0.02	13.58±0.02
4.5	13.66±0.04	13.68±0.04	13.63±0.03	13.66±0.02	13.65±0.02	13.62±0.02	13.59±0.02	13.56±0.02
5.0	13.60±0.03	13.62±0.03	13.57±0.03	13.61±0.02	13.60±0.02	13.58±0.01	13.56±0.01	13.54±0.01
5.5	13.56±0.03	13.57±0.03	13.52±0.02	13.56±0.02	13.56±0.01	13.55±0.01	13.53±0.01	13.51±0.01
6.0	13.51±0.02	13.53±0.02	13.47±0.02	13.51±0.02	13.52±0.01	13.52±0.01	13.51±0.01	13.49±0.01
6.5	13.48±0.02	13.49±0.02	13.43±0.02	13.47±0.02	13.48±0.01	13.48±0.01	13.48±0.01	13.46±0.01
7.0	13.45±0.02	13.45±0.02	13.40±0.02	13.44±0.02	13.45±0.01	13.45±0.01	13.45±0.01	13.44±0.01
7.5	13.42±0.02	13.42±0.02	13.37±0.02	13.40±0.01	13.42±0.01	13.42±0.01	13.42±0.01	13.42±0.01
8.0	13.39±0.01	13.40±0.01	13.34±0.01	13.38±0.01	13.39±0.01	13.40±0.01	13.40±0.01	13.39±0.01
8.5	13.37±0.01	13.37±0.01	13.31±0.01	13.35±0.01	13.36±0.01	13.37±0.01	13.37±0.01	13.37±0.01
9.0	13.35±0.01	13.35±0.01	13.29±0.01	13.32±0.01	13.34±0.01	13.34±0.01	13.34±0.01	13.34±0.01
9.5	13.33±0.02	13.33±0.02	13.27±0.01	13.30±0.01	13.31±0.01	13.32±0.01	13.32±0.01	13.31±0.01
10.0	13.31±0.02	13.31±0.02	13.25±0.02	13.28±0.02	13.29±0.02	13.30±0.01	13.29±0.01	13.29±0.01

TABLE C.37— Magnitude of the fitted galaxy of BLLac inside the aperture in the H filter.

Apert.	Seeing (arcsec)							
(arcsec)	1.0	2.0	3.0	4.0	5.0	6.0	7.0	8.0
1.0	14.09±0.44	13.86±0.44	13.61±0.44	13.45±0.44	13.31±0.44	13.20±0.44	13.11±0.44	13.04±0.44
1.5	13.83±0.25	13.69±0.25	13.51±0.25	13.39±0.25	13.28±0.25	13.18±0.25	13.10±0.25	13.04±0.25
2.0	13.58±0.20	13.56±0.20	13.44±0.20	13.35±0.20	13.25±0.20	13.16±0.20	13.09±0.20	13.03±0.20
2.5	13.40±0.16	13.42±0.15	13.34±0.15	13.28±0.15	13.20±0.15	13.13±0.15	13.06±0.15	13.00±0.15
3.0	13.26±0.15	13.29±0.15	13.25±0.15	13.21±0.15	13.16±0.15	13.09±0.15	13.04±0.15	12.98±0.15
3.5	13.15±0.10	13.18±0.10	13.16±0.10	13.15±0.10	13.11±0.10	13.06±0.10	13.01±0.10	12.96±0.10
4.0	13.07±0.08	13.09±0.08	13.08±0.08	13.09±0.08	13.06±0.08	13.02±0.08	12.98±0.08	12.94±0.08
4.5	13.00±0.08	13.02±0.08	13.01±0.08	13.03±0.08	13.01±0.08	12.98±0.08	12.95±0.08	12.92±0.08
5.0	12.93±0.07	12.95±0.08	12.95±0.08	12.97±0.08	12.96±0.08	12.95±0.08	12.92±0.08	12.89±0.07
5.5	12.88±0.07	12.90±0.07	12.89±0.07	12.92±0.07	12.91±0.07	12.91±0.07	12.89±0.07	12.86±0.07
6.0	12.84±0.06	12.85±0.06	12.84±0.06	12.87±0.07	12.87±0.07	12.87±0.06	12.86±0.06	12.84±0.06
6.5	12.80±0.06	12.81±0.06	12.80±0.06	12.82±0.06	12.83±0.06	12.83±0.06	12.82±0.06	12.81±0.06
7.0	12.76±0.06	12.77±0.06	12.76±0.06	12.78±0.06	12.80±0.06	12.80±0.06	12.79±0.05	12.79±0.05
7.5	12.73±0.06	12.74±0.06	12.73±0.06	12.75±0.06	12.76±0.05	12.77±0.05	12.77±0.05	12.76±0.05
8.0	12.70±0.05	12.71±0.05	12.69±0.05	12.72±0.05	12.73±0.05	12.74±0.05	12.74±0.05	12.73±0.04
8.5	12.68±0.05	12.68±0.05	12.67±0.05	12.69±0.05	12.70±0.05	12.71±0.04	12.71±0.04	12.71±0.04
9.0	12.65±0.05	12.66±0.05	12.64±0.05	12.66±0.05	12.67±0.05	12.68±0.04	12.68±0.04	12.68±0.04
9.5	12.63±0.05	12.63±0.05	12.62±0.05	12.64±0.05	12.65±0.04	12.65±0.04	12.65±0.04	12.65±0.03
10.0	12.61±0.05	12.61±0.05	12.59±0.05	12.61±0.05	12.62±0.04	12.63±0.04	12.63±0.03	12.62±0.03

TABLE C.38— Magnitude of the fitted galaxy of BLLac inside the aperture in the K filter.

Apert.	Seeing (arcsec)							
(arcsec)	1.0	2.0	3.0	4.0	5.0	6.0	7.0	8.0
1.0	13.58±0.15	13.39±0.15	13.18±0.15	12.99±0.15	12.86±0.15	12.76±0.15	12.68±0.15	12.60±0.15
1.5	13.42±0.11	13.28±0.11	13.10±0.11	12.93±0.11	12.81±0.11	12.71±0.11	12.62±0.11	12.55±0.11
2.0	13.17±0.08	13.11±0.08	12.99±0.08	12.86±0.08	12.76±0.08	12.67±0.08	12.60±0.08	12.53±0.08
2.5	12.95±0.04	12.98±0.04	12.92±0.05	12.82±0.05	12.74±0.05	12.66±0.05	12.59±0.04	12.53±0.04
3.0	12.81±0.03	12.85±0.04	12.82±0.04	12.75±0.04	12.69±0.04	12.63±0.04	12.57±0.04	12.52±0.03
3.5	12.71±0.03	12.74±0.04	12.73±0.04	12.68±0.04	12.64±0.04	12.59±0.04	12.54±0.03	12.49±0.03
4.0	12.61±0.04	12.65±0.04	12.65±0.04	12.62±0.04	12.59±0.04	12.55±0.04	12.51±0.03	12.47±0.03
4.5	12.53±0.04	12.57±0.04	12.58±0.04	12.56±0.04	12.54±0.04	12.51±0.04	12.48±0.03	12.44±0.03
5.0	12.47±0.03	12.51±0.04	12.51±0.04	12.49±0.04	12.49±0.04	12.47±0.03	12.44±0.03	12.41±0.02
5.5	12.42±0.04	12.45±0.04	12.45±0.04	12.44±0.04	12.44±0.04	12.43±0.03	12.41±0.03	12.39±0.02
6.0	12.37±0.04	12.40±0.04	12.40±0.04	12.39±0.04	12.40±0.04	12.39±0.03	12.38±0.03	12.36±0.02
6.5	12.33±0.04	12.35±0.04	12.35±0.04	12.35±0.04	12.35±0.04	12.36±0.03	12.35±0.03	12.33±0.02
7.0	12.29±0.04	12.31±0.04	12.31±0.04	12.30±0.04	12.32±0.04	12.32±0.03	12.31±0.03	12.30±0.03
7.5	12.26±0.04	12.28±0.04	12.28±0.04	12.27±0.04	12.28±0.04	12.29±0.04	12.29±0.03	12.28±0.03
8.0	12.23±0.05	12.25±0.05	12.24±0.05	12.23±0.04	12.25±0.04	12.26±0.04	12.26±0.03	12.25±0.03
8.5	12.20±0.05	12.22±0.05	12.21±0.05	12.20±0.05	12.22±0.04	12.22±0.04	12.23±0.03	12.22±0.03
9.0	12.18±0.05	12.19±0.05	12.19±0.05	12.18±0.05	12.19±0.04	12.20±0.04	12.20±0.03	12.20±0.03

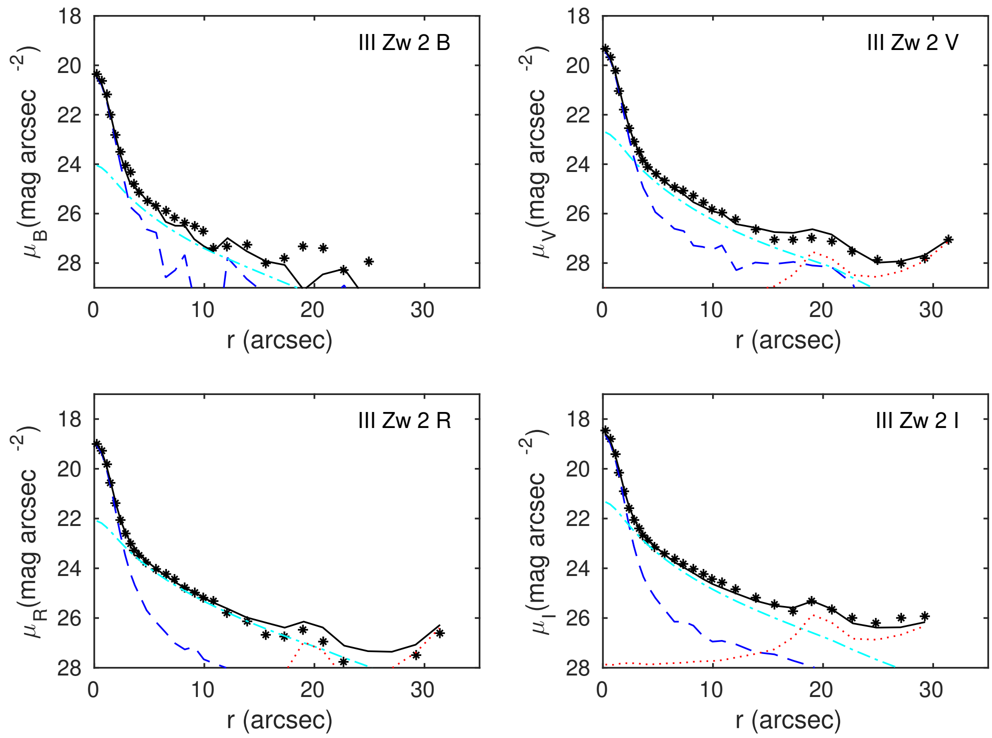

FIGURE C.1— Azimutally average profiles of III Zw 2. Asterisks represent the observed azimuthaly averaged profile. The blue dashed line is the nuclear point source model component, the cyan dot-dashed line the profile of the model host galaxy, the red dotted line the additional components corresponding to close object that were also fitted, and the solid line the sum of the profiles of the galaxy and nucleus source.

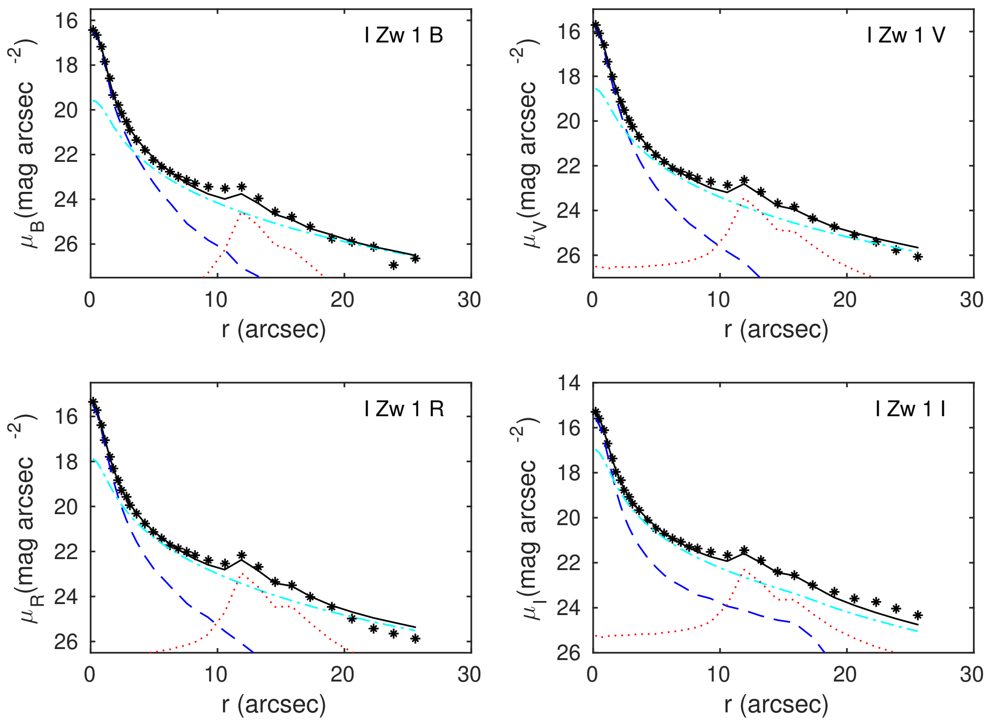

FIGURE C.2— Azimutally average profiles of I Zw 1. Asterisks represent the observed azimuthaly averaged profile. The blue dashed line is the nuclear point source model component, the cyan dot-dashed line the profile of the model host galaxy, the red dotted line the additional components corresponding to close object that were also fitted, and the solid line the sum of the profiles of the galaxy and nucleus source.

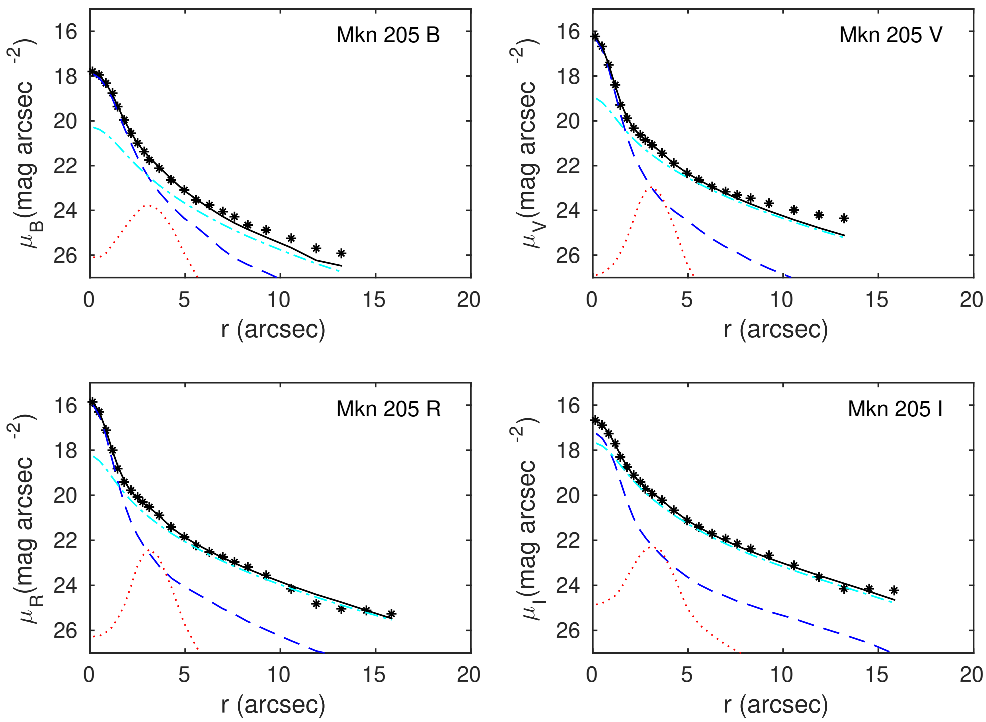

FIGURE C.3— Azimutally average profiles of Mkn 205. Asterisks represent the observed azimuthaly averaged profile. The blue dashed line is the nuclear point source model component, the cyan dot-dashed line the profile of the model host galaxy, the red dotted line the additional components corresponding to close object that were also fitted, and the solid line the sum of the profiles of the galaxy and nucleus source.

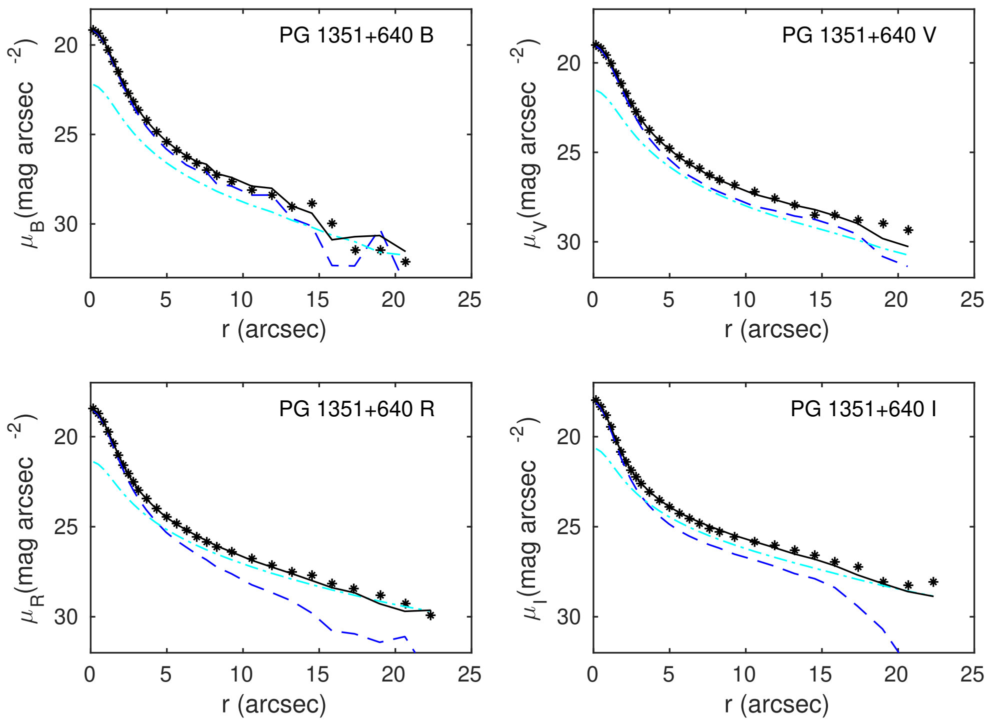

FIGURE C.4— Azimutally average profiles of PG 1351+64. Asterisks represent the observed azimuthaly averaged profile. The blue dashed line is the nuclear point source model component, the cyan dot-dashed line the profile of the model host galaxy, the red dotted line the additional components corresponding to close object that were also fitted, and the solid line the sum of the profiles of the galaxy and nucleus source.

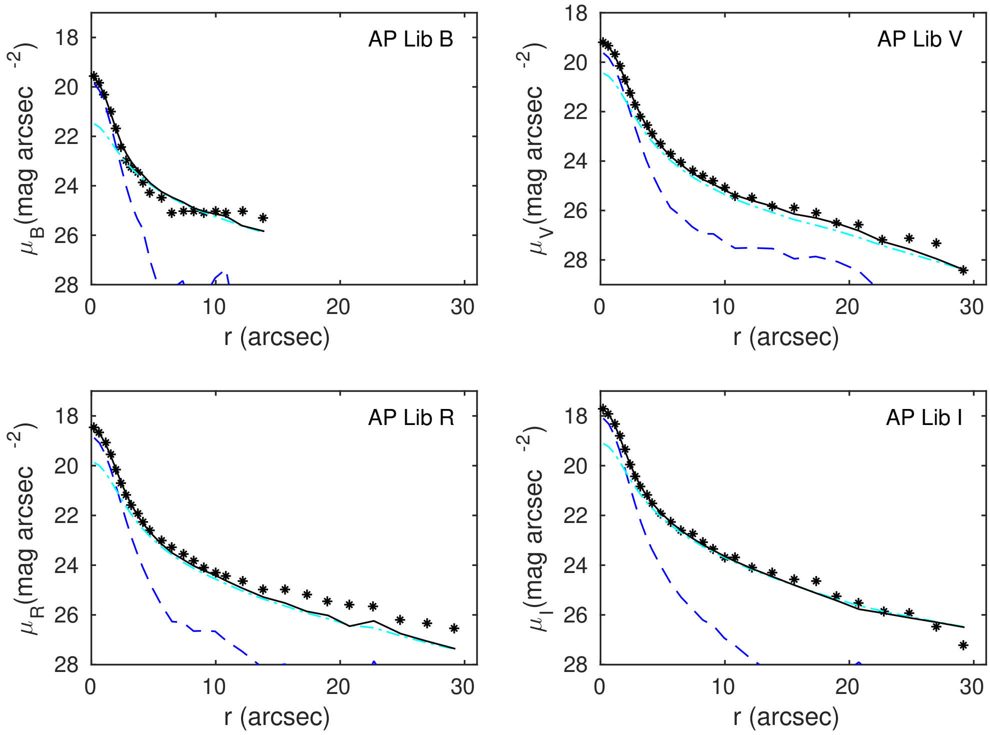

FIGURE C.5— Azimutally average profiles of AP Lib. Asterisks represent the observed azimuthaly averaged profile. The blue dashed line is the nuclear point source model component, the cyan dot-dashed line the profile of the model host galaxy, the red dotted line the additional components corresponding to close object that were also fitted, and the solid line the sum of the profiles of the galaxy and nucleus source.

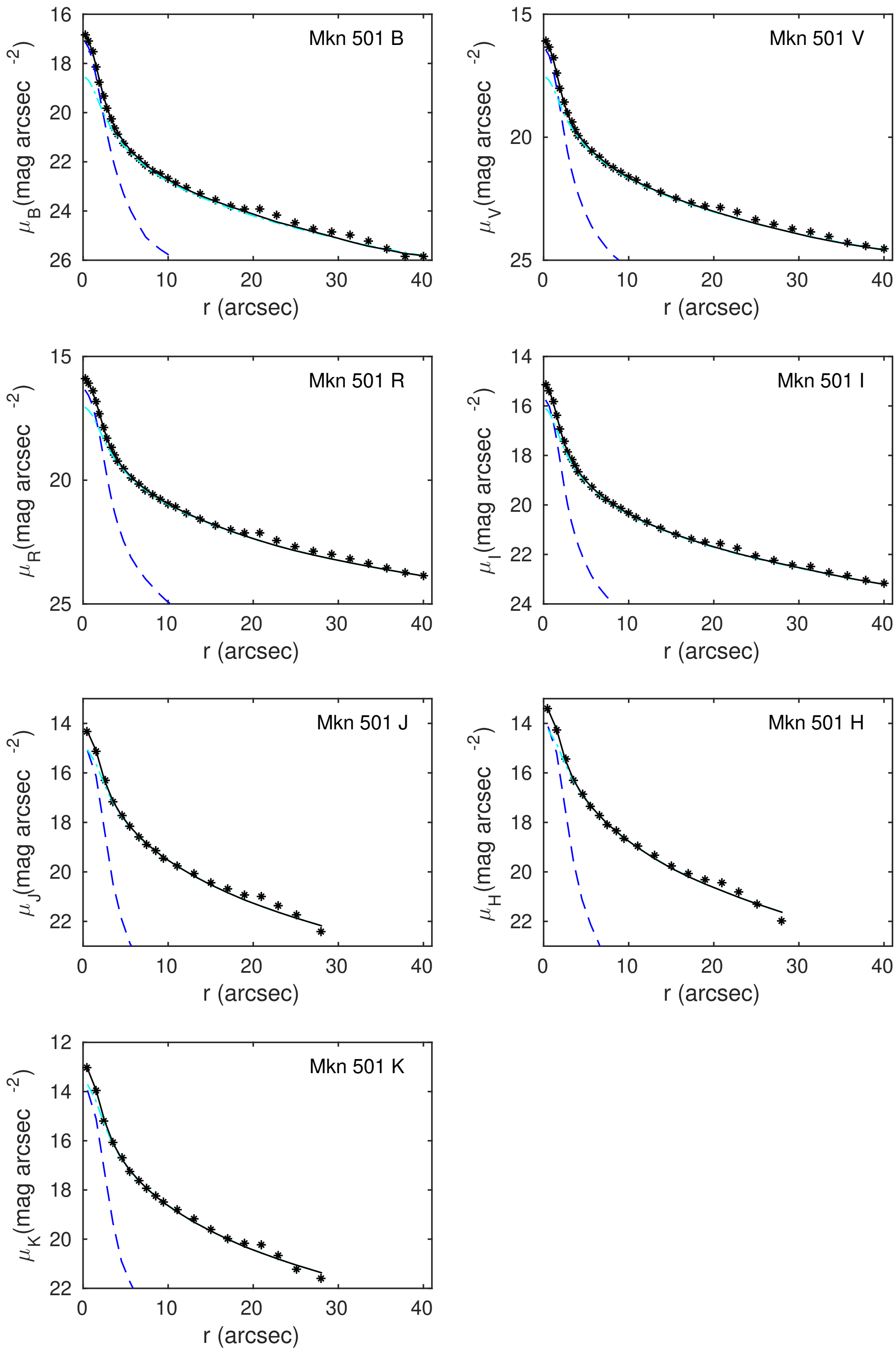

FIGURE C.6— Azimutally average profiles of Mkn 501. Asterisks represent the observed azimuthaly averaged profile. The blue dashed line is the nuclear point source model component, the cyan dot-dashed line the profile of the model host galaxy, the red dotted line the additional components corresponding to close object that were also fitted, and the solid line the sum of the profiles of the galaxy and nucleus source.

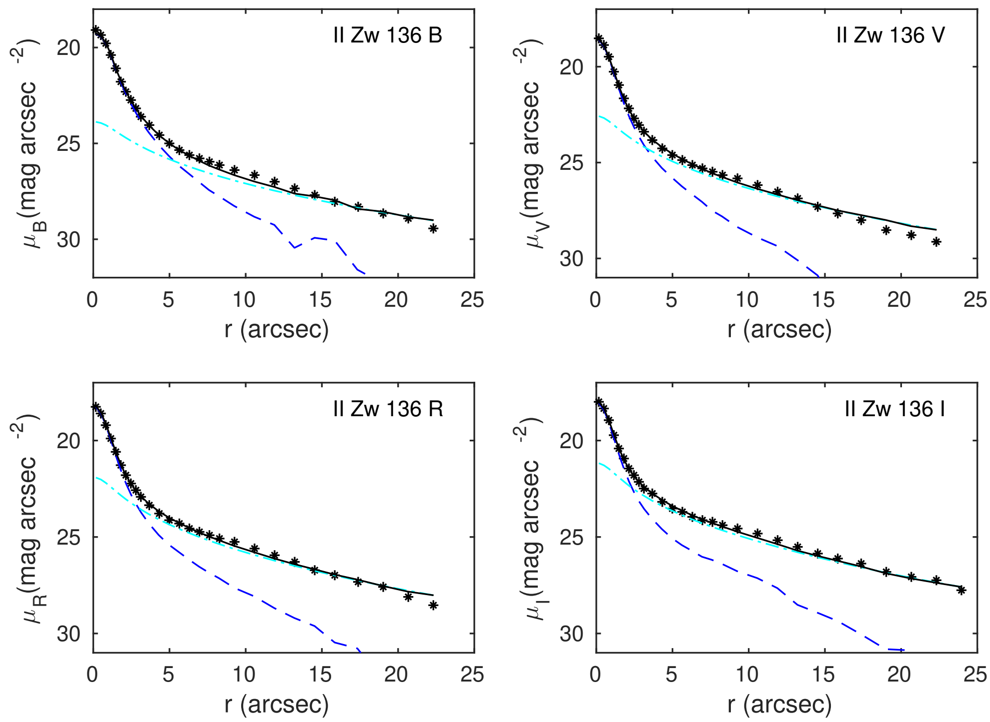

FIGURE C.7— Azimutally average profiles of II Zw 136. Asterisks represent the observed azimuthaly averaged profile. The blue dashed line is the nuclear point source model component, the cyan dot-dashed line the profile of the model host galaxy, the red dotted line the additional components corresponding to close object that were also fitted, and the solid line the sum of the profiles of the galaxy and nucleus source.

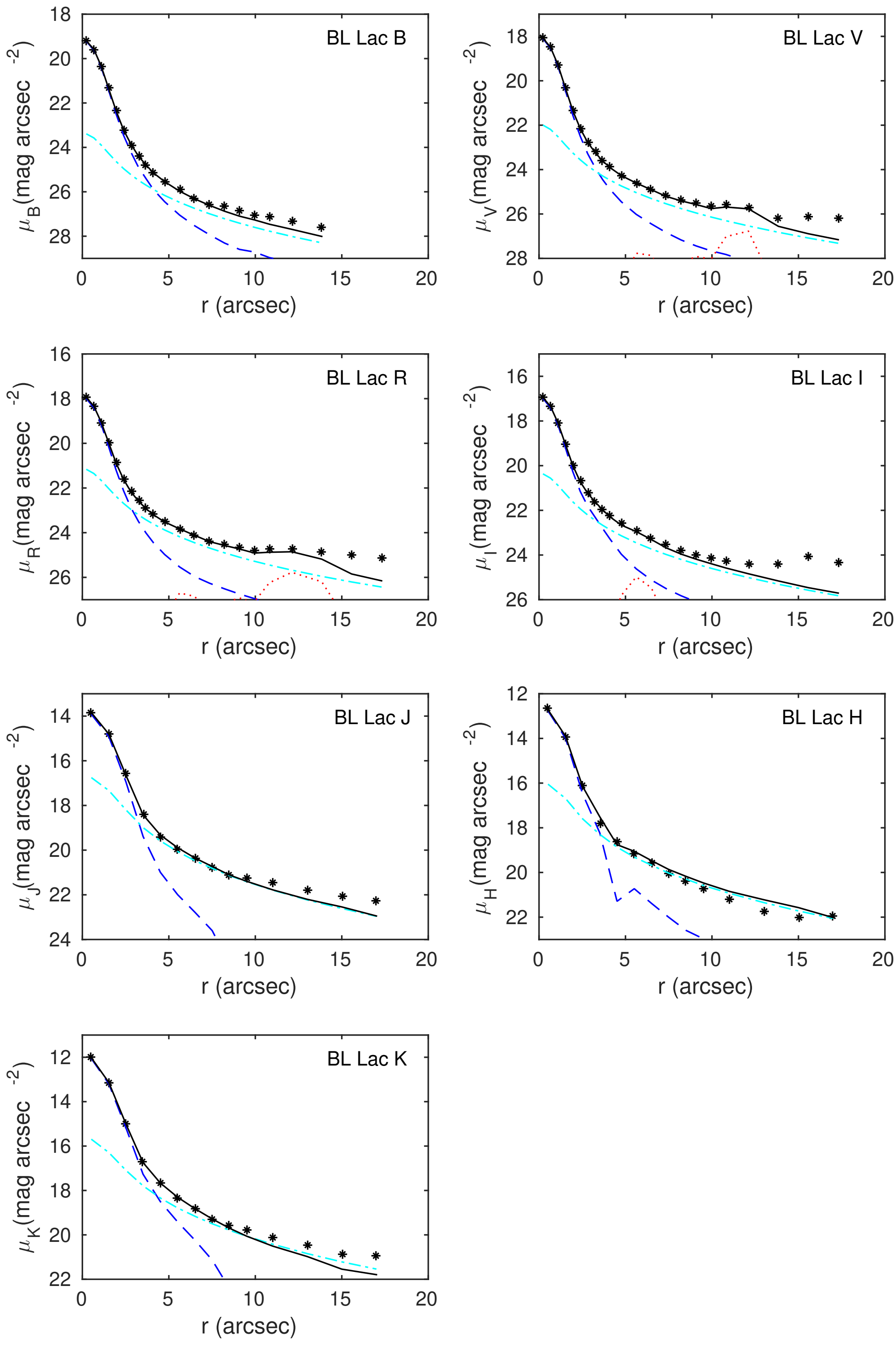

FIGURE C.8— Azimutally average profiles of BL Lac. Asterisks represent the observed azimuthaly averaged profile. The blue dashed line is the nuclear point source model component, the cyan dot-dashed line the profile of the model host galaxy, the red dotted line the additional components corresponding to close object that were also fitted, and the solid line the sum of the profiles of the galaxy and nucleus source.

D

Structure function of the light curves

The structure function (SF) is a measure of the temporal characteristics of a time series, in some way similar to the power density spectrum. Here, the SFs of our light curves are estimated and fitted to an analytical function that gives the power law index of the SF, a parameter that provides information about the process generating the variability, as well as longest correlation timescale.

The structure function (SF) was defined by Simonetti et al. (1985), and it gives the typical flux difference between two measurements as a function of the temporal separation. Its best property is the ability to discern the range of timescales that contributes to variations in the dataset. The first order structure function is defined as:

$$SF(\tau) = \left\langle [F(t) - F(t+\tau)]^2 \right\rangle , \tag{D.1}$$

where the "$\langle\rangle$" refers to an average made on those flux difference, $F(t) - F(t+\tau)$, of similar τ. The error bars are calculated with the dispersion of the data in each τ grouping.

This function gives information similar to the power spectral density (PSD), but the SF has a better behavior for non-periodic data and for data that are not evenly sampled since it is less sensitive to the sampling times and gaps in the light curve (Hughes et al. 1992; Lainela & Valtaoja 1993).

There is a correspondence between the power laws of the PSD and SF. If the power density spectrum has a form $PSD \propto f^{-\alpha}$, where f is the frequency, then the structure function is $SF \propto \tau^{\beta}$, with $\beta = \alpha - 1$ in the range $1 < \alpha < 3$ (Lainela & Valtaoja 1993). Thus, if in a plot $\log(SF)$ vs. $\log(\tau)$ there is a slope with $\beta = 1$, the process is of type shot noise; and if the slope is 0, the responsible process is flicker noise. A linear trend in the time series would produce $SF \propto \tau^2$. However, these SF properties are only true if the time series has a stationary behavior (Hughes et al. 1992; Lainela & Valtaoja 1993).

If the light curve has a characteristic timescale τ_c, the SF has a maximum of τ_c. Furthermore, if the signal is cyclic with a period of P, the SF has a maximum at $\tau = P/2$ and a minimum at

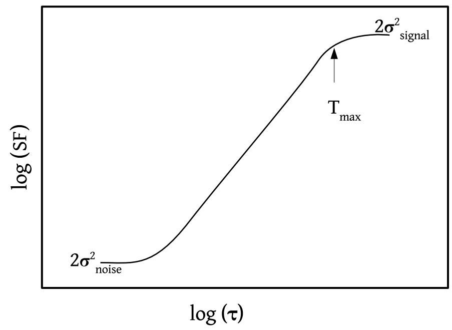

FIGURE D.1— Skecth showing the ideal structure function.

$\tau = P$ (Smith & Nair 1995).

On the other hand, for a random stationary process, the SF is related to the autocorrelation function of the process, $ACF(\tau)$, and its variance, σ^2, as $SF(\tau) = 2\sigma^2[1 - ACF(\tau)]$. However, the structure function is more general and is also defined for non-stationary processes (Lainela & Valtaoja 1993).

The structure function of an ideal measurement process has three components in the $\log SF$ vs. $\log \tau$ diagram shown in Fig. D.1: two plateaus at short and long timescales and a slope connecting both. For short τ, the structure function has a value $2\sigma^2_{noise}$, related to observational errors. For τ longer than the longest correlation timescale (T_{max}) there is the other horizontal plateau, with a value $2\sigma^2_{signal}$. At timescales larger than T_{max} the variations are completely uncorrelated. As stated before, the slope characterizes the nature of the process. If there are several mixed processes or cyclical variations, the situation is more complicated and difficult to analyze.

The structure function has been used by many authors to study the temporal properties of variability in AGNs (e.g., Hughes et al. 1992; Czerny et al. 2003; Agarwal et al. 2015; Raiteri et al. 2017). However, Emmanoulopoulos et al. (2010) presented a detailed discussion and a critical review of the properties of the SF. They pointed out that the SF may lead to spurious results and false timescales.

We have fitted the SF to obtain the index (β) of the power law part and the longest correlation timescale. The analytic function to be fitted is similar to the one used by Paltani et al. (1998):

$$SF(\tau) = 2\sigma^2_{noise} + \left\{ \begin{array}{ll} 2\sigma^2_{signal} \left(\dfrac{\tau}{T_{max}} \right)^{\beta} & , \text{if } \tau < T_{max} \\ 2\sigma^2_{signal} & , \text{if } \tau \geq T_{max} \end{array} \right\} \tag{D.2}$$

The fits were carried out with the non-linear least squares fitting program LSQNONLIN in Matlab. Some of the objects in our sample do not show a plateau at long timescales, and therefore, only the first two components of the SF were fitted in these sources ($SF(\tau) = 2\sigma^2_{noise} +$

Table D.1— Power lauw index (β) of the structure function calculated from the fit.

Object name	B	V	R	I	J	H	K
III Zw 2	0.81±1.35	1.12±0.22	0.94±0.23	1.76±0.73	-	-	-
I Zw 1	0.66±0.30	0.75±0.34	0.80±0.29	0.59±0.38	-	-	-
NAB 0205+02	0.37±0.44	0.39±0.34	0.74±0.55	1.22±5.80	-	-	-
3C 66A	1.48±0.29	1.38±0.21	1.21±0.16	1.32±0.23	0.94±0.92	1.30±0.68	1.63±4.89
AO 0235+16	0.78±0.51	0.85±0.25	0.90±0.25	0.92±0.37	0.75±0.29	1.29±0.42	0.48±0.35
PKS 0405-12	1.48±0.77	0.67±0.40	0.60±0.35	0.42±0.32	-	-	-
S5 0716+71	0.69±0.29	1.31±0.60	1.30±0.41	0.95±0.63	-	-	-
GB 0738+54	1.07±0.58	2.17±2.51	1.11±0.41	1.34±1.92	1.24± NaN	1.17± NaN	1.41±9.03
OJ 287	0.83±0.16	0.79±0.10	0.97±0.14	1.11±0.19	0.76±0.38	0.95±0.27	0.82±0.20
Mkn 205	1.20±0.93	0.71±0.18	0.65±0.17	0.75±0.76	-	-	-
3C 273	0.53±0.45	0.96±0.24	0.64±0.27	1.13±2.01	0.30±0.17	0.53±0.19	0.52±0.53
3C 279	1.63±1.14	1.31±0.92	1.72±0.78	2.39±1.78	0.80±0.46	1.77±0.84	1.93±0.71
PG 1351+640	0.79±0.48	1.05±0.24	1.23±0.40	1.40±1.21	-	-	-
3C 345	0.95±0.61	0.79±0.31	0.76±0.41	0.77±0.21	0.80±0.27	1.03±0.50	0.94±0.44
Mkn 501	0.86±0.33	0.91±0.17	0.95±0.47	1.20±0.70	0.22±0.18	0.42±0.19	0.20±0.16
3C 351	1.47±0.47	1.35±0.21	1.04±0.28	1.20±5.50	-	-	-
II Zw 136	0.49±0.29	0.51±0.32	0.58±0.14	1.34±0.90	-	-	-
BL Lac	2.36±0.82	1.38±0.27	1.79±0.51	2.58±2.46	0.99±0.57	1.76±1.39	0.68±0.67
3C 454.4	0.59±0.22	0.72±0.56	0.62±1.48	0.99±0.39	2.10±1.74	2.98±2.34	1.76±1.82

$K\tau^{\beta}$).

Figures D.2 shows the structure functions in the filter V of the objects in our sample with enough photometric data. The solid line in the figures represents the fit obtained. On the side of the long-term variations ($\tau \geq 1$ d), the SF was calculated using the nightly averages of the magnitudes. For the short-term variations ($\tau \lesssim 10$ d), the whole dataset was used. On timescales between $\sim 1 - 10$ d both datasets were used, and the differences of the SF on these timescales can help to visually assess the errors in the SF introduced by the sampling. Tables D.1 and D.2 display the power law indices of the SF and the logarithm of the longest correlation timescale of the variations. The errors of the parameters are the formal errors given by the fitting program. However, as pointed out by Emmanoulopoulos et al. (2010), the values of the points of the SF are not statistically independent of each other, which prevent a robust estimation of the parameters and errors of the fit. A robust estimation needs simulated datasets with a given power density spectrum and is beyond the scope of this thesis.

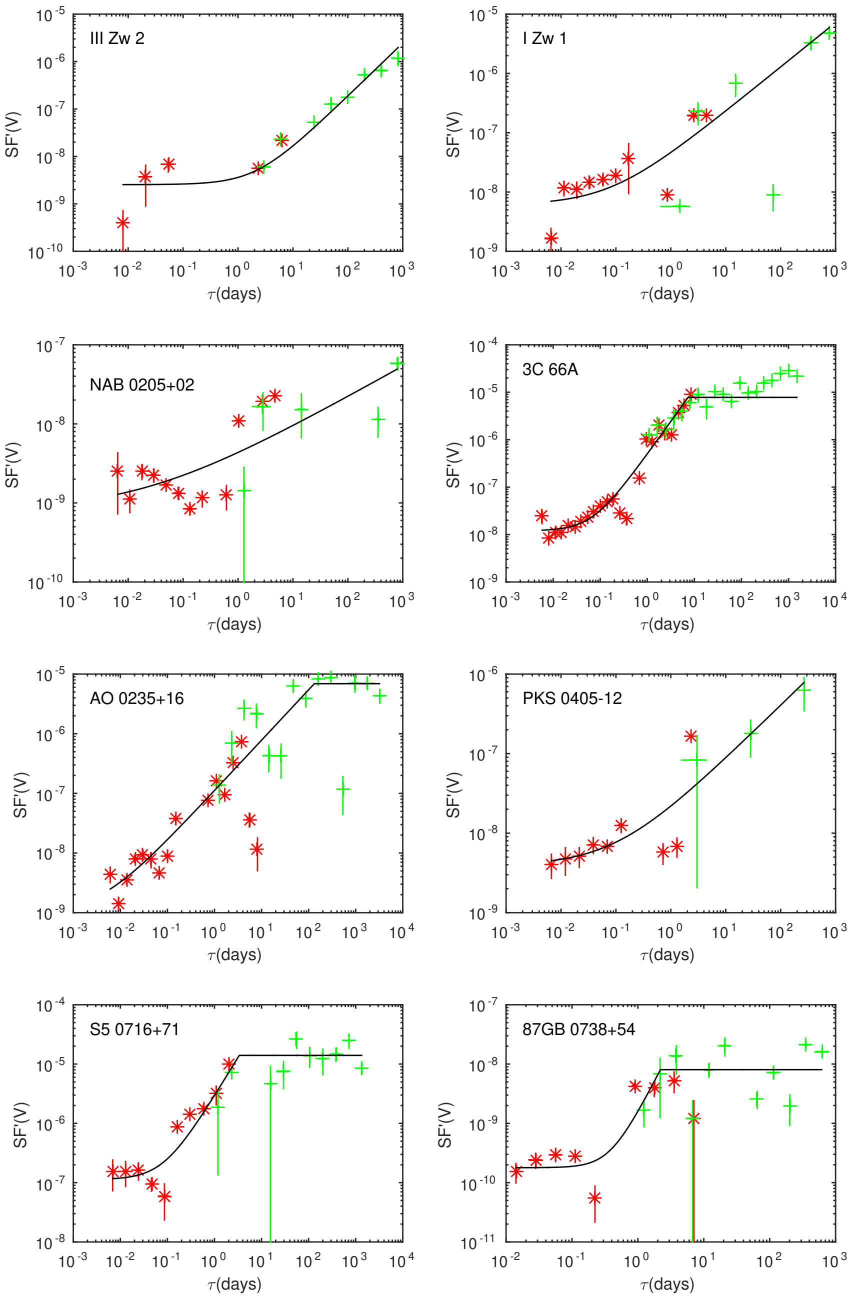

FIGURE D.2— Structure function of the AGNs in our sample in V. Green crosses are the SF using the nighty averages magnitudes and red stars using the whole dataset. The solid line is the best fit with the function given by Eq. D.2.

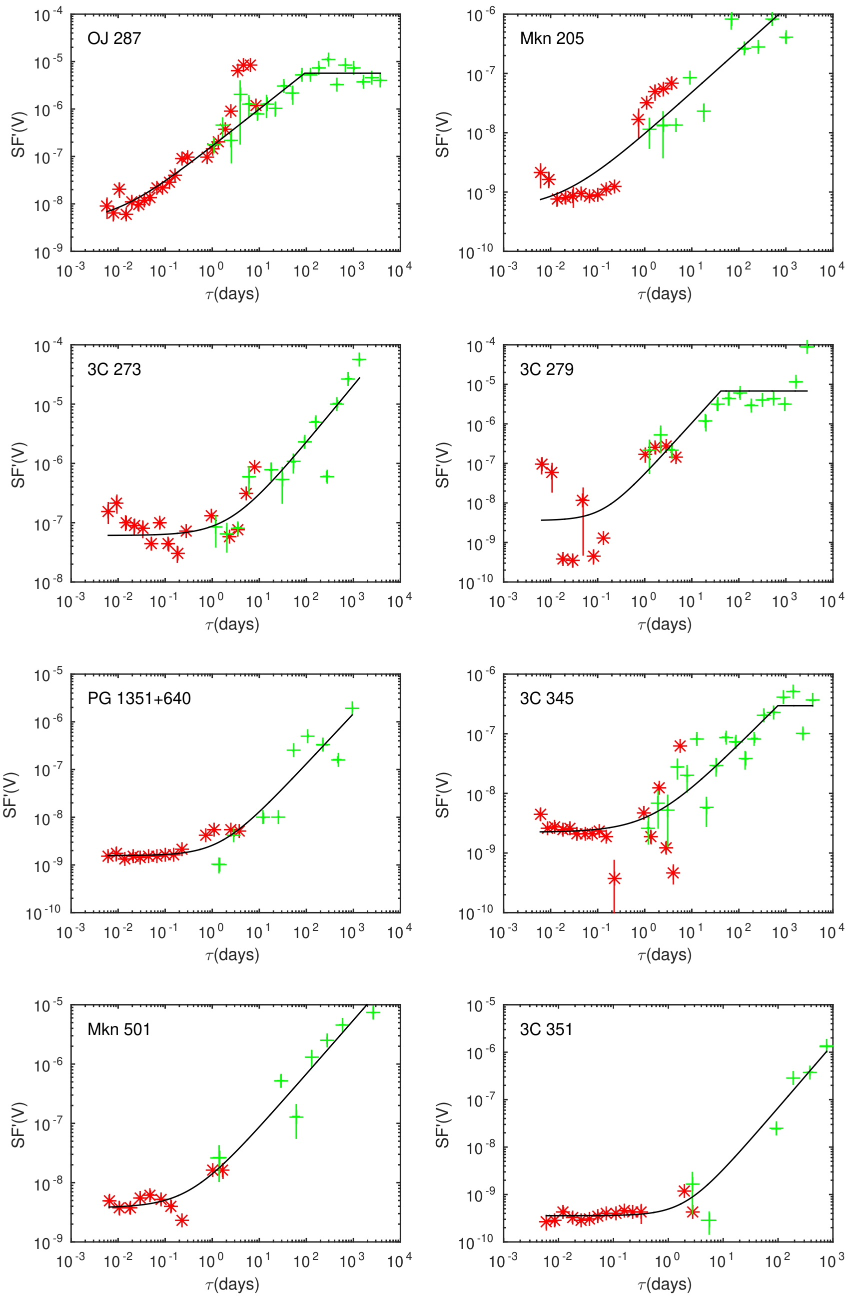

FIGURE D.2— (Cont.) Structure function of the AGNs in our sample in V. Green crosses are the SF using the nighty averages magnitudes and red stars using the whole dataset. The solid line is the best fit with the function given by Eq. D.2.

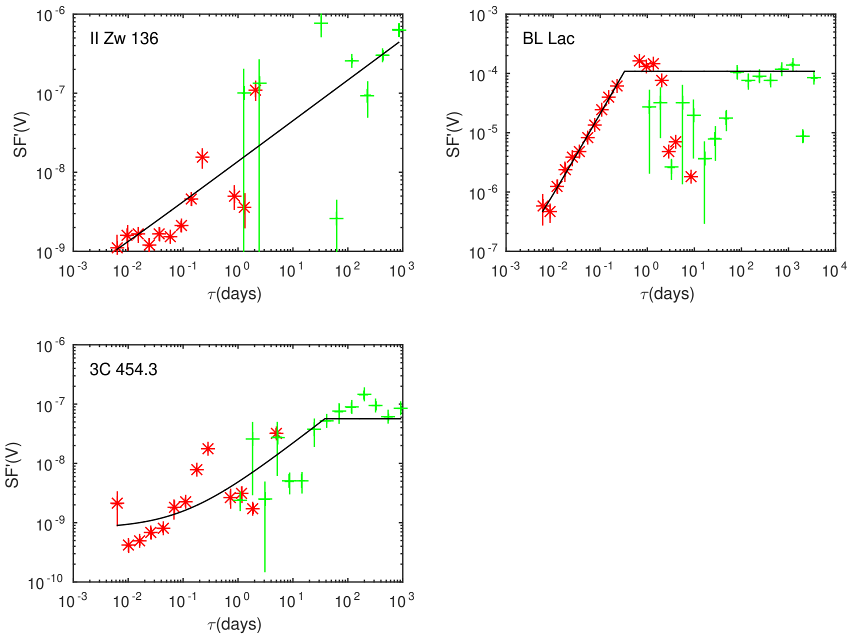

FIGURE D.2— (Cont.) Structure function of the AGNs in our sample in V. Green crosses are the SF using the nighty averages magnitudes and red stars using the whole dataset. The solid line is the best fit with the function given by Eq. D.2.

Table D.2— Logarithm of the longest timescale of variability ($\log T_{max}$; in days).

Object name	B	V	R	I	J	H	K
III Zw 2	-	-	-	-	-	-	-
I Zw 1	-	-	-	-	-	-	-
NAB 0205+02	-	-	-	-	-	-	-
3C 66A	0.86±0.16	0.87±0.16	1.05±0.22	0.98±0.25	1.02±0.51	0.43±0.23	0.40±0.74
AO 0235+16	2.18±1.35	2.12±0.70	1.90±0.62	1.87±0.89	1.62±0.61	0.69±0.27	1.88±1.23
PKS 0405-12	-	-	-	-	-	-	-
S5 0716+71	1.90±0.71	0.53±0.35	0.46±0.35	1.40±1.40	-	-	-
GB 0738+54	1.02±0.52	0.34±0.31	0.66±0.39	0.40±0.84	0.13±3.03	-0.20± 9.32	0.08±6.51
OJ 287	1.76±0.29	1.97±0.27	1.71±0.29	1.42±0.31	2.34±0.63	2.25±0.44	2.61±0.43
Mkn 205	-	-	-	-	-	-	-
3C 273	-	-	-	-	-	-	-
3C 279	1.62±0.89	1.62±0.93	1.31±0.50	1.14±0.67	2.09±0.95	1.06±0.32	0.94±0.21
PG 1351+640	-	-	-	-	-	-	-
3C 345	2.12±0.84	2.83±0.78	2.65±1.00	2.49±0.71	2.68±0.88	1.92±0.69	1.92±0.66
Mkn 501	-	-	-	-	-	-	-
3C 351	-	-	-	-	-	-	-
II Zw 136	-	-	-	-	-	-	-
BL Lac	-0.75±0.23	-0.48±0.15	-0.46±0.23	-0.58±0.37	0.69±0.61	-0.36±0.59	1.03±1.39
3C 454.4	2.20±0.86	1.58±1.00	0.70±3.53	1.04±0.62	1.96±1.30	2.01±0.30	1.92±1.11

Bibliography

Abraham, R. G., Crawford, C. S., & McHardy, I. M. 1991, MNRAS, 252, 482

Ackermann, M., Ajello, M., Atwood, W. B., et al. 2015, ApJ, 810, 14

Agarwal, A. & Gupta, A. C. 2015, MNRAS, 450, 541

Agarwal, A., Gupta, A. C., Bachev, R., et al. 2015, MNRAS, 451, 3882

Agarwal, A., Gupta, A. C., Bachev, R., et al. 2016, MNRAS, 455, 680

Aharonian, F., Akhperjanian, A. G., Bazer-Bachi, A. R., et al. 2007, ApJ, 664, L71

Akritas, M. G. & Bershady, M. A. 1996, ApJ, 470, 706

Alexander, T. 1997, in Astrophysics and Space Science Library, Vol. 218, Astronomical Time Series, ed. D. Maoz, A. Sternberg, & E. M. Leibowitz, 163

Alexander, T. 2013, ArXiv e-prints

Almaini, O., Lawrence, A., Shanks, T., et al. 2000, MNRAS, 315, 325

Antonucci, R. R. J. & Miller, J. S. 1985, ApJ, 297, 621

Bañados, E., Venemans, B. P., Mazzucchelli, C., et al. 2018, Nature, 553, 473

Baade, W. 1956, ApJ, 123, 550

Baade, W. & Minkowski, R. 1954, ApJ, 119, 206

Bachev, R. 2015, MNRAS, 451, L21

Bachev, R., Popov, V., Strigachev, A., et al. 2017, MNRAS, 471, 2216

Bachev, R., Semkov, E., Strigachev, A., et al. 2012, MNRAS, 424, 2625

Bachev, R., Strigachev, A., Semkov, E., et al. 2016, Galaxies, 4, 13

Baring, M. G., Böttcher, M., & Summerlin, E. J. 2017, MNRAS, 464, 4875

Beal, D. J. 2016, in 24th Southeast SAS Users Group Conference, https://analytics.ncsu.edu/sesug/2016/SD-181_Final_PDF.pdf, SD–181

Beckmann, V. & Shrader, C. R. 2012, Active Galactic Nuclei (Wiley-VCH)

Begelman, M. C., Fabian, A. C., & Rees, M. J. 2008, MNRAS, 384, L19

Bennett, A. S. 1963, MNRAS, 127, 3

Bertaud, C., Wlerick, G., Veron, P., et al. 1973, A&A, 24, 357

Bhatta, G., Webb, J. R., Hollingsworth, H., et al. 2013, A&A, 558, A92

Biteau, J. & Giebels, B. 2012, A&A, 548, A123

Blandford, R. D. & Königl, A. 1979, ApJ, 232, 34

Blandford, R. D. & Payne, D. G. 1982, MNRAS, 199, 883

Blandford, R. D. & Rees, M. J. 1974, MNRAS, 169, 395

Blandford, R. D. & Rees, M. J. 1978, in BL Lac Objects, ed. A. M. Wolfe, 328–341

Blandford, R. D. & Znajek, R. L. 1977, MNRAS, 179, 433

Bonning, E., Urry, C. M., Bailyn, C., et al. 2012, ApJ, 756, 13

Borgeest, U. & Schramm, K.-J. 1994, A&A, 284, 764

Bosman, S. E. I. 2017, PhD thesis, Institute of Astronomy, University of Cambridge

Böttcher, M. 2007, Ap&SS, 309, 95

Böttcher, M. & Chiang, J. 2002, ApJ, 581, 127

Brown, L. M. J., Robson, E. I., Gear, W. K., & Smith, M. G. 1989, ApJ, 340, 150

Buffington, A., Booth, C. H., & Hudson, H. S. 1991, PASP, 103, 685

Caccianiga, A. & Marchã, M. J. M. 2004, MNRAS, 348, 937

Caon, N., Capaccioli, M., & D'Onofrio, M. 1993, MNRAS, 265, 1013

Cardelli, J. A., Clayton, G. C., & Mathis, J. S. 1989, ApJ, 345, 245

Carini, M. T., Miller, H. R., Noble, J. C., & Sadun, A. C. 1991, AJ, 101, 1196

Carini, M. T., Walters, R., & Hopper, L. 2011, AJ, 141, 49

Cellone, S. A., Romero, G. E., & Combi, J. A. 2000, AJ, 119, 1534

Celotti, A. & Ghisellini, G. 2008, MNRAS, 385, 283

Chandra, S., Baliyan, K. S., Ganesh, S., & Joshi, U. C. 2011, ApJ, 731, 118

Charbonneau, D., Brown, T. M., Latham, D. W., & Mayor, M. 2000, ApJ, 529, L45

Chatterjee, R., Fossati, G., Urry, C. M., et al. 2013, ApJ, 763, L11

Choloniewski, J. 1981, Acta Astronomica, 31, 293

Chromey, F. R. & Hasselbacher, D. A. 1996, PASP, 108, 944

Ciotti, L. 1991, A&A, 249, 99

Courvoisier, T. J.-L., Robson, E. I., Hughes, D. H., et al. 1988, Nature, 335, 330

Czerny, B., Doroshenko, V. T., Nikołajuk, M., et al. 2003, MNRAS, 342, 1222

Czerny, B., Siemiginowska, A., Janiuk, A., & Gupta, A. C. 2008, MNRAS, 386, 1557

de Diego, J. 1994a, Ph.D. Thesis

de Diego, J. A. 1994b, Ph.D. Thesis

de Diego, J. A., Kidger, M. R., González-Pérez, J. N., & Lehto, H. J. 1997, A&A, 318, 331

de Vaucouleurs, G. 1948, Annales d'Astrophysique, 11, 247

de Vaucouleurs, G. 1953, MNRAS, 113, 134

de Vries, W. H., Becker, R. H., & White, R. L. 2003, AJ, 126, 1217

de Vries, W. H., Becker, R. H., & White, R. L. 2006, AJ, 131, 666

Di Matteo, T., Springel, V., & Hernquist, L. 2005, Nature, 433, 604

Dobrotka, A., Antonuccio-Delogu, V., & Bajčičáková, I. 2017, MNRAS, 470, 2439

Donato, F., Maurin, D., Salati, P., et al. 2001, ApJ, 563, 172

Edelson, R., Griffiths, G., Markowitz, A., et al. 2001, ApJ, 554, 274

Edelson, R., Mushotzky, R., Vaughan, S., et al. 2013, ApJ, 766, 16

Edelson, R., Turner, T. J., Pounds, K., et al. 2002, ApJ, 568, 610

Edelson, R. A. & Krolik, J. H. 1988, ApJ, 333, 646

Edge, D. O., Shakeshaft, J. R., McAdam, W. B., Baldwin, J. E., & Archer, S. 1959, MmRAS, 68, 37

Efstathiou, A. & Rowan-Robinson, M. 1995, MNRAS, 273, 649

Elvis, M., Wilkes, B. J., McDowell, J. C., et al. 1994, ApJS, 95, 1

Emmanoulopoulos, D., McHardy, I. M., & Uttley, P. 2010, MNRAS, 404, 931

Erwin, P. 2015, ApJ, 799, 226

Fan, J. H., Cheng, K. S., Zhang, L., & Liu, C. H. 1997, A&A, 327, 947

Fan, J. H. & Lin, R. G. 1999, ApJS, 121, 131

Fan, J. H. & Lin, R. G. 2000, ApJ, 537, 101

Fan, J. H., Rieger, F. M., Hua, T. X., et al. 2008, Astroparticle Physics, 28, 508

Fanaroff, B. L. & Riley, J. M. 1974, MNRAS, 167, 31P

Fath, E. A. 1909, Popular Astronomy, 17, 504

Feigelson, E. D. & Babu, G. J. 2012, Modern Statistical Methods for Astronomy (Cambridge University Press)

Feigelson, E. D., Bradt, H., McClintock, J., et al. 1986, ApJ, 302, 337

Ferland, G. J. & Mushotzky, R. F. 1982, ApJ, 262, 564

Fiorucci, M. & Tosti, G. 1996, A&AS, 117, 475

Ford, H. C., Harms, R. J., Tsvetanov, Z. I., et al. 1994, ApJ, 435, L27

Foschini, L., Ghisellini, G., Tavecchio, F., Bonnoli, G., & Stamerra, A. 2011, A&A, 530, A77

Fossati, G., Maraschi, L., Celotti, A., Comastri, A., & Ghisellini, G. 1998, MNRAS, 299, 433

Fritz, J., Franceschini, A., & Hatziminaoglou, E. 2006, MNRAS, 366, 767

Fukugita, M., Shimasaku, K., & Ichikawa, T. 1995, PASP, 107, 945

Garcia, A., Sodré, L., Jablonski, F. J., & Terlevich, R. J. 1999, MNRAS, 309, 803

Gaskell, C. M. 2009, New A Rev., 53, 140

Gaur, H., Gupta, A., Bachev, R., et al. 2017, Galaxies, 5, 94

Gaur, H., Gupta, A. C., Bachev, R., et al. 2015a, MNRAS, 452, 4263

Gaur, H., Gupta, A. C., Bachev, R., et al. 2015b, A&A, 582, A103

Gaur, H., Gupta, A. C., Lachowicz, P., & Wiita, P. J. 2010, ApJ, 718, 279

Gaur, H., Mohan, P., Wierzcholska, A., & Gu, M. 2018, MNRAS, 473, 3638

Gear, W. K., Robson, E. I., & Brown, L. M. J. 1986, Nature, 324, 546

George, I. M., Warwick, R. S., & Bromage, G. E. 1988, MNRAS, 232, 793

Ghisellini, G., ed. 2013, Lecture Notes in Physics, Berlin Springer Verlag, Vol. 873, Radiative Processes in High Energy Astrophysics

Ghisellini, G., Maraschi, L., & Tavecchio, F. 2009, MNRAS, 396, L105

Ghisellini, G. & Tavecchio, F. 2008, MNRAS, 387, 1669

Ghisellini, G., Villata, M., Raiteri, C. M., et al. 1997, A&A, 327, 61

Ghosh, K. K., Ramsey, B. D., Sadun, A. C., Soundararajaperumal, S., & Wang, J. 2000, ApJ, 537, 638

Gillessen, S., Eisenhauer, F., Trippe, S., et al. 2009, ApJ, 692, 1075

Gilliland, R. L. & Brown, T. M. 1988, PASP, 100, 754

Gilliland, R. L. & Brown, T. M. 1992, PASP, 104, 582

Gilliland, R. L., Brown, T. M., Duncan, D. K., et al. 1991, AJ, 101, 541

Gilliland, R. L., Brown, T. M., Kjeldsen, H., et al. 1993, AJ, 106, 2441

Giommi, P., Ansari, S. G., & Micol, A. 1995, A&AS, 109, 267

Giommi, P., Barr, P., Pollock, A. M. T., Garilli, B., & Maccagni, D. 1990, ApJ, 356, 432

Giommi, P., Massaro, E., Chiappetti, L., et al. 1999, A&A, 351, 59

Giveon, U., Maoz, D., Kaspi, S., Netzer, H., & Smith, P. S. 1999, MNRAS, 306, 637

González-Pérez, J. N., Kidger, M. R., & de Diego, J. A. 1996, A&A, 311, 57

González-Pérez, J. N., Kidger, M. R., & Martín-Luis, F. 2001, AJ, 122, 2055

Gopal-Krishna, Goyal, A., Joshi, S., et al. 2011, MNRAS, 416, 101

Gopal-Krishna, Sagar, R., & Wiita, P. J. 1995, MNRAS, 274, 701

Gopal-Krishna & Subramanian, K. 1991, Nature, 349, 766

Gopal-Krishna & Wiita, P. J. 1992, A&A, 259, 109

Gopal-Krishna & Wiita, P. J. 2018, Bulletin de la Societe Royale des Sciences de Liege, 87, 281

Goyal, A., Gopal-Krishna, Paul J., W., Stalin, C. S., & Sagar, R. 2013, MNRAS, 435, 1300

Goyal, A., Stawarz, Ł., Ostrowski, M., et al. 2017, ApJ, 837, 127

Goyal, A., ŏ141. Stawarz, Zola, S., et al. 2018, The Astrophysical Journal, 863, 175

Graham, A., Lauer, T. R., Colless, M., & Postman, M. 1996, ApJ, 465, 534

Granato, G. L., Zitelli, V., Bonoli, F., et al. 1993, ApJS, 89, 35

Greenstein, J. L. & Matthews, T. 1963, Nature, 197, 1041

Greenstein, J. L. & Schmidt, M. 1964, ApJ, 140, 1

Groth, E. J. 1986, AJ, 91, 1244

Grundahl, F. & Sorensen, A. N. 1996, A&AS, 116, 367

Guo, H. & Gu, M. 2016, ApJ, 822, 26

Gupta, A. C., Agarwal, A., Mishra, A., et al. 2017, MNRAS, 465, 4423

Gupta, A. C. & Joshi, U. C. 2005, A&A, 440, 855

Gupta, A. C., Kalita, N., Gaur, H., & Duorah, K. 2016, MNRAS, 462, 1508

Gupta, A. C., Krichbaum, T. P., Wiita, P. J., et al. 2012, MNRAS, 425, 1357

Hagen-Thorn, V. A. 1997, Astronomy Letters, 23, 19

Hagen-Thorn, V. A. & Marchenko, S. G. 1989, Astrofizika, 31, 231

Hagen-Thorn, V. A., Marchenko, S. G., & Iakovleva, V. A. 1985, Astrofizika, 22, 5

Hagen-Thorn, V. A., Marchenko, S. G., Takalo, L. O., et al. 1998, A&AS, 133, 353

Hao, J.-M., Wang, B.-J., Jiang, Z.-J., & Dai, B.-Z. 2010, Research in Astronomy and Astrophysics, 10, 125

Hartman, R. C., Bertsch, D. L., Dingus, B. L., et al. 1993, ApJ, 407, L41

Häußler, B., Bamford, S. P., Vika, M., et al. 2013, MNRAS, 430, 330

Hazard, C., Mackey, M. B., & Shimmins, A. J. 1963, Nature, 197, 1037

Heckman, T. M. 1980, A&A, 87, 152

Heidt, J. & Wagner, S. J. 1996, A&A, 305, 42

Heidt, J. & Wagner, S. J. 1998, A&A, 329, 853

Heil, L. M., Vaughan, S., & Uttley, P. 2012, MNRAS, 422, 2620

Helsel, D. R. 2011, Statistics for censored environmental data using minitab and R (Wiley)

Ho, L. C., Filippenko, A. V., & Sargent, W. L. W. 1997, ApJ, 487, 568

Hoffmeister, C. 1929, Astronomische Nachrichten, 236, 233

Homan, D. C., Ojha, R., Wardle, J. F. C., et al. 2001, ApJ, 549, 840

Honeycutt, R. K. 1992, PASP, 104, 435

Honeycutt, R. K., Adams, B., Grabhorn, R., et al. 1989, in Remote Access Automatic Telescopes, ed. D.S. Hayes, and R.M. Genet (Mesa, Fairborn), 105

Hook, I. M., McMahon, R. G., Boyle, B. J., & Irwin, M. J. 1994, MNRAS, 268, 305

Hovatta, T., Valtaoja, E., Tornikoski, M., & Lähteenmäki, A. 2009, A&A, 494, 527

Howell, S. B. 1989, PASP, 101, 616

Howell, S. B. 1992, in ASP Conf. Ser. 23: Astronomical CCD Observing and Reduction Techniques, 105

Howell, S. B. 1993, in IAU Colloq. 136: Stellar Photometry - Current Techniques and Future Developments, 318

Hoyle, F. & Fowler, W. A. 1963, Nature, 197, 533

Hu, S. M., Chen, X., Guo, D. F., Jiang, Y. G., & Li, K. 2014, MNRAS, 443, 2940

Hu, S. M., Wu, J. H., Zhao, G., & Zhou, X. 2006, MNRAS, 373, 209

Hudec, R., Bašta, M., Pihajoki, P., & Valtonen, M. 2013, A&A, 559, A20

Hughes, P. A., Aller, H. D., & Aller, M. F. 1992, ApJ, 396, 469

Hunt, L. K., Mannucci, F., Testi, L., et al. 1998, AJ, 115, 2594

Hunter, S. D., Bertsch, D. L., Dingus, B. L., et al. 1993, ApJ, 409, 134

Hyvönen, T., Kotilainen, J. K., Falomo, R., Örndahl, E., & Pursimo, T. 2007, A&A, 476, 723

Impey, C. D., Brand, P. W. J. L., Wolstencroft, R. D., & Williams, P. M. 1982, MNRAS, 200, 19

Jauncey, D. L. & Macquart, J.-P. 2001, A&A, 370, L9

Jefferys, W. H., Fitzpatrick, M. J., & McArthur, B. E. 1987, Celestial Mechanics, 41, 39

Jennison, R. C. & Das Gupta, M. K. 1953, Nature, 172, 996

Johansson, L. & Bergvall, N. 1990, A&AS, 86, 167

Jones, T. W. 1988, ApJ, 332, 678

Jones, T. W., Rudnick, L., Aller, H. D., et al. 1985, ApJ, 290, 627

Jorden, P. R., Deltorn, J.-M., & Oates, A. P. 1994, in Proc. SPIE Vol. 2198, p. 836-850, Instrumentation in Astronomy VIII, David L. Crawford; Eric R. Craine; Eds., 836–850

Jorstad, S. G., Marscher, A. P., Mattox, J. R., et al. 2001, ApJS, 134, 181

Joshi, R., Chand, H., Wiita, P. J., Gupta, A. C., & Srianand, R. 2012, MNRAS, 419, 3433

Kalita, N., Gupta, A. C., Wiita, P. J., Bhagwan, J., & Duorah, K. 2015, MNRAS, 451, 1356

Katajainen, S., Takalo, L. O., Sillanpää, A., et al. 2000, A&AS, 143, 357

Kataoka, J., Takahashi, T., Makino, F., et al. 2000, ApJ, 528, 243

Kaur, N., Sameer, Baliyan, K. S., & Ganesh, S. 2017, MNRAS, 469, 2305

Kawaguchi, T., Mineshige, S., Umemura, M., & Turner, E. L. 1998, ApJ, 504, 671

Kellermann, K. I., Sramek, R., Schmidt, M., Shaffer, D. B., & Green, R. 1989, AJ, 98, 1195

Kennedy, R., Bamford, S. P., Baldry, I., et al. 2015, MNRAS, 454, 806

Kewley, L. J., Groves, B., Kauffmann, G., & Heckman, T. 2006, MNRAS, 372, 961

Kidger, M. R., Gonzalez-Perez, J. N., de Diego, J. A., et al. 1995, A&AS, 113, 431

Kidger, M. R., Gonzalez-Perez, J. N., & Sadun, A. 1996, in Astronomical Society of the Pacific Conference Series, Vol. 110, Blazar Continuum Variability, ed. H. R. Miller, J. R. Webb, & J. C. Noble, 123

Kidger, M. R., Sillanpää, A., & Takalo, L. O. 1994a, in Workshop on Intensive Monitoring of OJ 287, 106

Kidger, M. R., Takalo, L. O., & de Diego, J. A. 1994b, A&A, 282, 369

Kirk, J. G., Rieger, F. M., & Mastichiadis, A. 1998, A&A, 333, 452

Kjeldsen, H. & Frandsen, S. 1992, PASP, 104, 413

Kniffen, D. A., Bertsch, D. L., Fichtel, C. E., et al. 1993, ApJ, 411, 133

Kokubo, M., Morokuma, T., Minezaki, T., et al. 2014, ApJ, 783, 46

Kormendy, J. & Richstone, D. 1995, ARA&A, 33, 581

Kotilainen, J. K. & Falomo, R. 2004, A&A, 424, 107

Kotilainen, J. K., Ward, M. J., Boisson, C., Depoy, D. L., & Smith, M. G. 1992a, MNRAS, 256, 149

Kotilainen, J. K., Ward, M. J., Boisson, C., et al. 1992b, MNRAS, 256, 125

Kraemer, S. B., Schmitt, H. R., & Crenshaw, D. M. 2008, ApJ, 679, 1128

Krolik, J. H. 1999, Active galactic nuclei : from the central black hole to the galactic environment (Princeton University Press)

Kumar, P. & Gopal-Krishna, Hum, C. 2015, MNRAS, 448, 1463

Kushwaha, P., Singh, K. P., & Sahayanathan, S. 2014, ApJ, 796, 61

Lainela, M. & Valtaoja, E. 1993, ApJ, 416, 485

Landolt, A. U. 1992, AJ, 104, 340

Lauer, T. R. 1999, PASP, 111, 1434

Lehto, H. J. & Valtonen, M. J. 1996, ApJ, 460, 207

Licandro, J., Serra-Ricart, M., Oscoz, A., Casas, R., & Osip, D. 2000, AJ, 119, 3133

Lorenzetti, D., Spinoglio, L., Massaro, E., & Perola, G. C. 1989, ApJS, 71, 175

Lovell, J. E. J., Rickett, B. J., Macquart, J.-P., et al. 2008, ApJ, 689, 108

Lyubarskii, Y. E. 1997, MNRAS, 292, 679

Malkan, M. A. & Sargent, W. L. W. 1982, ApJ, 254, 22

Mangalam, A. V. & Wiita, P. J. 1993, ApJ, 406, 420

Marscher, A. P. 2014, ApJ, 780, 87

Marscher, A. P. & Gear, W. K. 1985, ApJ, 298, 114

Massaro, E. & Trevese, D. 1996, A&A, 312, 810

Massey, P., Silkey, M., Garmany, C. D., & Degioia-Eastwood, K. 1989, AJ, 97, 107

Matthews, T. A. & Sandage, A. R. 1963, ApJ, 138, 30

Mattox, J. R., Wagner, S. J., Malkan, M., et al. 1997, ApJ, 476, 692

Mead, A. R. G., Ballard, K. R., Brand, P. W. J. L., et al. 1990, A&AS, 83, 183

Meng, N., Wu, J., Webb, J. R., Zhang, X., & Dai, Y. 2017, MNRAS, 469, 3588

Middei, R., Vagnetti, F., Antonucci, M., & Serafinelli, R. 2016, in Journal of Physics Conference Series, Vol. 689, Journal of Physics Conference Series, 012006

Mighell, K. J. & Leese, R. 1999, in ASP Conf. Ser. 189: Precision CCD Photometry, 50

Miller, H. R., Carini, M. T., & Goodrich, B. D. 1989, Nature, 337, 627

Miyoshi, M., Moran, J., Herrnstein, J., et al. 1995, Nature, 373, 127

Mocanu, G. R. & Marcu, A. 2012, Astronomische Nachrichten, 333, 166

Mohan, P., Gupta, A. C., Bachev, R., & Strigachev, A. 2016, MNRAS, 456, 654

Montagni, F., Maselli, A., Massaro, E., et al. 2006, A&A, 451, 435

Moore, R. L. & Stockman, H. S. 1984, ApJ, 279, 465

Morini, M., Chiappetti, L., Maccagni, D., et al. 1986, ApJ, 306, L71

Mortlock, D. J., Warren, S. J., Venemans, B. P., et al. 2011, Nature, 474, 616

Mushotzky, R. F., Done, C., & Pounds, K. A. 1993, ARA&A, 31, 717

Nandra, K., George, I. M., Mushotzky, R. F., Turner, T. J., & Yaqoob, T. 1997, ApJ, 476, 70

Naylor, T. 1998, MNRAS, 296, 339

Nenkova, M., Sirocky, M. M., Ivezić, Ž., & Elitzur, M. 2008, ApJ, 685, 147

Nesci, R., Maesano, M., Massaro, E., et al. 1998, A&A, 332, L1

Netzer, H. 2015, ARA&A, 53, 365

Netzer, H. & Peterson, B. M. 1997, in Astrophysics and Space Science Library, Vol. 218, Astronomical Time Series, ed. D. Maoz, A. Sternberg, & E. M. Leibowitz, 85

Newberry, M. V. 1992, in ASP Conf. Ser. 25: Astronomical Data Analysis Software and Systems I, 307

Nieppola, E., Tornikoski, M., & Valtaoja, E. 2006, A&A, 445, 441

Nilsson, K., Pasanen, M., Takalo, L. O., et al. 2007, A&A, 475, 199

Nilsson, K., Pursimo, T., Heidt, J., et al. 2003, A&A, 400, 95

Nilsson, K., Pursimo, T., Takalo, L. O., et al. 1999, PASP, 111, 1223

Osterbrock, D. E. 1989, Astrophysics of gaseous nebulae and active galactic nuclei (University Science Books)

Osterman, M. A., Miller, H. R., Marshall, K., et al. 2007, ApJ, 671, 97

Paczynski, B. 1996, ARA&A, 34, 419

Padovani, P. 2007, Ap&SS, 309, 63

Padovani, P. 2016, A&A Rev., 24, 13

Padovani, P., Alexander, D. M., Assef, R. J., et al. 2017, A&A Rev., 25, 2

Padovani, P. & Giommi, P. 1995, MNRAS, 277, 1477

Paliya, V. S., Böttcher, M., Diltz, C., et al. 2015, ApJ, 811, 143

Paltani, S., Courvoisier, T. J.-L., & Walter, R. 1998, A&A, 340, 47

Pandey, A., Gupta, A. C., & Wiita, P. J. 2017, ApJ, 841, 123

Papadakis, I. E., Boumis, P., Samaritakis, V., & Papamastorakis, J. 2003, A&A, 397, 565

Parker, M. L., Fabian, A. C., Matt, G., et al. 2015, MNRAS, 447, 72

Peng, C. Y., Ho, L. C., Impey, C. D., & Rix, H.-W. 2010, AJ, 139, 2097

Penny, A. J. & Leese, R. 1996a, in ASP Conf. Ser. 101: Astronomical Data Analysis Software and Systems V, 29

Penny, A. J. & Leese, R. 1996b, in ASP Conf. Ser. 101: Astronomical Data Analysis Software and Systems V, 29

Peterson, B. M., Ferrarese, L., Gilbert, K. M., et al. 2004, ApJ, 613, 682

Peterson, B. M., Wanders, I., Horne, K., et al. 1998, PASP, 110, 660

Pier, E. A. & Krolik, J. H. 1992, ApJ, 399, L23

Pietilä, H. 1998, ApJ, 508, 669

Poon, H., Fan, J. H., & Fu, J. N. 2009, ApJS, 185, 511

Potter, W. J. & Cotter, G. 2012, MNRAS, 423, 756

Pursimo, T., Nilsson, K., Takalo, L. O., et al. 2002, A&A, 381, 810

Pursimo, T., Takalo, L. O., Sillanpää, A., et al. 2000, A&AS, 146, 141

Qian, B. & Tao, J. 2004, PASP, 116, 161

Qian, S. J., Quirrenbach, A., Witzel, A., et al. 1991, A&A, 241, 15

Quirrenbach, A., Witzel, A., Wagner, S., et al. 1991, ApJ, 372, L71

Raiteri, C. M., Villata, M., Acosta-Pulido, J. A., et al. 2017, Nature, 552, 374

Raiteri, C. M., Villata, M., Aller, H. D., et al. 2001, A&A, 377, 396

Raiteri, C. M., Villata, M., D'Ammando, F., et al. 2013, MNRAS, 436, 1530

Raiteri, C. M., Villata, M., de Francesco, G., et al. 1998, A&AS, 132, 361

Raiteri, C. M., Villata, M., Smith, P. S., et al. 2012, A&A, 545, A48

Raiteri, C. M., Villata, M., Tosti, G., et al. 2003, A&A, 402, 151

Ramírez, A., de Diego, J. A., Dultzin, D., & González-Pérez, J.-N. 2009, AJ, 138, 991

Ramírez, A., de Diego, J. A., Dultzin-Hacyan, D., & González-Pérez, J. N. 2004, A&A, 421, 83

Rani, B., Gupta, A. C., Joshi, U. C., Ganesh, S., & Wiita, P. J. 2011, MNRAS, 413, 2157

Reynolds, C. S. & Nowak, M. A. 2003, Phys. Rep., 377, 389

Rickett, B. J., Witzel, A., Kraus, A., Krichbaum, T. P., & Qian, S. J. 2001, ApJ, 550, L11

Robinson, L. B., Wei, M. Z., Borucki, W. J., et al. 1995, PASP, 107, 1094

Romano, P. & Peterson, B. M. 1999, in ASP Conf. Ser. 175: Structure and Kinematics of Quasar Broad Line Regions, 55

Romero, G. E., Cellone, S. A., & Combi, J. A. 1999, A&AS, 135, 477

Romero, G. E., Cellone, S. A., Combi, J. A., & Andruchow, I. 2002, A&A, 390, 431

Rowan-Robinson, M. 1977, ApJ, 213, 635

Rybicki, G. B. & Lightman, A. P. 1986, Radiative Processes in Astrophysics (Wiley-VCH)

Sagar, R., Stalin, C. S., Gopal-Krishna, & Wiita, P. J. 2004, MNRAS, 348, 176

Sánchez Portal, M. 1999, MNRAS, 310, 117

Sandage, A. 1965, ApJ, 141, 1560

Sandage, A. R. 1971, in Pontificiae Academiae Scientiarum Scripta Varia, Proceedings of a Study Week on Nuclei of Galaxies, held in Rome, April 13-18, 1970, Amsterdam: North Holland, and New York: American Elsevier, 1971, edited by D.J.K. O'Connell., p.271, 271

Sanders, D. B., Phinney, E. S., Neugebauer, G., Soifer, B. T., & Matthews, K. 1989, ApJ, 347, 29

Sandrinelli, A., Covino, S., & Treves, A. 2014, A&A, 562, A79

Scaringi, S., Körding, E., Uttley, P., et al. 2012, MNRAS, 421, 2854

Scarpa, R., Urry, C. M., Falomo, R., Pesce, J. E., & Treves, A. 2000, ApJ, 532, 740

Scharwächter, J., Eckart, A., Pfalzner, S., et al. 2003, A&A, 405, 959

Schlegel, D. J., Finkbeiner, D. P., & Davis, M. 1998, ApJ, 500, 525

Schmidt, M. 1963, Nature, 197, 1040

Schmidt, M. & Matthews, T. A. 1964, ApJ, 139, 781

Schmitt, J. L. 1968, Nature, 218, 663

Schödel, R., Ott, T., Genzel, R., et al. 2002, Nature, 419, 694

Schramm, K.-J., Borgeest, U., Kuehl, D., Linde, J. V., & Linnert, M. D. 1994a, A&AS, 104, 473

Schramm, K.-J., Borgeest, U., Kuehl, D., et al. 1994b, A&AS, 106, 349

Sersic, J. L. 1968, Atlas de galaxias australes (Observatorio Astronomico, Cordoba, Argentina)

Seyfert, C. K. 1943, ApJ, 97, 28

Shakura, N. I. & Sunyaev, R. A. 1973, A&A, 24, 337

Siemiginowska, A., Kuhn, O., Elvis, M., et al. 1995, ApJ, 454, 77

Sikora, M., Begelman, M. C., & Rees, M. J. 1994, ApJ, 421, 153

Silk, J. & Rees, M. J. 1998, A&A, 331, L1

Sillanpaa, A., Haarala, S., Valtonen, M. J., Sundelius, B., & Byrd, G. G. 1988, ApJ, 325, 628

Sillanpaa, A., Takalo, L. O., Pursimo, T., et al. 1996a, A&A, 305, L17

Sillanpaa, A., Takalo, L. O., Pursimo, T., et al. 1996b, A&A, 315, L13

Simonetti, J. H., Cordes, J. M., & Heeschen, D. S. 1985, ApJ, 296, 46

Slipher, V. M. 1917, Lowell Observatory Bulletin, 3, 59

Smith, A. G. & Nair, A. D. 1995, PASP, 107, 863

Smith, E. P., Heckman, T. M., Bothun, G. D., Romanishin, W., & Balick, B. 1986a, ApJ, 306, 64

Smith, F. G. 1951, Nature, 168, 555

Smith, P. S., Balonek, T. J., Heckert, P. A., & Elston, R. 1986b, ApJ, 305, 484

Soldi, S., Türler, M., Paltani, S., et al. 2008, A&A, 486, 411

Spruit, H. C. 2010, in Lecture Notes in Physics, Berlin Springer Verlag, ed. T. Belloni, Vol. 794, 233

Stalin, C. S., Gopal Krishna, Sagar, R., & Wiita, P. J. 2004, Journal of Astrophysics and Astronomy, 25, 1

Stalin, C. S., Gopal-Krishna, Sagar, R., et al. 2006, MNRAS, 366, 1337

Stetson, P. B. 1987, PASP, 99, 191

Stickel, M., Fried, J. W., & Kuehr, H. 1993, A&AS, 98, 393

Subasavage, J. P., Bailyn, C. D., Smith, R. C., et al. 2010, in Proc. SPIE, Vol. 7737, Observatory Operations: Strategies, Processes, and Systems III, 77371C

Sukanya, N., Stalin, C. S., Jeyakumar, S., et al. 2016, Research in Astronomy and Astrophysics, 16, 27

Tadhunter, C. 2008, New A Rev., 52, 227

Takahashi, T., Tashiro, M., Madejski, G., et al. 1996, ApJ, 470, L89

Takalo, L. O., Sillanpaeae, A., & Nilsson, K. 1994, A&AS, 107, 497

Takalo, L. O., Sillanpaeae, A., Pursimo, T., et al. 1996, A&AS, 120, 313

Takalo, L. O., Sillanpaeae, A., Valtaoja, E., et al. 1998, A&AS, 129, 577

Tavecchio, F., Maraschi, L., & Ghisellini, G. 1998, ApJ, 509, 608

Tavecchio, F., Maraschi, L., Pian, E., et al. 2001, ApJ, 554, 725

Trèvese, D. & Vagnetti, F. 2002, ApJ, 564, 624

Turner, T. J., George, I. M., Nandra, K., & Mushotzky, R. F. 1997, ApJS, 113, 23

Turner, T. J., Romano, P., George, I. M., et al. 2001, ApJ, 561, 131

Ulrich, M.-H., Maraschi, L., & Urry, C. M. 1997, ARA&A, 35, 445

Urry, C. M. & Padovani, P. 1995, PASP, 107, 803

Urry, C. M., Scarpa, R., O'Dowd, M., et al. 2000, ApJ, 532, 816

Urry, C. M., Treves, A., Maraschi, L., et al. 1997, ApJ, 486, 799

Uttley, P., McHardy, I. M., & Vaughan, S. 2005, MNRAS, 359, 345

Uttley, P., McHardy, I. M., & Vaughan, S. 2017, A&A, 601, L1

Vagnetti, F., Trevese, D., & Nesci, R. 2003, ApJ, 590, 123

Valtaoja, E., Terasranta, H., Urpo, S., et al. 1992, A&A, 254, 71

Valtaoja, E., Valtaoja, L., Efimov, I. S., & Shakhovskoi, N. M. 1990, AJ, 99, 769

Valtonen, M. J., Ciprini, S., & Lehto, H. J. 2012, MNRAS, 427, 77

Valtonen, M. J., Nilsson, K., Sillanpää, A., et al. 2006, ApJ, 643, L9

Valtonen, M. J., Zola, S., Ciprini, S., et al. 2016, ApJ, 819, L37

Vaughan, S., Edelson, R., Warwick, R. S., & Uttley, P. 2003, MNRAS, 345, 1271

Vaughan, S. & Uttley, P. 2008, ArXiv e-prints

Veilleux, S. & Osterbrock, D. E. 1987, ApJS, 63, 295

Villata, M., Mattox, J. R., Massaro, E., et al. 2000a, A&A, 363, 108

Villata, M. & Raiteri, C. M. 1999, A&A, 347, 30

Villata, M., Raiteri, C. M., Ghisellini, G., et al. 1997, A&AS, 121, 119

Villata, M., Raiteri, C. M., Kurtanidze, O. M., et al. 2004, A&A, 421, 103

Villata, M., Raiteri, C. M., Kurtanidze, O. M., et al. 2002a, A&A, 390, 407

Villata, M., Raiteri, C. M., Popescu, M. D., et al. 2000b, A&AS, 144, 481

Villata, M., Raiteri, C. M., Tosti, G., et al. 2002b, Mem. Soc. Astron. Italiana, 73, 1191

Vovk, I. & Neronov, A. 2013, ApJ, 767, 103

Vulcani, B., Bamford, S. P., Häußler, B., et al. 2014, MNRAS, 441, 1340

Wagner, S., Sanchez-Pons, F., Quirrenbach, A., & Witzel, A. 1990, A&A, 235, L1

Wagner, S. J. & Witzel, A. 1995, ARA&A, 33, 163

Wagner, S. J., Witzel, A., Heidt, J., et al. 1996, AJ, 111, 2187

Wall, J. V. & Jenkins, C. R. 2003, Practical Statistics for Astronomers (Cambridge observing handbooks for research astronomers)

Wiita, P. J., Mangalam, A. V., & Chakrabarti, S. K. 1992, in American Institute of Physics Conference Series, 251–254

Winkler, H., Glass, I. S., van Wyk, F., et al. 1992, MNRAS, 257, 659

Woltjer, L. 1959, ApJ, 130, 38

Wu, J., Böttcher, M., Zhou, X., et al. 2012, AJ, 143, 108

Wu, J., Zhou, X., Ma, J., et al. 2007, AJ, 133, 1599

Wurtz, R., Stocke, J. T., & Yee, H. K. C. 1996, ApJS, 103, 109

Xilouris, E. M., Papadakis, I. E., Boumis, P., et al. 2006, A&A, 448, 143

Xiong, D., Bai, J., Zhang, H., et al. 2017, ApJS, 229, 21

Yan, D., Zeng, H., & Zhang, L. 2014, MNRAS, 439, 2933

Young, A. T. 1967, AJ, 72, 747

Zhang, B. K., Dai, B. Z., Wang, L. P., et al. 2012, MNRAS, 421, 3111

Zhang, Y. H. 2010, ApJ, 713, 180

Zhang, Y.-H. & Xie, G.-Z. 1996, A&AS, 119, 199

Zhang, Y. H., Xu, L., & Li, J. C. 2016, Astronomische Nachrichten, 337, 286

Zheng, Z., Wu, H., Mao, S., et al. 1999, A&A, 349, 735

Zitelli, V., Granato, G. L., Mandolesi, N., Wade, R., & Danese, L. 1993, ApJS, 84, 185

Acknowledgments

First of all, I would like to express my thanks to Mark Kidger, my advisor at the Instituto de Astrofísica de Canarias, for his support and for introducing me in the fascinating topic of blazars. He also taught me the many aspects of the optical and infrared observational astronomy during the multiple observing nights at the observatories of Teide and Roque de los Muchachos.

I would like to extend my sincere gratitude to Jürgen Schmitt, my advisor at the Hamburger Sternwarte, for his help and advice. He gave me the last push and motivation to finish this thesis and gave me the necessary time in completing the thesis, time that I should have invested in the TIGRE telescope.

I am also grateful to Luz Marina Cairós Barreto, Rafael Manso Sainz, Robert Mettin, Uwe Wolter, Jan Robrade, and Stefan Czesla for proofreading this work. They have all contributed significantly to make the text easier to read.

I very much appreciate the discussions with Alexander Hempelmann and Marco Mittag. The topic of these discussions was sometimes not related to this thesis, but they were always encouraging and inspiring. Many thanks to Dieter Engels for the wise advice and helpful suggestions he has given to me in the final process of this thesis.

I would like to acknowledge the support of the technical staff of the Canary Islands observatories. Without their help, I could not obtain the data necessary for this thesis. I am also grateful to my colleagues of the Hamburger Sternwarte and the IAC for the friendly working environment.

Many thanks to Luzma, Robert, Oli, and Rafa for the support and understanding.

Finally, I want to dedicate this thesis to my parents that could not see this work finished. They always provided me with the support, continuous encouragement, and attention.